SIMULATIONS OF INCOMPRESSIBLE VISCOUS THERMAL FLOWS BY LATTICE BOLTZMANN METHOD

PENG YAN

NATIONAL UNIVERSITY OF SINGAPORE

2004

SIMULATIONS OF INCOMPRESSIBLE VISCOUS THERMAL FLOWS BY LATTICE BOLTZMANN METHOD

PENG YAN

(*B. Eng., M. Eng., Nanjing University of Aeronautics and Astronautics, China*)

A THESIS SUBMITTED

FOR THE DEGREE OF DOCTOR OF PHILOSOPHY

DEPARTMENT OF MECHANICAL ENGINEERING

NATIONAL UNIVERSITY OF SINGAPORE

2004

ACKNOWLEDGEMENTS

TABLE OF CONTENTS

Summary

In recent years, lattice Boltzmann method (LBM) has been developed into an alternative computational fluid dynamics (CFD) tool. Unlike the conventional CFD solvers, which are based on the discretization of the macroscopic continuum equations, this scheme is based on the mesoscopic kinetic equations. When a simplified kinetic equation is developed, solving the complicated kinetic equations such as the full Boltzmann equation and following each particle as in the molecular dynamics simulations are avoided. So this method has become very popular and many successful applications such as in turbulence flows, multiphase flows and chemical-reaction flows have been conducted. However, it still needs some improvements in order to be developed into a practical and competitive CFD solver. One of them is its use for the thermal applications, which is one of the most challenging issues left with LBM research. This includes the development of good thermal models and their applications on the arbitrary meshes. The aim of our project was to do some constructive work in these two areas: to improve and develop thermal models and to apply these thermal models on the arbitrary mesh so as to solve the practical thermal problems with complex geometries.

In this project, most of our research work is based on the internal energy density distribution function (IEDDF) thermal model, since numerical simulations have shown it to be a good and stable thermal model. Firstly, a new implementation for the Neumann thermal boundary condition was proposed in order to extend the IEDDF thermal model to be used for the practical thermal applications. Then based on the physical background that the compression work done by pressure and viscous heat dissipation can be neglected for

incompressible thermal flows, a simplified IEDDF thermal model for the incompressible thermal flows was proposed. Thirdly, in order to solve the real three-dimensional thermal problems, a three-dimensional thermal model for LBM was proposed. In addition, a new axisymmetric lattice Boltzmann thermal model was proposed in order to solve an important kind of quasi-three-dimensional thermal flows.

In order to apply these thermal models to solve the practical thermal problems on the arbitrary meshes, the finite volume LBM (FVLBM) technique and Taylor series expansion- and least squares- based LBM (TLLBM) technique were introduced in the thermal models. Firstly, FVLBM technique was tested. A new implementation of the wall boundary condition for FVLBM was proposed in order to make this FVLBM scheme suitable for the practical applications before we applied it in the IEDDF thermal model. Numerical results showed that at low Rayleigh numbers, the use of FVLBM technique in the IEDDF thermal model could get satisfactory results; while at high Rayleigh numbers, this thermal scheme displayed large numerical diffusions. Then the TLLBM technique was used for the IEDDF thermal model. Numerical results on a wide range of Rayleigh numbers showed its applicability and flexibility for the thermal applications with complex geometries.

In summary, many practical thermal models were proposed and used on the arbitrary meshes by introducing the FVLBM technique or TLLBM technique into these thermal models, which may provide a step forward for the LBM applications in the thermo-hydrodynamic areas.

LIST OF TABLES

LIST OF FIGURES

NOMENCLATURE

Greek letters

Chapter 1

Introduction

1.1 Background

Fluid mechanics has its wide applications in many areas. In the automobile and engine industry, in order to improve the performance of modern cars and trucks, the study of external flow over the body of a vehicle, or the internal flow through the engine is necessary. In the civil engineering area, problems involving the rheology of rivers and lakes are also related to the fluid mechanics. In the environmental engineering area, the discipline of heating, air conditioning and general air circulation through buildings has its basis in the fluid mechanics. In the study of naval architecture, the hydrodynamics problems associated with ships, submarines and so on cannot be solved without the help of fluid mechanics.

1.1.1 Difficulty of Navier-Stokes solvers in complex flows

In general, fluid motion is governed by the continuity, Navier-Stokes (NS) and energy equations:

$$\frac{\partial \rho}{\partial t} + \nabla \cdot (\rho \boldsymbol{u}) = 0 \tag{1.1}$$

$$\frac{\partial \boldsymbol{u}}{\partial t} + \boldsymbol{u} \cdot \nabla \boldsymbol{u} = -\frac{1}{\rho} \nabla p + \nu \nabla^2 \boldsymbol{u} + \varsigma \nabla (\nabla \cdot \boldsymbol{u}) \tag{1.2}$$

$$\rho \left(\frac{\partial e}{\partial t} + \boldsymbol{u} \cdot \nabla e \right) = \nabla \cdot (k \nabla T) + \prod : \nabla \boldsymbol{u} \tag{1.3}$$

where ρ, $\boldsymbol{u}$, p, e, and T are the density, velocity, thermodynamic pressure, internal energy and absolute temperature of the fluid, respectively; ν is the kinematic viscosity; ς is the second viscosity coefficient and k is the thermal conductivity; $\prod = \rho\nu(\nabla\boldsymbol{u} + \boldsymbol{u}\nabla)$ is the stress tensor. Equations (1.1)-(1.3) form a second-order partial differential equation system, which is difficult to get the closed-form analytic solution except for a small number of special cases. With the development of computer technology, computational fluid dynamics (CFD) is developed to solve the NS equations or equations resultant from them by using different kinds of numerical techniques, such as the finite difference method, finite volume method and finite element method.

However, the NS equations are based on the continuum assumption and this assumption breaks down at some conditions. Take porous flows and multiphase flows as examples. For porous flows, the mean free path of molecule is comparable to the characteristic length scale of the flow; for multiphase flows, there exists the interface in inhomogeneous flows. So these kinds of fluid motion cannot be efficiently solved by NS solvers, which demand the use of particle-based methods.

1.1.2 Particle-based methods

There are a number of particle-based methods, such as molecular dynamics, lattice gas automaton and lattice Boltzmann method.

1.1.2.1 Molecular dynamics

Direct simulation of molecular dynamics is one of the particle-based methods. It models the individual molecules that make up the fluid. If the inter-molecular interactions are modeled correctly, the system of molecules should be able to represent the behavior of fluid. But it needs large computer resources to store all the information of every particle, such as its previous and new positions and velocities. It is also very time consuming even for a small volume of fluid, because individual molecules interact with each other and their new trajectories are to be updated constantly.

1.1.2.2 Lattice gas automaton

The fact that different microscopic interactions can lead to the same form of macroscopic equations is the starting point for the development of lattice gas automaton (LGA). Instead of considering a large number of real individual molecules as in molecular dynamics, a much smaller number of fluid 'particles' are used. A 'particle' represents a large group of molecules that possess the same properties on average. This reduces the amount of data that need to be stored significantly. Although its dimension is much larger than the molecule, its largest dimension is considerably smaller than the smallest length scale of simulation. The particles reside on the nodes in a regular lattice and are restricted to move on the links of a regular underlying grid in discrete time step. A set of Boolean variable $n_\alpha(x,t)$, $(\alpha = 1,\cdots,M)$ is used to describe the particles' occupation, where M is the number of particle velocity directions at each node. The evolution equation for LGA is as follows:

$$n_\alpha\left(\boldsymbol{x}+\boldsymbol{e}_\alpha,t_{n+1}\right)=n_\alpha\left(\boldsymbol{x},t_n\right)+\Omega_\alpha\left(n(\boldsymbol{x},t_n)\right) \qquad (1.4)$$

where $\boldsymbol{e}_\alpha$ is the local particle velocity.

Starting from an initial state, the configuration of particles at each time step evolves in two sequential sub-steps: streaming and collision. In the streaming process, each particle moves to the nearest node in the direction of its velocity; and during the collision process, particles arriving at the same node interact and change their velocity directions according to the scattering rule. For simplicity, the exclusion principle that at a given time, no more than one particle with a given velocity is allowed at a particular node is imposed for the memory efficiency, which leads to a Fermi-Dirac local equilibrium distribution. The conservation laws are incorporated into the update rules that are applied at each discrete time step.

Since all the collisions occur at the same time and the properties of fluid are only requested at the lattice sites and discrete times, it is very easy to apply the parallel algorithm. That is also one of the reasons why this method can run much faster than molecular dynamics simulations on a computer. However, some problems arise due to its great simplification: the results are usually plagued by noise because Boolean variables are used; the simulation does not preserve Galilean invariance, since the Fermi-Dirac equilibrium distribution is used. Various modifications have been made to overcome these difficulties and lattice Boltzmann method is one of the outcomes.

1.1.2.3 Lattice Boltzmann method

The main difference between LGA and lattice Boltzmann method (LBM) is that LBM replaces the particle occupation variables n_α (Boolean variables) used in LGA by the single-particle distributions (real variables) $f_\alpha = \langle n_\alpha \rangle$ and neglects the individual particle motion and particle-particle correlations in the kinetic equation, where $\langle \ \rangle$ denotes an ensemble average. This procedure eliminates the statistical noise in LGA, since the primitive variables are the averaged particle distributions. Instead of using Fermi-Dirac equilibrium distribution function, Maxwell-Boltzmann equilibrium distribution function is used to preserve Galilean invariance. The governing equation is similar to LGA:

$$f_\alpha\left(\boldsymbol{x}+\boldsymbol{e}_\alpha, t_{n+1}\right) = f_\alpha\left(\boldsymbol{x}, t_n\right) + \Omega_\alpha \tag{1.5}$$

and it keeps the advantage of locality in LGA, which is essential to parallelism.

McNamara & Aanetti uses the Boltzmann to simulate lattice-gas automata in 1988. Higuera & Jimenez (1989) made an important simplification for equation (1.5). They linearized the collision operator. Later, it is replaced by Bhatnagar-Gross-Krook (BGK) collision operator by Koelman (1991), Qian et al. (1992) and others. It is assumed that the distribution is close to the local equilibrium state and it shifts to the equilibrium state by a relaxation process. The use of lattice BGK model makes the computations more efficient and allows the flexibility of transport coefficients.

LBM has the following three distinct advantages:

Firstly, the convection operator (or streaming process) of LBM in phase space (or particle velocity space) is linear. This feature contrasts with the nonlinear

convection terms in NS equations. Simple convection combined with a collision operator (or relaxation process) allows the recovery of nonlinear macroscopic advections through the multi-scale expansions.

Secondly, the pressure in LBM is calculated using the equation of State. In contrast, in the direct numerical simulation of incompressible NS equations, the pressure satisfies Poisson equation with velocity strains acting as sources. Solving Poisson equation for the pressure often produces numerical difficulties, which requires special treatments, such as the iteration or relaxation.

Thirdly, LBM utilizes a minimal set of particle velocities in the phase space. In the traditional kinetic theory with Maxwell-Boltzmann equilibrium distribution, the phase space is a complete functional space. The averaging process involves information from the whole particle velocity phase space. While in LBM, because only one or two speeds and a few moving directions are used, the transformation between the distributions and macroscopic quantities is greatly simplified and consists of only some simple arithmetic calculations.

LBM has all the above advantages except the round-off freedom in LGA, with all the difficulties of LGA overcome. It is worthwhile to mention again that LBM is a particle-based method and it is an ideal method for parallelism. Thus LBM with BGK collision model is selected as the numerical method used in our study.

1.2 Literature review

Although there are just more than ten years after the first paper about the use of LGA in fluid mechanics was published, LBM has been widely used in different areas of fluid flow applications (Chen & Doolen, 1998). We will give detailed descriptions in the following sections.

1.2.1 Flows with simple boundaries

In the simulation of single-component, isothermal fluid flows, LBM is found to be as stable, accurate and computationally efficient as classical computational methods (Martinez et al., 1994a). It can be easily used in the fluid flows with simple geometries. LBM simulation of the two-dimensional driven cavity flow was carried out thoroughly by Hou et al. (1995a). Their studies covered a wide range of Reynolds numbers from 10 to 10,000. They carefully compared the simulation results of the stream function and locations of vortex centers with the previous study (Ghia et al. 1982). The differences of the numerical results were less than 1%, which lay in the range of the numerical uncertainty of solutions using other numerical methods. Hou (1995b) also simulated the three-dimensional cubic cavity flow and the results compared well with the experimental work by Prasad & Koseff (1989). Luo (1997) studied the two-dimensional symmetric sudden expansion channel flow and reproduced the symmetry-breaking bifurcation for this flow observed previously. LBM simulation of the flow around a two-dimensional circular cylinder or an octagonal

cylinder has also been studied by many groups (Higuera & Succi 1989; Wagner 1994;

Nobel et al. 1996).

1.2.2 Flows in complex geometries

An attractive feature of LBM is that the no-slip bounce-back boundary

condition costs little computational time. This makes LBM very suitable for simulating

flows in the complicated geometries, such as flows past porous media. For flows

through porous media, the wall boundaries are extremely complicated and an efficient

scheme for handling wall-fluid interaction is essential. Previous conventional methods

such as the finite difference schemes and networking models are limited either to the

simple physics or small geometry sizes. Succi et al. (1989) used LBM to simulate the

porous flow in a three-dimensional random medium and confirmed Darcy's law.

Cancelliere et al. (1990) made a detailed study and found that the permeability is a

function of the solid fraction in a system of randomly positioned spheres of equal radii.

Their results agreed well with the well-known Brinkman approximation and semi

empirical Kozeny-Carman equation. Heijs & Lowe (1995) studied the validity of

Kozeny-Carman equation for the soil samples where the flow occurs only through

some specific continuously connected pores, neglecting the flows occurring at smaller

scales. Flow through the sandstones has been simulated by Buckles et al. (1994), Soll

et al. (1994) and Ferreol & Rothman (1995) independently. They obtained the

permeability for sandstones and found that the permeability shows large variations in

the space and flow directions, which in general agreed well with experimental

measurements. Spaid & Phelan (1997) investigated the injection process in resin transfer modeling. For this heterogeneous porous media simulation, good agreement between LBM simulation and the lubrication theory for cell permeability was reported. Latest studies further confirm the reliability of LBM in modeling fluid flows in porous media. For example, Zeiser et al. in 2002 employed LBM to examine the pressure drops in fix-bed reactors, taking account of all effects of flow characteristics caused by radial and circumferential inhomogeneities of packings. Tölke et al. (2002) present simulation results for the flow of an air-water mixture in a waste-water batch reactor and the saturation hysteresis effect in soil flow. Yoshino & Inamuro (2003) studied the transport phenomena in a three-dimensional porous structure in order to investigate the characteristics of heat and mass transfer at a pore scale in the structure using LBM.

1.2.3 Simulation of turbulence flows

Simulation of turbulence flows is a challenge for the numerical methods. Since LBM can be used for smaller viscosities, it is interesting to use LBM for DNS to simulate the fluid flows at high Reynolds numbers. Extensive studies on using LBM for DNS have been made by many authors. Martinez et al. (1994a) studied the decaying turbulence of a shear layer at a Reynolds number of 10,000. Two-dimensional forced turbulence was simulated by Qian et al. (1995) to study the energy inverse cascade range. LBM simulation of the three-dimensional isotropic turbulence has been studied by Chen et al. (1992) and Trevino & Higuera (1994), respectively. Three-dimensional non-homogeneous turbulent flows such as the shear

flow were studied by Benzi et al. (1996). For higher Reynolds numbers, it is more convenient to use LES in LBM. A subgrid-scale (SGS) model was introduce by Hou et al. (1996) in LBM and made a correction for the relaxation time by considering the effects of Smagorinsky filtered large-scale strain rate. Flows in a two-dimensional cavity at Reynolds numbers up to 10^6 were carried out. In the same year, Eggels carried out a large-eddy simulation of turbulent flow in a baffled stirred tank reactor. Recent simulations such as by Lu et al. (2002) and Feiz et al. (2003a, b) have demonstrated the potential of LBM-LES model as a useful computational tool for investigating turbulent flows using LBM in engineering applications.

1.2.4 Multiphase and multi-component flows

Simulations of multi-phase and multi-component flows are among the most successful applications of LBM. The dynamics of multiphase and multi-component flows has practical importance in engineering applications, including the oil-water flow in porous media, the boiling fluids, the liquid metal melting and solidification. The numerical simulation of these flows is a challenging subject because of the difficulties in modeling interface dynamics. Traditional numerical schemes have been successfully used for simple interfacial boundaries. LBM provides an alternative and competitive method for simulating the complicated multiphase and multi-component fluid flows, in particular for three-dimensional flows. Gunstensen et al. (1991) were the first to develop a multi-component model using LBM. In their models, two different fluids are represented by the red and blue particle distributions. However, it is

time-consuming and causes an anisotropic surface tension that induces unphysical vortices near interface. Shan & Chen (1993) and Shan & Doolen (1995) improved this model by using the model interactions to modify the surface–tension-related collision operator. Both models are based on the phenomenological models of interface dynamics and are probably most suitable for the isothermal multi-component flows. To account for the thermodynamics of non-ideal and multi-component fluids, Swift et al. (1995, 1996) used the free-energy-based LBM approach. Numerical simulations to the problems associated with the interfacial phenomena showed that good accuracy was achieved when the results were compared with theoretical predictions. He, Shan and Doolen (1998a) also developed a new model with the consistent temperature concept. It is linked to the kinetic theory of dense gases and the intermolecular interactions are formulated using the approximation of Enskog extension of the Boltzmann equation. The two-component version of this model was proposed by He et al. (1999) and has been successfully used to simulate Rayleigh-Taylor instability. Recent theoretical results (Luo & Girimaji, 2002, 2003) have proven that the LBM model for multi-component fluids can be rigorously derived from corresponding kinetic equations. This provides a unified framework to treat the LBM models for multiphase and multi-component fluids and set these models on a more rigorous foundation.

1.2.5 Simulation of particles in fluids

The difficulty of simulating the particle suspensions in fluid is that it should consider the effect of fluid-particle interaction. Ladd (1993, 1994a, 1994b, 1997)

conducted this pioneering work and did some interesting applications in this area. Significant improvements and applications were mostly associated with Behrend (1995) and Aidun & Lu (1995). The accuracy of Ladd's scheme was carefully and extensively studied for creeping flows and other flows at finite Reynolds numbers. The results compared well with the finite-difference and finite-element results. In addition, Brownian motion has also been studied by Ladd (1993) and Dufty & Ernst (1996) using LBM. Their methods allow the treatment of Brownian short-time regime and pre-Brownian time regime for the first time. Since Brownian motion is driven by the fluctuations in fluids, some stochastic terms should be added to the distribution to include such fluctuation. By doing this, Segre et al. (1995) showed the close agreement between the experimental measurements and simulation results using LBM. Because LBM has been demonstrated as an effective simulation tool for particulate suspensions in fluids, it has been successfully applied to simulate suspensions with single particle by Qi et al. (1999, 2002a, 2003) or with multiple particles (Ladd, 2002 and Qi et al., 2002b).

1.2.6 Reaction & diffusion problems

LBM was extended by Dawson et al. (1993) to describe a set of reaction–diffusion equations advected by the NS equations. Chemical reaction flows were investigated by Chen et al. (1995) to study the geochemical processes such as the dissolution on the rock surface. Flekkøy et al. (1996) carried out a study of the creeping flow in a Hele-Shaw cell to investigate the inertial effect at very small

Reynolds numbers. Filippova & Hänel (2000a) proposed a novel LBM model to simulate the low Mach number combustion. In their model, the equilibrium distribution function takes into account the variable density. The numerical simulation of flow in which the hot oxidizer goes through the periodical grids of porous burners produced satisfactory results. This shows that their model is efficient in real applications.

1.2.7 Simulation of micro-flows

In contrast to macro flows described by continuum mechanics, micro-flows are dominated by the following four effects: non-continuum, surface dominated, low Reynolds number and multi-scale, multi-physics. Kinetic theory is capable of dealing with these effects to certain extent. Due to its kinetic origin, LBM has the potential to simulate micro-flows for which the continuum description is invalid. It has been successfully applied to the pressure-driven micro-channel flow (Huang, 1998 and Lim et al., 2002), mixing of binary fluids in micro-channels with patterned substrates and fluid-substrate interaction (Kuksenok et al., 2001, 2002), and electro-kinetic flow around a corner or a wedge in micro-channels (Thamida & Chang, 2002)

1.2.8 Other applications

LBM is shown to be promising in several other directions. Aharonov & Rothman (1993), Giraud et al. (1997, 1998) and Lallemand et al. (2003) used LBM to

simulate the viscoelastic flows; Martinez et al. (1994b) applied it to the magneto hydrodynamics; Boghosian et al. (1996) extended it to the study of micro-emulsions.

1.3 Research areas of LBM

From the above literature review, we found that LBM has been developed as a promising alternative method for CFD and achieved huge success in many practical application areas. However, there still exist some areas left for improvement compared with the conventional CFD methods, since it is a quite new method. One is its use in the thermal applications, and the other is its use on the arbitrary mesh.

1.3.1 Its use in the thermal applications

Currently, the thermo-hydrodynamic LBM is one of the most challenging issues left in LBM research. Despite several brilliant attempts, to date, a consistent thermo-hydrodynamic LBM scheme working over a wide range of temperatures is still missing. The main difficulty is the numerical instability, which is, in part a result of linear collision operator and simplicity of the spatial-temporal dynamics of LBM (Lallemand & Luo, 2003a).

The existing thermal LBM will fall into the following several groups: Boltzmann-Enskog method, multi-speed approach, passive-scalar approach, two-distribution model and the others.

1.3.1.1 Boltzmann-Enskog method

Luo (1998) suggested that the difficulty of solving the thermal problems could be overcome by going back to the Boltzmann equation for the dense gases, the time-honored Enskog equation. He suggested solving the Boltzmann-Enskog equation in exactly the same way as that used in solving the Boltzmann equation for dilute gases. Luo's theory seems promising in analyzing the macro limit of lattice Boltzmann equations (LBEs) for non-ideal fluids, but its practical value remains to be demonstrated because so far no simulation results are available.

1.3.1.2 Multi-speed approach

The multi-speed approach is a straightforward extension of LBM isothermal models, which uses only the density distribution in the streaming and collision processes. To obtain the temperature evolution equation at the macroscopic level, additional speeds are necessary and the equilibrium distribution function must include the higher-order velocity terms. Alexander, Chen and Sterling firstly proposed the thirteen speeds scheme in 1993 that expanded the equilibrium distribution function to the third order of velocity. But in their model, Prandtl number is fixed at the value of 1/2. This is due to BGK model, which uses only one relaxation time for viscous and heat transfer. They used this model on the hexagonal lattice to simulate Couette flow with a temperature gradient between two parallel planes and their results agreed well with the theoretical predictions. Vahala et al. (1995) also used this model to study the effect of two-dimensional shear velocity turbulence on a steep temperature gradient

profile. Qian (1993) developed similar three-dimensional thermal LBM models based on 21 and 25 velocities. The limitation of fixed Prandtl number was partially removed by Chen et al. (1997) using a two-time relaxation operator. All the above multi-speed schemes provide the basic mechanisms of momentum and heat transfer, but they do not cover the issue of nonlinear momentum and heat transfer. To remove this shortcoming, Y. Chen (1994b) in his thesis proposed the higher-order parametric equilibrium distribution function to satisfy the full set of thermo-hydrodynamic constraints. Nevertheless, the multi-speed scheme suffers the severe numerical instability and the temperature variation is limited to a narrow range. Chen & Teixeira (2000) pointed out that the origin of reduced stability is related to the lack of a global H-theorem. In the same year, they proposed a scheme that stabilized the multi-speed scheme by identifying a temperature–dependent factor in the equilibrium distribution function. This leads directly to the removal of Galilean–invariance artifact and relaxes the requirement of instantaneous accuracy of this factor. This results in a stable scheme but introduces the artificial thermal diffusion strongly dependent on the bulk velocity. A lot of recent work may provide new direction for this approach.

1.3.1.3 Passive-scalar approach

The passive-scalar approach utilizes the fact that the macroscopic temperature satisfies the same evolution equation as a passive scalar if the viscous heat dissipation and compression work done by the pressure are negligible. In a passive-scalar based LBM thermal model, the temperature is simulated using a separate distribution that is

independent of the density distribution. So it enhances the numerical stability. Massaioli et al. (1993) used this passive-scalar scheme to simulate the two-dimensional Rayleigh-Benard (RB) convections. In the same year, Bartoloni et al. used this idea for the highly parallel three-dimensional simulations of Rayleigh-Benard turbulence. Extensive studies of the two-dimensional and three-dimensional Rayleigh-Benard convections were made by Shan (1997). He derived the scalar equation for the temperature based on the two-component model. The calculated critical Rayleigh numbers for RB convections agreed well with theoretical predictions. The Nusselt number as a function of the Rayleigh number for two-dimensional simulations was in good agreement with previous numerical simulations using other methods. Obviously, this approach will become more useful if the viscous heat dissipation and compression work done by the pressure can be correctly incorporated into the model.

1.3.1.4 Two-distribution model

The two-distribution model also called the internal energy density distribution function (IEDDF) thermal model was proposed by He et al. (1998b). This model has shown the great improvement in the stability over the previous LBM thermal models. It is based on the discovery that the lattice Boltzmann isothermal models can be actually derived by discretizing the continuous Boltzmann equation in the temporal, spatial and velocity spaces. Following the same procedure, a new LBM thermal model can be derived by discretizing the continuous evolution equation for the internal

energy density distribution. This new scheme is similar to the passive-scalar approach

because it also uses an independent distribution to simulate the temperature evolution.

Hence its numerical stability is similar to that of the passive-scalar thermal model.

However, this model can incorporate the viscous heat dissipation and compression

work done by the pressure, which cannot be done in the passive-scalar thermal model.

1.3.1.5 Other thermal models

In recent years, attempts are also taken from a different way by using higher

isotropic lattices. Pavlo et al. (1998a, 1998b) proposed the non-space filling lattices,

typically octagons, which offer a higher degree of isotropy to solve the thermal

problems. They have proposed the two-dimensional and three-dimensional lattice

models. Some preliminary simulations for the two-dimensional jet flow between

planes held at constant temperatures were reported in 2002. Some interesting work has

also been done by Onishi (2001) and Guo (2002), respectively. Instead of using more

particle velocities than the isothermal models, they used fewer particle speeds (i.e.

only four-speed particle model) in their thermal models. The applications of their

models are limited to the two-dimensional flows and the possibility of their uses in the

three-dimensional flows is still not clear. It appears recently that some thermal models

use various shock capturing schemes to simulate fully compressible Euler (Hinton et

al. 2001, Shi et al. 2001) or NS equations (Sun 2000, Mason 2002). The numerical

accuracy of these shock capturing schemes remains mostly unknown. It is not clear for

the benefit of these schemes to the thermal applications. In 2003b, Lallemand and Luo

proposed to use a hybrid scheme in which the LBM flow simulation was decoupled from the solution of temperature equation by finite-difference techniques.

1.3.1.6 Our research work on the thermal models

From the above literature review, we can see that most of the current thermal models are faced with the stability problem or in the preliminary stage of development. More research work is needed to assess on the quantitative grounds of how thermodynamics is correctly represented by the LBM thermal models in two and three dimensions. Among the above-mentioned thermal models, the currently published research work on the IEDDF thermal model has shown that this thermal model is very stable and convenient for implementation. So we started our research work in this challenging area by using the IEDDF thermal model.

Since the IEDDF thermal model is a new model, it still lacks benchmarks. Particularly, all the preceding benchmarks have been done with the use of periodic boundary condition. Therefore, it is important to analyze the validity for the IEDDF model in the presence of solid boundaries for the purpose of engineering applications. In addition, this model is limited to solve the thermal problems with Dirichlet boundary condition. So in this thesis, we did more benchmark studies for this model, especially those applications with solid boundaries. We also extended this thermal model to be used for the thermal applications with Neumann boundary condition, which is necessary for the real practical thermal applications. Then its use on the

arbitrary mesh was developed by using the finite volume technique and the technique of Taylor series expansion- and least squares- based LBM, respectively.

Based on the original IEDDF thermal model and the properties of incompressible thermal flows, we proposed a new simplified IEDDF thermal model for the incompressible flows. The computational efficiency has been greatly improved as compared with the original IEDDF thermal model when solving the incompressible thermal flows.

In order to solve the three-dimensional thermal flows, we proposed a three-dimensional IEDDF thermal model and used it to solve the three-dimensional natural convection problems in a cubic enclosure. This is the first time that the LBM thermal model was used in the real three-dimensional thermal applications.

1.3.2 Its use on the arbitrary mesh

LBM so far lags behind the conventional CFD methods in the simulations of fluid flows in the realistically complicated geometries. This traces back to the constraints of working along the light-cones $d\boldsymbol{x}/dt = \boldsymbol{e}$. This restricts LBM to the lattice-isotropy in the physical space, which makes the scheme macroscopically similar to a uniform Cartesian-grid solver. Various methods have been proposed to remedy this unsatisfactory state of affairs, such as the finite volume method, finite difference method, multiscale method, interpolation-supplemented LBM (ISLBM) and Taylor series expansion- and least squares- based LBM (TLLBM).

1.3.2.1 Finite volume LBM

Finite volume LBM (FVLBM) is to define the coarse grids of virtually arbitrary shape whose cells typically contain several original lattice units, so that the coarse grids need not be tied down to the symmetries of underlying fine grids where the dynamics of differential lattice Boltzmann equation (LBE) takes place. The evolution equation for the mean value in the cell requires the evaluation of flux across the boundaries of cell. A piece-wise constant, piece-wise linear or piecewise-parabolic interpolation can be used to approximate the flux. Succi et al. (1995) were the first to propose a finite-volume formulation of LBM. However, the empirical formulae used are quite complicated even for the simple rectangular mesh, and a free parameter has to be introduced and adjusted in order to minimize the numerical diffusion. Chen (1998) developed another finite-volume scheme. With properly chosen forms of state-flux functions, both exact conservation laws and equilibrium balance conditions are achieved as in the original LBM. However, the irregular meshes used in all the above-mentioned approaches are not satisfactory in the sense that the topology of mesh is not arbitrary. Recently, a new finite volume method was proposed by Xi et al. (1998, 1999a, 1999b), which has great geometrical flexibility without compromising the simplicity of conventional LBM. It is based on the modern finite-volume method and successfully used on both the structured and unstructured grids.

1.3.2.2 Finite difference method

It is recognized by some groups that the differential form of LBE is nothing but a set of hyperbolic partial differential equations, so it becomes natural to observe that both time and space derivatives can be discretized in many ways, not just obeying $dx/dt = e$. One example is that Cao et al. (1997) developed a number of finite difference LBE methods based on higher-order time marching schemes, as combined with various spatial discretization schemes. It has been successfully demonstrated for various flows in bounded geometries, such as the two-dimensional Taylor vortex flow, Couette flow with the temperature gradient between walls, and so on.

1.3.2.3 Grid-refinement LBM

Filippova and Hanel (1998) presented the grid-refinement LBM scheme with boundary-fitting formulation on the curvilinear boundaries. It uses the concept of hierarchical grid refinement. The calculation is based on a coarse grid covering the whole integration domain. In a critical region, a finer grid is superposed to the basic coarser grid. The calculation proceeds with large time-step accordingly to the coarse grid; while on the finer grid, several time steps according to the refinement ratio are performed to advance to the same time level. This feature is very important for the computations of time-dependent flows. But for the computations of steady-state incompressible flows, the use of several smaller time-steps on the fine grid would increase the computational time. In order to remove this drawback, the use of smaller amount of time-steps on the fine grid was proposed (2000b). For the time-dependent

computation, this is connected with the change of 'molecular' speeds on the fine grid so that the temporal accuracy will not be impaired in certain limits. For the steady-state computation, the saving of CPU time can be even larger, since the same amount of time steps can be chosen on coarse and fine grids as well. They tested and validated their scheme by calculating the moderate Reynolds number flows around the cylinder and wing.

1.3.2.4 Interpolation–supplement LBM

He, Luo and Dembo (1996) proposed the interpolation–supplement LBM (ISLBM). The discrete distributions are still to move along the straight paths $dx/dt = e$, but an interpolation step is introduced after the stream and collision steps to determine the density distributions at the grid points for the next time step. To minimize the numerical viscosity, the second-order interpolation is used. He & Doolen (1997) revisited the problem of the two-dimensional flow around circular cylinder using this method. In their simulation, the underlying lattice was square but a spatial interpolation was used, which improved the numerical accuracy. Lift and drag coefficients, wake lengths and separation angles at different Reynolds numbers were in good agreement with those predicted by previous experimental and numerical studies.

1.3.2.5 Taylor series expansion- and least squares- based LBM (TLLBM)

In order to implement LBM more efficiently for the flows with arbitrary geometries, the Taylor series expansion- and least squares- based LBM (TLLBM),

which is based on the standard LBM, Taylor series expansion and least squares approach, was proposed by Shu et al. in 2001. The final form is an algebraic formulation, in which the coefficients $a_{1,k}$ depend only on the coordinates of mesh points and lattice velocity, and can be computed once in advance. It can be consistently used in any kind of lattice model. This new method possesses the following features: Firstly, it is suitable for the arbitrary geometry and does not introduce any coordinate transformation technique. Secondly, in order to avoid the increase of numerical discretization errors, it does not include any derivative operation. Thirdly, the matrix least square theorem is used to obtain the optimum solution of differential equations. Finally, the present method keeps the merit of easy parallel computing of the standard LBE. Numerical experiments on the isothermal flows have shown that this method is an efficient and flexible approach for practical engineering applications. It should be mentioned that the hyper viscosity is increased (Niu. et al., 2004).

1.3.2.6 Our research work on the arbitrary mesh

From the above literature review, we can see that all the above-mentioned methods, especially the finite volume LBM and TLLBM have been used in the isothermal flows with complex geometries. We decided to use these two methods to extend the IEDDF thermal model to be used on the arbitrary mesh, since all the current thermal models including the IEDDF thermal model are restricted to the regular grids. While in fact, the flow and thermal fields in different kinds of enclosed spaces are of great importance due to their wide applications such as in solar collector-receivers,

insulation and flooding protection for buried pipes used for district heating and cooling, cooling systems in nuclear reactors, etc. These all need LBM thermal solvers on the arbitrary mesh. No studies have been reported on the thermal applications with arbitrary geometries due to the combined complexities of the use of LBM for the thermal problems and it use on the arbitrary mesh.

Firstly, we used the finite volume LBM technique proposed by Xi (1998, 1999a, 1999b) to extend the IEDDF thermal model for its use on the arbitrary mesh. However, through the literature review, we found that all the applications using this FVLBM were limited to the periodic boundary conditions at the inlet and outlet because of the failure to implement the wall boundary conditions. In order to develop this FVLBM, we proposed a new implementation of wall boundary conditions in this thesis, which is based on the half-covolume scheme and bounce-back rule for the non-equilibrium distribution. Using this implementation of wall boundary conditions, the flow problems with different inlet and outlet boundaries can be successfully solved. Then we developed a new scheme using this FVLBM technique and IEDDF thermal model to solve the thermal problems on the arbitrary mesh. Numerical simulations of the natural convection in a square cavity on the non-uniform grids were carried out and the accuracy of this scheme was compared with a NS solver. The numerical results at high Rayleigh numbers showed that using the FVLBM technique, large numerical diffusion exists, which reveals to its inaccuracy. So we moved to another way by using the TLLBM technique.

We proposed a new thermal scheme by using the TLLBM technique in the IEDDF thermal model. Numerical simulations of the same natural convection in a square cavity at a wide range of Rayleigh numbers were carried out. Numerical results at high Rayleigh numbers agreed well with a NS solver, which means that this new scheme is an efficient and accurate method to solve the thermal problems on the arbitrary mesh. Then we successfully used this scheme to solve the complex thermal problems with curved boundaries such as the natural convection in the annulus between a square outer cylinder and a circular inner cylinder.

1.3.3 Work on a special kind of flows

Axisymmetric thermal flows are quasi-three-dimensional flows. Its complexity is between two-dimensional flows and real three-dimensional flows. It covers many important flows such as the forced and mixed convections in the vertical concentric cylindrical annuli and Czochralski crystal growth problems. Since these flow problems are defined on the cylindrical coordinate system, they are quite different from the problems defined on the Cartesian coordinate system when using LBM. Special treatment is needed; otherwise the real three-dimensional LBM has to be used for these axisymmetric flows. In this thesis, we developed an effective new numerical scheme to solve this kind of important thermal flows using LBM.

1.4 Contribution of the dissertation

In this thesis, the following contribution works are carried out. For its use in the

thermal applications, extend the IEDDF thermal model for flows with Neumann boundary condition; develop simplified IEDDF thermal models for two and three dimensions; propose a thermal model for axisymmetric thermal flows. For its use on arbitrary mesh, especially for thermal flows, test FVLBM and TLLBM. For FVLBM, propose a new scheme for wall boundary conditions. For TLLBM, it is found to be a good technique to solve the flow problems with complex geometry.

The work done in this thesis may help the improvement of LBM in its thermal applications, which may contribute to its development as an alternative method to solve the real practical fluid problems comparable to the conventional CFD methods or even better in some areas where the conventional CFD methods cannot be used.

1.5 Organization of the dissertation

The thesis is organized as follows:

In Chapter 2, the basic concepts related to LBM with BGK models are introduced. Some knowledge about the equilibrium distribution function, discrete velocity models, boundary conditions and the stability of LBM are presented.

Chapter 3 shows the theory of the IEDDF thermal model and our proposed implementation scheme for the Neumann boundary condition. The numerical simulations of the natural convection in a square cavity have been carried out to validate the IEDDF thermal model and our new implementation for the Neumann boundary condition. The accuracy and grid-independence study using this improved thermal model are thoroughly investigated.

In Chapter 4, a FVLBM proposed by Xi (1998, 1999a, 1999b) is introduced and our new implementation of the wall boundary condition for this FVLBM is described in details. Numerical simulations on driven cavity flows and expansion flows show that our new implementation of the wall boundary condition improves the applicability of this FVLBM. Then we apply this FVLBM technique to the IEDDF thermal model in order to solve the thermal flows on the arbitrary mesh. The numerical results show that this scheme has large numerical diffusion at high Rayleigh number, which leads to its invalidity. So this FVLBM technique is not suitable for the thermal flows with high Rayleigh numbers.

In Chapter 5, in order to simulate the thermal flows with arbitrary geometries at high Rayleigh numbers, another new thermal scheme based on the TLLBM technique and the IEDDF thermal model is presented. Numerical simulations of the natural convection in a square cavity on the non-uniform grids at a wide range of Rayleigh numbers have been carried out. Compared with FVLBM thermal scheme, the TLLBM thermal scheme is more stable at high Rayleigh numbers. So this scheme is also employed to study the complex thermal flows with curved boundaries such as the natural convection in a horizontal concentric annulus between a square outer cylinder and a circular inner cylinder. Numerical results for Rayleigh numbers ranging from 10^4 to 10^6 and aspect ratios between 1.67 and 5.0 are presented, which agree well with the available data in the literature.

In Chapter 6, axisymmetric thermal flows are studied using LBM. A new scheme is developed by using the idea that inserting the position and time dependent

source terms into the evolution equation of the standard LBM and making it recover the governing equations on the cylindrical coordinate system by Chapman-Enskog expansion.

In Chapter 7, considering the fact that the compression work done by the pressure and the viscous heat dissipation can be neglected for the incompressible thermal flows, a new simplified IEDDF thermal model is proposed for these incompressible thermal flows. It does not have any gradient term and is much easier to be implemented. This model is validated by the numerical simulation of the natural convection in a square cavity at a wide range of Rayleigh numbers. Its accuracy and efficiency have been thoroughly studied, showing the high efficiency of this new scheme when solving incompressible thermal flows. Its compressibility effect has also been studied.

In Chapter 8, we successfully develop a new three-dimensional IEDDF thermal model for the real three-dimensional thermal flows. Numerical simulation results of the three-dimensional natural convection in a cubic enclosure show the validity of our new three-dimensional thermal model.

In Chapter 9, we draw some conclusions and some recommendations are also given.

Chapter 2

Basic concepts of LBM

2.1 Introduction

In this chapter, we will give a brief introduction about the newly developed method called LBM. We will talk about how LBM is derived, the integrants of LBM and its connection with the conventional continuity and NS equations. Boundary condition is a very important issue for the implementation of LBM. Different ways of implementing the boundary conditions are presented. At the end, the stability of LBM will be briefly discussed.

2.2 The origin of LBM

There are two different ways to obtain LBM. One is from the lattice-gas cellular automata (LGCA); the other is from the continuous Boltzmann equation.

2.2.1 From lattice-gas cellular automata to LBM

The field of LGCA started in 1986 with the famous paper of Frisch, Hasslacher and Pomeau. These authors showed that a kind of billiard game with collisions that conserve the mass and momentum would lead to the NS equations in the macroscopic limit when the underlying lattice possesses a sufficient symmetry. The first LBM was introduced by McNamara & Zanetti in 1988 based on LGCA because they used the same lattices (FHP and FCHC) and applied the same collisions. Instead of using Boolean

variables, it used the continuous single-particle distribution which interacts locally and propagates after collision to the next neighbor node. Fermi-Dirac distributions were used as the equilibrium distribution functions. The next step in the development for LBM was the simplification of the collision operator. The linearized collision operator was firstly used by Higuera and Jimenez in 1989. The choice of Boltzmann distribution as the equilibrium distribution function gave much more flexibility to LBM, leading to the Galilean invariant macroscopic equations without the scaling of time and allowing tuning the viscosity. Then the next development for the collision operator, which was based on the collisions of a certain LGCA, was replaced by the single time relaxation BGK approximation by Koelman (1991), Qian et al. (1992) and the others. These lattice BGK (LBGK) models marked a new level of abstraction: collisions are not defined explicitly anymore. Thus the LBGK model has been widely used.

2.2.2 Approximation to the continuum Boltzmann equation

It has been shown recently by two groups independently (He & Luo 1997, Abe 1997) that LBM can be directly derived from the continuous Boltzmann equation when the latter is discretized in both the time and phase space in some special manner.

In the derivation, the starting point is the continuous Boltzmann equation with the BGK approximation:

$$\frac{\partial f}{\partial t} + \boldsymbol{e} \cdot \nabla f = -\frac{1}{\tau^{'}}\left(f - f^{eq}\right) \tag{2.1}$$

where $f \equiv f(\boldsymbol{x},\boldsymbol{e},t)$ is the single-particle density distribution; $\boldsymbol{e}$ is the microscopic velocity; $\tau^{'}$ is the relaxation time due to the collision and f^{eq} is the equilibrium density

distribution function. Boltzmann-Maxwellian distribution is used as the equilibrium distribution function:

$$f^{eq} \equiv \frac{\rho}{(2\pi RT)^{D/2}} \exp\left(-\frac{(e-u)^2}{2RT}\right) \tag{2.2}$$

where R is the ideal gas constant and D is the dimension of the space. The macroscopic density, velocity and internal energy can be obtained from the (microscopic velocity) moments of the density distribution f:

$$\rho = \int f\, d\boldsymbol{e} = \int f^{eq}\, d\boldsymbol{e} \tag{2.3a}$$

$$\rho\boldsymbol{u} = \int \boldsymbol{e} f\, d\boldsymbol{e} = \int \boldsymbol{e} f^{eq}\, d\boldsymbol{e} \tag{2.3b}$$

$$\rho e = \int \frac{(\boldsymbol{e}-\boldsymbol{u})^2}{2} f\, d\boldsymbol{e} = \int \frac{(\boldsymbol{e}-\boldsymbol{u})^2}{2} f^{eq}\, d\boldsymbol{e} \tag{2.3c}$$

The internal energy has the following relationship with the temperature T:

$$e = \frac{D_0}{2} RT = \frac{D_0}{2} N_A k_B T \tag{2.4}$$

where D_0 is the number of degrees of the freedom for a particle; N_A is Avogadro's number and k_B is the Boltzmann constant.

Equation (2.1) can be formally rewritten in the form of an ordinary differential equation:

$$\frac{df}{dt} + \frac{1}{\tau'} f = \frac{1}{\tau'} f^{eq} \tag{2.5}$$

where $\dfrac{d}{dt} \equiv \dfrac{\partial}{\partial t} + \boldsymbol{e} \cdot \nabla$ is the time derivative along the characteristic line $d\boldsymbol{x}/dt = \boldsymbol{e}$. The above equation (2.5) can be formally integrated over a time step of δt:

$$f\left(\boldsymbol{x}+\boldsymbol{e}\delta t,\boldsymbol{e},t+\delta t\right)=\frac{1}{\tau^{'}}e^{-\delta t/\tau^{'}}\int_{0}^{\delta t}e^{-t^{'}/\tau^{'}}f^{eq}\left(\boldsymbol{x}+\boldsymbol{e}t^{'},\boldsymbol{e},t+t^{'}\right)dt^{'}+e^{-\delta t/\tau^{'}}f\left(\boldsymbol{x},\boldsymbol{e},t\right) \qquad (2.6)$$

Assuming that δt is small enough and f^{eq} is smooth enough locally, the following approximation can be made:

$$f^{eq}\left(\boldsymbol{x}+\boldsymbol{e}t^{'},\boldsymbol{e},t+t^{'}\right)=\left(1-\frac{t^{'}}{\delta t}\right)f^{eq}\left(\boldsymbol{x},\boldsymbol{e},t\right)+\frac{t^{'}}{\delta t}f^{eq}\left(\boldsymbol{x}+\boldsymbol{e}\delta t,\boldsymbol{e},t+\delta t\right)+o\left(\delta t^{2}\right) \quad 0\leq t^{'}\leq\delta t$$

$$(2.7)$$

The leading terms neglected in the above approximation are of the order of $o\left(\delta t^{2}\right)$. With this approximation, equation (2.6) becomes

$$f\left(\boldsymbol{x}+\boldsymbol{e}\delta t,\boldsymbol{e},t+\delta t\right)-f\left(\boldsymbol{x},\boldsymbol{e},t\right)=\left(e^{-\delta t/\tau^{'}}-1\right)\left[f\left(\boldsymbol{x},\boldsymbol{e},t\right)-f^{eq}\left(\boldsymbol{x},\boldsymbol{e},t\right)\right]+$$
$$\left[1+\frac{\tau^{'}}{\delta t}\left(e^{-\delta t/\tau^{'}}-1\right)\right]\times\left[f^{eq}\left(\boldsymbol{x}+\boldsymbol{e}\delta t,\boldsymbol{e},t+\delta t\right)-f^{eq}\left(\boldsymbol{x},\boldsymbol{e},t\right)\right] \qquad (2.8)$$

If we expand $e^{-\delta t/\tau^{'}}$ in its Taylor expansion and further neglect the terms of order $o\left(\delta t^{2}\right)$ or smaller on the right-hand side of equation (2.8), we obtain

$$f\left(\boldsymbol{x}+\boldsymbol{e}\delta t,\boldsymbol{e},t+\delta t\right)-f\left(\boldsymbol{x},\boldsymbol{e},t\right)=-\frac{1}{\tau}\left[f\left(\boldsymbol{x},\boldsymbol{e},t\right)-f^{eq}\left(\boldsymbol{x},\boldsymbol{e},t\right)\right] \qquad (2.9)$$

where $\tau\equiv\tau^{'}/\delta t$ is the dimensionless relaxation time.

In order to numerically evaluate the hydrodynamic moments, the appropriate discretization in the momentum space $\boldsymbol{e}$ must be accomplished. With appropriate discretization, the integration in the momentum space can be approximated by the quadrature up to a certain degree of accuracy, that is

$$\int\psi(\boldsymbol{e})f^{eq}\left(\boldsymbol{x},\boldsymbol{e},t\right)d\boldsymbol{e}=\sum_{\alpha}W_{\alpha}\psi\left(\boldsymbol{e}_{\alpha}\right)f^{eq}\left(\boldsymbol{x},\boldsymbol{e}_{\alpha},t\right) \qquad (2.10)$$

where $\psi(\boldsymbol{e})=1,\boldsymbol{e},\dfrac{(\boldsymbol{e}-\boldsymbol{u})^{2}}{2}$ and W_{α} are the weight coefficients.

Assuming that the fluid velocity is a small parameter (compared with the sound speed), the equilibrium distribution function is obtained by a truncated small velocity expansion.

$$
\begin{aligned}
f^{eq} &= \frac{\rho}{(2\pi RT)^{D/2}}\exp\left(-\boldsymbol{e}^2\big/2RT\right)\exp\left\{(\boldsymbol{e}\cdot\boldsymbol{u})\big/RT - \boldsymbol{u}^2\big/2RT\right\} \\
&= \frac{\rho}{(2\pi RT)^{D/2}}\exp\left(-\boldsymbol{e}^2\big/2RT\right)\times\left\{1 + \frac{(\boldsymbol{e}\cdot\boldsymbol{u})}{RT} + \frac{(\boldsymbol{e}\cdot\boldsymbol{u})^2}{2(RT)^2} - \frac{\boldsymbol{u}^2}{2RT}\right\} + \mathrm{O}\!\left(\boldsymbol{u}^3\right)
\end{aligned}
\tag{2.11}
$$

A proper equilibrium distribution function leads to the recovery of the NS equations.

2.3 The integrants of LBM

LBM has three main integrants: the kinetic equation, the lattice models and the equilibrium distribution functions.

2.3.1 The kinetic equation

In the kinetic equation, one of the major difficulties when dealing with LBM is the complicated nature of the collision integral. The simpler operator $J(f)$ which replaces the collision operator $Q(f,f)$ should respect two constraints. One is that $J(f)$ conserves the collision invariants ψ_k of $Q(f,f)$, that is

$$
\int \psi_k J(f) d^3\boldsymbol{x} d^3\boldsymbol{u} = 0 \ , \ (k = 0,1,2,3,4)
\tag{2.12}
$$

where $\psi_0 = 1$, $\ (\psi_1,\psi_2,\psi_3) = \boldsymbol{u}$ and $\psi_4 = \boldsymbol{u}^2$. The other is that the collision term should express the tendency to the Maxwellian distribution (*H*-theorem). Both constraints are fulfilled by the model called BGK approximation. So the kinetic equation is simplified to the well-established lattice BGK equation.

$$f(\boldsymbol{x}+\boldsymbol{e}\delta t,\boldsymbol{e},t+\delta t)-f(\boldsymbol{x},\boldsymbol{e},t)=-\frac{1}{\tau}\left[f(\boldsymbol{x},\boldsymbol{e},t)-f^{eq}(\boldsymbol{x},\boldsymbol{e},t)\right]$$

(2.13)

2.3.2 The requirements of the lattice models

The isothermal lattice models should satisfy the isotropy of the lattice tensors to the 2nd and 4th rank. For the thermal lattice models, isotropic lattice tensors up to the 6th rank are required. The lattice tensors with odd rank vanish because of the symmetry of the lattice models.

A lattice tensor of the nth rank is defined as

$$L_{\alpha_1\alpha_2......\alpha_n}=\sum_i e_{i\alpha_1}e_{i\alpha_2}......e_{i\alpha_n}$$

(2.14)

where $e_{i\alpha_v}$ is the Cartesian component of the lattice velocity e_{α_i}.

An isotropic tensor has the following definition: A tensor $T_{\alpha_1\alpha_2......\alpha_n}$ of the nth rank is called isotropic if it is invariant with respect to the arbitrary orthogonal transformations O (rotations and reflections)

$$T_{\alpha_1\alpha_2......\alpha_n}=T_{\beta_1\beta_2......\beta_n}O_{\alpha_1\beta_1}O_{\alpha_2\beta_2}......O_{\alpha_n\beta_n}.$$

(2.15)

According to Theorem of H. Jeffreys & B. S. Jeffreys proposed in 1956, an isotropic tensor of the 2nd rank is proportional to $\delta_{\alpha\beta}$. There are three different (linear independent) isotropic tensors of the 4th rank and those are $\delta_{\alpha\beta}\delta_{\gamma\delta}$, $\delta_{\alpha\gamma}\delta_{\beta\delta}$, $\delta_{\alpha\delta}\delta_{\beta\gamma}$, which can be combined to the most general form $T_{\alpha\beta\gamma\delta}=a\delta_{\alpha\beta}\delta_{\gamma\delta}+b\delta_{\alpha\gamma}\delta_{\beta\delta}+c\delta_{\alpha\delta}\delta_{\beta\gamma}$, where a, b, and c are arbitrary constants. Isotropic tensors of the rank $n\geq4$ consist of only the products of the second rank δ tensors.

The associated lattice tensors of rank four are usually non-isotropic because the symmetry group of the corresponding lattices is not large enough. But the isotropy of the 4th rank tensors can be recovered by introducing weights for the different speeds. These generalized lattice tensors defined as $G_{\alpha_1\alpha_2......\alpha_n} = \sum_i w_i c_{i\alpha_1} c_{i\alpha_2} ......c_{i\alpha_n}$ occur naturally in the multi-scale analysis of the multi-speed models.

2.3.3 The equilibrium distribution function

The Maxwellian distribution is used as the equilibrium distribution function. At the low Mach number approximation, the general form of this equilibrium distribution function can be written as

$$f_\alpha^{eq} = A_\alpha + B_\alpha(e \cdot u) + C_\alpha(e \cdot u)^2 + D_\alpha u^2 .$$ (2.16)

The coefficients A, B, C and D depend on ρ, but not on u. These coefficients are determined in order to recover the NS equations correctly.

2.3.4 Examples of the two-dimensional lattice models

The commonly used two-dimensional lattice models, which satisfy all the above-mentioned requirements, are D2Q7 and D2Q9 (DnQm means m speed model in n dimensions). The configurations of these two lattice models are shown in Figure 2.1.

For D2Q7, the lattice velocities are defined as

$$e_\alpha = \begin{cases} (0,0) & \alpha = 0 \\ \left(\cos\frac{2\pi(\alpha-1)}{6}, \sin\frac{2\pi(\alpha-1)}{6}\right) & \alpha = 1,2,3,4,5,6 \end{cases}$$ (2.17)

The equilibrium distribution functions are given as

$$f_0^{eq} = d_0 - \rho \boldsymbol{u}^2 = \beta_1 \rho - \rho \boldsymbol{u}^2 \tag{2.18a}$$

$$f_\alpha^{eq} = d + \frac{1}{3}\rho \left[(\boldsymbol{e}\cdot\boldsymbol{u}) + 2(\boldsymbol{e}\cdot\boldsymbol{u})^2 - \frac{1}{2}\boldsymbol{u}^2 \right]$$
$$= \frac{\rho - \beta_1\rho}{6} + \frac{1}{3}\rho \left[(\boldsymbol{e}\cdot\boldsymbol{u}) + 2(\boldsymbol{e}\cdot\boldsymbol{u})^2 - \frac{1}{2}\boldsymbol{u}^2 \right] \tag{2.18b}$$

where β_1 is an adjustable parameter, d_0 is the density of the rest particle and d is the density of the moving particles. If the density ratio of the rest and moving particles is defined as $\lambda = d_0/d$, the pressure is determined by the isothermal equation of State:

$$p = 3d = \frac{(1-\beta_1)\rho}{2} = \frac{3}{\lambda + 6}\rho \tag{2.19}$$

and the sound speed is

$$c_s^2 = \frac{1-\beta_1}{2} = \frac{3}{\lambda + 6} \tag{2.20}$$

The viscosity is related to the relaxation time through the following equation:

$$\upsilon = \frac{\tau - 1/2}{4} \tag{2.21}$$

For D2Q9, the lattice velocities are defined as

$$\boldsymbol{e}_\alpha = \begin{cases} 0 & \alpha = 0 \\ \left(\cos[(\alpha-1)\pi/2], \sin[(\alpha-1)\pi/2]\right)c & \alpha = 1,2,3,4 \\ \sqrt{2}\left(\cos[(\alpha-5)\pi/2 + \pi/4], \sin[(\alpha-5)\pi/2 + \pi/4]\right)c & \alpha = 5,6,7,8 \end{cases} \tag{2.22}$$

The equilibrium distribution functions are given as

$$f_\alpha^{eq} = w_\alpha \rho \left[1 + \frac{3\boldsymbol{e}_\alpha \cdot \boldsymbol{u}}{c^2} + \frac{9(\boldsymbol{e}_\alpha \cdot \boldsymbol{u})^2}{2c^4} - \frac{3\boldsymbol{u}^2}{2c^2} \right] \tag{2.23}$$

where $w_0 = 4/9$, $w_\alpha = 1/9$ for $\alpha = 1,2,3,4$ and $w_\alpha = 1/36$ for $\alpha = 5,6,7,8$.

The pressure is determined by the isothermal equation of state:

$$p = \frac{1}{3}\rho \tag{2.24}$$

and the sound speed is

$$c_s^2 = \frac{1}{3} \tag{2.25}$$

The viscosity is related to the relaxation time by

$$\upsilon = \frac{\tau - 1/2}{3} \tag{2.26}$$

2.3.5 Examples of the three-dimensional lattice models

The commonly used three-dimensional lattice models are D3Q15, D3Q19 and D3Q27. The configurations of D3Q15 and D3Q19 models are shown in Figure 2.2 and Figure 2.3. Their equilibrium distribution functions have the same form as

$$f_\alpha^{eq} = w_\alpha \rho \left[1 + \frac{3 e_\alpha \cdot u}{c^2} + \frac{9 (e_\alpha \cdot u)^2}{2 c^4} - \frac{3 u^2}{2 c^2} \right] \tag{2.27}$$

The pressure in all the three models is determined by the same isothermal equation of state $p = \frac{1}{3}\rho$ and the sound speed is $c_s^2 = \frac{1}{3}$. In all the three lattice models, the viscosity is related to the relaxation time by $\upsilon = \frac{\tau - 1/2}{3}$.

For D3Q15, the lattice velocities are defined as

$$\boldsymbol{e}_\alpha = \begin{cases} 0 & \alpha = 0 \\ (\pm 1,0,0), \ (0,\pm 1,0), \ (0,0,\pm 1) & \alpha = 1 - 6 \\ (\pm 1,\pm 1,\pm 1) & \alpha = 7 - 14 \end{cases} \tag{2.28}$$

The coefficients for the equilibrium distribution functions are $w_0 = 2/9$, $w_\alpha = 1/9$ for $\alpha = 1\text{-}6$ and $w_\alpha = 1/72$ for $\alpha = 7\text{-}14$.

For D3Q19, the lattice velocities are defined as

$$
\boldsymbol{e}_\alpha = \begin{cases} 0 & \alpha = 0 \\ (\pm 1,0,0),\ (0,\pm 1,0),\ (0,0,\pm 1) & \alpha = 1-6 \\ (\pm 1,\pm 1,0),\ (\pm 1,0,\pm 1),\ (0,\pm 1,\pm 1) & \alpha = 7-18 \end{cases} \tag{2.29}
$$

The coefficients for the equilibrium distribution functions are $w_0 = 1/3$, $w_\alpha = 1/18$ for $\alpha = $1-6 and $w_\alpha = 1/36$ for $\alpha = $7-18.

For D3Q27, the lattice velocities are defined as

$$
\boldsymbol{e}_\alpha = \begin{cases} 0 & \alpha = 0 \\ (\pm 1,0,0),\ (0,\pm 1,0),\ (0,0,\pm 1) & \alpha = 1-6 \\ (\pm 1,\pm 1,0),\ (\pm 1,0,\pm 1),\ (0,\pm 1,\pm 1) & \alpha = 7-18 \\ (\pm 1,\pm 1,\pm 1) & \alpha = 19-26 \end{cases} \tag{2.30}
$$

The coefficients for the equilibrium distribution functions are $w_0 = 8/27$, $w_\alpha = 2/27$ for $\alpha = $1-6, $w_\alpha = 1/54$ for $\alpha = $7-18 and $w_\alpha = 1/216$ for $\alpha = $19-26.

These three three-dimensional lattice models have been assessed by Mei et al. (2000) in terms of the efficiency, accuracy and robustness in the lid driven cavity flow. D3Q19 was found to be the best lattice model for the case investigated. D3Q15 exhibited the velocity oscillation and was prone to the computational instability. The more complicated model D3Q27 did not necessarily give more accurate results than D3Q19 model with the same spatial resolution.

2.4 Recovery of the NS equations

To derive the macroscopic hydrodynamic equations, Chapman-Enskog expansion is used, which is essentially a formal multiscaling expansion:

$$\frac{\partial}{\partial t} = \varepsilon \frac{\partial}{\partial t_1} + \varepsilon^2 \frac{\partial}{\partial t_2}, \quad \frac{\partial}{\partial x} = \varepsilon \frac{\partial}{\partial x_1} \tag{2.31}$$

where ε is a small parameter. This formula assumes that the diffusion time scale t_2 is much slower than the convection time scale t_1. Likewise, the one-particle density distribution f_α can be expanded formally about the local equilibrium density distribution function f_α^{eq},

$$f_\alpha = f_\alpha^{eq} + \varepsilon f_\alpha^{(neq)} \tag{2.32}$$

Here f_α^{eq} depends on the local macroscopic variables (ρ and $\rho\boldsymbol{u}$) and should satisfy the following constraints:

$$\sum_\alpha f_\alpha^{eq} = \rho \qquad \sum_\alpha f_\alpha^{eq} \boldsymbol{e}_\alpha = \rho\boldsymbol{u} \tag{2.33}$$

$f_\alpha^{(neq)} = f_\alpha^{(1)} + \varepsilon f_\alpha^{(2)} + o(\varepsilon^2)$ is the non-equilibrium density distribution, which satisfies the following constraints:

$$\sum_\alpha f_\alpha^{(k)} = 0 \qquad \sum_\alpha f_\alpha^{(k)} \boldsymbol{e}_\alpha = 0 \tag{2.34}$$

for both $k=1$ and $k=2$.

Performing the Taylor series expansion for equation (2.13) in the time and spatial space, we obtain the following continuum form of the kinetic equation accurate to the second order in ε:

$$\frac{\partial f_\alpha}{\partial t} + \boldsymbol{e}_\alpha \cdot \nabla f_\alpha + \varepsilon \left(\frac{1}{2} \boldsymbol{e}_\alpha \boldsymbol{e}_\alpha : \nabla\nabla f_\alpha + \boldsymbol{e}_\alpha \cdot \nabla \frac{\partial f_\alpha}{\partial t} + \frac{1}{2} \frac{\partial^2 f_\alpha}{\partial t^2} \right) = \frac{\Omega_\alpha}{\varepsilon} \tag{2.35}$$

where $\Omega_\alpha = -\frac{1}{\tau} \left[f(\boldsymbol{x}, \boldsymbol{e}, t) - f^{eq}(\boldsymbol{x}, \boldsymbol{e}, t) \right].$

Using equations (2.31) and (2.32) and collecting the first order in ε results in:

$$\frac{\partial f_\alpha^{eq}}{\partial t_1} + \boldsymbol{e}_\alpha \cdot \nabla_1 f_\alpha^{eq} = -\frac{f_\alpha^{eq}}{\tau} \qquad (2.36)$$

Collecting the second order in ε results in:

$$\frac{\partial}{\partial t_1} f_\alpha^{(1)} + \frac{\partial}{\partial t_2} f_\alpha^{eq} + \boldsymbol{e}_\alpha \cdot \nabla f_\alpha^{(1)} + \frac{1}{2} \boldsymbol{e}_\alpha \boldsymbol{e}_\alpha : \nabla\nabla f_\alpha^{eq} + \boldsymbol{e}_\alpha \cdot \nabla \frac{\partial}{\partial t_1} f_\alpha^{eq} + \frac{1}{2} \frac{\partial^2}{\partial t_1^2} f_\alpha^{eq} = -\frac{1}{\tau} f_\alpha^{(2)}$$

$$(2.37)$$

which can be simplified to the following equation:

$$\frac{\partial f_\alpha^{(1)}}{\partial t_2} + \left(1 - \frac{2}{\tau}\right)\left[\frac{\partial f_\alpha^{(1)}}{\partial t_1} + \boldsymbol{e}_\alpha \cdot \nabla_1 f_\alpha^{(1)}\right] = -\frac{f_\alpha^{(2)}}{\tau} \qquad (2.38)$$

The summation of equation (2.36) in the particle velocity space gives the first-order continuity equation:

$$\frac{\partial \rho}{\partial t_0} + \nabla_1 \cdot (\rho \boldsymbol{u}) = 0 \qquad (2.39)$$

The summation of equation (2.36) multiplied by $\boldsymbol{e}_\alpha$ in the particle velocity space gives the first-order momentum equation:

$$\frac{\partial (\rho \boldsymbol{u})}{\partial t_0} + \nabla_1 \cdot \prod^{(0)} = 0 \qquad (2.40)$$

where $\prod^{(0)} = \sum_\alpha \boldsymbol{e}_\alpha \boldsymbol{e}_\alpha f_\alpha^{eq}$.

The summation of equation (2.38) in the particle velocity space gives the second-order continuity equation:

$$\frac{\partial \rho}{\partial t_1} = 0 \qquad (2.41)$$

The summation of equation (2.38) multiplied by $\boldsymbol{e}_\alpha$ in the particle velocity space gives the second-order momentum equation:

$$\frac{\partial(\rho \boldsymbol{u})}{\partial t_1} + \nabla_1 \cdot \Pi^{(1)} = 0 \tag{2.42}$$

where $\Pi^{(1)} = \left(1 - \frac{1}{2\tau}\right)\sum_\alpha \boldsymbol{e}_\alpha \boldsymbol{e}_\alpha f_\alpha^{(1)}$.

The summation of equation (2.39) and equation (2.41) leads to the macroscopic continuity equation:

$$\frac{\partial \rho}{\partial t} + \nabla \cdot (\rho \boldsymbol{u}) = 0 \tag{2.43}$$

The summation of equation (2.40) and equation (2.42) leads to the macroscopic momentum equation:

$$\frac{\partial(\rho \boldsymbol{u})}{\partial t} + \nabla \cdot \Pi = 0 \tag{2.44}$$

The accuracy of equation (2.43) and equation (2.44) is the second order in ε. The momentum flux tensor in equation (2.44) has the form

$$\Pi_{\gamma\beta} = \sum_\alpha (\boldsymbol{e}_\alpha)_\gamma (\boldsymbol{e}_\alpha)_\beta \left[f_\alpha^{eq} + \left(1 - \frac{1}{2\tau}\right) f_\alpha^{(1)} \right] \tag{2.45}$$

where $(\boldsymbol{e}_\alpha)_\gamma$ is the component of the particle velocity $\boldsymbol{e}_\alpha$ in the γ - coordinate direction.

To specify the detailed form of $\Pi_{\gamma\beta}$, the lattice structure and the corresponding equilibrium distribution function have to be specified. For simplicity and without the loss of the generality, we take D2Q9 as an example.

Inserting the lattice velocities and their equilibrium distribution functions into equation (2.45), we have

$$\Pi_{\gamma\beta}^{(0)} = \sum_\alpha (\boldsymbol{e}_\alpha)_\gamma (\boldsymbol{e}_\alpha)_\beta f_\alpha^{eq} = p\delta_{\gamma\beta} + \rho \boldsymbol{u}_\gamma \boldsymbol{u}_\beta \tag{2.46}$$

$$\Pi_{\gamma\beta}^{(1)} = \left(1 - \frac{1}{2\tau}\right) \sum_{\alpha} (\boldsymbol{e}_{\alpha})_{\gamma} (\boldsymbol{e}_{\alpha})_{\beta} f_{\alpha}^{1} = \nu \left(\nabla_{\gamma} (\rho \boldsymbol{u}_{\beta}) + \nabla_{\beta} (\rho \boldsymbol{u}_{\gamma})\right) \tag{2.47}$$

where $p = \rho/3$ is the pressure, which gives a constant sound speed $c_s = 1/\sqrt{3}$; and $\nu = (2\tau - 1)/6$ is the kinematic viscosity.

The resulting momentum equation is

$$\rho \left(\frac{\partial \boldsymbol{u}_{\gamma}}{\partial t} + \nabla_{\beta} \cdot (\boldsymbol{u}_{\gamma} \boldsymbol{u}_{\beta}) \right) = -\nabla_{\gamma} p + \nu \nabla_{\beta} \cdot \left(\nabla_{\gamma} (\rho \boldsymbol{u}_{\beta}) + \nabla_{\beta} (\rho \boldsymbol{u}_{\gamma}) \right) \tag{2.48}$$

Equation (2.43) and equation (2.48) are exactly the same as the incompressible NS equations if the density variation $\delta\rho$ is small enough.

This means that LBM can recover the incompressible NS equations. When NS equations are valid, LBM can get the same result as the NS solvers. But LBM has discrete and kinetically 'molecular' properties in nature, so it still can be used when the continuum assumption breaks down. This indicates that the applications of LBM are wider than the applications of the NS solvers.

2.5 Boundary conditions in LBM

The implementation of the boundary conditions is an essential issue in LBM, since the boundary conditions determine the actual dynamics of the fluid flows. There are a lot of papers published about the implementation of the boundary conditions. A lot of work done in this thesis is also related to the implementation of the boundary conditions, especially the wall boundary condition.

The ways to deal with the wall boundary condition are originally taken from LGA. In order to obtain the no-slip velocity boundary condition, a bounce-back scheme for the

particle density distribution at a solid wall was used by Wolfram (1986). In this so-called bounce-back scheme, the particle density distribution streams to a wall node and simply scatters back to the node it comes from. The obvious advantage of this bounce-back scheme is its easy implementation in the real applications, which is very important for the problems with complex geometries such as the flows through porous media. However, it is found that the bounce-back condition only has the first-order numerical accuracy at the boundaries when BGK collision model is used. This degrades the accuracy of LBM because LBM has the second-order accuracy in the interior flow fields.

To improve the numerical accuracy of LBM on the boundaries, several improved bounce-back schemes and other kinds of boundary treatments have been proposed. Ziegler (1993) proposed the second-order halfway bounce-back scheme by shifting the non-slip boundary into the fluid by half of one mesh unit. In the same year, Skordos suggested that the velocity gradients should be included in the equilibrium distribution function at the wall nodes. Inamuro et al. (1995) corrected the bounce-back scheme by introducing a counter slip velocity at the wall. Maier et al. (1996) modified the bounce-back condition to make the net momentum tangent to the wall become zero and preserve the momentum normal to the wall. However, all the above-mentioned improved bounce-back conditions cannot keep the second-order accuracy when the treatments are used in the curved boundaries. Zou & He (1997) extended the bounce-back condition to be used for the non-equilibrium part of the density distribution.

Besides the bounce-back boundary condition and its improved forms, other implementations of boundary conditions have been proposed by several researchers. In 1995, Noble et al. proposed a hydrodynamic boundary condition. In their treatment, a pressure or a velocity constraint is used on the wall and the unknown density distributions

are calculated by using the conservation equations of mass, moment and energy. It is worth mentioning that this implementation of boundary condition can also be applied to other kinds of boundaries such as the inlet and outlet boundaries of channel flows. However, it is only applicable to simple boundaries and the unknown density distributions should not exceed the available number of conservation equations. Filippova et al. (1998) introduced a boundary-fitting condition for the complex boundaries based on the Cartesian grids. This implementation of the boundary condition is based on the combination of the concepts of bounce-back scheme and interpolation of the density distributions on the wall so as to achieve the second-order accuracy on the boundaries with arbitrary shape. So it requires more computational effort and is very inconvenient in the implementation because the boundary does not exactly lie on the grid points. Chen et al. (1996) proposed a second-order extrapolation scheme, starting from the viewpoint that LBM is a special finite difference scheme of kinetic equation. They adopt the staggered mesh discretization from the traditional finite difference method. The unknown particle density distributions on the wall can be obtained from the extrapolation of the density distributions within the flow. In 1999, Mei et al. developed a second-order accurate treatment for the curved boundary. It is an improvement of the scheme proposed by Filippova et al. (1998). For FVLBM, Peng et al. (1999a) proposed the half covolume scheme for the wall boundary. It treats the boundary nodes as the interior nodes except that for the boundary nodes, the flux across the boundaries should be included. However, there still exist some problems when it is used in the practical applications. A new implementation of the boundary condition for FVLBM was proposed in this thesis based on the half-covolume scheme and bounce-back rule for the non-equilibrium density distribution.

Recently, Bouzidi et al. (2001) proposed a new scheme for wall boundary conditions. It uses the bounce-back and interpolations. Based on this, Ginzburg & d'Humieres (2003) presented a general framework called multi-reflection boundary conditions for several previously introduced boundary conditions for LBM, such as the bounce-back rule and linear and quadratic interpolations. It gives theoretical tools to study the existing link-type boundary conditions and their corresponding accuracy and designs boundary conditions for general flows which are third-order kinetic accurate. The good stability of these schemes is highlighted by some simulations of moving obstacles: a cylinder between flat walls and a sphere in a cylinder.

2.6 Stability of LBM

Stability is a key property of any numerical scheme since it helps to protect against numerical runaways due to the cumulative error build-up or other generic sources of inaccuracy. For the explicit schemes, the basic notion is that the lattice is a discrete world that can only support signals with a finite propagation speed.

For linear stability, Succi in his book (2002) has done some analysis for the stability of LBM and we will list some important results here.

The relaxation parameter obeys the following inequality:

$$0 < \frac{1}{\tau} < 2 \tag{2.49}$$

In view of the expression of the fluid viscosity $\upsilon \sim \left(\tau - \frac{1}{2} \right)$, equation (2.49) is precisely the condition for the fluid viscosity to be positive. The fact that $\frac{1}{2}$ exists in the expression

of the viscosity comes from the second-order terms in the Taylor series expansion of the streaming operator. This matches the intuitive notion of the negative viscosity as physical instability. The limit of $1/\tau \to 0$ breaks the adiabatic assumption that begets the convergence of a hyperbolic equation to a diffusive equation. The other extreme $1/\tau \to 2$ cannot be reached, because it gives rise to the sub-grid scales which the scheme is not able to dissipate, thereby leading to a catastrophe. This will be the issue of the nonlinear stability.

The linear stability analysis is also carried out in detail by Lallemand & Luo in 2000. A systematic and general procedure to analyze the LBE models is described in the paper. The proposed procedure can be readily applied to analyze more complicated LBE models.

For non-linear stability, a rigorous theoretical analysis is impossible and a number of general guiding criteria are given by Sterling & Chen (1996) and Pavlo et al. (1998b). One of these guiding criteria is the concept of the conservativeness of a numerical scheme, namely the ability to ensure that the physically conserved quantities remain conserved exactly in the lattice as well.
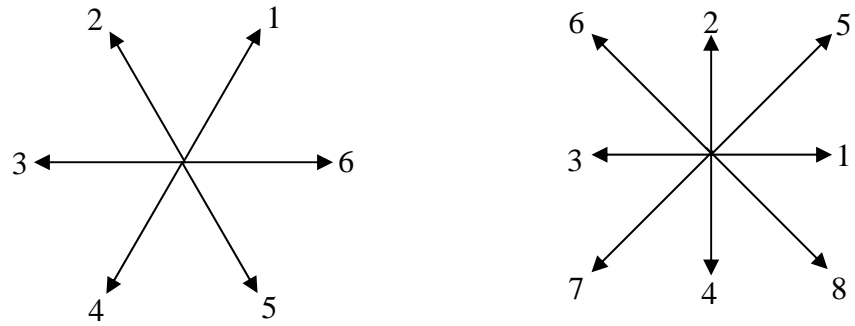
Figure 2.1 The lattice velocities of D2Q7 and D2Q9
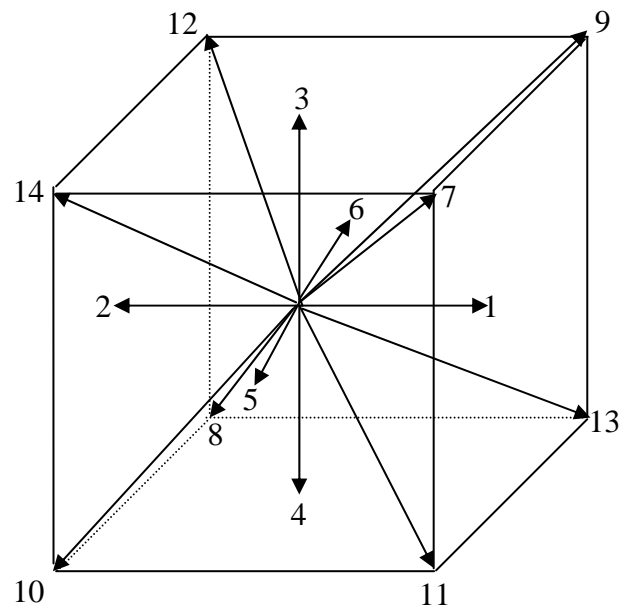
Figure 2.2 The lattice velocities of D3Q15
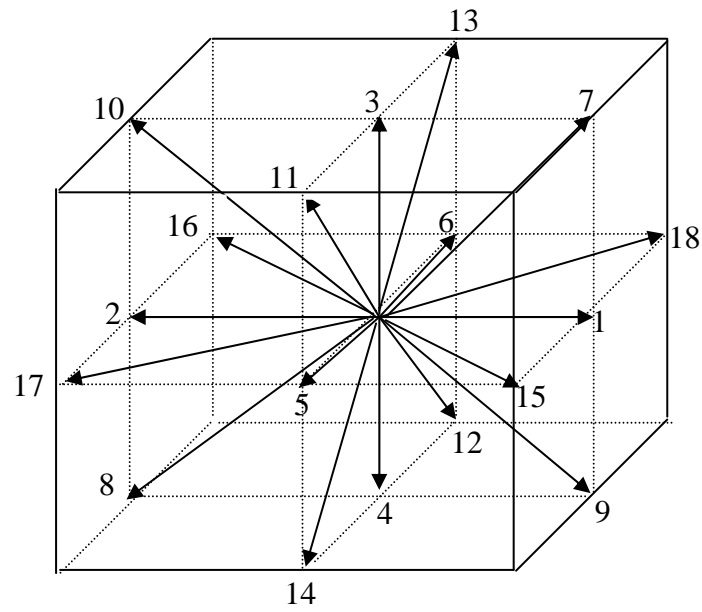
Figure 2.3 The lattice velocities of D3Q19

Chapter 3

Development of the IEDDF thermal model

3.1 Introduction

As mentioned in Chapter 1, the lack of a satisfactory thermal model for LBM is one of the shortcomings that hamper its use in the general applications as a practical CFD tool. The IEDDF thermal model proposed by He et al. (1998b) has proven itself to be an acceptable one among the current thermal models. It greatly improves the stability compared with some other thermal models. At the same time, it can incorporate the viscous heat dissipation and compression work done by pressure. However, because the IEDDF thermal model is a relatively new model, it still needs a lot of benchmarks, especially the numerical simulations in the presence of the solid boundaries. In addition, this model is limited to the applications with Dirichlet boundary condition. So in this study, we developed a new implementation scheme for Neumann boundary condition and did the benchmark study with the solid boundaries.

In this chapter, firstly, the IEDDF thermal model was described, including the introduction of the internal energy density distribution, the evaluation of the macroscopic variables and the discretization of the continuous Boltzmann equations. Secondly, the non-dimensional form of this thermal model was derived. Then, the detailed information about the implementation of the boundary conditions, especially Neumann boundary condition, was given. Finally, in order to test the properties of this thermal model and validate our implementation of Neumann boundary condition, the numerical simulations

of Couette flows and the natural convection in a square cavity were carried out. The accuracy of this model was investigated and the grid-independence study for the natural convection in a square cavity on a wide range of Rayleigh numbers was thoroughly carried out.

3.2 The IEDDF thermal model

The IEDDF thermal model was developed on the basis of the recent discovery that the LBM isothermal models can be directly derived by properly discretizing the continuous Boltzmann equation in the temporal, spatial and velocity spaces (He & Luo 1997, Abe 1997). Following the same procedure, the IEDDF thermal model was derived by discretizing the continuous Boltzmann evolution equation for the internal energy density distribution. So firstly, the energy density distribution was introduced and its continuous Boltzmann evolution equation was derived; then this continuous Boltzmann equation was discretized in a special manner. We described this process thoroughly in the following sections.

3.2.1 Internal energy density distribution and its continuous Boltzmann evolution equation

Kinetic theory states that the evolution equation for the single-particle density distribution in a fluid system obeys the following continuous Boltzmann equation

$$\partial_t f + (e \cdot \nabla) f = \Omega(f) + F_f \tag{3.1}$$

where f is the single-particle density distribution; e is the microscopic particle velocity;

$\Omega(f) = -\dfrac{f - f^{eq}}{\tau_v}$ is the collision term, in which f^{eq} is Boltzmann-Maxwellian

equilibrium distribution function and τ_v is the relaxation time for density distribution;

$F_f = \boldsymbol{G} \cdot \nabla_e f$ is the term due to the external force $\boldsymbol{G}$ acting on the unit mass.

Macroscopic variables can be calculated by

$$\rho = \int f d\boldsymbol{e} \tag{3.2a}$$

$$\rho \boldsymbol{u} = \int \boldsymbol{e} f \, d\boldsymbol{e} \tag{3.2b}$$

$$\frac{\rho DRT}{2} = \int \frac{(\boldsymbol{e} - \boldsymbol{u})^2}{2} f d\boldsymbol{e} \tag{3.2c}$$

where D is the dimension of space, R is the ideal gas constant and T is the temperature.

According to equation (3.2c), a new variable called the internal energy density distribution is introduced:

$$g = \frac{(\boldsymbol{e} - \boldsymbol{u})^2}{2} f \tag{3.3}$$

From equation (3.1), the evolution equation for g should satisfy:

$$\partial_t g + (\boldsymbol{e} \cdot \nabla) g = \frac{(\boldsymbol{e} - \boldsymbol{u})^2}{2} \Omega(f) - f(\boldsymbol{e} - \boldsymbol{u}) \cdot [\partial_t \boldsymbol{u} + (\boldsymbol{e} \cdot \nabla)\boldsymbol{u}] \tag{3.4}$$

It will become

$$\partial_t g + (\boldsymbol{e} \cdot \nabla) g = -\frac{g - g^{eq}}{\tau_c} - f(\boldsymbol{e} - \boldsymbol{u}) \cdot [\partial_t \boldsymbol{u} + (\boldsymbol{e} \cdot \nabla)\boldsymbol{u}] \tag{3.5}$$

after introducing a new collision model for the internal energy density distribution. This collision model satisfies the following relationship:

$$\frac{(e-u)^2}{2}\Omega(f) = -\frac{g-g^{eq}}{\tau_c} \tag{3.6}$$

where

$$g^{eq} = \frac{(e-u)^2}{2}f^{eq} = \frac{\rho(e-u)^2}{2(2\pi RT)^{D/2}}\exp\left[-\frac{(e-u)^2}{2RT}\right] \tag{3.7}$$

and τ_c is the relaxation time for internal energy density distribution.

Then the macroscopic temperature can be calculated by:

$$\frac{\rho DRT}{2} = \int g d\boldsymbol{e} \tag{3.8}$$

3.2.2 Discretization of the continuous Boltzmann equations

In the previous section, the continuous Boltzmann evolution equation for the internal energy density distribution is derived. Equations (3.1) and (3.5) should be discretized in the temporal, spatial and particle velocity space properly so as to recover the correct macroscopic equations. In order to do this, an accurate and computationally efficient numerical scheme is constructed.

In most of the previous isothermal LBM, equation (3.1) is integrated using the first-order scheme. The second-order truncation error is absorbed into the physical viscous term. The effect is that the viscosity changes from $\tau_v RT$ to $(\tau_v - 0.5\delta t)RT$. For the thermal model, however, the viscosity is involved not only in the momentum equations but also in the energy equation. The second-order truncation error is no longer trivial. Shown in the work of He et al. (1998b), the viscous heat dissipation term comes from the non-equilibrium part of the density distribution. This term only depends on the first-order Chapman-Enskog approximation and is not affected by the second-order truncation error

that comes from the second-order Chapman-Enskog expansion. This means that the viscosity in the viscous heat dissipation should be $\tau_v RT$. To eliminate this inconsistency, integrate equations (3.1) and (3.5) by adopting a second-order scheme and introduce the new variables $\overline{f}$ and $\overline{g}$ to avoid the implicitness of the scheme. The evolution equations for $\overline{f}$ and $\overline{g}$ become:

$$\overline{f}_\alpha(\boldsymbol{x}+\boldsymbol{e}_\alpha\delta t,t+\delta t)-\overline{f}_\alpha(\boldsymbol{x},t)=-\frac{\delta t}{\tau_v+1/2\,\delta t}\left[\overline{f}_\alpha(\boldsymbol{x},t)-f_\alpha^{eq}(\boldsymbol{x},t)\right]+\frac{\tau_v F_{f\alpha}\delta t}{\tau_v+1/2\,\delta t} \tag{3.9}$$

$$\overline{g}_\alpha(\boldsymbol{x}+\boldsymbol{e}_\alpha\delta t,t+\delta t)-\overline{g}_\alpha(\boldsymbol{x},t)=-\frac{\delta t}{\tau_c+1/2\,\delta t}\left[\overline{g}_\alpha(\boldsymbol{x},t)-g_\alpha^{eq}(\boldsymbol{x},t)\right]-\frac{\tau_c f_\alpha(\boldsymbol{x},t)q_\alpha\delta t}{\tau_c+1/2\,\delta t} \tag{3.10}$$

where

$$\overline{f}_\alpha = f_\alpha + \frac{\delta t}{2\tau_v}\left(f_\alpha - f_\alpha^{eq}\right) - \frac{\delta t}{2}F_{f\alpha} \tag{3.11}$$

$$\overline{g}_\alpha = g_\alpha + \frac{\delta t}{2\tau_c}\left(g_\alpha - g_\alpha^{eq}\right) + \frac{\delta t}{2}f_\alpha q_\alpha \tag{3.12}$$

$$q_\alpha = (\boldsymbol{e}_\alpha - \boldsymbol{u})\cdot\left[\frac{1}{\rho}(-\nabla p + \nabla\cdot\Pi) + (\boldsymbol{e}_\alpha - \boldsymbol{u})\cdot\nabla\boldsymbol{u}\right] \tag{3.13}$$

To derive a discrete scheme, the velocity space must be discretized appropriately. To recover the continuity and momentum equations at the NS level, the microscopic velocity space must be discretized to guarantee that the zeroth through third moments of the equilibrium density distribution function are exact. D2Q9 model can satisfy this requirement. For the recovery of the macroscopic energy equation, it involves the zeroth through second order moments of the equilibrium internal energy density distribution. So higher order quadrature is needed for the thermal model. Fortunately, through some straight forward algebra, shown in the paper of He et al. (1998b), it can be proved that the

zeroth through the second order moments of higher requirement part vanish. So D2Q9 model is still valid for this thermal model.

When D2Q9 is used, the equilibrium distribution functions for the internal energy density distribution are:

$$g_0^{eq} = -\frac{2\rho\varepsilon}{3}\frac{u^2}{c^2} \tag{3.14a}$$

$$g_{1,2,3,4}^{eq} = \frac{\rho\varepsilon}{9}\left[\frac{3}{2} + \frac{3}{2}\frac{e_\alpha \cdot u}{c^2} + \frac{9}{2}\frac{(e_\alpha \cdot u)^2}{c^4} - \frac{3}{2}\frac{u^2}{c^2}\right] \tag{3.14b}$$

$$g_{5,6,7,8}^{eq} = \frac{\rho\varepsilon}{36}\left[3 + 6\frac{e_\alpha \cdot u}{c^2} + \frac{9}{2}\frac{(e_\alpha \cdot u)^2}{c^4} - \frac{3}{2}\frac{u^2}{c^2}\right] \tag{3.14c}$$

The macroscopic density, velocity and temperature are calculated by

$$\rho = \sum_\alpha \overline{f}_\alpha \tag{3.15a}$$

$$\rho u = \sum_\alpha e_\alpha \overline{f}_\alpha + \frac{\rho G \delta t}{2} \tag{3.15b}$$

$$\rho\varepsilon = \sum_\alpha \overline{g}_\alpha - \frac{\delta t}{2}\sum_\alpha f_\alpha q_\alpha \tag{3.15c}$$

where

$$\varepsilon = \frac{DRT}{2} \tag{3.16}$$

Using Chapman-Enskog expansion, equation (3.9) will recover the continuity and momentum equations at the NS level with the viscosity satisfying

$$\nu = \tau_\nu RT \tag{3.17}$$

Equation (3.10) will recover the energy equation

$$\partial_t(\rho\varepsilon) + \nabla \cdot (\rho u \varepsilon) = \nabla \cdot (\rho \chi \nabla \varepsilon) + \Pi : \nabla u - p\nabla \cdot u \tag{3.18}$$

with the thermal diffusivity satisfying

$$\chi = 2\tau_c RT \tag{3.19}$$

3.3 Non-dimensional form for the IEDDF thermal model

In order to obtain useful and comparable results for the fluid flows, the non-dimensional form for the IEDDF thermal model was derived and used in the following numerical simulations.

3.3.1 Non-dimensional form for the density distribution

When the external force is the buoyancy force, the Boussinesq approximation is applied, that is

$$\boldsymbol{G} = \beta g(T - T_m)\boldsymbol{j} \tag{3.20}$$

where β is the thermal expansion coefficient; g is the acceleration due to the gravity and $\boldsymbol{j}$ is the unit vector denoting the vertical direction opposite to that of the gravity; $T_m = \dfrac{T_0 + T_1}{2}$ is the average temperature, where T_0 and T_1 represent the low and high temperatures, respectively. With this buoyancy force, the evolution equation (3.1) for the density distribution becomes:

$$\partial_t f + (\boldsymbol{e} \cdot \nabla)f = -\frac{f - f^{eq}}{\tau_v} + \frac{\beta g(T - T_m)\boldsymbol{j} \cdot (\boldsymbol{e} - \boldsymbol{u})}{RT} f^{eq} \tag{3.21}$$

Using $c = \sqrt{3RT_m}$ as the characteristic velocity, H as the characteristic length, $H/\sqrt{3RT_m}$ as the characteristic time, ρ_0 as the characteristic density and $T^{'} = (T - T_m)/(T_1 - T_0)$ as the non-dimensional temperature for equation (3.21), the non-dimensional form becomes:

$$\partial_t f' + \left(e' \cdot \nabla'\right)f' = -\frac{f' - f'^{eq}}{\tau_v'} + \frac{H\beta g \Delta T}{RT_m}T' j \cdot \left(e' - u'\right)f'^{eq} \qquad (3.22)$$

where $\Delta T = T_1 - T_0$ and the superscript $'$ denotes dimensionless parameters.

Using the relationship $\nu = \tau_v RT_m = \tau_v' \dfrac{H}{\sqrt{3RT_m}}RT_m$, $\chi = 2\tau_c RT_m = 2\tau_c' \dfrac{H}{\sqrt{3RT_m}}RT_m$ and

$Ra = \dfrac{\beta g \Delta T H^3}{\nu\chi}$, equation (3.22) becomes

$$\partial_t f' + \left(e' \cdot \nabla'\right)f' = -\frac{f' - f'^{eq}}{\tau_v'} + R_a \frac{2\tau_v'\tau_c'}{3}T' j \cdot \left(e' - u'\right)f'^{eq} \qquad (3.23)$$

The non-dimensional forms for the equilibrium density distribution functions are

$$f'^{eq}_\alpha = w_\alpha \rho'\left[1 + 3e_\alpha' \cdot u' + \frac{9}{2}\left(e_\alpha' \cdot u'\right)^2 - \frac{3}{2}u'^2\right] \qquad (3.24)$$

3.3.2 Non-dimensional form for the internal energy density distribution

Using $T'' = T/T_m$ as the non-dimensional temperature for the internal energy density distribution evolution equation, the non-dimensional form for equation (3.5) becomes

$$\partial_t g' + \left(e' \cdot \nabla'\right)g' = -\frac{g' - g'^{eq}}{\tau_c'} - f'\left(e' - u'\right)\cdot\left[\partial_t u' + \left(e' \cdot \nabla'\right)u'\right] \qquad (3.25)$$

The non-dimensional forms for the equilibrium internal energy density distribution functions become

$$g'^{eq}_0 = -\frac{2\rho'\varepsilon'}{3}u'^2 \qquad (3.26a)$$

$$g'^{eq}_{1,2,3,4} = \frac{\rho'\varepsilon'}{9}\left[1.5 + 1.5\left(e_\alpha' \cdot u'\right) + 4.5\left(e_\alpha' \cdot u'\right)^2 - 1.5u'^2\right] \qquad (3.26b)$$

$$g^{'eq}_{5,6,7,8} = \frac{\rho^{'}\varepsilon^{'}}{36}\left[3 + 6\left(e_{\alpha}^{'}\cdot u^{'}\right) + 4.5\left(e_{\alpha}^{'}\cdot u^{'}\right)^{2} - 1.5u^{'2}\right]$$ (3.26c)

where $\varepsilon^{'} = T^{''}/3$

Because of the limitation of the IEDDF thermal model itself, two different non-dimensional temperatures have to be used. In order to build the connection between these two different non-dimensional temperatures, the temperature ratio $r = \Delta T/T_{m}$ is introduced and it should be smaller than 0.4 because of the incompressibility requirement. Then the two non-dimensional temperatures have the following relationship

$$T^{'} = \frac{T^{''} - 1}{r}$$ (3.27)

3.3.3 Determination of the two non-dimensional relaxation times

Seen from equations (3.23) and (3.25), the two non-dimensional relaxation parameters $\tau_{v}^{'}$ and $\tau_{c}^{'}$ play an important role in the evolution equations. Their values are determined from the viscosity and thermal diffusivity, respectively. Since the dynamic similarity for most thermal flows depends on two dimensionless parameters: Prandtl number Pr defined as $\mathrm{Pr} = \dfrac{v}{\chi}$ and Rayleigh number Ra, the two non-dimensional relaxation parameters can be determined from these two dimensionless parameters.

Starting from the definition of Prandtl number and Rayleigh number, the following equations can be obtained using equations (3.17) and (3.19):

$$\mathrm{Pr} = \frac{v}{\chi} = \frac{\tau_{v}RT_{m}}{2\tau_{c}RT_{m}} = \frac{\tau_{v}^{'}}{2\tau_{c}^{'}}$$ (3.28)

$$Ra = \frac{g\beta\Delta TH^3}{v\chi} = \frac{V_c^2 H^2}{\tau_v RT_m 2\tau_c RT_m} = \frac{V_c^{'2} 3RT_m H^2}{\tau_v' H / \sqrt{3RT_m} RT_m 2\tau_c' H / \sqrt{3RT_m} RT_m} = \frac{9V_c^{'2}}{2\tau_v' \tau_c'} \quad (3.29)$$

where $V_c = \sqrt{g\beta H\Delta T}$ is the characteristic thermal speed and should be chosen carefully so that the low Mach number approximation holds.

Once these two dimensionless parameters Pr and Ra are given, the two non-dimensional relaxation parameters τ_v' and τ_c' can be determined using equations (3.28) and (3.29). Usually V_c' is chosen to be less than 0.3.

Since only the non-dimensional form is used in the following sections and the dimensional form does not appear any more, the prime for the non-dimensional form is omitted for simplicity.

3.4 Wall boundary conditions

We define the incoming distributions as the distributions going from the outside environment to the inside flow and the outgoing distributions as the distributions going from the inside flow to the outside environment. Generally speaking, the problem of formulating boundary conditions within LBM consists of finding an appropriate relationship expressing the incoming distributions (unknown) as a function of the outgoing ones (known). The bounce-back rule of the non-equilibrium distributions is used here to determine the incoming distributions from the outgoing ones.

According to Grad's (1949) "thirteen-moment" system, the non-equilibrium density distribution is written as

$$f^{neq} = f^{eq}\left(\frac{\Pi:(e_\alpha-u)(e_\alpha-u)}{2pRT} - \frac{S\cdot(e_\alpha-u)}{2pRT}\left(1-\frac{(e_\alpha-u)^2}{(D+2)RT}\right)\right) \quad (3.30)$$

where Π and S are the stress tensor and heat flux vector, respectively. The terms involving $O(u^2)$ and higher order can be neglected since the non-equilibrium distribution itself is very small, which leads to

$$f^{neq} = f^{eq} \left(\frac{\Pi : e_\alpha e_\alpha}{2(RT)^2} - \frac{S \cdot e_\alpha}{2(RT)^2} \left(1 - \frac{e_\alpha^2}{(D+2)RT} \right) \right) \qquad (3.31)$$

For isothermal flows, the heat transfer term can be neglected and the above equation becomes:

$$f^{neq} = f^{eq} \frac{\Pi : e_\alpha e_\alpha}{2(RT)^2} \qquad (3.32)$$

So the following relationship should be satisfied:

$$f_\alpha^{neq,iso} = f_\beta^{neq,iso} \qquad (3.33)$$

where α and β have the opposite directions. For the solid static wall, this is just the commonly used bounce-back condition.

For the thermal problems, neglecting again all the terms involving $O(u^2)$, the non-equilibrium distribution for the internal energy density distribution is written as:

$$g_\alpha^{neq} = e_\alpha^2 f_\alpha^{neq,iso} - w_\alpha e_\alpha^2 \frac{S \cdot e_\alpha}{2(RT)^2} \left(1 - \frac{e_\alpha^2}{(D+2)RT} \right) \qquad (3.34)$$

This suggests the useful thermodynamic boundary condition for Dirichlet boundary condition:

$$g_\alpha^{neq} - e_\alpha^2 f_\alpha^{neq,iso} = -\left(g_\beta^{neq} - e_\beta^2 f_\beta^{neq,iso} \right) \qquad (3.35)$$

Since in this model, the density distribution does not take into account the temperature variations, its non-equilibrium part satisfies the boundary condition (3.33), and plays the role of $f^{neq,iso}$ in the energy boundary condition (3.35). The velocity on the wall is used

when the equilibrium density distribution function in equation (3.33) is calculated in order to enforce the no-slip boundary condition. And the temperature on the wall is used when the equilibrium internal energy density distribution function in equation (3.35) is calculated in order to satisfy Dirichlet boundary condition.

However, Neumann boundary condition happens in many real thermal applications. For Neumann boundary condition, the temperature on the boundary is unknown and only the heat flux (the derivative of the temperature) is given. So the temperature in the equilibrium internal energy density distribution function is unknown and the boundary condition (3.35) cannot be used directly. There are two ways to solve this problem. One way is to find the relationship between the macroscopic Neumann boundary condition and the messcopic internal energy density distribution. This is very complicated and involves the physical explanation of the heat flux itself. The other way is to try to transfer it to Dirichlet boundary condition, avoiding the complicated derivations of the first method. The second method is chosen by us. Using the conventional second-order finite difference scheme to approximate the derivative of the temperature so as to obtain the approximate temperature on the boundary, equation (3.35) can now be used. In order to obtain the accurate value of the temperature on the boundary, iteration for the temperature is needed.

The temperature on the wall can be determined from the heat flux by the conventional second-order finite difference approximation

$$T_w = \left(4T_2 - T_3 - \left(\partial T/\partial x\right) \times 2\Delta x\right)/3 \tag{3.36}$$

where T_2 is the temperature in the fluid on the first gridline next to the wall and T_3 is the temperature in the fluid on the second gridline next to the wall. After obtaining the

temperature on the wall, the equilibrium internal energy density distribution functions can be calculated using this temperature and Dirichlet boundary condition (3.35) can be used.

3.5 Numerical Simulations

The thermal model and its properties were tested by the following numerical simulations of Couette flows with a temperature gradient. The new implementation for the Neumann boundary condition was validated by the numerical simulations of the natural convection in a square cavity.

The convergence criterion for these two cases is set to

$$\max_{i,j} \left| \sqrt{(u_{i,j}^2 + v_{i,j}^2)^{n+1}} - \sqrt{(u_{i,j}^2 + v_{i,j}^2)^n} \right| \leq 10^{-8}, \max_{i,j} \left| T_{i,j}^{n+1} - T_{i,j}^n \right| \leq 10^{-8} \tag{3.37}$$

where n and $n+1$ are the old and new time levels, respectively.

3.5.1 Couette flows with a temperature gradient

This case provides a good test for the ability of the thermal model to describe the viscous heat dissipation. The configuration of this flow is sketched in Figure 3.1. The bottom wall is fixed and the top boundary moves at the speed of U. T_0 and T_1 are the temperatures at the bottom and top boundaries, respectively. y is the distance from the bottom boundary. H is the height of the channel. No external force is involved in this problem. The analytic temperature profile is:

$$\frac{T - T_0}{T_1 - T_0} = \frac{y}{H} + \frac{\Pr Ec}{2} \frac{y}{H} \left(1 - \frac{y}{H} \right) \tag{3.38}$$

where $Ec = U^2 / c_\nu (T_1 - T_0)$ is the Eckert number and c_ν is the specific heat at constant volume.

3.5.1.1 Boundary conditions. Besides the wall boundaries, this flow contains the inlet and outlet boundaries. The boundary conditions for these inlet and outlet boundaries are periodical. The particle velocity directions at the inlet and outlet boundaries are illustrated in Figure 3.2.

At the inlet, the distributions of $f_{in6}, f_{in3}, f_{in7}, f_{in2}, f_{in4}$ and $g_{in6}, g_{in3}, g_{in7}, g_{in2}, g_{in4}$ are determined from equations (3.9) and (3.10) respectively; at the outlet, the distributions of $f_{out5}, f_{out1}, f_{out8}, f_{out2}, f_{out4}$ and $g_{out5}, g_{out1}, g_{out8}, g_{out2}, g_{out4}$ are calculated from these two equations respectively. The rest of the distributions for the density and internal energy density distributions at the inlet and outlet will be determined from the periodical boundary conditions. They are $f_{in5} = f_{out5}$, $f_{in1} = f_{out1}$, $f_{in8} = f_{out8}$, $g_{in5} = g_{out5}$, $g_{in1} = g_{out1}$, $g_{in8} = g_{out8}$ and $f_{out6} = f_{in6}, f_{out3} = f_{in3}, f_{out7} = f_{in7}$, $g_{out6} = g_{in6}$, $g_{out3} = g_{in3}$, $g_{out7} = g_{in7}$.

At the corner points, there is a little difference. Take the bottom corner point at the inlet as an example. The distributions of $f_{in3}, f_{in7}, f_{in4}$ and $g_{in3}, g_{in7}, g_{in4}$ are determined from equations (3.9) and (3.10) respectively. The distributions of f_{in2}, f_{in5} and g_{in2}, g_{in5} are determined from the bounce-back rule of the non-equilibrium distributions expressed by equations (3.33) and (3.35) respectively. The rest of the distributions are determined from the periodical boundary conditions as $f_{in1} = f_{out1}$, $f_{in6} = f_{out6}$, $f_{in8} = f_{out8}$ and $g_{in1} = g_{out1}$, $g_{in6} = g_{out6}$, $g_{in8} = g_{out8}$.

3.5.1.2 Results and discussions. In order to evaluate the accuracy of this thermal model and study its ability to describe the viscous heat dissipation, numerical simulations for a wide range of Prandtl number and Eckert number were carried out. In these simulations, the parameters used were $U = 0.1c, \quad H = 20, \quad \tau_\nu = 0.5 \quad$ and $T_0 = 1$.

The temperature profiles along the vertical direction for Ec=4, 20 and 40 respectively are presented in Figure 3.3. The Prandtl number for these three cases is Pr=0.5. Figure 3.4 shows the temperature profiles for Pr=0.25,1.25 and 2.5 respectively. The Eckert number for these three cases is Ec=8. In these two figures, the lines represent the analytic solutions obtained by equation (3.38), and the marks represent the numerical results using the present IEDDF thermal model. As shown in these two figures, the numerical results agree very well with the analytic solutions. The product of $PrEc$ represents the ratio between viscous dissipation and heat conduction. When $PrEc$ is small, the effect of heat conduction overweighs the effect of viscous dissipation, so the temperature profile is almost linear. When $PrEc$ increases, the effect of viscous dissipation becomes more important. So the temperature profile deviates from linearity. The larger $PrEc$ is, the further away the temperature profile deviates from linearity. The present numerical simulations predict this tendency very well.

Since the present numerical simulations span over a wide range of values of $PrEc$, it is clear that this thermal model can successfully simulate viscous heat dissipation problems.

3.5.2 Natural convection in a square cavity

Buoyancy force driven flow in a square cavity with vertical sides, which are differentially heated, is a suitable vehicle for testing and validating numerical approaches used for a wide variety of practical problems. This problem has been extensively studied by many researchers such as David (1983) and Shu & Xue (1998). Since this problem has both Dirichlet and Neumann boundary conditions for the temperature, it was used here to validate our new implementation of Neumann boundary condition in the IEDDF thermal model.

In such a cavity, the temperature on the left boundary is higher than that on the right boundary. The top and bottom boundaries are adiabatic. The temperature difference between walls introduces a temperature gradient in a fluid. The consequent density difference induces a convective fluid motion. The configuration of this flow is sketched in Figure 3.5.

Nusselt number Nu is one of the most important dimensionless parameters in describing the convective heat transport property. Its average in the whole flow domain and along the particular vertical line x_0 can be defined by:

$$\overline{Nu} = \frac{H}{\chi \Delta T} \frac{1}{H^2} \int_0^H \int_0^H q_x(x, y) dx dy \tag{3.39}$$

$$\overline{Nu_{x_0}} = \frac{H}{\chi \Delta T} \frac{1}{H} \int_0^H q_x(x_0, y) dy \tag{3.40}$$

where $q_x(x, y) = uT(x, y) - \chi \left(\frac{\partial}{\partial x}\right) T(x, y)$ is the local heat flux in horizontal direction x.

3.5.2.1 Validation of the numerical results. The numerical simulations of this flow were carried out on a wide range of Rayleigh numbers from 10^3 to 10^6. Table 3.1 shows the

numerical results of the maximum horizontal velocity u_{max} on the vertical mid-plane of the cavity and its location y, the maximum vertical velocity v_{max} on the horizontal mid-plane of the cavity and its location x and the average Nusselt number throughout the cavity $\overline{Nu}$ using the present IEDDF thermal model. For comparison, the obtained results of velocities using LBM are rescaled using χ/H as the characteristic velocity. The numerical results obtained by Shu and Xue (1998) using differential quadrature (DQ) method are also included for comparison.

From Table 3.1, the numerical simulation results using the present IEDDF thermal model agree very well with the benchmark results using DQ method at a wide range of Rayleigh numbers. At a high Rayleigh number, the difference between the numerical results using these two different methods is larger than that at the low Rayleigh number. The reason may be that at a high Rayleigh number, the compressibility has more effect on the results, since the compressible equation is used for this incompressible problem with assumption of low-Mach-number approximation. Another reason may be that at a high Rayleigh number, when the flow becomes weakly turbulent, the solution given by the Boussinesq approximation deviates gradually from those by the exact equations. This means that the Boussinesq approximation may not properly describe the flow behavior under realistic temperature conditions beyond a certain Rayleigh number (Mlaouah et al., 1997).

With the increase of Rayleigh number, the values of u_{max}, v_{max} and $\overline{Nu}$ are increased greatly; and the position of maximum vertical velocity on horizontal mid-plane becomes nearer to the wall. This can be explained by the following reason. The higher is the Rayleigh number, the larger is the temperature difference. The increasing temperature

difference results in larger buoyancy force that drives the fluid motion to become stronger. This can be seen from the larger value of u_{max} and v_{max}. As a result, most of the fluid near the wall is driven into the motion and the heat transfer ability increases, leading to the smaller value of x where the maximum vertical velocity occurs and larger value of $\overline{Nu}$.

Another trend about Nusselt number is that it was slightly smaller than that of the corresponding benchmark result. The same trend was observed in the simulation of Rayleigh-Benard convection (Shan, 1997; He, 1998b). This may be due to the fact that the macroscopic equation of LBM is equivalent to the NS equations only up to the second-order of the macroscopic flow velocity. The higher order terms in the expanded Boltzmann-Maxwellian equilibrium distribution function are truncated by the so-called low-Mach number approximation. The higher order terms that have not been written explicitly in the macroscopic equations of LBM may no longer be negligible at high Rayleigh numbers.

3.5.2.2 Grid-dependence study. In order to further study the property of this thermal model with the new implementation of Neumann boundary condition, the grid-independence study on this natural convection problem for a wide range of Rayleigh numbers from 10^3 to 10^6 was carried out. Tables 3.2 to 3.5 show the grid-independence study results.

Seen from Tables 3.2-3.5, at the same Rayleigh number, with the increase of the grid number, difference between the results using two different methods became smaller. At low Rayleigh numbers, good results can be obtained by using small number of grids. When Rayleigh number is increased, larger number of grids is needed to obtain the

accurate results. This can be explained by the thinning of thermal boundary layer with increasing Rayleigh numbers. In order to resolve the thermal properties within thinner layer, more grids are needed.

It can be seen from Table 3.2 that when the mesh size was above 101×101, the computed numerical results remained the same. Thus, the mesh size of 101×101 was fine enough to obtain the accurate numerical results at a Rayleigh number of 10^3. This conclusion also suggests that at a Rayleigh number of 10^4, the grid independence study can start from mesh size of 101×101. Following the same procedure, it could be seen from Table 3.3, Table 3.4 and Table 3.5 that the mesh size of 151×151, 201×201 and 251×251 were fine enough for Rayleigh numbers of 10^4, 10^5 and 10^6 respectively. These conclusions agree well with the above-mentioned phenomena that the minimum fine grid number needed to obtain accurate results increases with increasing of Rayleigh numbers.

3.5.2.3 Analysis of the flow and thermal fields. Figure 3.6 and Figure 3.7 show the streamlines and isotherms at $Ra=10^3$, 10^4, 10^5 and 10^6. These plots agreed well with those obtained by Shu and Xue (1998). It was observed that the hot fluid near left wall moves upward and then turns towards the right wall, while the cold fluid near right wall moves downward and then turns towards the left wall. As shown in Figure 3.6 and Figure 3.7, when the Rayleigh number increases, the mixture of hot and cold fluids is enhanced by stronger natural convection current and the temperature gradients near left and right walls increase, resulting in larger heat transfers within the square cavity. This leads to the increase of stream function value ψ and Nusselt numbers Nu, which could be seen in Table 3.2-3.5.

In Figure 3.6, the special points in the streamline patterns are the stagnant points. The stagnant point is the point where $u = v = 0$. As indicated in Figure 3.6, a stagnant point could either be a focus or a saddle, depending on the Rayleigh number. For $Ra=10^3$ and 10^4, there was only one focus at $x/H = y/H = 0.5$ with uni-cellular, clockwise rotating flow. For $Ra=10^5$, the focus split up in a saddle at $x/H = y/H = 0.5$ and two new foci, forming two clockwise rotating rolls. For $Ra=10^6$, the saddle at $x/H = y/H = 0.5$ further split up in a focus and two new saddles, giving a total of three clockwise rotating rolls. This is in good agreement with Henkes and his co-workers' results (1988).

From the above two figures, it can be seen that this IEDDF thermal model with our new implementation of Neumann boundary condition can capture the correct flow and thermal patterns for the practical flow problems.

3.6 Conclusions

A new implementation of Neumann boundary condition for the IEDDF thermal model was proposed in order to solve the practical thermal problems with both Dirichlet and Neumann boundary conditions. The numerical simulation results of Couette flows and the natural convection in a square cavity over a wide range of Rayleigh numbers agree very well with the analytic or benchmark results, showing that this scheme is at least as accurate as conventional NS solvers. The results of natural convection in a square cavity also show that our implementation of Neumann boundary condition is valid in solving Neumann thermal flows. However, from the viewpoint of the practical applications of this IEDDF thermal model for the more complicated thermo-hydrodynamic problems, further studies on the use of IEDDF thermal model on the arbitrary mesh and its corresponding

implementation of boundary conditions are necessary. These works will be carried out in the following chapters.

Table 3.1 Comparison of the numerical results for the natural convection in a square cavity using two different methods

Ra	10^3		10^4		10^5		10^6	
Method	LBM	DQ	LBM	DQ	LBM	DQ	LBM	DQ
u_{max}	3.650	3.649	16.155	16.190	34.278	34.736	63.638	64.775
y	0.810	0.815	0.825	0.825	0.852	0.855	0.843	0.850
v_{max}	3.700	3.698	19.666	19.638	68.243	68.640	218.68	220.64
x	0.175	0.180	0.120	0.120	0.068	0.065	0.037	0.035
$\overline{Nu}$	1.117	1.118	2.239	2.245	4.507	4.523	8.788	8.800

Table 3.2 Grid-dependence study for the natural convection in a square cavity at $Ra=10^3$

Mesh	51×51	101×101	127×127	DQ	Davis
$\left|\psi_{mid}\right|$	1.170	1.175	1.175	1.175	1.174
u_{max}	3.636	3.649	3.650	3.649	3.649
y	0.820	0.810	0.810	0.815	0.813
v_{max}	3.702	3.700	3.700	3.698	3.697
x	0.180	0.180	0.175	0.180	0.178
$\overline{Nu}$	1.116	1.117	1.117	1.118	1.118
$\overline{Nu_{1/2}}$	1.114	1.116	1.116	1.118	1.118
$\overline{Nu_0}$	1.103	1.110	1.097	1.118	1.117
Nu_{max}	1.465	1.481	1.479	1.506	1.505
y	0.140	0.090	0.090	0.090	0.092
Nu_{min}	0.722	0.672	0.670	0.691	0.692
y	1.000	1.000	1.000	1.000	1.000

Table 3.3 Grid-dependence study for the natural convection in a square cavity at $Ra=10^4$

Mesh	101×101	151×151	201×201	DQ	Davis
$\left\lvert \psi_{mid} \right\rvert$	5.063	5.069	5.071	5.075	5.071
u_{max}	16.158	16.156	16.155	16.190	16.178
y	0.820	0.820	0.825	0.825	0.823
v_{max}	19.704	19.679	19.666	19.638	19.617
x	0.120	0.1200	0.120	0.120	0.119
$\overline{Nu}$	2.232	2.237	2.239	2.245	2.243
$\overline{Nu_{1/2}}$	2.224	2.231	2.235	2.245	2.243
$\overline{Nu_0}$	2.192	2.183	2.177	2.248	2.238
Nu_{max}	3.576	3.479	3.432	3.543	3.528
y	0.150	0.147	0.145	0.145	0.143
Nu_{min}	0.617	0.593	0.565	0.586	0.586
y	1.000	1.000	1.000	1.000	1.000

Table 3.4 Grid-dependence study for the natural convection in a square cavity at $Ra=10^5$

Mesh	151×151	201×201	251×251	DQ	Davis
$\left\lvert \psi_{mid} \right\rvert$	9.102	9.103	9.109	9.117	9.111
$\left\lvert \psi_{max} \right\rvert$	9.648	9.644	9.649	9.618	9.612
x	0.287	0.285	0.284	0.285	0.285
y	0.607	0.605	0.604	0.600	0.600
u_{max}	34.194	34.245	34.278	34.736	34.730
y	0.853	0.855	0.852	0.855	0.855
v_{max}	68.282	68.276	68.243	68.640	68.590
x	0.067	0.065	0.068	0.065	0.066
$\overline{Nu}$	4.494	4.501	4.507	4.523	4.519
$\overline{Nu_{1/2}}$	4.487	4.496	4.503	5.524	4.519
$\overline{Nu_0}$	4.446	4.430	4.417	4.527	4.509
Nu_{max}	7.984	7.833	7.743	7.788	7.717
y	0.080	0.080	0.090	0.080	0.081
Nu_{min}	0.767	0.758	0.743	0.725	0.729
y	1.000	1.000	1.000	1.000	1.000

Table 3.5 Grid-dependence study for the natural convection in a square cavity at $Ra=10^6$

Mesh	201×201	251×251	301×301	DQ	Davis
$\left\|\psi_{mid}\right\|$	16.359	16.369	16.368	16.270	16.320
$\left\|\psi_{max}\right\|$	16.832	16.827	16.829	16.714	16.750
x	0.150	0.148	0.150	0.150	0.151
y	0.555	0.552	0.550	0.550	0.547
u_{max}	63.251	63.527	63.638	64.775	64.630
y	0.840	0.844	0.843	0.850	0.850
v_{max}	218.33	218.47	218.68	220.64	219.36
x	0.040	0.040	0.037	0.035	0.038
$\overline{Nu}$	8.766	8.781	8.788	8.762	8.800
$\overline{Nu_{1/2}}$	8.759	8.775	8.782	8.727	8.799
$\overline{Nu_0}$	8.562	8.500	8.457	8.721	8.817
Nu_{max}	18.514	18.148	17.885	16.070	17.925
y	0.040	0.036	0.037	0.040	0.038
Nu_{min}	0.986	1.012	1.010	1.665	0.989
y	1.000	1.000	1.000	1.000	1.000
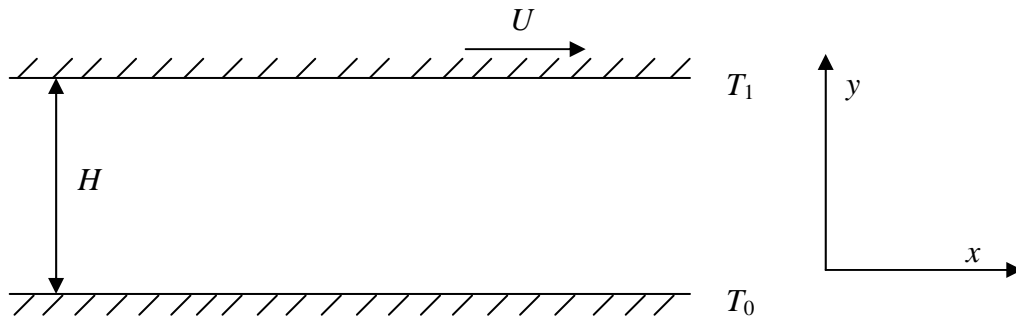
Figure 3.1 The configuration of Couette flow with a temperature gradient
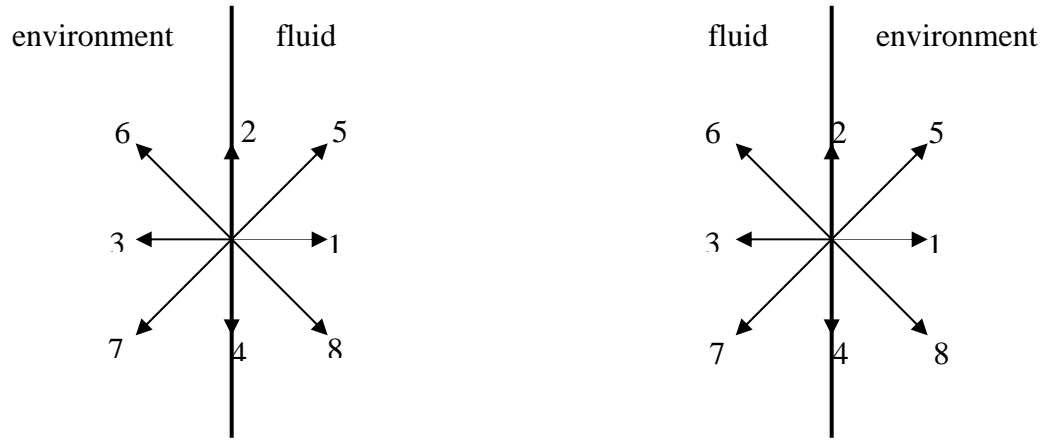
Figure 3.2 Particle velocity directions at the inlet and outlet boundaries
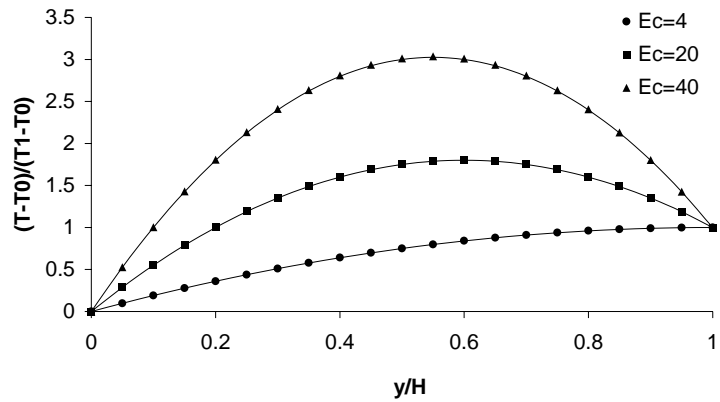
Figure 3.3 Temperature profiles along the vertical direction for Couette flow at *Pr*=0.5
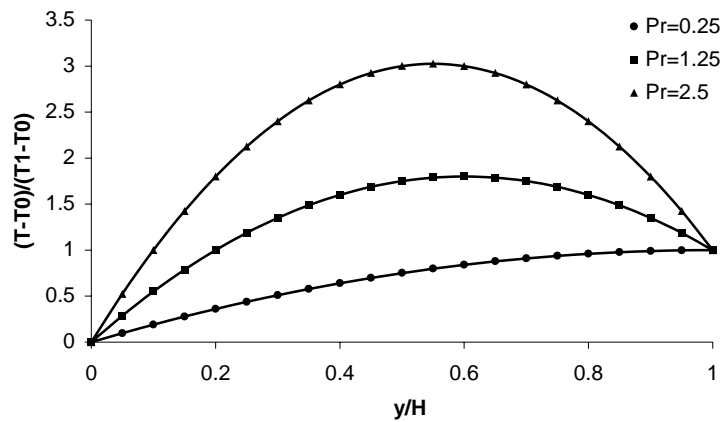
Figure 3.4 Temperature profiles along the vertical direction for Couette flow at *Ec*=8

$$U=0, V=0, \frac{\partial T}{\partial y} = 0$$

$U=0$
$V=0$
$T_1=1$

$U=0$
$V=0$
$T_0=0$

$$U=0, V=0, \frac{\partial T}{\partial y} = 0$$
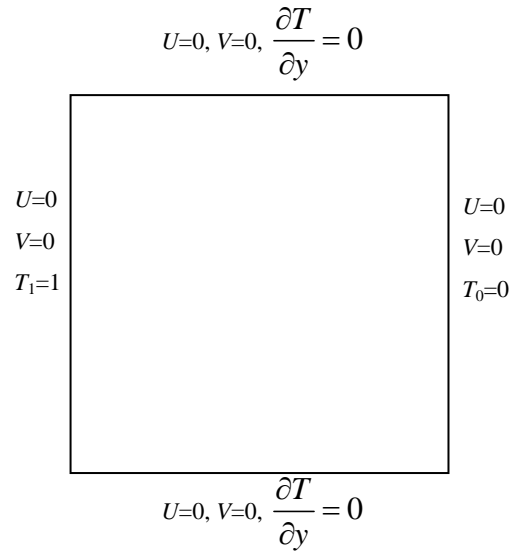
Figure 3.5 Configuration of the natural convection in a square cavity
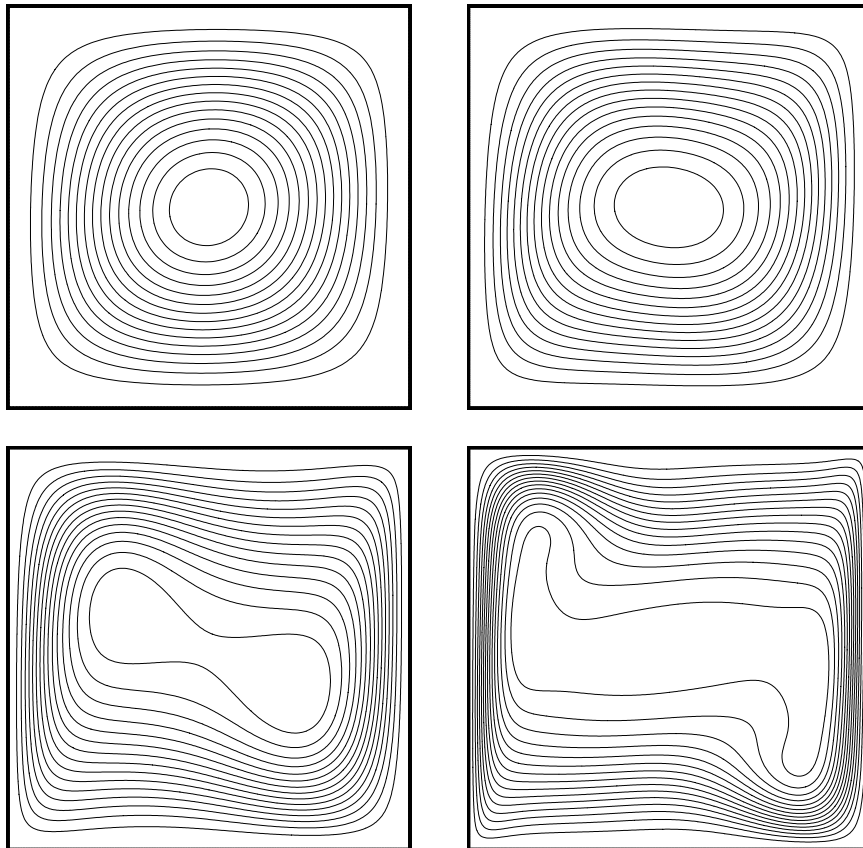
Figure 3.6 Streamlines of the natural convection in a square cavity
at $Ra=10^3, 10^4, 10^5$ and 10^6
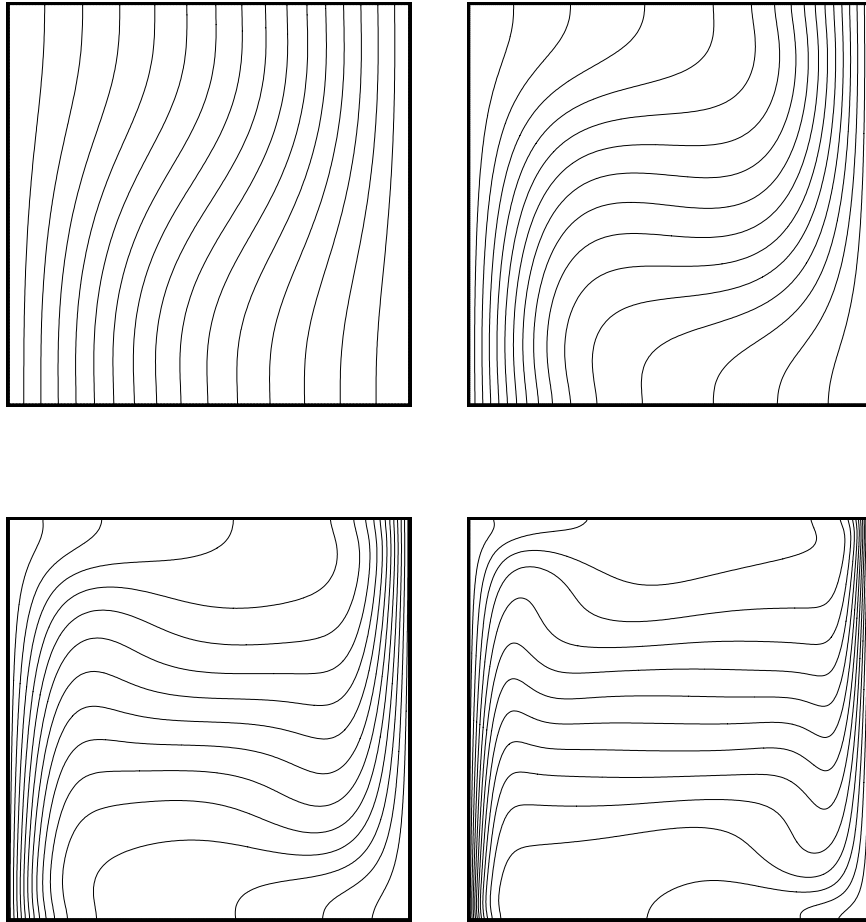
Figure 3.7 Isotherms of the natural convection in a square cavity
at $Ra=10^3, 10^4, 10^5$ and 10^6

Chapter 4

Finite volume LBM and its use in IEDDF thermal model

4.1 Introduction

As stated in Chapter 3, from the viewpoint of practical applications of IEDDF thermal model to solve more complicated thermo-hydrodynamic problems, further studies on the use of IEDDF thermal model on the arbitrary mesh and its corresponding implementation of boundary conditions are inevitable.

As mentioned in Chapter 1, although LBM has notable advantages over conventional methods, there are still some shortcomings in the implementation of LBM models. One of these is the lack of a satisfactory thermal model pointed out in the previous chapter. Another is that LBM defined on Cartesian-like grids is restricted to a special class of uniform and regular spatial lattices. Some researchers have attempted to extend its applicability to the irregular lattices. Among them, a new method was proposed by Xi et al. (1998, 1999a, 1999b), which can be used on the irregular meshes with arbitrary connectivity. It is based on the modern finite volume method and keeps the simplicity of conventional LBM. So this finite volume LBM (FVLBM) is selected by us to extend the current IEDDF thermal model to be used on the arbitrary mesh.

Before we do that, there still exist some problems for this new FVLBM. One of them is that the implementation of wall boundary conditions hinders its wide applications. The half-covolume technique was introduced by Peng et al. (1999a, 1999b) for the solid boundary condition. This method is quite general and simple in the sense that it does not

assume the fluid properties and orientations of boundary walls. It is very robust when the inlet and outlet boundaries are periodical. However, it will cause some problems when it is used in other flow problems such as the velocity profile being given at the inlet. In order to solve this problem and make FVLBM more useful in a practical sense, a new implementation of wall boundary condition for FVLBM is proposed by Chew et al. (2002). It is based on the half-covolume technique and bounce-back rule for the non-equilibrium distribution. In addition, the problem that arises from the implementation of wall boundary condition is more severe at the corner points even when we use our new proposed wall boundary condition. For example, for the two-dimensional driven cavity problem, the small vortex at left bottom corner cannot be obtained when our new implementation of wall boundary condition without any special treatment at corner points is used. So some special treatments are needed at corner nodes. Considering the fact that both the complete bounce back scheme and the half-covolume technique do not distinguish the particle directions among distributions, our proposed scheme for the wall boundary condition, which is a combination of the half-covolume and bounce-back scheme, is very easy to implement in a computer code. It is validated by its applications to the two-dimensional expansion channel flows and driven cavity flows.

Then we try to use this FVLBM in IEDDF thermal model so as to extend this thermal model to be used on the arbitrary mesh. For thermal flow problems, besides the above-mentioned lattice-uniformity restriction as in isothermal flows, the complexity of thermal problem itself greatly hampers its applications for flows with complex geometries. In order to solve this problem, we will apply the FVLBM technique in the IEDDF thermal model in this chapter.

This chapter is organized as follows: firstly, we will give an introduction about FVLBM proposed by Xi et al. (1998, 1999a, 1999b) and its corresponding implementation of wall boundary conditions. Then the limitation of this implementation of wall boundary conditions is pointed out and a new implementation scheme is proposed. We will give a detailed explanation about this new scheme. Its validity is confirmed by applications to two-dimensional expansion channel flows and driven cavity flows. Thirdly, we will use this improved FVLBM in IEDDF thermal model. This extension is validated by numerical simulations of the natural convection in a square cavity on non-uniform grids. Finally, some conclusions are drawn.

4.2 Finite volume LBM and its implementation of wall boundary conditions

4.2.1 Finite volume LBM

The finite volume LBM (FVLBM) proposed by Xi et al. starts with the lattice Boltzmann equation (LBE) in the differential form, which reads:

$$\frac{\partial f_\alpha}{\partial t} + \boldsymbol{e}_\alpha \cdot \nabla f_\alpha = -\frac{f_\alpha - f_\alpha^{eq}}{\tau} + \beta \boldsymbol{e}_\alpha \cdot \boldsymbol{F} \tag{4.1}$$

where

$$\beta = \frac{1}{\sum_\alpha e_{\alpha x}^2} = \frac{1}{\sum_\alpha e_{\alpha y}^2} \tag{4.2}$$

A finite cell surrounding an interior node P is shown in Figure 4.1. In this figure, P_1 to P_8 are eight neighboring grid points around the interior point P. The integration of equation (4.1) is performed on the control volume $ABCDEFGH$, where AB, BC to HA are the edges

of the control volume. *A*, *C*, *E* and *G* are the midpoints of lines PP_1, PP_3, PP_5 and PP_7 respectively; *B*, *D*, *F* and *H* are the geometric centers of the elements of $PP_1P_2P_3$, $PP_3P_4P_5$, $PP_5P_6P_7$ and $PP_7P_8P_1$ respectively.

The cell-vertex type is used here. In this type of the formulation, all the density distributions at the grid nodes are known while the distributions at other locations are unknown and should be interpolated from the known values at the grid points using the standard interpolation technique.

The integration of equation (4.1) is firstly done over the polygon *PABC*.

The integration of the first term in equation (4.1) is approximated as

$$\int_{PABC} \frac{\partial f_\alpha}{\partial t} d\sigma = \frac{\partial f_\alpha(P)}{\partial t} s_{PABC} \qquad (4.3)$$

where s_{PABC} is the area of the polygon *PABC* and $f_\alpha(P)$ is the value of f_α at the grid point *P*. In what follows, the grid-node index is given in the parentheses following f_α. In the above equation, f_α is assumed constant over the area of element *PABC* to prevent solving a set of equations.

The integration of the second term in equation (4.1) gives the fluxes through the four edges of *PA*, *AB*, *BC* and *CP*. Since the summation over all the polygons like *PABC*, *PCDE*, *PEFG* and *PGHA* will be done, the net fluxes through the internal edges (*PA*, *PC*, *PE*, *PG*) will cancel out. Therefore, the explicit expression for these internal edges will be omitted and represented by I_s. So the integration of the second term is:

$$\int_{PABC} \boldsymbol{e}_\alpha \cdot \nabla f_\alpha d\sigma = \boldsymbol{e}_\alpha \cdot \int_{AB} f_\alpha d\boldsymbol{l} + \boldsymbol{e}_\alpha \cdot \int_{BC} f_\alpha d\boldsymbol{l} + I_s \qquad (4.4)$$

With the standard assumption of the bi-linearity of f_α in the quadrilateral elements, the flux through the edge of *AB* is given by

$$\boldsymbol{e}_\alpha \cdot \int_{AB} f_\alpha \, d\boldsymbol{l} = \boldsymbol{e}_\alpha \cdot \boldsymbol{n}_{AB} l_{AB} \left[f_\alpha(A) + f_\alpha(B) \right] / 2 \tag{4.5}$$

where $\boldsymbol{n}_{AB}$ is the unit vector normal to the edge AB and l_{AB} is the length of the edge AB.

The flux through other edges can be calculated in the same way as for the edge AB.

With the same assumption of the bi-linearity of f_i^{eq} over the quadrilateral elements, the integration over the collision term in equation (4.1) results in the following formula:

$$-\int_{PABC} \frac{1}{\tau} \left(f_\alpha - f_\alpha^{eq} \right) d\sigma = -\frac{s_{PABC}}{\tau} \left[\Delta f_\alpha(P) + \Delta f_\alpha(A) + \Delta f_\alpha(B) + \Delta f_\alpha(C) \right] / 4 \tag{4.6}$$

where

$$\Delta f_\alpha(P) = f_\alpha(P) - f_\alpha^{eq}(P), \ \Delta f_\alpha(A) = f_\alpha(A) - f_\alpha^{eq}(A)$$

$$\Delta f_\alpha(B) = f_\alpha(B) - f_\alpha^{eq}(B), \ \Delta f_\alpha(C) = f_\alpha(C) - f_\alpha^{eq}(C) \tag{4.7}$$

Here $f_\alpha(A)$, $f_\alpha(B)$, $f_\alpha(C)$ and their corresponding equilibrium distribution functions $f_\alpha^{eq}(A)$, $f_\alpha^{eq}(B)$, $f_\alpha^{eq}(C)$ are the values at the non-grid nodes A, B, and C, respectively. They should be obtained by interpolation from the values on four grid nodes of the element $PP_1P_2P_3$,

$$f_\alpha(A) = \left[f_\alpha(P) + f_\alpha(P_1) \right] / 2, \quad f_\alpha^{eq}(A) = \left[f_\alpha^{eq}(P) + f_\alpha^{eq}(P_1) \right] / 2,$$

$$f_\alpha(B) = \left[f_\alpha(P) + f_\alpha(P_1) + f_\alpha(P_2) + f_\alpha(P_3) \right] / 4$$

$$f_\alpha^{eq}(B) = \left[f_\alpha^{eq}(P) + f_\alpha^{eq}(P_1) + f_\alpha^{eq}(P_2) + f_\alpha^{eq}(P_3) \right] / 4$$

$$f_\alpha(C) = \left[f_\alpha(P) + f_\alpha(P_3) \right] / 2, \quad f_\alpha^{eq}(C) = \left[f_\alpha^{eq}(P) + f_\alpha^{eq}(P_3) \right] / 2, \tag{4.8}$$

With equations (4.3), (4.4) and (4.6), the integration of equation (4.1) over the polygon $PABC$ is complete. The integration over other polygons follows the same procedure. The integration over the whole control volume $ABCDEFGH$ is just the sum of

the contributions from all the integrations over different polygons *PABC*, *PCDE*, *PEFG* and *PGHA*. Therefore, f_α at the grid node *P* is updated as follows:

$$f_\alpha(P, t + \Delta t) = f_\alpha(P, t) + \frac{\Delta t}{s_P}\left(\sum_{aroundP}(collision) - \sum_{aroundP}(fluxes)\right) + \Delta t \beta e_\alpha \cdot F \qquad (4.9)$$

where s_P is the total area of the control volume *ABCDEFGH* around the grid node *P*; 'collision' and 'fluxes' refer, respectively, to the finite-volume-integrated contributions from the collision term and flux terms.

4.2.2 Half-covolume scheme for wall boundary conditions

The half-covolume technique was proposed by Peng et al. (1999a, 1999b) for the above FVLBM. An example of finite cell surrounding a boundary node *P* is shown in Figure 4.2. Let *P*, P_5 and P_1 be boundary nodes separating the fluid (upper half) from the environment (lower half). As for the interior fluid nodes, the value of f_α at *P* is updated through equation (4.9) except that the control volume is not complete in the 2π directions, as the polygons *PEFG* and *PGHA* do not exist. This leads to the difference when integrating the second term of equation (4.1) over the polygons *PABC* and *PCDE*. The flux terms over the edges *PA* and *EP*, which are omitted in the case of the interior nodes, must be included in the calculation. They are actually easy to be evaluated by using equation (4.5). The velocity of the wall boundary is used when $f_\alpha{}^{eq}$ for the boundary nodes are calculated in order to enforce the no-slip boundary condition.

This is an effective implementation of the wall boundary condition for the fluid flows when the inlet and outlet boundaries are periodical. This can be verified by the following cases.

4.2.2.1 Two-dimensional Poiseuille flow between two parallel plates. Poiseuille flow is driven by a constant pressure gradient imposed on the flow. In the present simulation, the external force $F = 2.604 \times 10^{-5}$ is exerted in the x direction. The total mesh points of 64×32 are used. The analytical solution for this case is $u(y) = FL^2 /(8\rho \upsilon)\left[1 - (2y/L - 1)^2\right]$, where L is the channel width. Figure 4.3 shows the numerical result using FVLBM together with the analytical solution. It can be seen that the agreement is excellent.

4.2.2.2 Two-dimensional rotating Couette flow between two concentric cylinders. For this rotating Couette flow, the outer cylinder rotates with tangential velocity U, while the inner cylinder is stationary. In the simulation, the radii for the inner cylinder and outer cylinder are R_1=30 and R_2=60, respectively; the tangential velocity for the outer cylinder is U=0.01. The mesh points of 180×30 are used. The analytical solution for this problem is

$u(r) = \dfrac{UR_2 r - \left(UR_1{}^2 R_2\right)/r}{R_2{}^2 - R_1{}^2}$. Figure 4.4 shows the numerical result of the steady velocity profile using FVLBM and the corresponding analytical solution. We can see from this figure that the agreement is also excellent.

4.2.2.3 Plane Couette flow with a half-cylinder of radius R resting on the bottom plane. For this flow problem, the top plane moves with the velocity U in the x direction, and the bottom plane with a half cylinder of radius R resting on it is at rest. The mesh is generated using the elliptic grid generation method and illustrated in Figure 4.5. In this simulation, R=20 is the radius of the cylinder; U=0.1 is the speed of the top plane, and the area of the flow field is $9.5R \times 6R$. The mesh size used is 100×60. Figure 4.6 shows the

velocity profile across *y* in the center of the channel. Good agreements between the present result and that given by Xi et al. (1999b) are found.

4.3 New implementation of wall boundary conditions for FVLBM

It was found from the above section that the half-covolume technique for the wall boundary condition is very effective in solving the flow problems where the inlet and outlet boundaries are periodical. However, it would cause some problems when it was used in other cases such as the flow problem with the velocity profile being given at the inlet boundary. The reason for this may lie in the inconsistency with Grad's thirteen-moment expansion, which is needed to be satisfied for a robust and efficient boundary condition. In order to solve this problem, a new implementation scheme for the wall boundary is proposed.

4.3.1 Half-covolume plus bounce-back scheme

According to Grad's "thirteen-moment" system, the non-equilibrium density distribution function should satisfy

$$f_\alpha^{neq,iso} = f_\beta^{neq,iso} \tag{4.10}$$

where α and β have the opposite directions. On the solid stationary wall, the above equation is actually the bounce back condition. This implies that the physical background of the bounce back rule is the compliance of Grad's thirteen-moment expansion. When the compliance with Grad's thirteen-moment expansion or the bounce back rule is broken, the

no-slip boundary condition on the solid wall may not be guaranteed. This is the reason why the half-covolume method is invalid in some cases. Based on this principal, we proposed a new implementation of wall boundary condition called half-covolume plus bounce back scheme, which combines the half-covolume technique and the bounce back rule for the non-equilibrium distribution.

As an example, we consider the case of the bottom wall. The nine-speed model on the bottom wall is shown in Figure 4.7. On the bottom wall, the distributions at the directions 1, 3, 4, 7 and 8 are determined by the half-covolume technique, while the distributions at the directions 2, 5 and 6 are determined by the bounce back rule for the non-equilibrium distribution through equation (4.10).

4.3.2 Validation of the half-covolume plus bounce-back scheme

In order to test the validity of this new implementation scheme for the wall boundary condition and see whether the difficulty faced by the half-covolume scheme can be solved, the numerical simulations for the expansion channel flow are carried out. The configuration of this expansion channel flow is shown in Figure 4.8. This problem has been chosen by a workshop of International Association for Hydraulic Research (IAHR) working group (Napolitano & Orlandi, 1985) as a suitable test case for assessing the capabilities of different numerical methods on the subject of computing laminar flows in the complex geometry. The total length of the channel is chosen to be $Re/3$. The lower boundary (solid wall) of the channel is given by the following expression:

$$y_l(x) = \frac{1}{2}\left[\tanh\left(2 - \frac{30 \cdot x}{Re}\right) - \tanh(2)\right] \tag{4.11}$$

4.3.2.1 Implementation of the wall boundary condition. On the lower wall boundary, firstly, the half-covolume scheme was tried. No convergent results could be obtained. Then our proposed half-covolume plus bounce-back scheme was used. Good results were obtained, which would be shown in Section 4.3.2.3.

4.3.2.2 Inlet and outlet boundary conditions. For this flow problem, besides the wall boundary condition, there are inlet and outlet boundaries. Figure 4.9 shows the schematic plot of particle velocity directions at the inlet and outlet boundaries.

At the inlet boundary, the velocity profile is given as

$$\begin{cases} u = 1.5 \times \left(2y - y^2\right) \\ v = 0 \end{cases}$$
(4.12)

for $0 \leq y \leq 1$.

This given velocity profile boundary condition is realized by using the velocity boundary condition for the density distribution proposed by Zou and He (1997). As shown in Figure 4.9, at the inlet, the distributions f_6 , f_3 , f_7 , f_2 and f_4 are determined by the half-covolume technique. We need to calculate the values of f_1 , f_5 and f_8 using the boundary condition. Since u and v are specified at the inlet, the following equations should be satisfied according to the relationship between the macroscopic flow properties and the particle density distributions.

$$f_1 + f_5 + f_8 = \rho - \left(f_2 + f_6 + f_3 + f_7 + f_4 + f_9\right)$$
(4.13a)

$$f_1 + f_5 + f_8 = \rho u + f_6 + f_3 + f_7$$
(4.13b)

$$f_5 - f_8 = \rho v + f_4 + f_7 - f_6 - f_2$$
(4.13c)

There are four unknowns f_1, f_5, f_8 and ρ in the above three equations (4.13a)-(4.13c). An additional condition should be introduced and the bounce back rule is considered correct for the non-equilibrium part of the particle distribution normal to the inlet, that is

$$f_1 - f_1^{eq} = f_3 - f_3^{eq} \qquad (4.13d)$$

Solving the above four equations (4.13a)-(4.13d), we can get

$$\rho = \frac{1}{1-u}\left[f_2 + 2(f_6 + f_3 + f_7) + f_4 + f_9\right] \qquad (4.14a)$$

$$f_1 = f_3 - f_3^{eq} + f_1^{eq} \qquad (4.14b)$$

$$f_5 = \frac{\rho u + \rho v}{2} + \frac{2f_7 + f_3 - f_1 - f_2 + f_4}{2} \qquad (4.14c)$$

$$f_8 = \frac{\rho u - \rho v}{2} + \frac{2f_6 + f_3 - f_1 + f_2 - f_4}{2} \qquad (4.14d)$$

If the node is the corner node, some special treatment is needed. Take the bottom node at the inlet as an example. The distributions f_3, f_4 and f_7 are determined by the half-covolume technique and we need to calculate the values for f_1, f_2, f_5, f_6 and f_8 using the boundary condition. There are only four equations (4.13a)-(4.13d) for these five unknown distributions and the unknown density at this point, so two extra conditions should be introduced. One extra condition can be obtained by considering that this node is also a node on the solid wall with zero velocity. So the value for the distribution f_2 can be determined from the wall boundary condition. That is the bounce back rule for the non-equilibrium density distribution function:

$$f_2 = f_4 \qquad (4.15)$$

The other extra condition can be obtained by the assumption that the density at this node is the same as the density at its neighboring flow node, so the density ρ is the known variable. The remaining unknown variables f_5, f_6 and f_8 can be determined from equations (4.13a)-(4.13c). They are:

$$f_5 = f_7 \tag{4.16}$$

$$f_6 = f_8 = \frac{1}{2}\left[\rho - \left(f_0 + f_1 + f_2 + f_3 + f_4 + f_5 + f_7\right)\right] \tag{4.17}$$

At the outlet boundary, all the density distributions at any node are extrapolated from its neighboring interior nodes.

4.3.2.3 Results and discussion. The numerical simulations for this expansion channel flow are carried out at a wide range of Reynolds numbers. The mesh size used for all the cases is 71×31. The convergence criterion is set to

$$\sum_{i,j}\left|\sqrt{(u_{i,j}^2 + v_{i,j}^2)^{n+1}} - \sqrt{(u_{i,j}^2 + v_{i,j}^2)^n}\right| / \sum_{i,j}\left|\sqrt{(u_{i,j}^2 + v_{i,j}^2)^n}\right| \leq 10^{-7} \tag{4.18}$$

Figure 4.10 - Figure 4.12 show the streamlines and wall vorticity distributions for $Re = 10$, $Re = 100$ and $Re = 150$, respectively. In these three figures, the separation region is clearly shown in the streamlines for each case. In the wall vorticity distribution for each case, the numerical result using the present FVLBM with our proposed implementation of the wall boundary condition is represented by the solid line. The benchmark solution of IAHR workshop given by Cliffe et al. using a finite element method with results being grid-independent, which is represented by the symbols, is also included for comparison. Good agreement can be found.

In order to further study the property of this flow, we put the wall vorticity distributions at different Reynolds numbers in one picture. Figure 4.13 displays the wall vorticity distributions at different Reynolds numbers of 10, 100 and 150. It is confirmed from this figure that as Reynolds number increases to the value of much larger than 1, the solution takes on a quasi-self-similar form, i.e. the wall vorticity becomes independent of Re when plotted vs. x/x_{out}.

From this numerical simulation, it can be seen that our new implementation of the wall boundary condition is valid and can be used to solve flow problems with the complex geometry.

4.3.3 Special treatment on the wall corner points

For some flow problems, which contain the wall corner points such as the four corner points in the driven cavity flow, the implementation of the boundary condition at these wall corner points is very important.

4.3.3.1 Extrapolation scheme. Take the left bottom corner point as an example. At this corner point, the particle velocity directions for the nine-speed model are show in Figure 4.14. Seen from this figure, the density distributions at the directions 1,2,3,4,5 and 7 are determined from the half-covolume plus bounce-back scheme. We need to determine the values at the directions 6 and 8. For the conventional standard LBM, the values at these two directions have little influence on the numerical simulation results, because they do not contribute any information into the interior parts. But for FVLBM, these values will be used when calculating the distributions at these two directions on the interior points

neighboring to this corner point. So it is very crucial for the choice of the values at these two directions for FVLBM.

Take Reynolds number of 100 as an example. The values of the equilibrium distribution functions were given for the density distributions at these two directions at the beginning. The primary and the right bottom vortices can be captured correctly, while the left bottom small vortex cannot be obtained. This means that the equilibrium distribution boundary condition does not have enough accuracy for the complex flow pattern. The left bottom small vortex is plagued by the numerical errors. In order to increase the accuracy, the first order extrapolation scheme at these two directions was tried. At these two directions, the values of the distributions are obtained by the extrapolation from the distributions on the two neighboring interior points. The numerical results using this special treatment on the corner point are reasonably accurate. The left bottom small vortex is well captured. These results will be shown in the following section.

4.3.3.2 Results and discussion. In order to further validate our new implementation of the wall boundary condition, especially the special treatment on the wall corner points, the numerical simulations of the driven cavity flow at a wide range of Reynolds numbers were carried out.

(1) *Re*=100

The results of the streamlines, vorticity and pressure contours at *Re*=100 are shown in Figure 4.15 - Figure 4.17. The mesh size used is 101×101.

According to the present study, as shown in Figure 4.15, the center of the primary vortex is at $x=0.617$, $y=0.737$; the center of the left corner vortex is at $x=0.030$, $y=0.037$; and the center of the right corner vortex is at $x=0.945$, $y=0.060$. These results are in good agreement with those by Ghia et al. (1982) ($x=0.6172$, $y=0.7344$ for the primary vortex, $x=0.0313$, $y=0.0391$ for the left corner vortex, and $x=0.9453$, $y=0.0625$ for the right corner vortex.). The small left corner vortex is correctly captured, which shows that our special treatment on the corner points is needed and effective.

Figure 4.18 and Figure 4.19 show the u-velocity profile along the vertical centerline and v-velocity profile along the horizontal centerline. The numerical results of Ghia et al. (1982) are also included for comparison. From these two figures, good agreement can be found.

(2) $Re=400$

In order to study the property of FVLBM at medium Reynolds number, numerical computation was performed at $Re=400$. The results of the streamlines, vorticity and pressure contours are shown in Figure 4.20 -Figure 4.22. The mesh sizes used is 151×151.

According to the present study, the center of the primary vortex is at $x=0.560$, $y=0.600$; the center of the left corner vortex is at $x=0.066$, $y=0.040$; and the center of the right corner vortex is at $x=0.892$, $y=0.121$. These results are in good agreement with those by Ghia et al. ($x=0.5547$, $y=0.6055$ for the primary vortex, $x=0.0508$, $y=0.0469$ for the left corner vortex, and $x=0.8906$, $y=0.1250$ for the right corner vortex.).

Figure 4.23 and Figure 4.24 show the comparison of u-velocity profile along vertical centerline and v-velocity profile along horizontal centerline using FVLBM with results of Ghia et al. From these two pictures, acceptable agreement can be found.

Compared with the results at *Re*=100, the difference between our results and Ghia's results is bigger at *Re*=400. This difference may be decreased by increasing the grid number. However, on the other hand, this suggests that FVLBM has the diffusion problem with the increase of Reynolds number. Much larger number of mesh points is needed for high Reynolds number in order to obtain the accurate numerical results.

(3) *Re*=1000

To further study the diffusion property of FVLBM, the numerical computation at *Re*=1000 was performed. The mesh size used is 251×251. The convergence rate is very slow. The *u*-velocity profile along the vertical centerline and *v*-velocity profile along the horizontal centerline are shown in Figure 4.25 and Figure 4.26, respectively. The results of Ghia et al. (1982) are also included for comparison.

Seen clearly from Figure 4.25 and Figure 4.26, although a large number of mesh points is used, there still exist remarkable derivations from the benchmark results. This confirms that the diffusion problem is the striking shortcoming of FVLBM for the simulation of fluid flows at high Reynolds numbers.

4.4 Use of FVLBM in the IEDDF thermal model

In Chapter 3, we have shown that the IEDDF thermal model is considered to be a good thermal model. But till now, this thermal model is mainly used in flow fields with uniform grids. In order to solve the practical thermal problems with complex geometries, this model should be extended for its applications on the arbitrary mesh. We try to fulfill this objective by using the FVLBM technique. After developing the above implementation

of wall boundary condition, the FVLBM scheme is used in the IEDDF thermal model so as to extend the current thermal model for uses in real engineering applications.

4.4.1 Application of FVLBM in IEDDF thermal model

As shown in Chapter 3, for the IEDDF thermal model, the lattice Boltzmann equations in the differential forms are:

$$\partial_t f + (e \cdot \nabla) f = -\frac{f - f^{eq}}{\tau_v} + F_f \tag{4.19a}$$

$$\partial_t g + (e \cdot \nabla) g = -\frac{g - g^{eq}}{\tau_c} - f q \tag{4.19b}$$

The integration of equation (4.19a) has been stated in Section 4.2.1. Equation (4.19b) can be integrated following the same procedure as for equation (4.19a). We choose the same finite cell as shown in Figure 4.1 for the integration of the internal energy density distribution and use the cell-vertex type as for the density distribution.

The integration of the first term in equation (4.19b) over the element of *PABC* is approximated as

$$\int_{PABC} \frac{\partial g_\alpha}{\partial t} d\sigma = \frac{\partial g_\alpha(P)}{\partial t} s_{PABC} \tag{4.20}$$

The integration of the second term in equation (4.19b) over the element *PABC* will give the energy fluxes through the four edges *PA*, *AB*, *BC* and *CP*. They can be written as:

$$\int_{PABC} e_\alpha \cdot \nabla g_\alpha d\sigma = e_\alpha \cdot n_{AB} l_{AB} [g_\alpha(A) + g_\alpha(B)]/2 +$$
$$e_\alpha \cdot n_{BC} l_{BC} [g_\alpha(B) + g_\alpha(C)]/2 + I_s' \tag{4.21}$$

With the same assumption as in Section 4.2.1 that the bi-linearity of g_α and g_α^{eq} over the quadrilateral elements is satisfied, their values on the non-grid points can be

interpolated from the known values at the grid points using the same interpolation technique as shown in Section 4.2.1. They are:

$$g_\alpha(A) = \left[g_\alpha(P) + g_\alpha(P_1)\right]/2, \quad g_\alpha^{eq}(A) = \left[g_\alpha^{eq}(P) + g_\alpha^{eq}(P_1)\right]/2,$$

$$g_\alpha(B) = \left[g_\alpha(P) + g_\alpha(P_1) + g_\alpha(P_2) + g_\alpha(P_3)\right]/4$$

$$g_\alpha^{eq}(B) = \left[g_\alpha^{eq}(P) + g_\alpha^{eq}(P_1) + g_\alpha^{eq}(P_2) + g_\alpha^{eq}(P_3)\right]/4$$

$$g_\alpha(C) = \left[g_\alpha(P) + g_\alpha(P_3)\right]/2, \quad g_\alpha^{eq}(C) = \left[g_\alpha^{eq}(P) + g_\alpha^{eq}(P_3)\right]/2, \tag{4.22}$$

Then the integration of the collision term on the right-hand side of equation (4.19b) over the element *PABC* results in the following formula:

$$-\int_{PABC} \frac{1}{\tau_c}\left(g_\alpha - g_\alpha^{eq}\right)d\sigma = -\frac{s_{PABC}}{\tau_c}\left[\Delta g_\alpha(P) + \Delta g_\alpha(A) + \Delta g_\alpha(B) + \Delta g_\alpha(C)\right]/4 \tag{4.23}$$

where

$$\Delta g_\alpha = g_\alpha - g_\alpha^{eq} \tag{4.24}$$

For the extra term *fq* on the right-hand side of equation (4.19b), we can integrate it as:

$$-\int_{PABC} fq\, d\sigma = -s_{PABC}\left[f_\alpha(P)q_\alpha(P) + f_\alpha(A)q_\alpha(A) + f_\alpha(B)q_\alpha(B) + f_\alpha(C)q_\alpha(C)\right]/4 \tag{4.25}$$

where

$$q_\alpha(A) = \left[q_\alpha(P) + q_\alpha(P_1)\right]/2 \tag{4.26a}$$

$$q_\alpha(B) = \left[q_\alpha(P) + q_\alpha(P_1) + q_\alpha(P_2) + q_\alpha(P_3)\right]/4 \tag{4.26b}$$

$$q_\alpha(C) = \left[q_\alpha(P) + q_\alpha(P_3)\right]/2 \tag{4.26c}$$

The integration of equation (4.19b) over the polygon *PABC* is complete. The integration over the whole control volume *ABCDEFGH* is just the sum of the

contributions from the different polygons *PABC*, *PCDE*, *PEFG* and *PGHA*. Therefore, g_α

at the grid node *P* is updated as follows:

$$g_\alpha(P, t + \Delta t) = g_\alpha(P, t) + \frac{\Delta t}{s_P}\left(\sum_{aroundP}(collision) - \sum_{aroundP}(fluxes) + \sum_{aroundP}(fq)\right) \tag{4.27}$$

4.4.2 Implementation of the thermal boundary conditions

For the density distribution f_α, the implementation of the boundary conditions has

been clearly shown in Section 4.3.

For the internal energy density distribution g_α, our proposed implementation of

boundary condition called the half-covolume plus bounce-back rule for the non-

equilibrium distribution can still be used. We will again take the bottom wall as an

example. The schematic plot of particle velocity directions of the nine-speed model on this

wall has been shown in Figure 4.7. The internal energy density distributions at the

directions 7, 4, 8, 3 and 1 are determined by the half-covolume technique. That is, they are

treated as the interior fluid nodes. The value of g_α at *P* is updated through equation (4.27)

except that the control volume is not complete in the 2π directions, as the polygons *PEFG*

and *PGHA* do not exist. This leads to the difference when integrating the second term of

equation (4.19b) over the polygons *PABC* and *PCDE*. The energy flux terms over the

edges *PA* and *EP*, which are omitted in the case of the interior nodes, must be included in

the   calculation.   They   are   actually   easy   to   be   calculated   as

$\boldsymbol{e}_\alpha \cdot \boldsymbol{n}_{PA} l_{PA}[g_\alpha(A) + g_\alpha(P)]/2 + \boldsymbol{e}_\alpha \cdot \boldsymbol{n}_{EP} l_{EP}[g_\alpha(E) + g_\alpha(P)]/2$.

For Dirichlet boundary condition, the remaining distributions at directions 5, 2 and 6 are determined from the bounce back rule for the non-equilibrium internal energy density distribution through the following equation:

$$g_\alpha^{neq} - e_\alpha^2 f_\alpha^{neq,iso} = -\left(g_\beta^{neq} - e_\beta^2 f_\beta^{neq,iso}\right) \tag{4.28}$$

where α and β have the opposite directions. The temperature of the boundary wall is used when g_α^{eq} for the boundary nodes are calculated in order to satisfy the given temperature condition on the wall.

For Neumann boundary condition, firstly, the temperature on the wall is approximated by the conventional second order extrapolation from the given heat flux so as to transfer it to Dirichlet boundary condition as shown in Section 3.4, Chapter 3. Then equation (4.28) can be used. Iteration is needed in order to get the accurate temperatures on the boundary. By this means, the heat flux condition is enforced on the boundaries.

4.5 Numerical simulations using the finite volume lattice thermal model

In order to verify whether the use of FVLBM technique in the IEDDF thermal model can extend the current thermal model to solve the thermal flows on the arbitrary mesh, we carried out the computation for a sample problem. The problem considered is a natural convection in a two-dimensional square cavity. A typical non-uniform grid is used in the present study, which is shown in Figure 4.27. It can be seen clearly from this figure that the mesh points are stretched towards the walls so as to capture the thin boundary

layer. In the middle part of the flow field, the mesh is relatively coarse since the velocity and temperature gradients are not very large in this region.

The convergence criterion for all the following cases is set to

$$\max_{i,j}\left|\sqrt{(u_{i,j}^2+v_{i,j}^2)^{n+1}}-\sqrt{(u_{i,j}^2+v_{i,j}^2)^n}\right|\le 10^{-8},\max_{i,j}\left|T_{i,j}^{n+1}-T_{i,j}^n\right|\le 10^{-8} \tag{4.29}$$

where n and $n+1$ represent the old and new time levels, respectively.

4.5.1 Validation of the finite volume lattice thermal model

The numerical simulations of the natural convection in a square cavity for Rayleigh numbers of $10^3\sim10^5$ were carried out. Table 4.1 shows the numerical results of the maximum horizontal velocity $u_{\max}$ on the vertical mid-plane of the cavity and its location y, the maximum vertical velocity $v_{\max}$ on the horizontal mid-plane of the cavity and its location x, the average Nusselt number throughout the cavity $\overline{Nu}$ and the value of the stream function at the center point of the cavity. Note that all the results are obtained from the computations on the non-uniform grids as shown in Figure 4.27. The numerical results of a NS solver given by Shu and Xue (1998) using DQ method are also included for comparison.

From Table 4.1, we can see that the numerical results obtained by using the finite volume lattice thermal model generally agree well with the benchmark results of Shu and Xue at low Rayleigh numbers of 10^3 and 10^4. The deviation of the results from the benchmark results at high Rayleigh number of 10^5 is very clear. At $Ra=10^5$, the convergence is very slow because the time step used has to be very small. For $Ra=10^6$, no converged solution can be obtained. From these observations, conclusion can be drawn that the numerical diffusion of FVLBM technique affects the efficiency, accuracy and

convergence of the IEDDF thermal model at high Rayleigh numbers. So the FVLBM technique in the IEDDF thermal model can only be used for the thermal applications on the arbitrary mesh at low Rayleigh numbers.

4.5.2 Comparison of the numerical results on uniform and non-uniform grids

In order to investigate the efficiency of using FVLBM technique in the IEDDF thermal model for thermal applications, the numerical simulations on both uniform and non-uniform grids at the same Rayleigh numbers were carried out. On the uniform grids, the conventional LBM was used; on the non-uniform grids, the finite volume thermal model was used. Table 4.2 and Table 4.3 show the comparison of numerical results using two different methods at Rayleigh number of 10^3 and 10^4, respectively.

It can be observed from these two tables that, at low Rayleigh numbers, for the same grid number, the calculated Nusselt number and other results on the non-uniform grids are more accurate than those on the uniform grids. For example, as can be seen from Table 4.2, at Rayleigh number of 10^3, using the same grid number of 51×51, the calculated $\overline{Nu}$ and $Nu_{1/2}$ on the non-uniform grids are 1.118 and 1.117, while the calculated $\overline{Nu}$ and $Nu_{1/2}$ on the uniform grid are only 1.116 and 1.114. When the grid size of the uniform grid is increased to 101×101, the calculated $\overline{Nu}$ and $Nu_{1/2}$ become 1.117 and 1.116. As compared with the benchmark data of $\overline{Nu}$ and $Nu_{1/2}$, which are 1.118 and 1.118, it is clear that the use of the mesh size of 51×51 on the non-uniform grids using the finite volume lattice thermal model gives much better results than the use of the same mesh size

on the uniform grids using the standard LBM. Even when more mesh points are used on the uniform grids, the use of non-uniform grids with smaller mesh size still gives better results. This is because when non-uniform grids are used, it is easy for us to use very small mesh spacing near the wall boundary so as to capture the thin boundary layer while using large mesh spacing in the low gradient flow region. In contrast, when the same mesh spacing is used by the uniform grids, the number of mesh points used in the whole flow field could be very large in order to capture the thin boundary layer. This example clearly shows the advantage of using non-uniform grids in the simulation of fluid flows even when the flow is confined in a simple and regular geometry. This also shows the necessity of extending the current thermal model to be used on the arbitrary mesh. At low Rayleigh numbers, the use of FVLBM technique in the IEDDF thermal model is an effective way.

4.6 Conclusions

A new implementation of wall boundary conditions for FVLBM has been developed in this chapter. It is based on the half-covolume technique and the bounce-back rule for the non-equilibrium distribution. Using this new implementation of wall boundary conditions, the flow problems such as the expansion channel flows and driven cavity flows can be correctly solved using FVLBM.

This FVLBM technique is then applied in the IEDDF thermal model to extend the current thermal model to be used on the arbitrary mesh, which is a requirement for practical engineering applications. The numerical simulations of the natural convection in a square cavity at Rayleigh numbers ranging from 10^3 to 10^5 on non-uniform grids were carried out. At low Rayleigh numbers, the numerical results compare well with benchmark

data obtained by a NS solver, which shows the validity of the use of FVLBM technique in the IEDDF thermal model. Compared with the numerical results on uniform grids using the standard LBM, less grid numbers are needed to obtain the same accurate results.

However, from the present work, it was also found that at a high Reynolds number or Rayleigh number, the numerical diffusion of this FVLBM technique affects the efficiency, accuracy and convergence of the numerical simulations. So the use of the present FVLBM scheme in the IEDDF thermal model is not a perfect way to extend the current thermal model for practical thermal applications with complex geometries, when high Reynolds numbers or Rayleigh numbers are often encountered. We need to find another method to fulfill this objective. This leads to the further studies in the following chapters.

Table 4.1 Comparison of the numerical results between the finite volume lattice thermal model and a NS solver for the natural convection in a square cavity

Ra	10^3		10^4		10^5	
Method	FVLBM	DQ	FVLBM	DQ	FVLBM	DQ
Grid size	51×51	-	101×101	-	151×151	-
u_{max}	3.649	3.649	16.154	16.190	35.251	34.736
y	0.814	0.815	0.824	0.825	0.864	0.855
v_{max}	3.699	3.698	19.653	19.638	66.746	68.640
x	0.166	0.180	0.121	0.120	0.065	0.065
$\overline{Nu}$	1.118	1.118	2.246	2.245	4.185	4.523
$\left|\psi_{mid}\right|$	1.176	1.175	5.081	5.075	8.977	9.117

Table 4.2 Comparison of the numerical results on uniform and non-uniform grids for the natural convection in a square cavity at $Ra=10^3$

Mesh	51×51 (uniform)	101×101 (uniform)	DQ	51×51 (non-uniform)
$\left|\psi_{mid}\right|$	1.170	1.175	1.175	1.176
u_{max}	3.636	3.649	3.649	3.649
y	0.820	0.810	0.815	0.814
v_{max}	3.702	3.700	3.698	3.699
x	0.180	0.180	0.180	0.166
$\overline{Nu}$	1.116	1.117	1.118	1.118
$Nu_{1/2}$	1.114	1.116	1.118	1.117
Nu_0	1.103	1.110	1.118	1.090
Nu_{max}	1.465	1.481	1.506	1.489
y	0.140	0.090	0.090	0.090
Nu_{min}	0.722	0.672	0.691	0.636
y	1.000	1.000	1.000	1.000

Table 4.3 Comparison of the numerical results on uniform and non-uniform grids for the natural convection in a square cavity at $Ra=10^4$

Mesh	101×101 (uniform)	151×151 (uniform)	DQ	101×101 (non-uniform)
$\left|\psi_{mid}\right|$	5.063	5.069	5.075	5.081
u_{max}	16.158	16.156	16.190	16.154
y	0.820	0.820	0.825	0.824
v_{max}	19.704	19.679	19.638	19.653
x	0.120	0.120	0.120	0.121
$\overline{Nu}$	2.232	2.237	2.245	2.246
$Nu_{1/2}$	2.224	2.231	2.245	2.254
Nu_0	2.192	2.183	2.248	2.144
Nu_{max}	3.576	3.479	3.543	3.360
y	0.150	0.147	0.145	0.147
Nu_{min}	0.617	0.593	0.586	0.487
y	1.000	1.000	1.000	1.000
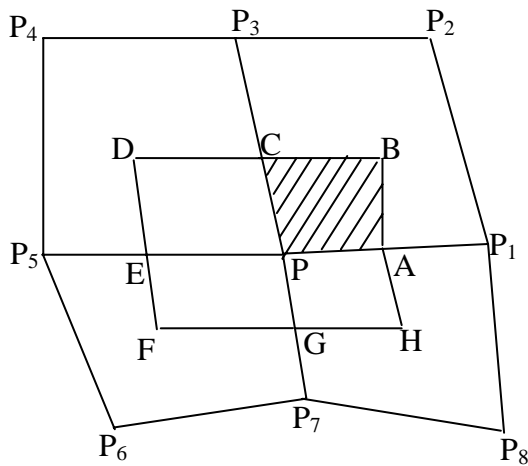
Figure 4.1 Diagram of a finite cell surrounding an interior node *P* for FVLBM
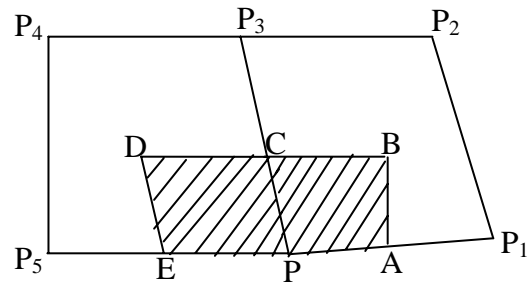
Figure 4.2 Diagram of a finite cell surrounding a boundary node *P* for FVLBM
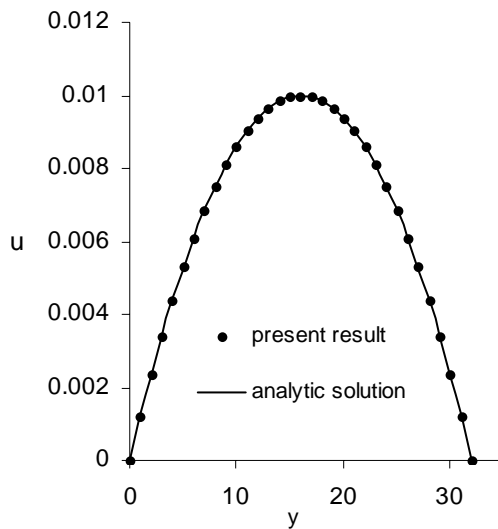
Figure 4.3 Velocity profile using FVLBM
for Poiseuille flow as compared
with the analytic solution.
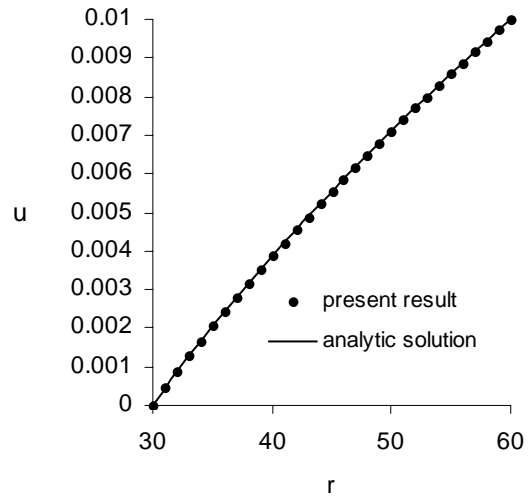
Figure 4.4 Velocity profile using FVLBM
for the rotating Couette flow as compared
with the analytic solution.
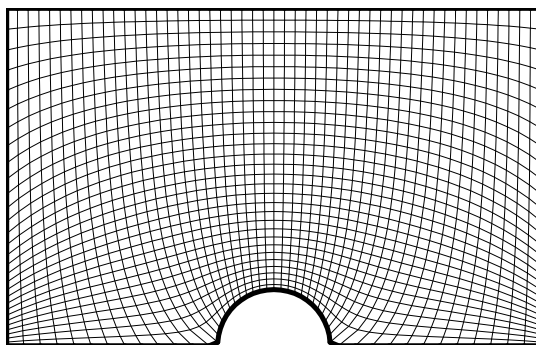
Figure 4.5 Mesh used for the plane
Couette flow with a half cylinder resting
on the bottom plane
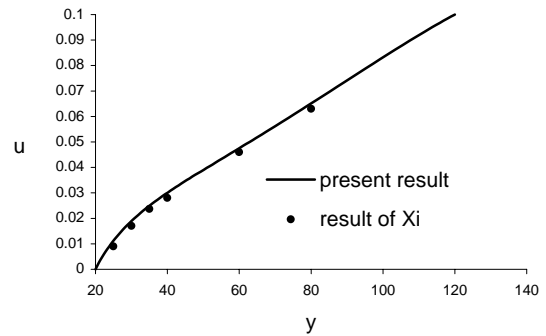
Figure 4.6 Velocity profile u along y in
the center of the channel for the plane
Couette flow with a half cylinder resting
on the bottom plane.
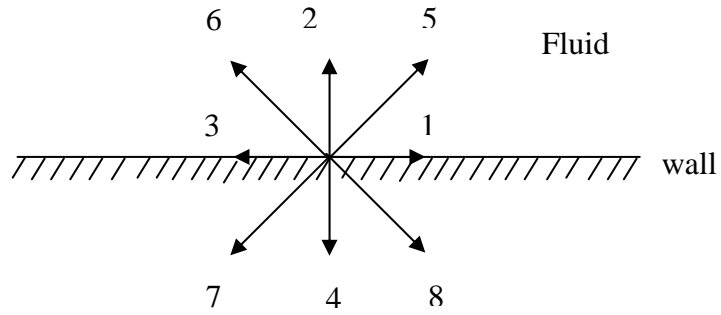
Figure 4.7 Schematic plot of particle velocity directions on the bottom wall.
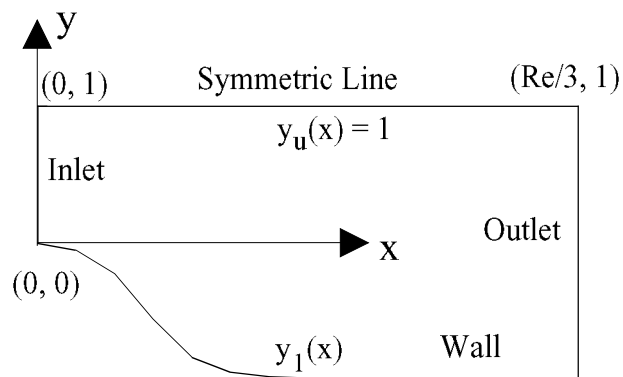
Figure 4.8 Geometry of an expansion channel
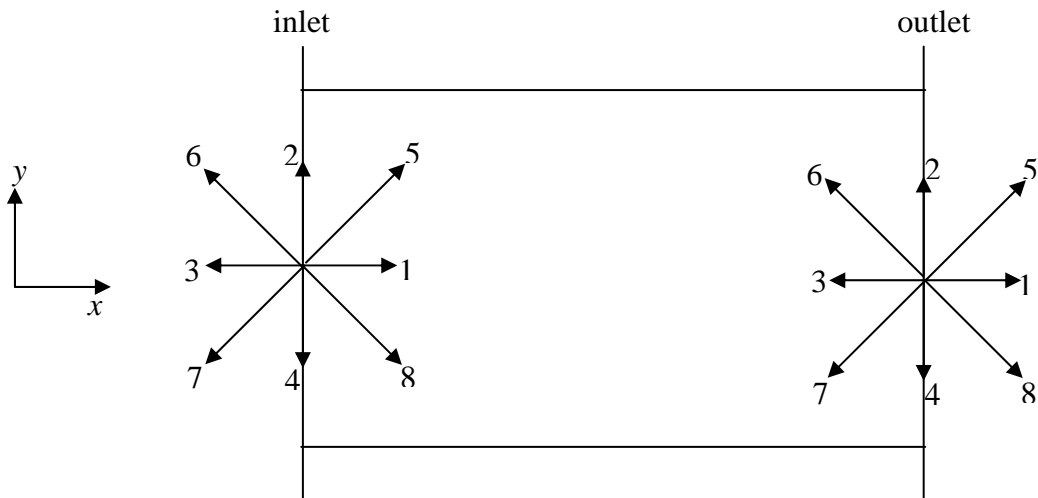
Figure 4.9 Schematic plot of particle velocity directions at the inlet and outlet boundaries for the expansion channel flow.
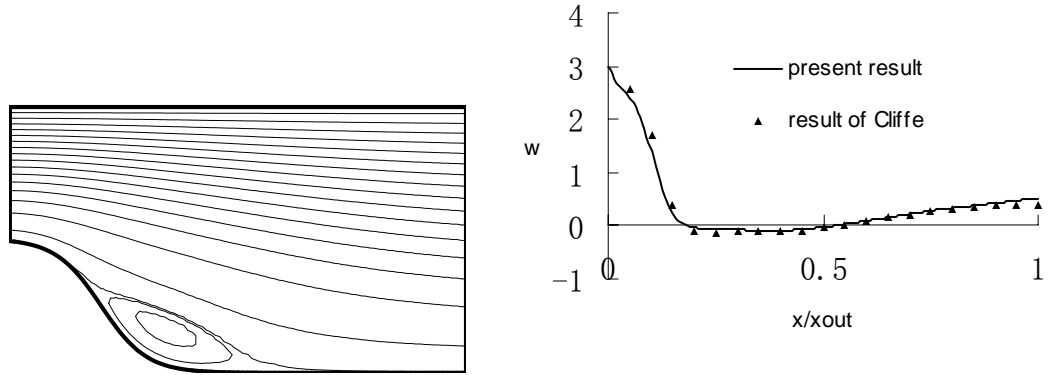
Figure 4.10 Streamlines and wall vorticity distribution for expansion channel flow at
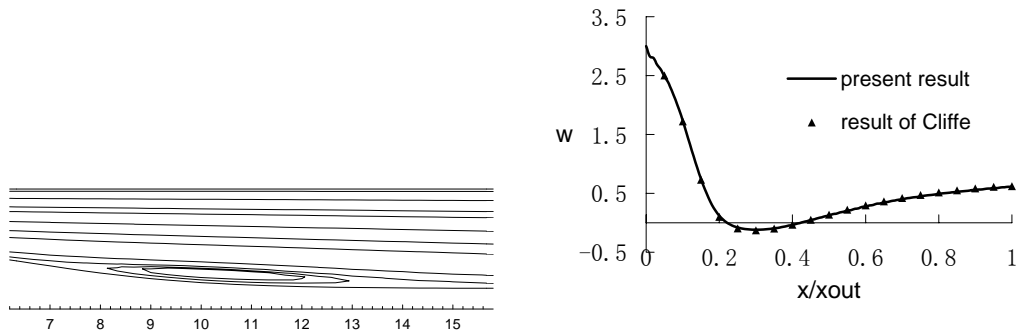
$Re = 10$

Figure 4.11 Streamlines and wall vorticity distribution for expansion channel flow at

$Re = 100$
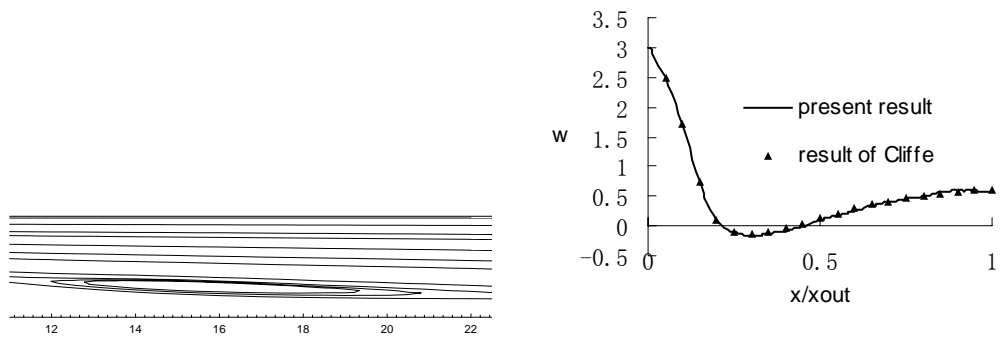
Figure 4.12 Streamlines and wall vorticity distribution for expansion channel flow at

$Re = 150$
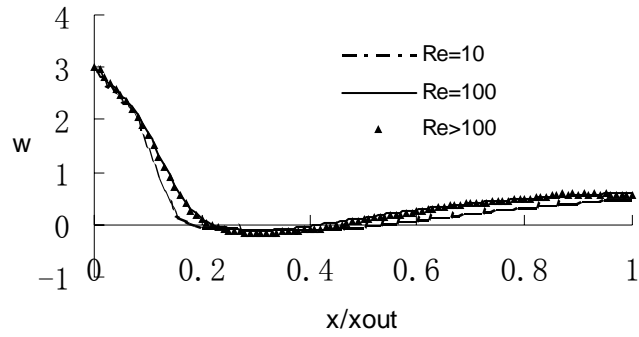
Figure 4.13 Wall vorticity distributions at different Reynolds numbers for expansion channel flows
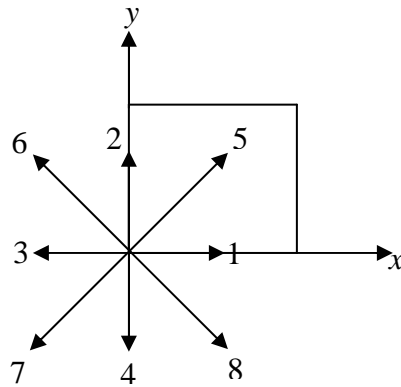
Figure 4.14 Schematic plot of particle velocity directions at the left-bottom corner point for driven cavity flow
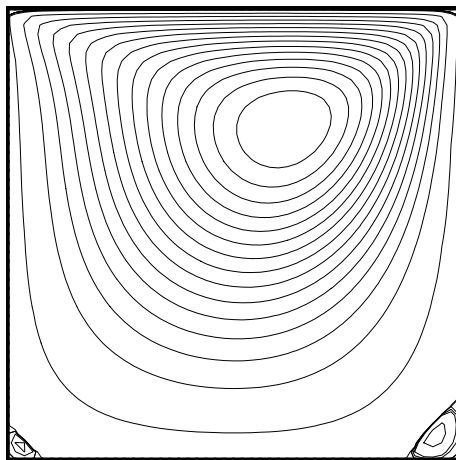
Figure 4.15 Streamlines for driven cavity flow at *Re*=100
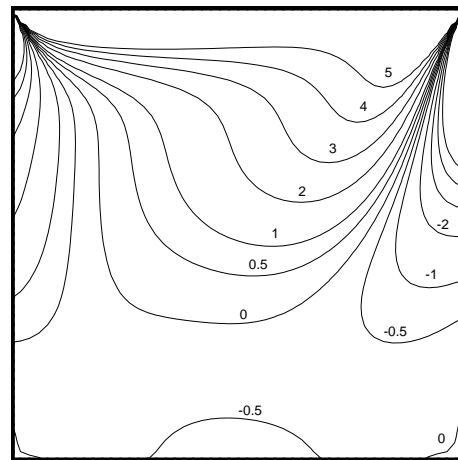
Figure 4.16 Vorticity contours for driven cavity flow at *Re*=100
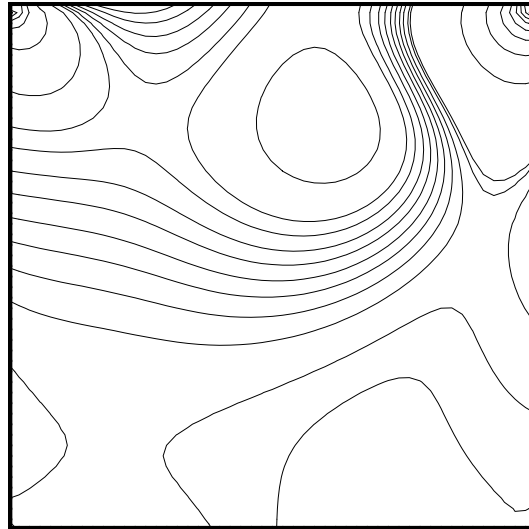
Figure 4.17 Pressure contours for driven cavity flow at *Re*=100
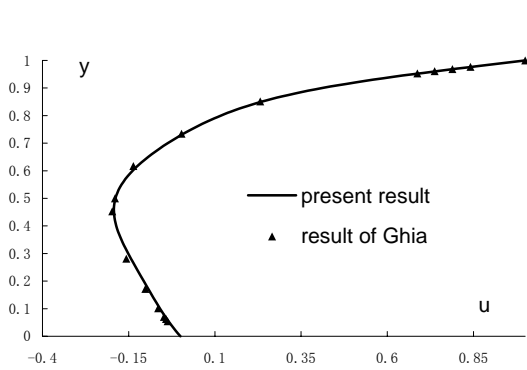
Figure 4.18 *U*-velocity profile along
vertical centerline for driven cavity
flow at *Re*=100
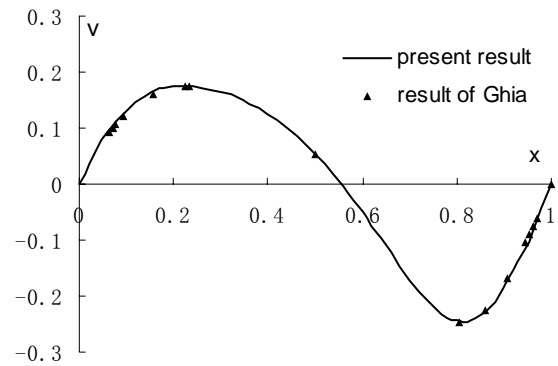
Figure 4.19 *V*-velocity profile along
horizontal centerline for driven cavity
flow at *Re*=100
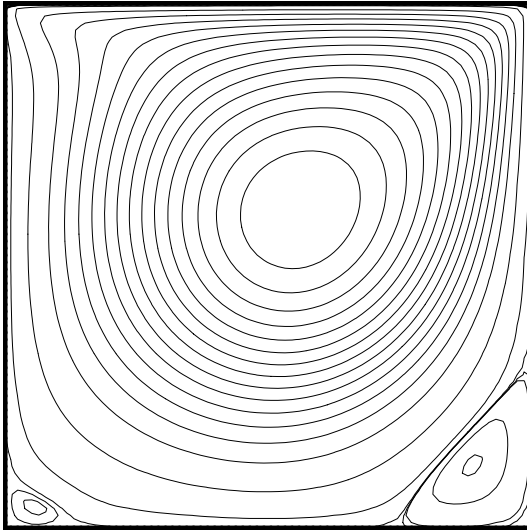
Figure 4.20 Streamlines for
driven cavity flow at *Re*=400
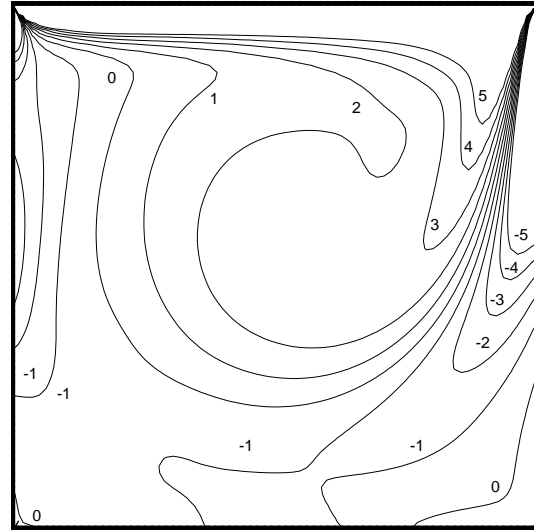
Figure 4.21 Vorticity contours for
driven cavity flow at *Re*=400
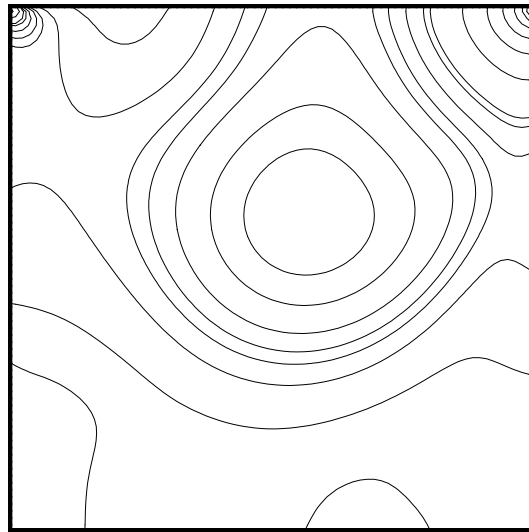
Figure 4.22 Pressure contours for driven cavity flow at *Re*=400
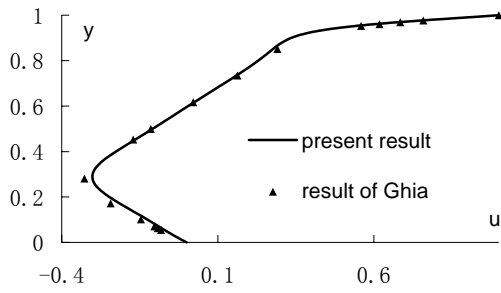
Figure 4.23 *U*-velocity profile along vertical centerline for driven cavity flow at *Re*=400
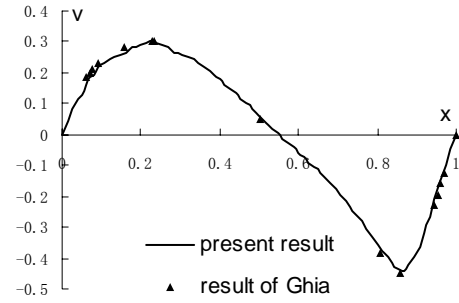
Figure 4.24 *V*-velocity profile along horizontal centerline for driven cavity flow at *Re*=400
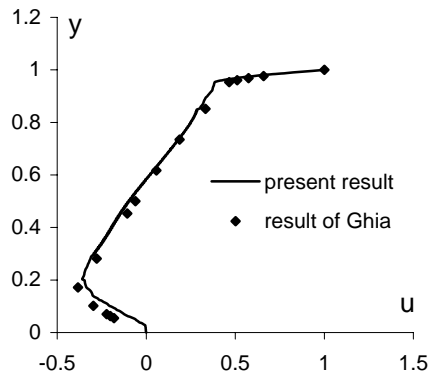
Figure 4.25 *U*-velocity profile along vertical centerline for driven cavity flow at *Re*=1000
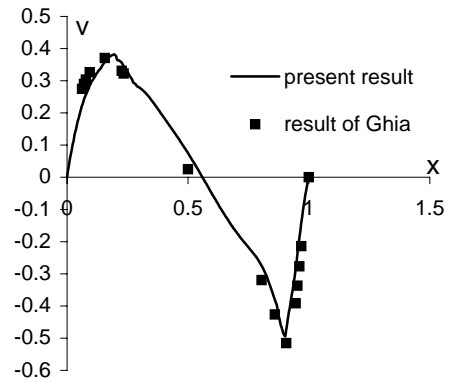
Figure 4.26 *V*-velocity profile along horizontal centerline for driven cavity flow at *Re*=1000
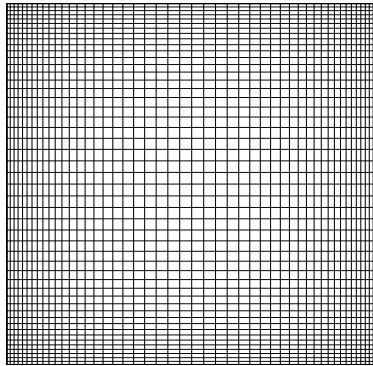
Figure 4.27 A typical non-uniform mesh used in a square cavity

Chapter 5

Use of TLLBM in IEDDF thermal model

5.1 Introduction

In Chapter 4, FVLBM was developed and used in IEDDF thermal model in order to extend the current thermal model for more practical applications with arbitrary geometries. Good results could be obtained at low Reynolds or Reyleigh numbers, but the results at high Reynolds or Rayleigh numbers were not good enough for the engineering applications. The reason may be that in the region where the flow gradient is very large, the numerical diffusion of FVLBM may be too large and affect the accuracy and convergence of the numerical results. So this method is not a perfect way to extend the current thermal model for real practical applications. We should find another method that has no or little diffusion at high Reynolds or Rayleigh numbers. Taylor series expansion- and Least squares- based LBM (TLLBM) proposed by Shu et al. (2001) is just such a good method. It is based on the standard LBM, Taylor series expansion and least squares approach. It has the following good features. It keeps the local property of the conventional LBM; the final form is an algebraic formulation, in which the coefficients only depend on the coordinates of mesh points and lattice velocity, and can be computed once in advance. In addition, this new method can be consistently used in any kind of lattice model. Numerical experiments on isothermal flows have shown that this method is an efficient and flexible approach for practical isothermal applications with arbitrary

geometries. Especially, its ability to solve flow problems at very high Reynolds numbers accurately means that this method does not have the diffusion problem. So in this chapter, we attempt to apply this method to the IEDDF thermal model in order to examine whether accurate results could be obtained at high Rayleigh numbers for thermal applications with complex geometries.

This chapter was organized as the following: firstly, we gave a brief introduction about TLLBM. Secondly, a new thermal model was developed by applying the TLLBM technique in the IEDDF thermal model. The implementation of wall boundary conditions for this thermal model was also described. Thirdly, the numerical simulations of the natural convection in a square cavity on both uniform and non-uniform grids were carried out to validate our new thermal model, especially its ability to solve thermal flows at high Rayleigh numbers. Then its applications on the natural convective heat transfer in a horizontal concentric annulus between a square outer cylinder and a heated circular inner cylinder were thoroughly studied. This case was used to show that our new thermal model has the ability to solve the practical and complex thermal problems with curved boundaries. In the end, we drew some conclusions.

5.2 Taylor series expansion- and Least squares- based LBM

Taylor series expansion- and Least squares- based LBM (TLLBM) is based on the well-known fact that the distribution is a continuous function in the physical space and can be well defined in any mesh system. Taking the two dimensional problem as an example and starting with the standard lattice Boltzmann equation (LBE), the two dimensional, standard LBE with BGK approximation can be written as

$$f_\alpha(x + e_{\alpha x}\delta t, y + e_{\alpha y}\delta t, t + \delta t) = f_\alpha(x, y, t) - \frac{f_\alpha(x, y, t) - f_\alpha^{eq}(x, y, t)}{\tau}, \alpha = 0,1,...,N \qquad (5.1)$$

where δt is the time step and $\boldsymbol{e}_\alpha(e_{\alpha x}, e_{\alpha y})$ is the particle velocity in α direction; N is the number of the discrete particle velocities. Obviously, the standard LBE consists of two steps: collision and streaming.

Suppose that a particle is initially at the grid point (x, y, t). Along α direction, after the local collision, this particle will stream to the position $(x + e_{\alpha x}\delta t, y + e_{\alpha y}\delta t, t + \delta t)$. For a uniform lattice, $\delta x = e_{\alpha x}\delta t$, $\delta y = e_{\alpha y}\delta t$. So, $(x + e_{\alpha x}\delta t, y + e_{\alpha y}\delta t)$ is on the grid point. In other words, equation (5.1) can be used to update the distributions exactly at the grid points. However, for a non-uniform grid, $(x + e_{\alpha x}\delta t, y + e_{\alpha y}\delta t)$ is usually not at the grid point $(x + \delta x, y + \delta y)$, since $\delta x \neq e_{\alpha x}\delta t$, $\delta y \neq e_{\alpha y}\delta t$. In the numerical simulation, only the distributions at the mesh points for all the time levels are needed, so that the macroscopic properties such as the density, flow velocity and temperature can be evaluated at every mesh point. To get the distribution at the grid point $(x + \delta x, y + \delta y)$ and the time level $t + \delta t$ from the known distribution at the position $(x + e_{\alpha x}\delta t, y + e_{\alpha y}\delta t)$ and at the same time level $t + \delta t$, the Taylor series expansion is applied. Note that the time level for the position $(x + e_{\alpha x}\delta t, y + e_{\alpha y}\delta t)$ and the grid point $(x + \delta x, y + \delta y)$ is the same, that is, $t + \delta t$. So, the expansion in the time direction is not necessary and only the expansion in the spatial direction is needed. Figure 5.1 shows the configuration of the particle movement along α direction. We will use this figure to illustrate how Taylor series expansion in the spatial direction is done.

As shown in Figure 5.1, for simplicity, point A represents the grid point (x_A, y_A), point A' represents the position $(x_A + e_{\alpha x}\delta t, y_A + e_{\alpha y}\delta t)$, and point P represents another grid point (x_P, y_P) with $x_P = x_A + \delta x$, $y_P = y_A + \delta y$. The distribution at point A' at time level $t + \delta t$ is known after the collision and streaming processes according to equation (5.1)

$$f_\alpha(A', t + \delta t) = f_\alpha(A, t) - \frac{f_\alpha(A, t) - f_\alpha^{eq}(A, t)}{\tau} \tag{5.2}$$

For the general case, A' may not coincide with the mesh point P. We are only interested in the value of the density distribution at this mesh point P, not point A'. In order to get the value at point P from the known value at point A', we truncate Taylor series expansion for the density distribution at A' to the second order derivative terms around P. So $f_\alpha(A', t + \delta t)$ can be approximated by the corresponding distribution and its derivatives at the mesh point P as

$$f_\alpha(A', t + \delta t) = f_\alpha(P, t + \delta t) + \Delta x_A \frac{\partial f_\alpha(P, t + \delta t)}{\partial x} + \Delta y_A \frac{\partial f_\alpha(P, t + \delta t)}{\partial y} +$$

$$\frac{1}{2}(\Delta x_A)^2 \frac{\partial^2 f_\alpha(P, t + \delta t)}{\partial x^2} + \frac{1}{2}(\Delta y_A)^2 \frac{\partial^2 f_\alpha(P, t + \delta t)}{\partial y^2} + \tag{5.3}$$

$$\Delta x_A \Delta y_A \frac{\partial^2 f_\alpha(P, t + \delta t)}{\partial x \partial y} + O[(\Delta x_A)^3, (\Delta y_A)^3]$$

where $\Delta x_A = x_A + e_{\alpha x}\delta t - x_P$, $\Delta y_A = y_A + e_{\alpha y}\delta t - y_P$. When a uniform grid is used, that is, $\Delta x_A = \Delta y_A = 0$, equation (5.3) is reduced to the standard LBE. This expansion involves six unknowns, that is, one distribution at this grid point P at the time level $t + \delta t$, two first order derivatives, and three second-order derivatives at that point. In order to avoid the finite difference approximation of these derivatives, we borrow the idea from the Runge-

Kutta method. There are six unknowns, so we do Taylor series expansion on six points so as to form the linear equation system in which the six unknowns are the variables.

To illustrate this process, as shown in Figure 5.1, the particles at six mesh points P, A, B, C, D, E at the time level t will stream to the positions P', A', B', C', D', E' at the time level $t + \delta t$ after the local collision process. Their distributions at these new positions can be computed through equation (5.1). Using the second order Taylor series expansion for the density distributions at these new positions in terms of the distribution and its derivatives at the mesh point P, the following equation system can be obtained

$$f'_i = \{s_i\}^T \{W\} = \sum_{j=1}^{6} s_{i,j} W_j, \qquad i = P, A, B, C, D, E \tag{5.4}$$

where

$$f'_i = f_\alpha(x_i, y_i, t) - \frac{f_\alpha(x_i, y_i, t) - f_\alpha^{eq}(x_i, y_i, t)}{\tau} \tag{5.5a}$$

$$\{s_i\}^T = \{1, \Delta x_i, \Delta y_i, (\Delta x_i)^2 / 2, (\Delta y_i)^2 / 2, \Delta x_i \Delta y_i\} \tag{5.5b}$$

$$\Delta x_i = x_i + e_{\alpha x} \delta t - x_P, \quad \Delta y_i = y_i + e_{\alpha y} \delta t - y_P \quad i = P, A, B, C, D, E \tag{5.5c}$$

$$\{W\} = \{f_\alpha, \frac{\partial f_\alpha}{\partial x}, \frac{\partial f_\alpha}{\partial y}, \frac{\partial^2 f_\alpha}{\partial x^2}, \frac{\partial^2 f_\alpha}{\partial y^2}, \frac{\partial^2 f_\alpha}{\partial x \partial y}\}^T \tag{5.5d}$$

f'_i is the post-collision state of the distribution at the ith point and the time level $t + \delta t$, $\{s_i\}^T$ is a vector with six elements formed by the coordinates of the mesh points and the particle velocities, $\{W\}$ is the vector of the unknowns at the mesh point P and the time level $t + \delta t$, which also has six elements. $s_{i,j}$ is the jth element of the vector $\{s_i\}^T$ and W_j is the jth element of the vector $\{W\}$. Our target is to find the first element in the vector

{W}, that is, $W_1 = f_\alpha(P, t + \delta t)$. Equation system (5.4) can be put into the following matrix form

$$[S]\{W\} = \{f'\} \tag{5.6}$$

where $\quad \{f'\} = \{f_P', f_A', f_B', f_C', f_D', f_E'\}^T \tag{5.7a}$

$$[S] = [s_{i,j}] = \begin{bmatrix} \{s_P\}^T \\ \{s_A\}^T \\ \{s_B\}^T \\ \{s_C\}^T \\ \{s_D\}^T \\ \{s_E\}^T \end{bmatrix} = \begin{bmatrix} 1 & \Delta x_P & \Delta y_P & (\Delta x_P)^2/2 & (\Delta y_P)^2/2 & \Delta x_P \Delta y_P \\ 1 & \Delta x_A & \Delta y_A & (\Delta x_A)^2/2 & (\Delta y_A)^2/2 & \Delta x_A \Delta y_A \\ 1 & \Delta x_B & \Delta y_B & (\Delta x_B)^2/2 & (\Delta y_B)^2/2 & \Delta x_B \Delta y_B \\ 1 & \Delta x_C & \Delta y_C & (\Delta x_C)^2/2 & (\Delta y_C)^2/2 & \Delta x_C \Delta y_C \\ 1 & \Delta x_D & \Delta y_D & (\Delta x_D)^2/2 & (\Delta y_D)^2/2 & \Delta x_D \Delta y_D \\ 1 & \Delta x_E & \Delta y_E & (\Delta x_E)^2/2 & (\Delta y_E)^2/2 & \Delta x_E \Delta y_E \end{bmatrix} \tag{5.7b}$$

It is worthwhile to mention that this is not the only way to choose six points around *P*. You can choose any six points around *P* as shown in Figure 5.1.

Since [S] is a 6×6 dimensional matrix, it is very difficult to get an analytical expression for the solution of equation system (5.6). A numerical algorithm is needed to get the solution. Clearly, when the coordinates of the mesh points are given, the particle velocity and time step size are specified, the matrix [S] is determined and does not change with time.

In the practical applications, a direct matrix solver was tried. However, it was found that the matrix [S] might be singular or ill conditioned. To overcome this difficulty and make the method be more general, the least squares approach was introduced to optimize equation (5.6). For simplicity, let the mesh point *P* be represented by the index $i = 0$, and its adjacent points be represented by the index $i = 1, 2, ..., M$, where *M* is the number of the selected neighboring points around *P* and it should be larger than 5. According to the least squares method, the following equation system can be obtained

$$[S]^T[S]\{W\} = [S]^T\{f'\} \tag{5.8}$$

$$\text{where } [S] = \begin{bmatrix} 1 & \Delta x_0 & \Delta y_0 & (\Delta x_0)^2/2 & (\Delta y_0)^2/2 & \Delta x_0 \Delta y_0 \\ 1 & \Delta x_1 & \Delta y_1 & (\Delta x_1)^2/2 & (\Delta y_1)^2/2 & \Delta x_1 \Delta y_1 \\ - & - & - & - & - & - \\ - & - & - & - & - & - \\ - & - & - & - & - & - \\ 1 & \Delta x_M & \Delta y_M & (\Delta x_M)^2/2 & (\Delta y_M)^2/2 & \Delta x_M \Delta y_M \end{bmatrix}_{(M+1)\times 6} \tag{5.9a}$$

$$\Delta x_i = x_i + e_{\alpha x}\delta t - x_0, \ \Delta y_i = y_i + e_{\alpha y}\delta t - y_0, \text{ for } i = 0,1,2,...,M \tag{5.9b}$$

$$\{f'\} = \{f'_0, f'_1,..., f'_M\}^T \tag{5.9c}$$

From equation (5.8), we can obtain

$$\{W\} = \left([S]^T[S]\right)^{-1}[S]^T\{f'\} = [A]\{f'\} \tag{5.10}$$

The first element in the vector {W} can be expressed by

$$W_1 = f_\alpha(x_0, y_0, t+\delta t) = \sum_{k=1}^{M+1} a_{1,k} f'_{k-1} \tag{5.11}$$

where $a_{1,k}$ are the elements of the first row in the matrix $[A]$, which is determined by the coordinates of the mesh points, the particle velocity and time step size, and will not be changed in the calculation procedure. We can calculate once and store them in advance, so little computational effort is introduced as compared with the standard LBE. On the other hand, equation (5.11) does not depend on the mesh structure. It only needs to know the coordinates of mesh points. Thus, we can say that it can be easily used to solve flow problems with complex geometries.

Previous numerical simulations have shown that this method is an efficient and flexible approach for isothermal flow problems with complex geometries at very high Reynolds numbers. (Shu et al. 2002 & 2003, Chew et al. 2002, Niu et al. 2003.) In the

following section, this method is applied to the IEDDF thermal model so as to extend the current thermal model for practical thermal applications with complex geometries.

5.3 Application of TLLBM in IEDDF thermal model

5.3.1 The formulation

As we know from Chapter 3, for the IEDDF thermal model, the density and internal energy density distributions satisfy the following evolution equations, respectively:

$$\overline{f}_\alpha(\boldsymbol{x}+\boldsymbol{e}_\alpha\delta t,t+\delta t)-\overline{f}_\alpha(\boldsymbol{x},t)=-\frac{\delta t}{\tau_v+0.5\delta t}\left[\overline{f}_\alpha(\boldsymbol{x},t)-f_\alpha^{eq}(\boldsymbol{x},t)\right]+\frac{\tau_v F_\alpha \delta t}{\tau_v+0.5\delta t} \qquad (5.12a)$$

$$\overline{g}_\alpha(\boldsymbol{x}+\boldsymbol{e}_\alpha\delta t,t+\delta t)-\overline{g}_\alpha(\boldsymbol{x},t)=-\frac{\delta t}{\tau_c+0.5\delta t}\left[\overline{g}_\alpha(\boldsymbol{x},t)-g_\alpha^{eq}(\boldsymbol{x},t)\right]-\frac{\tau_c f_\alpha(\boldsymbol{x},t)q_\alpha \delta t}{\tau_c+0.5\delta t} \qquad (5.12b)$$

When these two equations are used to solve the thermal problems on the arbitrary grids, $(x+e_{\alpha x}\delta t, y+e_{\alpha y}\delta t)$ is usually not at the grid point $(x+\delta x, y+\delta y)$. So TLLBM technique has to be applied. Following the same procedure as shown in the previous section for the density distribution, after applying the TLLBM technique to the governing equations (5.12a) and (5.12b), the density distribution $\overline{f}$ and internal energy density distribution $\overline{g}$ at each grid point are updated by:

$$\overline{f_\alpha}(x_0,y_0,t+\delta t)=W_1=\sum_{k=1}^{M_1+1}a_{1,k}\,\overline{f'_{k-1}} \qquad (5.13a)$$

$$\overline{g_\alpha}(x_0,y_0,t+\delta t)=W'_1=\sum_{k=1}^{M_2+1}a'_{1,k}\,\overline{g'_{k-1}} \qquad (5.13b)$$

where

118

$$\overline{f'}_k = \left(1 - \frac{\delta t}{\tau_v + 0.5\delta t}\right)\overline{f}_\alpha(x_k, y_k, t) + \frac{\delta t}{\tau_v + 0.5\delta t} f_\alpha^{eq}(x_k, y_k, t) + \frac{\tau_v F_\alpha \delta t}{\tau_v + 0.5\delta t} \qquad (5.14a)$$

$$\overline{g'}_k = \left(1 - \frac{\delta t}{\tau_c + 0.5\delta t}\right)\overline{g}_\alpha(x_k, y_k, t) + \frac{\delta t}{\tau_c + 0.5\delta t} g_\alpha^{eq}(x_k, y_k, t) - \frac{\tau_c f_\alpha q_\alpha \delta t}{\tau_c + 0.5\delta t} \qquad (5.14b)$$

$$\{W'\} = \{g_\alpha, \frac{\partial g_\alpha}{\partial x}, \frac{\partial g_\alpha}{\partial y}, \frac{\partial^2 g_\alpha}{\partial x^2}, \frac{\partial^2 g_\alpha}{\partial y^2}, \frac{\partial^2 g_\alpha}{\partial x \partial y}\}^T \qquad (5.14c)$$

M_1 is the number of the selected neighboring points around P for the density distribution; M_2 is the number of the selected neighboring points around P for the internal energy density distribution. They should be larger than 5. $a'_{1,k}$ are the elements of the first row in the matrix $[A']$, which is derived in the same way as in $[A]$. These two matrixes are different if the different particle velocity models are chosen or different neighboring points around P are selected for the two density distributions.

When the same particle velocity model and the same neighboring points around P are chosen for the density and internal energy density distributions, the geometric matrix A and A' are the same, which can save both the computational time and storage space. In this chapter, we choose the grid point P and its surrounding eight points *A, B, C, D, E, F, G, H* as shown in Figure 5.1 to form the matrix A and matrix A'. The D2Q9 lattice model is used for both density distributions. So the matrix A' is the same as A. Although Figure 5.1 is illustrated along the particle direction of 45^0, the point distribution shown in this figure can be applied to other particle directions including the horizontal and vertical directions.

5.3.2 Wall boundary conditions

The implementation of wall boundary conditions is very important in the numerical simulations. The bounce-back rule of the non-equilibrium distribution proposed by Zou and He (1997) which has been described in Chapter 3 is used here. At the outgoing directions, the density distribution and internal energy density distribution are calculated from the governing equations (5.13a) and (5.13b). For the rest of the distributions which are at the incoming directions, their values are determined by the so-called bounce back rule for the non-equilibrium distribution. For the Neumann boundary condition, we deal with it in the same way as shown in Chapter 3. For the wall corner points, the extrapolation scheme is used at some special directions for the density and internal energy density distributions, which has been explained in detail in Chapter 4 and will not be repeated here.

5.4 Simulations of thermal flows with simple boundaries

In order to verify whether our proposed new thermal model can solve the thermal problems on the arbitrary mesh, firstly, we carried out the computation for the thermal flows with simple boundaries. The problem considered is the natural convection in a two-dimensional square cavity. A typical non-uniform grid as shown in Figure 4.27 in Chapter 4 is used here. The grids are stretched towards all the walls.

The convergence criterion for all the cases in this chapter is set to

$$\max_{i,j}\left|\sqrt{(u_{i,j}^2 + v_{i,j}^2)^{n+1}} - \sqrt{(u_{i,j}^2 + v_{i,j}^2)^n}\right| \le 10^{-8}, \max_{i,j}\left|T_{i,j}^{n+1} - T_{i,j}^n\right| \le 10^{-8} \tag{5.15}$$

where n and $n+1$ represent the old and new time levels, respectively.

5.4.1 Validation of the numerical results

Numerical simulations of this natural convection problem were carried out on the non-uniform grids at a wide range of Rayleigh numbers of $10^3 \sim 10^6$. Table 5.1 shows the numerical results of the maximum horizontal velocity $u_{\max}$ on the vertical mid-plane of the cavity and its location y, the maximum vertical velocity $v_{\max}$ on the horizontal mid-plane of the cavity and its location x, the average Nusselt number throughout the cavity $\overline{Nu}$ and the value of the stream function at the center point of the cavity. The numerical results of a NS solver given by Shu and Xue (1998) using DQ method are also included for comparison.

From Table 5.1, we can see that the numerical results obtained by our proposed new thermal model generally agree well with the benchmark results of Shu and Xue in a wide range of Rayleigh numbers. The deviation of the two results at high Rayleigh number is larger than that at low Rayleigh number, but it is still within 3%. The reason for the larger deviation at high Rayleigh number may be due to the fact that at high Rayleigh number, the temperature variation is very large; while in the IEDDF thermal model, the mean temperature is used as the reference temperature. This may introduce some error at high Rayleigh numbers. Another reason may be that at high Rayleigh numbers, when the flow becomes weakly turbulent, the solution given by the Boussinesq approximation deviates gradually from the true solution.

From this table, we can see that the use of the TLLBM technique in the IEDDF thermal model can solve the thermal problems on the non-uniform grids at high Rayleigh

numbers successfully. Compared with the thermal model with the use of FVLBM technique proposed in the last chapter, this new thermal model has wider applicability.

5.4.2 Comparison of the numerical results on uniform and non-uniform grids

In order to investigate the efficiency of this new thermal model, the numerical simulations on both the uniform grids using the standard LBM and non-uniform grids using our new thermal model at the same Rayleigh number were carried out. Tables 5.2-5.5 show the comparison of the numerical results using two different methods at Rayleigh numbers of 10^3, 10^4, 10^5 and 10^6.

It can be observed from Tables 5.2-5.5 that, using the same number of the grid points at the same Rayleigh number, the calculated Nusselt number and other results on the non-uniform grids are more accurate than those on the uniform grids when compared with the benchmark results using DQ method. This clearly shows the advantage of using non-uniform grids in the simulation of flow problems, even when the physical domain is regular. Because the grids are stretched towards the walls for non-uniform grids, the grid spacing is much smaller than that for uniform grids near the walls when the same grid number is used. It is easier for non-uniform grids to capture the properties in the thin boundary layer, especially at high Rayleigh numbers.

As far as the computational efficiency is concerned, for the same grid number, the calculation time on non-uniform grids using the TLLBM thermal model is more than that on uniform grids using the standard IEDDF thermal model. But it will take much less grid numbers for non-uniform grids than uniform grids to obtain the same accurate results. The

combining result of these two effects is that it will take less computation time for the TLLBM thermal model with non-uniform grids to get the results at the same accuracy. Take $Ra=10^3$ as an example. All the following computations are done on Pentium III 1600. It will take 87.30s to get the convergent result on uniform grids with the mesh size of 51×51 using the standard IEDDF thermal model, while it has to take 242.85s for non-uniform grids with the same grid size using the TLLBM thermal model. But as shown in Table 5.2, when compared with the benchmark data, the grid size using uniform grids should be increased to 101×101 in order to obtain results as accurate as those of the mesh size of 51×51 on non-uniform grids. When the grid size is increased to 101×101 for uniform grids, the calculation time is 574.25s, much longer than that for non-uniform grids. This example shows that the TLLBM thermal model is faster than the standard IEDDF thermal model to get the same accurate results.

5.5 Simulations of thermal flows with complex geometries

In practice, thermal flows in engineering applications are often involved with complex geometries. For example, the flow and thermal fields in different kinds of enclosed space are of great importance due to their wide applications such as in solar collector-receivers, insulation and flooding protection for buried pipes used for district heating and cooling, cooling systems in nuclear reactors, etc. A large number of literatures were published in the past few decades for this kind of problems. For concentric and eccentric cases in a horizontal annulus between two circular cylinders, the flow and thermal fields have been well studied. Comparatively, little work has been conducted in more complex domains, such as the annulus between a square outer cylinder and a circular

inner cylinder. In this section, we will show that the TLLBM technique together with the IEDDF thermal model can also provide very accurate results for these kinds of complex thermal problems.

A schematic view of a horizontal concentric annulus between a square outer cylinder and a heated circular inner cylinder is shown in Figure 5.2. *L* is the length of square cylinder and r_i is the radius of circular cylinder. ξ and η are transformed coordinates. Heat is generated uniformly within the circular inner cylinder, which is placed concentrically within the cold square cylinder. A typical grid used is shown in Figure 5.3. It can be seen clearly from this figure that mesh points are stretched towards the walls so as to capture the thin boundary layers. In the middle part of flow field, the mesh is relatively coarse since the velocity and temperature gradients are not very large in this region.

5.5.1 Boundary conditions for the curved wall

The bounce-back rule of the non-equilibrium distribution is used. However, its implementation on the curved boundary is more difficult than the flat wall. For the curved boundary, the directions for the outgoing and incoming distributions cannot be determined so easily as those for the flat wall. These directions are changing at each point on the curved boundary. We should find out which directions belong to the outgoing distributions and which directions belong to the incoming distributions before we use the bounce-back boundary condition.

At the inner circular cylinder, the outgoing distributions at a boundary point can be determined by satisfying the condition of $e \cdot n < 0$, where n is the outward vector at that

boundary point normal to the boundary. Incoming distributions are defined by the condition of $e \cdot n > 0$. At the outer square cylinder, the outgoing distributions are defined by the condition of $e \cdot n \geq 0$, while the incoming distributions are defined by $e \cdot n < 0$.

For the outgoing distributions, their values are calculated from the evolution equations (5.13a) and (5.13b); for the incoming distributions, their values are determined from the bounce-back rule of the non-equilibrium distribution. At the inner circular cylinder, at some special points on this wall boundary, there exist distributions whose directions satisfy the condition $e \cdot n = 0$. Their values are determined from the extrapolation scheme from their neighboring points in the flow fields at these directions. This process is the same as that for some special directions at the corner wall points as shown in Chapter 4.

5.5.2 Definition of Nusselt numbers

The local heat transfer rate on the inner cylinder can be computed by

$$q = h(T_i^* - T_o^*) = -k \frac{\partial T^*}{\partial n} \tag{5.16}$$

where T^* is the dimensional temperature, T_i^*, T_o^* are respectively the temperatures on the inner and outer cylinders, h represents the local heat transfer coefficient, k is the thermal diffusivity. From equation (5.16), we can get

$$h = -k \frac{\partial T}{\partial n} \tag{5.17}$$

Here T is the non-dimensional temperature, which is defined as $T = \dfrac{T^* - T_o^*}{T_i^* - T_o^*}$. $\dfrac{\partial T}{\partial n}$ is the

temperature gradient in the direction normal to the wall boundary, which can be calculated

as

$$\frac{\partial T}{\partial n} = \frac{\xi_x^{\,2} + \xi_y^{\,2}}{\sqrt{\xi_x^{\,2} + \xi_y^{\,2}}} \frac{\partial T}{\partial \xi} + \frac{\xi_x \eta_x + \xi_y \eta_y}{\sqrt{\xi_x^{\,2} + \xi_y^{\,2}}} \frac{\partial T}{\partial \eta} \tag{5.18}$$

where, as shown in Figure 5.2, the wall surface is a grid line of $\eta = $ constant , on which

$\partial T / \partial \xi = 0$.

The average heat transfer coefficient $\bar{h}$ can be computed as

$$\bar{h} = \frac{1}{2\pi} \int_0^{2\pi} h\, d\xi \tag{5.19}$$

Since at the steady state, the Nusselt numbers along the inner and outer walls are the same,

there is no need to pay separate attention to the average Nusselt numbers for the outer and

inner boundaries. The average Nusselt number for the inner boundary is determined by

$$\overline{Nu} = \frac{\bar{h}S}{k} = -\frac{S}{2\pi} \int_0^{2\pi} \frac{\partial T}{\partial n}\, d\xi = -\frac{S}{2\pi} \int_0^{2\pi} \left(\frac{\xi_x \eta_x + \xi_y \eta_y}{\sqrt{\xi_x^{\,2} + \xi_y^{\,2}}} \frac{\partial T}{\partial \eta} \right) d\xi \tag{5.20}$$

where S is defined as half of the circumferential length of the inner cylinder surface due to

the symmetry, which is the same as that in the work of Moukalled and Acharya (1996) for

comparison.

5.5.3 Validation of the numerical results

As discussed before, most research work focused on the study of the natural

convection in the annuli between either concentric or eccentric circular cylinders. Only a

few publications involved the study of the natural convection in an annulus between an outer square cylinder and an inner circular cylinder. The work of Moukalled and Acharya (1996), Shu and Zhu (2002) were among such studies. Moukalled and Acharya studied numerically the natural heat transfer between a heated horizontal cylinder placed concentrically inside a square enclosure. Three different aspect ratios defined as $rr = \dfrac{L}{2r_i}$ and four different Rayleigh numbers were considered. NS equations were solved in a body-fitted coordinate system using a control volume-based numerical procedure. Their numerical data were validated by comparing with some experimental data and found to be in good agreement. Recently, the global method of differential quadrature (DQ) was applied by Shu and Zhu to simulate this natural convection problem. Their work consisted of the numerical results for Rayleigh numbers ranging from 10^4 to 10^6 and the aspect ratios between 1.67 and 5.0. So in this study, both the results of Moukalled and Acharya and the results of Shu and Zhu are used to validate our numerical data.

Calculations were carried out at Rayleigh numbers of 10^4, 10^5, 10^6 and the aspect ratios of 5.0, 2.5, 1.67. The numerical results of the maximum stream function ψ_{max} and the average Nusselt number $\overline{Nu}$ calculated using our new TLLBM thermal model together with the benchmark results are listed in Table 5.6 It is noted that the reference length used in the definition of Rayleigh number is the side length of the square cylinder, L. The mesh size used in the present study is 101×161 for $Ra=10^4$, 129×201 for $Ra=10^5$, and 251×321 for $Ra=10^6$. From Table 5.6, it can be seen that at low Rayleigh numbers of 10^4 and 10^5, the results using three different methods compare very well with each other. At high Rayleigh number of 10^6, there are some deviations between the present results and the reference data. But the maximum difference is still within 2.5%, which lies in the

range of the numerical uncertainty of the solutions. So we can say that the present results are very accurate, even at high Rayleigh number. The application of the TLLBM technique in the IEDDF thermal model can solve the complex thermal problems accurately and effectively.

5.5.4 Analysis of the flow and thermal fields

The flow and thermal fields for the nine cases with $Ra = 10^4$, 10^5, 10^6 and $rr = 5.0$, 2.5, 1.67 are numerically analyzed. The respective streamlines and isotherms are shown in Figures 5.4-5.5. From these two figures, it is found that both the aspect ratio and Rayleigh number are critical to the flow and thermal fields. For the thermal fields as shown in Figure 5.4, it can be seen that the heat transfer is mainly dominated by the conduction at low Rayleigh number of 10^4, and by the convection at high Rayleigh numbers of 10^5 and 10^6. For the flow fields as shown in Figure 5.5, it can be observed that the flow is generally symmetrical about the vertical centerline through the center of the inner circular cylinder. It moves up along the inner heated circular cylinder. When the flow reaches the top of the outer square cylinder, it then moves horizontally outwards and goes down along the vertical sidewalls of the outer square cylinder. These two figures have the same trend as those of Shu and Zhu. The details are discussed below.

At the low Rayleigh number of 10^4, for all the three aspect ratios, the patterns of the streamlines and isotherms are the same. The maximum stream function is very small and the circulation of the flow is very weak. The heat transfer is mainly dominated by the conduction and a little stagnant area exists near the bottom of the square cylinder. The flow velocity is too small to affect the temperature distribution. As the aspect ratio

decreases from $rr = 5.0$ to $rr = 1.67$, the inner circular cylinder becomes bigger and the physical domain between the inner and outer cylinders is reduced. The thermal conduction and convection are confined in smaller area, which increases the heat transfer ability. This can be reflected in the increase of $\overline{Nu}$ as shown in Table 5.6.

As Rayleigh number increases, for each aspect ratio, the circulation of the flow becomes stronger, and as a result, the maximum stream function increases a lot; the convection part plays a more important role in the heat transfer. The stagnant area increases at the bottom of the outer square cylinder, and the thermal boundary layer becomes thinner and thinner. So the overall Nusselt number increases with Rayleigh number. At high Rayleigh numbers, the heat transfer is mainly dominated by the convection.

When the Rayleigh number is increased from 10^4 to 10^5, the aspect ratio is critical to the patterns of the flow and thermal fields. For the thermal fields, for all three aspect ratios, a plume begins to appear on the top of the inner circular cylinder. For the flow fields, for the case of $rr = 5.0$ and $rr = 2.5$, there are only two eddies, and these two eddies move closer and closer with the increase of Rayleigh number. But for the case of $rr = 1.67$, these two eddies gradually evolve into four eddies with increasing Rayleigh number, but they are still symmetrical about the vertical centerline. In addition, two tiny eddies begin to appear above the circular cylinder near the vertical centerline when Rayleigh number reaches 10^5.

When the Rayleigh number is further increased from 10^5 to 10^6, for the case of $rr = 5.0$ and $rr = 2.5$, the patterns of flow and thermal fields do not have too much change. There is only one plume on top of the inner circular cylinder in the thermal fields and two eddies in the flow fields. While for the case of $rr = 1.67$, in the thermal field, instead of

one plume, two plumes begin to appear on top of the inner circular cylinder. As Rayleigh number increases to 10^6, the two plumes become bigger, and a third plume appears above the top of the inner cylinder with reversed direction. Two tiny eddies on top of the inner cylinder probably cause the formation of the third plume in reversed direction.

From the above discussion, it is clear that the aspect ratio and Rayleigh number greatly affect the flow and thermal fields. As Rayleigh number increases, the flow is enhanced, and the thermal plume is formed. For $rr = 5.0$ and $rr = 2.5$, only one plume is formed on the top of the inner cylinder and two eddies exist symmetrically about the vertical center line. However, for $rr = 1.67$, two plumes and one additional plume in the opposite direction are formed above the inner cylinder, and four eddies exist symmetrically about the vertical center line when Rayleigh number increases to 10^6. It seems that a critical aspect ratio rr may exist to distinguish whether one plume or three plumes exist in the isotherms, and whether two eddies or four eddies exist in the streamlines.

From Figures 5.4 and 5.5, we can see that our numerical scheme is able to capture the above physical phenomena correctly.

5.6 Conclusions

The explicit TLLBM technique is applied to the IEDDF thermal model in order to solve the thermal problems with complex geometries. The numerical simulations of natural convection in a square cavity at Rayleigh numbers ranging from 10^3 to 10^6 on non-uniform grids validate our new scheme. The numerical results compare very well with the benchmark data obtained by a NS solver. Less grid number is needed to obtain accurate

results using non-uniform grids. Furthermore, its applicability to solve the complicated thermal problems with curved boundaries, such as the natural convection in a horizontal concentric annulus between a square outer cylinder and a circular inner cylinder, is also demonstrated. Numerical results at Rayleigh numbers ranging from 10^4 to 10^6 and aspect ratios between 1.67 and 5.0 are presented, which agree well with available data in the literature. It is also found in this study that both the aspect ratio and Rayleigh number are critical to the patterns of the flow and thermal fields. It is suggested that a critical aspect ratio may exist at high Rayleigh number to distinguish the flow and thermal patterns.

From these numerical simulations, we can see that the use of the TLLBM technique in the IEDDF thermal model is an effective and flexible way to extend the current thermal model to be used on the arbitrary grids, which is very important for the practical engineering applications. Till now, our objective has been fulfilled. It should be emphasized again that this new thermal scheme is an explicit method; it keeps the local feature of the standard LBM and no solution of the differential equations is involved. So it can be easily applied to any complex geometry.

So far, we have demonstrated the present method in two-dimensional flow problems. It is necessary to extend it to three-dimensional flow problems that are related to a lot of engineering applications. In order to do this, the thermal model for three dimensional applications should be proposed firstly. The TLLBM technique can then be applied to the new three-dimensional thermal model so as to extend its use on the arbitrary mesh. This is the challenging work which we are going to pursue in the following chapters.

Table 5.1 Comparison of the numerical results between the TLLBM thermal model and a NS solver for the natural convection in a square cavity

Ra	10^3		10^4		10^5		10^6	
Method	TLLBM	DQ	TLLBM	DQ	TLLBM	DQ	TLLBM	DQ
Grid size	51×51	-	101×101	-	151×151	-	201×201	-
u_{max}	3.646	3.649	16.158	16.190	34.301	34.736	63.590	64.775
y	0.814	0.815	0.824	0.825	0.852	0.855	0.844	0.850
v_{max}	3.694	3.698	19.676	19.638	68.188	68.640	218.32	220.64
x	0.180	0.180	0.121	0.120	0.065	0.065	0.037	0.035
$\overline{Nu}$	1.117	1.118	2.244	2.245	4.520	4.523	8.804	8.800
$\left|\psi_{mid}\right|$	1.175	1.175	5.071	5.075	9.104	9.117	16.313	16.270

Table 5.2 Comparison of the numerical results on uniform and non-uniform grids for the natural convection in a square cavity at $Ra=10^3$

Mesh	51×51(uni)	101×101(uni)	DQ	51×51(non)
$\left|\psi_{mid}\right|$	1.170	1.175	1.175	1.175
u_{max}	3.636	3.649	3.649	3.646
y	0.820	0.810	0.815	0.814
v_{max}	3.702	3.700	3.698	3.694
x	0.180	0.180	0.180	0.180
$\overline{Nu}$	1.116	1.117	1.118	1.117
$Nu_{1/2}$	1.114	1.116	1.118	1.118
Nu_0	1.103	1.110	1.118	1.110
Nu_{max}	1.465	1.481	1.506	1.491
y	0.140	0.090	0.090	0.110
Nu_{min}	0.722	0.672	0.691	0.684
y	1.000	1.000	1.000	1.000

Table 5.3 Comparison of the numerical results on uniform and non-uniform grids for the natural convection in a square cavity at $Ra=10^4$

Mesh	101×101(uni)	151×151(uni)	DQ	101×101(non)
$\left\|\psi_{mid}\right\|$	5.063	5.069	5.075	5.071
u_{max}	16.158	16.156	16.190	16.158
y	0.820	0.820	0.825	0.824
v_{max}	19.704	19.679	19.638	19.676
x	0.120	0.120	0.120	0.121
$\overline{Nu}$	2.232	2.237	2.245	2.244
$Nu_{1/2}$	2.224	2.231	2.245	2.244
Nu_0	2.192	2.183	2.248	2.189
Nu_{max}	3.576	3.479	3.543	3.498
y	0.150	0.147	0.145	0.138
Nu_{min}	0.617	0.593	0.586	0.580
y	1.000	1.000	1.000	1.000

Table 5.4 Comparison of the numerical results on uniform and non-uniform grids for the natural convection in a square cavity at $Ra=10^5$

Mesh	151×151(uni)	201×201(uni)	DQ	151×151(non)
$\left\|\psi_{mid}\right\|$	9.102	9.103	9.117	9.104
$\left\|\psi_{max}\right\|$	9.648	9.644	9.618	9.631
x	0.287	0.285	0.285	0.287
y	0.607	0.605	0.600	0.606
u_{max}	34.194	34.245	34.736	34.301
y	0.853	0.855	0.855	0.852
v_{max}	68.282	68.276	68.640	68.188
x	0.067	0.065	0.065	0.065
$\overline{Nu}$	4.494	4.501	4.523	4.520
$Nu_{1/2}$	4.487	4.496	5.524	4.518
Nu_0	4.446	4.430	4.527	4.355
Nu_{max}	7.984	7.833	7.788	7.895
y	0.080	0.080	0.080	0.075
Nu_{min}	0.767	0.758	0.725	0.715
y	1.000	1.000	1.000	1.000

Table 5.5 Comparison of the numerical results on uniform and non-uniform grids for the natural convection in a square cavity at $Ra=10^6$

Mesh	201×201(uni)	251×251(uni)	DQ	201×201(non)	251×251(non)
$\left\|\psi_{mid}\right\|$	16.359	16.369	16.270	16.313	16.316
$\left\|\psi_{max}\right\|$	16.832	16.827	16.714	16.815	16.800
x	0.150	0.148	0.150	0.176	0.174
y	0.555	0.552	0.550	0.763	0.765
u_{max}	63.251	63.527	64.775	63.590	63.640
y	0.840	0.844	0.850	0.844	0.848
v_{max}	218.33	218.47	220.64	218.32	218.41
x	0.040	0.040	0.035	0.037	0.038
$\overline{Nu}$	8.766	8.781	8.762	8.814	8.818
$Nu_{1/2}$	8.759	8.775	8.727	8.803	8.810
Nu_0	8.562	8.500	8.721	8.291	8.200
Nu_{max}	18.514	18.148	16.070	18.813	18.000
y	0.040	0.036	0.040	0.034	0.035
Nu_{min}	0.986	1.012	1.665	0.852	0.883
y	1.000	1.000	1.000	1.000	1.000

Table 5.6 Comparison of ψ_{max} and $\overline{Nu}$ for the natural convection in an annulus between an outer square cylinder and a heated inner circular cylinder

case	rr	Ra	ψ_{max}			$\overline{Nu}$		
			Present	Shu	Moukalled	Present	Shu	Moukalled
1	5.0	10^4	1.73	1.71	1.73	2.08	2.08	2.071
2	2.5		0.97	0.97	1.02	3.24	3.24	3.331
3	1.67		0.48	0.49	0.50	5.39	5.40	5.826
4	5.0	10^5	10.09	9.93	10.15	3.79	3.79	3.825
5	2.5		8.25	8.10	8.38	4.84	4.86	5.08
6	1.67		5.08	5.10	5.10	6.20	6.21	6.212
7	5.0	10^6	22.00	20.98	25.35	5.96	6.11	6.107
8	2.5		25.21	24.13	24.07	8.75	8.90	9.374
9	1.67		21.63	20.46	21.30	11.65	12.00	11.62
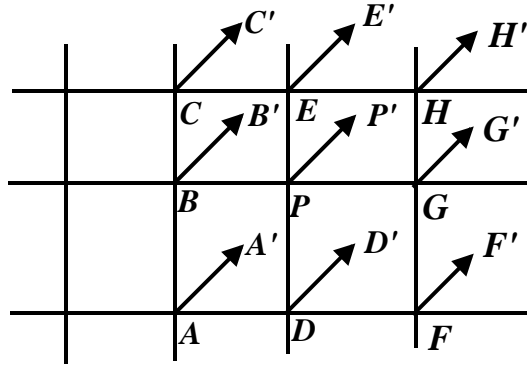
Figure 5.1 Configuration of the particle movement along α direction
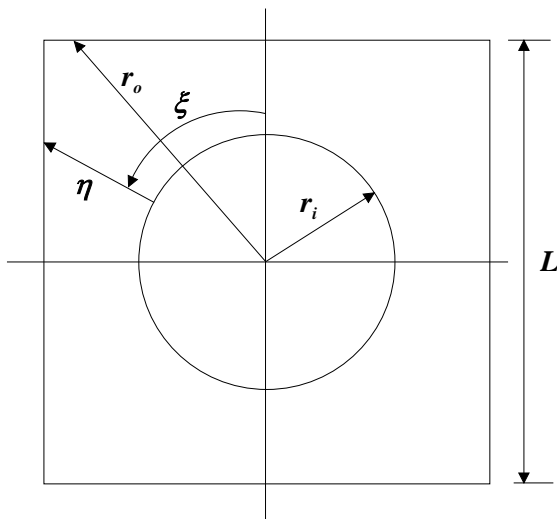
Figure 5.2 Sketch of the physical domain for a concentric annulus between a square outer cylinder and a circular inner cylinder
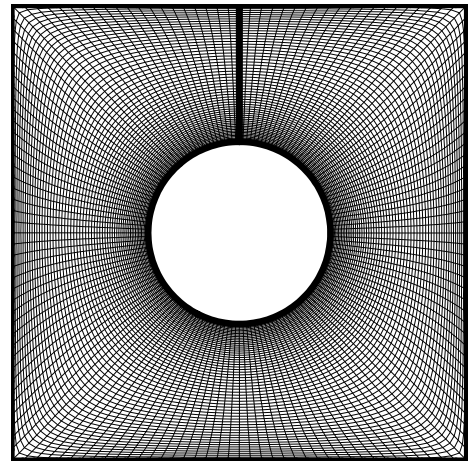
Figure 5.3 A typical non-uniform mesh used for a concentric annulus between a square outer cylinder and a circular inner cylinder
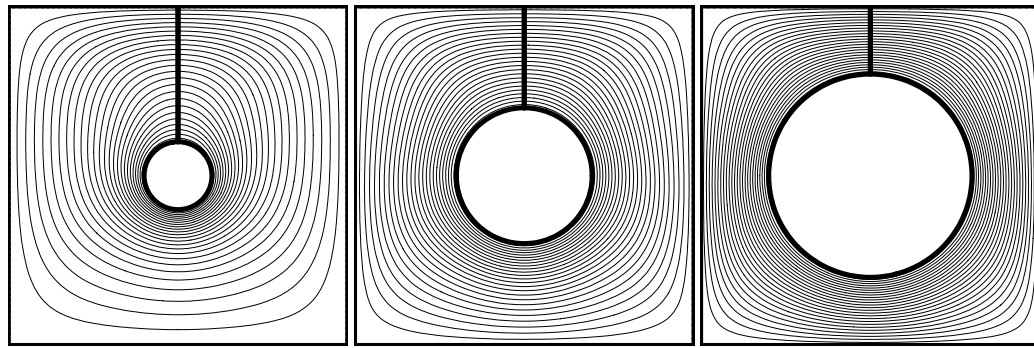
rr=5   rr=2.5   rr=1.67

(a) $Ra=10^4$
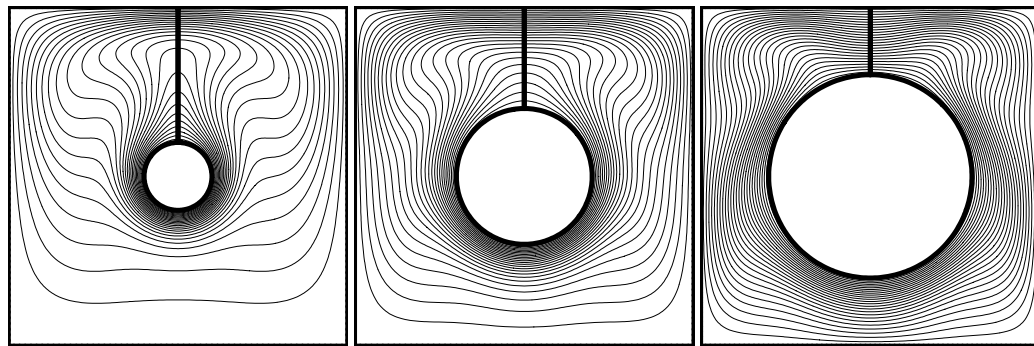
rr=5   rr=2.5   rr=1.67
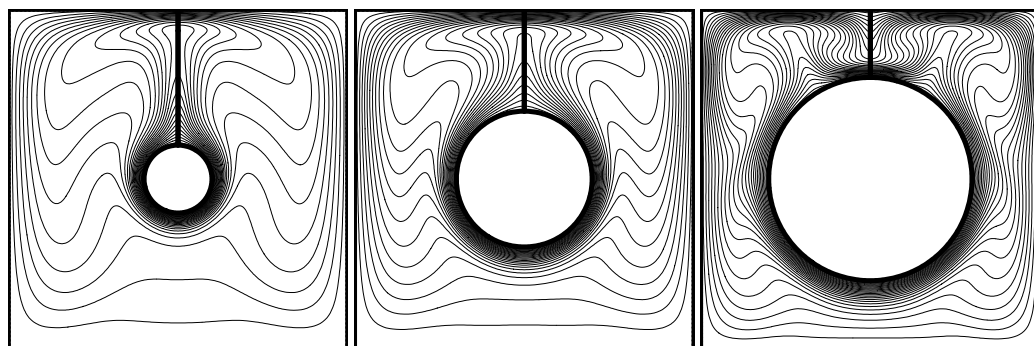
(b) $Ra=10^5$

rr=5   rr=2.5   rr=1.67

(c) $Ra=10^6$

Figure 5.4 Isotherms for the natural convection in an annulus between an outer square cylinder and a heated inner circular cylinder using the TLLBM thermal model
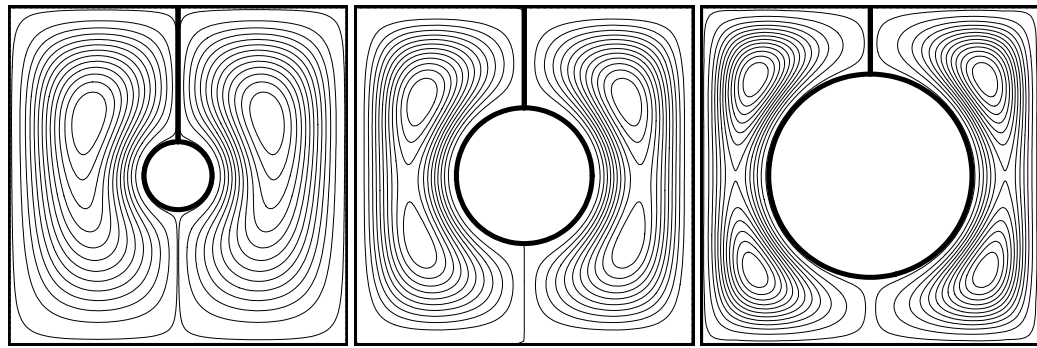
rr=5 rr=2.5 rr=1.67

(a) Ra=10^4
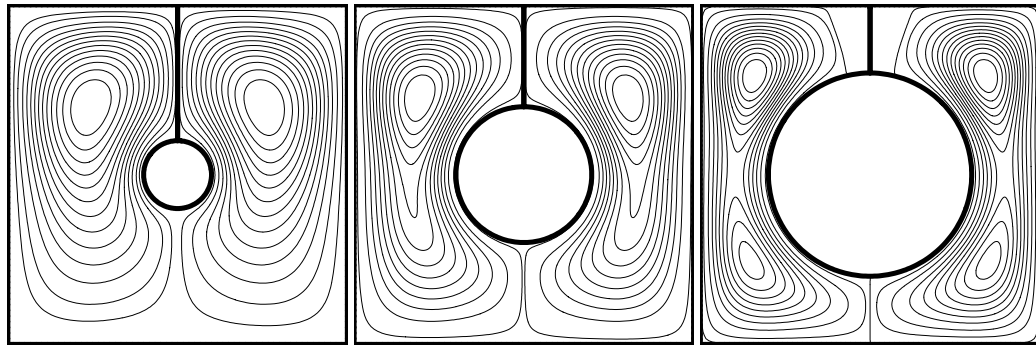
rr=5 rr=2.5 rr=1.67

(b) Ra=10^5
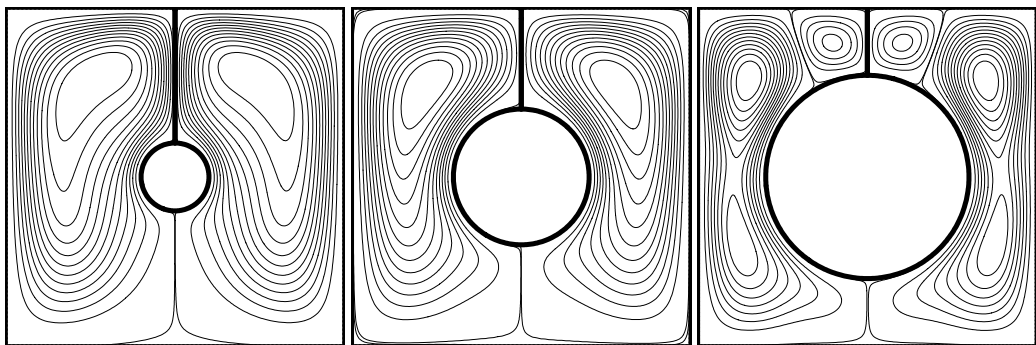
rr=5 rr=2.5 rr=1.67

(c) Ra=10^6

Figure 5.5 Streamlines for the natural convection in an annulus between an outer square cylinder and a heated inner circular cylinder using the TLLBM thermal model

Chapter 6

Simulation of the axisymmetric thermal flows

6.1 Introduction

In previous chapters, IEDDF thermal model has been developed into an effective thermal model to solve real practical thermal problems. Then this model is extended to be used for thermal applications on arbitrary grids by using FVLBM and TLLBM. Numerical results have shown that the use of TLLBM in IEDDF thermal model is an efficient and convenient way to solve thermal problems with complex geometries. All the previous studies are concerned about applications in two dimensions. We aim to develop a three-dimensional thermal model for three-dimensional thermal applications in following chapters. Before we do that, we will first study one kind of important thermal flows, which is called axisymmetric thermal flows. It contains many important flows such as the mixed convection flows in a vertical concentric cylindrical annuli and Czochralski crystal growth problems. For the conventional NS solvers in the cylindrical coordinate system, these axisymmetric flows are quasi- three-dimensional problems, rather than the real three-dimensional flows, since there is no change for any variable in the azimuthal direction. However, these flows become much more complicated when using LBM.

As we have known from Chapter 2, the standard LBM is based on the Cartesian coordinate system and it will recover the continuity and NS equations by the Chapman-Enskog expansion. The use of FVLBM or TLLBM will not change this property. The detailed explanation of this will be given in the methodology section. As the axisymmetric

flows are defined on the cylindrical coordinate system, if we use the standard LBM, we can only use the Cartesian coordinate system to solve such kind of cylindrical flow problems. This means that we have to use the three-dimensional lattice model to solve the three-dimensional problems, which complicate the problem as compared with the conventional NS solvers. In order to avoid such complication and find an effective way to solve this kind of important flows, we proposed a new scheme. By inserting the position, time and particle velocity dependent source terms into the evolution equation of the standard LBM, we aim to recover it on the macroscopic level to the continuity and NS equations defined in the cylindrical coordinate system by Chapman-Enskog expansion. This new scheme is based on the idea proposed by Halliday et al. in 2001, and it has the following good features. Like conventional CFD solvers, it solves the quasi- three-dimensional problem instead of the real three-dimensional problem for an axisymmetric flow. At the same time, it is applied on a uniform rectangular grid in the cylindrical coordinate system, which adheres to the inherit property of LBM. The curved boundary can also be well defined using the uniform rectangular grid. This will be described in the methodology section.

The mixed convection in a vertical concentric cylindrical annuli and the Wheeler's benchmark problem in Czochralski crystal growth are taken here as the test examples to validate our new scheme. The mixed convection flow in vertical concentric cylindrical annuli occurs in diverse engineering design problems, e.g. rotating electric motor equipment, chemical vapor deposition process, turbine rotor cooling, and heat exchangers design. Czochralski crystal growth technique has been widely used for the melt-crystal growth in the modern technology, which is needed for the scientific appraisal of crystallography, topography and tensor properties of all crystalline materials. The

modeling and understanding of the heat and mass transfer for this flow have become an important issue in the optimization of the Czochralski technique in order to grow more uniform and better quality crystals.

6.2 Mathematical model

6.2.1 Standard lattice Boltzmann method

The evolution equation for the standard LBM is as follows:

$$f_\alpha(\boldsymbol{x}+\boldsymbol{e}_\alpha\delta t, t+\delta t) - f_\alpha(\boldsymbol{x},t) = -\frac{f_\alpha(\boldsymbol{x},t) - f_\alpha^{eq}(\boldsymbol{x},t)}{\tau} \tag{6.1}$$

Using the current commonly used lattice models defined on the Cartesian coordinate system (x, y) such as D2Q9 and D2Q7 and performing the Chapman-Enskog expansion, the following macroscopic equations in the Cartesian coordinate system can be recovered:

$$\frac{\partial u}{\partial x} + \frac{\partial v}{\partial y} = 0 \tag{6.2a}$$

$$\frac{\partial u}{\partial t} + u\frac{\partial u}{\partial x} + v\frac{\partial u}{\partial y} = -\frac{1}{\rho}\frac{\partial p}{\partial x} + \upsilon\nabla^2 u \tag{6.2b}$$

$$\frac{\partial v}{\partial t} + u\frac{\partial v}{\partial x} + v\frac{\partial v}{\partial y} = -\frac{1}{\rho}\frac{\partial p}{\partial y} + \upsilon\nabla^2 v \tag{6.2c}$$

From equations (6.2a)-(6.2c), we can see that the continuity and NS equations recovered by Chapman-Enskog expansion are for the Cartesian coordinate system. However, for the steady axisymmetric flow problems, the governing equations are defined on the cylindrical coordinate system (r, z) and they are given as:

$$\frac{1}{r}\frac{\partial(ru)}{\partial r} + \frac{\partial w}{\partial z} = 0 \tag{6.3a}$$

$$u\frac{\partial u}{\partial r} + w\frac{\partial u}{\partial z} - \frac{v^2}{r} = -\frac{1}{\rho}\frac{\partial p}{\partial r} + \upsilon\left(\nabla^2 u - \frac{u}{r^2}\right) \qquad (6.3b)$$

$$u\frac{\partial v}{\partial r} + w\frac{\partial v}{\partial z} + \frac{uv}{r} = \upsilon\left(\nabla^2 v - \frac{v}{r^2}\right) \qquad (6.3c)$$

$$u\frac{\partial w}{\partial r} + w\frac{\partial w}{\partial z} = -\frac{1}{\rho}\frac{\partial p}{\partial z} + \upsilon\nabla^2 w + g\beta(T - T_c) \qquad (6.3d)$$

$$u\frac{\partial T}{\partial r} + w\frac{\partial T}{\partial z} = \frac{k}{\rho c_p}\nabla^2 T \qquad (6.3e)$$

where $\nabla^2 = \frac{1}{r}\frac{\partial}{\partial r}\left(r\frac{\partial}{\partial r}\right) + \frac{\partial^2}{\partial z^2}$; (u,v,w) are the radial, azimuthal and axial velocity

components; g is the gravitational acceleration; k is the thermal conductivity and c_p is the

specific heat at constant pressure. Since the variables do not change at the azimuthal

direction, there is no θ - derivative in the governing equations. So this kind of flow

problems is actually solved in (r,z) coordinate system for the conventional NS solvers.

They are two-dimensional problems although there are three velocity components.

If we use the standard LBM to solve these axisymmetric flows on the Cartesian

coordinate system, we have to solve the real three-dimensional problems using three-

dimensional lattice models. This makes the problem more complex as compared with the

conventional methods. Furthermore, when the uniform grids are used, the curved

boundary cannot be accurately represented. So this problem has to be solved on the non-

uniform grids by introducing FVLBM or TLLBM. In order to avoid these complications,

we should find a way to transform the standard LBM to some specific form with which

the Chapman-Enskog expansion would recover the continuity and NS equations in the

cylindrical coordinate system.

6.2.2 Axisymmetric lattice Boltzmann model

Since the azimuthal coordinate and its derivatives vanish, there are only two coordinate variables: z and r for an axisymmetric problem. In order to compare the governing equations in the cylindrical coordinate system with those in the two-dimensional Cartesian coordinate system, we make the following simple transformation. By making the replacements of $(z,r) \rightarrow (y,x)$, $(w,u) \rightarrow (v,u)$, $(v) \rightarrow (w)$, we can obtain a pseudo-Cartesian representation for equations (6.3a), (6.3b) and (6.3d):

$$\frac{\partial u}{\partial x} + \frac{\partial v}{\partial y} = -\frac{u}{x} \tag{6.4a}$$

$$\frac{\partial u}{\partial t} + u\frac{\partial u}{\partial x} + v\frac{\partial u}{\partial y} = -\frac{1}{\rho}\frac{\partial p}{\partial x} + \upsilon\nabla^2 u + \frac{w^2}{x} + \upsilon\left(\frac{1}{x}\frac{\partial u}{\partial x} - \frac{u}{x^2}\right) \tag{6.4b}$$

$$\frac{\partial v}{\partial t} + u\frac{\partial v}{\partial x} + v\frac{\partial v}{\partial y} = -\frac{1}{\rho}\frac{\partial p}{\partial y} + \upsilon\nabla^2 v + g\beta(T-T_c) + \upsilon\left(\frac{1}{x}\frac{\partial v}{\partial x}\right) \tag{6.4c}$$

where $\nabla^2 = \frac{\partial^2}{\partial x^2} + \frac{\partial^2}{\partial y^2}$. Compared with the real two-dimensional governing equations

(6.1a)-(6.1c) in the Cartesian coordinate system, these equations contain the additional terms that are underlined. We can consider them as the inertia forces from the coordinate transformation. As we know, with Chapman-Enskog expansion, the standard LBM can recover the continuity and NS equations in the Cartesian coordinate system. If we consider the underlined terms as forces, by inserting the position, time and particle velocity dependent forcing terms into the standard LBM and following the same Chapman-Enskog expansion, we may recover equations (6.4a)-(6.4c) by choosing the proper forms of the external forcing terms.

As emphasized by Halliday et al. (2001), in order to model the departures from the equilibrium in correspondence with the unadjusted LBGK scheme, there is no "equilibrium" for the external forcing terms and these external forcing terms should be at least of $O(\delta t)$. Incorporating such time, spatial and particle velocity dependent force terms into the evolution equation of the standard LBM gives:

$$f_\alpha(\boldsymbol{x}+\boldsymbol{e}_\alpha\delta t,t+\delta t)-f_\alpha(\boldsymbol{x},t)=-\frac{f_\alpha(\boldsymbol{x},t)-f_\alpha^{eq}(\boldsymbol{x},t)}{\tau}+\delta t G+\delta t F_1+\delta t^2 F_2 \qquad (6.5)$$

where $G = g\beta(T - T_c)\boldsymbol{j}\cdot(\boldsymbol{e}-\boldsymbol{u})f^{eq}$ is used to recover the buoyancy force in the governing equation (6.4c). Since the form of this force term is known, we only need to consider the force terms of F_1 and F_2. The force term G can be omitted in the following derivation procedure for brevity.

The Taylor series expansion of equation (6.5) retaining terms up to $O(\delta t^2)$ results in:

$$\delta t[\partial_t + \boldsymbol{e}_\alpha\cdot\nabla]f_\alpha + \frac{\delta t^2}{2}[\partial_t + \boldsymbol{e}_\alpha\cdot\nabla]^2 f_\alpha + O(\delta t^3) = -\frac{1}{\tau}(f_\alpha - f_\alpha^{eq}) + \delta t F_1 + \delta t^2 F_2 \qquad (6.6)$$

The Chapman-Enskog expansion of the above Taylor series expanded evolution equation plus the force terms at $O(\delta t)$ and $O(\delta t^2)$ are

$$(\partial_{t0} + e_{\alpha\gamma}\partial_\gamma)f_\alpha^{eq} = -\frac{1}{\tau}f_\alpha^{(1)} + F_1 \qquad (6.7a)$$

$$\partial_{t1}f_\alpha^{eq} + \left(1 - \frac{1}{2\tau}\right)(\partial_{t0} + \boldsymbol{e}_\alpha\cdot\nabla)f_\alpha^{(1)} + \frac{1}{2}(\partial_{t0} + \boldsymbol{e}_\alpha\cdot\nabla)F_1 = -\frac{1}{\tau}f_\alpha^{(2)} + F_2 \qquad (6.7b)$$

The summation of equation (6.7a) and the summation of equation (6.7a) multiplied by $\boldsymbol{e}_\alpha$ give the continuity and Euler equations.

$$\partial_{t0}\rho + \nabla \cdot (\rho \boldsymbol{u}) = \sum_{\alpha} F_1 \tag{6.8a}$$

$$\partial_{t0}(\rho \boldsymbol{u}) + \nabla \cdot \Pi^{(0)} = \sum_{\alpha} F_1 \boldsymbol{e}_\alpha \tag{6.8b}$$

where $\Pi^{(0)} = \sum_{\alpha} \boldsymbol{e}_\alpha \boldsymbol{e}_\alpha f_\alpha^{eq}$

Compared with the convection part of equations (6.4a)-(6.4c), we can get

$$\sum_{\alpha} F_1 = \frac{-\rho u}{x} \tag{6.9a}$$

$$\sum_{\alpha} F_1 e_{\alpha\gamma} = \frac{\rho w^2}{x} \delta_{\gamma x} \tag{6.9b}$$

The summation of equation (6.7b) and the summation of equation (6.7b) multiplied by $\boldsymbol{e}_\alpha$

are

$$\partial_{t1}\rho + \frac{1}{2}\partial_{t0}\left(\sum_{\alpha} F_1\right) + \frac{1}{2}\nabla \cdot \left(\sum_{\alpha} F_1 \boldsymbol{e}_\alpha\right) = \sum_{\alpha} F_2 \tag{6.10a}$$

$$\partial_{t1}(\rho \boldsymbol{u}) + \left(1 - \frac{1}{2\tau}\right)\nabla \cdot \Pi^{(1)} + \frac{1}{2}\partial_{t0}\left(\sum_{\alpha} \boldsymbol{e}_\alpha F_1\right) + \frac{1}{2}\nabla \cdot (\boldsymbol{e}_\alpha \boldsymbol{e}_\alpha F_1) = \sum_{\alpha} F_2 \boldsymbol{e}_\alpha \tag{6.10b}$$

where $\Pi^{(1)} = \sum_{\alpha} \boldsymbol{e}_\alpha \boldsymbol{e}_\alpha f_\alpha^{(1)}$

Equation (6.10a) plus equation (6.8a) and equation (6.10b) plus equation (6.8b) should recover the continuity and NS equations (6.4a)-(6.4c). So the following relationship should be satisfied.

$$\sum_{\alpha} F_2 = \frac{1}{2x}\left[\partial_x(\rho u^2) + \partial_y(\rho uv) + \partial_x(p) + \partial_x(\rho w^2) - \frac{2\rho w^2}{x}\right] \tag{6.11a}$$

$$\sum_{\alpha} F_2 e_{\alpha x} = -\frac{w}{x}\left[\partial_x(\rho uw) + \partial_y(\rho vw) + \frac{\rho uw}{x}\right] - \frac{1}{6x}\partial_x(\rho u) + \frac{\rho u}{6x^2} \tag{6.11b}$$

$$\sum_{\alpha} F_2 e_{\alpha y} = -\frac{1}{6x}\partial_y(\rho u) + \frac{\upsilon}{x}\left[\partial_x(\rho v) - \partial_y(\rho u)\right] \tag{6.11c}$$

During the derivation, D2Q9 lattice model is used.

Solving equations (6.9a) – (6.9b) and equations (6.11a) – (6.11c), the final forms of the external forces can be represented as:

$$F_1 = w_\alpha \left(F_{10} + 3F_{11}e_{\alpha x} + 3F_{12}e_{\alpha y}\right) \tag{6.12a}$$

where $w_\alpha = 4/9$ for $\alpha = 0$, $w_\alpha = 1/9$ for $\alpha = 1,2,3,4$, $w_\alpha = 1/36$ for $\alpha = 5,6,7,8$.

$$F_{10} = -\frac{\rho u}{x}, \; F_{11} = \frac{\rho w^2}{x}, F_{12} = 0$$

$$F_2 = w_\alpha \left(F_{20} + 3F_{21}e_{\alpha x} + 3F_{22}e_{\alpha y}\right) \tag{6.12b}$$

where $F_{20} = \frac{1}{2x}\left[\partial_x(\rho u^2) + \partial_y(\rho uv) + \partial_x(p) + \partial_x(\rho w^2) - \frac{2\rho w^2}{x}\right]$,

$$F_{21} = -\frac{w}{x}\left[\partial_x(\rho uw) + \partial_y(\rho vw) + \frac{\rho uw}{x}\right] - \frac{1}{6x}\partial_x(\rho u) + \frac{\rho u}{6x^2}$$

$$F_{22} = -\frac{1}{6x}\partial_y(\rho u) + \frac{\upsilon}{x}\left[\partial_x(\rho v) - \partial_y(\rho u)\right]$$

By adding these force terms to the standard LBM, the governing equations (6.4a) – (6.4c), which are the same as equations (6.3a), (6.3b) and (6.3d) defined on the cylindrical coordinate system, can be correctly recovered by Chapman-Enskog expansion.

Note that the form of the source terms is not unique. During the above derivation, F_1 and F_2 are determined independently. The form of F_1 can be used explicitly to determine an appropriate form for F_2. It can be seen clearly that equations (6.5) and (6.12) have singularity at $x = 0$, which is the axisymmetric line for some problems. Fortunately, this difficulty can be easily overcome by implementing the axisymmetric boundary

condition at $x = 0$. In other words, equations (6.5) and (6.12) are only applied at position of $x \neq 0$.

Although the explicit inclusion of the gradients to the standard LBM undermines the simple formulation of the standard LBM, these terms are necessary to recover their target dynamics and the discretization scheme of these gradients has no effect on the stability of the scheme itself. We can just use the simple central difference scheme to do the numerical discretization.

The azimuthal velocity and temperature are obtained through the following equations by using the first order forward difference scheme in time and second order central difference scheme in space.

$$\frac{\partial w}{\partial t} + u \frac{\partial w}{\partial x} + v \frac{\partial w}{\partial y} + \frac{uw}{x} = \upsilon \left(\nabla^2 w + \frac{1}{x} \frac{\partial w}{\partial x} - \frac{w}{x^2} \right) \tag{6.13a}$$

$$\frac{\partial T}{\partial t} + u \frac{\partial T}{\partial x} + v \frac{\partial T}{\partial y} = \frac{k}{\rho c_p} \left(\nabla^2 T + \frac{1}{x} \frac{\partial T}{\partial x} \right) \tag{6.13b}$$

where $\nabla^2 = \dfrac{\partial^2}{\partial x^2} + \dfrac{\partial^2}{\partial y^2}$.

From the above derivation, it can be seen that after such transformation, the axisymmetric flow problem in the cylindrical coordinate system can be solved on the uniform rectangular two-dimensional grids, which adheres to the inherent property, i.e. lattice-uniformity, of LBM. The curved boundary can be well defined using the uniform rectangular grid. So there is no need to introduce FVLBM or TLLBM technique. At the same time, it also avoids the solution of the real three-dimensional problem in the Cartesian coordinate system for such quasi- three-dimensional flow problems.

6.3 Numerical simulations

In order to validate our new axisymmetric lattice Boltzmann model, we carried out the numerical simulations of two important axisymmetric flows. One is the mixed convection in the vertical concentric cylindrical annuli. In this case, all the boundaries are wall boundaries, so the implementation of boundary conditions is not too difficult. The other is the Wheeler's benchmark problem in Czochralski crystal growth. This case is more complex than the first case, since it has three different kinds of boundary conditions: the wall boundary condition, free surface and axisymmetric boundary conditions. So much attention has to be paid to the implementation of boundary conditions for this case.

The convergence criterion for all the cases studied in this chapter is set to

$$\max_{i,j} \left| \sqrt{(u_{i,j}^2 + v_{i,j}^2)^{n+1}} - \sqrt{(u_{i,j}^2 + v_{i,j}^2)^n} \right| \leq 10^{-8} \tag{6.14a}$$

and

$$\max_{i,j} \left| w_{i,j}^{n+1} - w_{i,j}^n \right| \leq 10^{-8}, \quad \max_{i,j} \left| T_{i,j}^{n+1} - T_{i,j}^n \right| \leq 10^{-8} \tag{6.14b}$$

where n and $n+1$ represent the old and new time levels, respectively.

6.3.1 Mixed convection in the vertical concentric cylindrical annuli

The classical hydrodynamic stability of Taylor vortex flows in rotating cylindrical annulus has received considerable attention. However, such kind of thermal rotating flow has not been thoroughly investigated. Improving the equipment design for the engineering applications requires closer examination of these combined thermally induced and rotationally induced flows.

The schematic diagram of the physical system studied is shown in Figure 6.1. The annular with height H is bounded by two stationary adiabatic horizontal plates. The gap width $D = r_o - r_i$ is the distance between the concentric cylinders. The inner cylinder of radius r_i is rotated and kept at a constant high temperature of T_H. The outer cylinder of radius r_o is stationary and maintained at the temperature of T_L, which is lower than that of the inner cylinder. When Prandtl number $\mathrm{Pr} = \upsilon/\chi$ is fixed at 0.7, this system is governed by the parameter $\sigma = Gr/(\mathrm{Re}^2)$ and two geometric parameters of the aspect ratio $A = H/D$ and radial ratio $\eta = r_o/r_i = x_o/x_i$. The Grashof and Reynolds numbers are defined as $Gr = (g\beta\Delta TD^3)/\upsilon^2$ and $\mathrm{Re} = (\Omega_i r_i D)/\upsilon = (\Omega_i x_i D)/\upsilon$ respectively. In the present study, A is chosen to be 10, η is 2 and σ is selected to be 0, 0.01 and 0.05, respectively, with respect to Re=100.

In addition to the flow fields and temperature distributions, the physical quantities of primary interest are the local Nusselt numbers at the inner and outer cylinders. They are defined as

$$Nu = -\left. r\frac{\partial T}{\partial r}\right|_{r=r_i,r_0} = -\left. x\frac{\partial T}{\partial x}\right|_{x=x_i,x_0} \tag{6.15}$$

The mean Nusselt number can be obtained by integrating the local Nusselt number along the vertical direction of the cylinders. It is defined as follows

$$\overline{Nu} = \frac{1}{A}\int_0^A Nu\,dy \tag{6.16}$$

6.3.1.1 Boundary conditions. The boundary conditions for the present system are as follows: on the inner cylinder $x = R = r_i = x_i$, $0 \le y \le A$: $T = 1$, $u = v = 0$, $w = \Omega x_i$; on the

outer cylinder $R = r_0 = x_0$, $0 \le y \le A$: $T = 0$, $u = v = 0$, $w = 0$; on the top and bottom

walls $y = 0, A$, $x_i \le x \le x_0$: $u = v = w = 0, \partial T/\partial y = 0$. The boundary conditions for u

and v are realized by the corresponding boundary conditions for the density distributions.

Since all the boundaries are wall boundaries, the bounce back condition for the non-

equilibrium distribution is used. The macroscopic boundary conditions for w and T are

used directly when we solve equations (6.13a) and (6.13b).

6.3.1.2 Results and discussions. In a mixed convection problem, the parameter σ is used

to measure the relative importance of the buoyancy force and the centrifugal force. In the

present study, three different values of σ were chosen. They were σ =0, 0.01 and 0.05

with respect to Re=100.

Table 6.1 shows the numerical results of the mean Nusselt number on the inner

cylinder at the condition σ =0, 0.01 and 0.05 respectively, using the present new scheme.

The grid size of 31×301 is used for all these cases. The benchmark data given by Ho and

Tu (1993) and Ball and Farouk (1987) are also included for comparison. From Table 6.1,

we can see that the calculated mean Nusselt number on the inner cylinder using our new

scheme for each case agrees very well with those computed by the conventional CFD

methods. It can also be seen that when σ is sufficiently small, the average Nusselt

number decreases with the increase of σ. This can be explained by the influence of the

presence of the buoyancy force. For the sake of the clarity in this discussion, a vortex will

be considered positive when its rotation is in the same direction as the natural convection

flow, i.e. when the flow immediately adjacent to the heated inner cylinder is in the upward

direction. The presence of the buoyancy force generates two effects on the rotationally

induced isothermal flow. Firstly, the centrifugal force becomes less pronounced than that for the isothermal flow at a constant Re since the fluid particles adjacent to the heated inner cylinder is lighter than the isothermal fluid. Secondly, the positive sense thermal circulation flow which is generated in a differentially heated cavity subsequently increases the intensity of the isothermal positive vortex cell and decreases the intensity of the isothermal negative vortex cell. Combining these two effects, the local heat transfer rates along the hot wall are reduced on the upper parts but enhanced on the lower parts. But the overall effect is the decrease with the increase of σ when σ is much less than 0.1.

Figure 6.2 shows the streamlines, vortices and isotherms at various σ. They have the same trend as those obtained by Ball & Farouk (1987). This figure describes how the buoyancy force influences the flow patterns and the isothermal contours. In this figure, vertical boundaries on the left and right hand sides represent the inner and outer cylinder walls of the annulus, respectively. For $\sigma=0$, there is no buoyancy force and it is a forced convection flow. Symmetric counter-rotating cells exist along the entire length of the annulus at $Re=100$. This Reynolds number is greater than the theoretical Re_{crit} of 63 at $\eta=2$ (Koschmieder, 1993). So this flow is characterized by the counter-rotating toroidal vortice (Taylor vortices). It is noted that for this case, five pairs of the counter-rotating cells are present, corresponding to a non-dimensional wave number $a=(\pi A)/\lambda=6.283$. This compares quite well with the value found for an infinitely long annulus of $a=6.4$. Each pair occupies the same volume. Heat transfer across the annular gap from the heated inner wall is accomplished by the centrifugally induced flow. When σ is increased to $\sigma=0.01$, the flow is still dominated by the centrifugal force and the buoyancy force has very little effect on the flow pattern. So the flow pattern and the average Nusselt number

are very similar to those at $\sigma = 0$. When σ is increased to 0.05, the influence of the buoyancy force is apparent in the flow configuration. The flow pattern changes from a five-pair to a four-pair Taylor cell state. Each pair still occupies the same volume. But in each pair, the positive cell is much larger. This is also due to the influence of the buoyancy force. The tendency of the warmer fluid particles adjacent to the heated inner cylinder to rise is sufficiently strong to overcome the regular spacing characteristic of the Taylor instability.

6.3.2 Wheeler's benchmark problem

For Wheeler's (1990) benchmark problem in Czochralski crystal growth, the combination of the natural convection due to thermal gradients between the crystal and crucible and the forced convection due to the rotations of the crystal and crucible makes this problem very complex in terms of the thermodynamics and hydrodynamics. Several numerical methods have been developed to simulate such crystal growth flow problems (Shu et al., 1997; Xu et al., 1997). They all solve the conventional NS equations. The discretization of the convection terms in NS equations is very important for the numerical simulation of such flow and it is common to choose the second order central difference scheme. However, with the increase of the heat conduction or rotations of the crystal and crucible, which is required in Czochralski growth technique in order to grow larger crystals with less imperfection, the convection terms in the governing equations become dominant. This makes the second-order central difference scheme be unsuitable due to the enhanced numerical instability. This problem has been reported by Xu et al. They found that the use of the central difference scheme failed to provide converged solution at high

Grashof and Reynolds numbers. In order to improve the stability condition, low-order upwind scheme has to be used, but its high numerical diffusive properties may give rise to less accurate solution. In view of the discretization problem for the convection terms in conventional methods, we use our new scheme to simulate such kind of crystal growth problem. The kinetic nature of LBM introduces some important features that distinguish it from other conventional numerical methods. One of these is that the convection operator of LBM in phase space is linear, so there is no need to do any discretization for this convection term. As a result, the above-mentioned difficulty can be avoided.

The implementation of boundary conditions is much more complicated than the above studied case. That is also the reason we choose this case so as to study how our new scheme can solve the complicated and practical axisymmetric thermal problems. We will give a detailed description on the implementation of boundary conditions in the following section.

6.3.2.1 Wheeler's benchmark problem. The configuration of the Wheeler's benchmark problem for Czochralski crystal growth is shown in Figure 6.3. It consists of a vertical cylindrical crucible of radius R_c filled with a melt to a height H and rotating with an angular velocity Ω_c. The melt is bounded above by a coaxial crystal of radius $R_x < R_c$ rotating with an angular velocity Ω_x. The system is normalized in the following way: the characteristic length is R_c; the characteristic velocity is $c = \delta x / \delta t$. The non-dimensional temperature is $T' = \dfrac{T - T_x}{T_c - T_x}$. The non-dimensional parameters for Reynolds numbers, Prandtl and Grashof numbers are defined respectively as

$$\mathrm{Re}_x = \frac{R_c{}^2 \Omega_x}{\upsilon}, \quad \mathrm{Re}_c = \frac{R_c^2 \Omega_c}{\upsilon}, \quad \mathrm{Pr} = \frac{\upsilon}{\chi}, \quad Gr = \frac{g\beta(T_c - T_x)R_c{}^3}{\upsilon^2} \qquad (6.17)$$

In the present study, Prandtl number is fixed at

$$\mathrm{Pr} = 0.05 \qquad (6.18)$$

The non-dimensional parameter τ in equation (6.5) is determined by its relationship with

the non-dimensional kinetic viscosity $\tau = (3\upsilon')/\delta t + 0.5$. When Reynolds number Re_x is

given non-zero, the non-dimensional kinetic viscosity is obtained by $\upsilon' = v_x/(\mathrm{Re}_x \beta)$;

when Gr is given, the non-dimensional kinetic viscosity is obtained by $\upsilon' = v_h/\sqrt{Gr}$. v_x

and $v_h = \sqrt{\beta g(T_c - T_x)R_c}$ are the non-dimensional velocity for the crystal at $x = R_x$ and

the non-dimensional characteristic velocity for the natural convection problem,

respectively. To ensure the code working properly in the near-incompressible regime, we

carefully choose the values of v_x and v_h. They are required to be less than 0.3. In the

present study, they are chosen to be 0.1 at low Reynolds or Grashof numbers and be 0.15

at high Reynolds or Grashof numbers.

6.3.2.2 Boundary conditions. The macroscopic boundary conditions defined in (r,z)

coordinate system for this flow problem are given by:

$$u = w = \frac{\partial v}{\partial r} = \frac{\partial T}{\partial r} = 0 \qquad\qquad \text{for } r = 0, \quad 0 \le z \le \alpha; \qquad (6.19a)$$

$$u = v = 0, \quad w = \Omega_c R_c, \quad T = T_c \qquad\qquad \text{for } r = 1, \quad 0 \le z \le \alpha; \qquad (6.19b)$$

$$u = v = \frac{\partial T}{\partial z} = 0, \quad w = r\Omega_c R_c \qquad\qquad \text{for } z = 0, \quad 0 \le r \le 1; \qquad (6.19c)$$

$$\frac{\partial u}{\partial z} = \frac{\partial w}{\partial z} = v = 0, \quad T = T_x + \frac{(r-\beta)}{(1-\beta)}(T_c - T_x) \qquad \text{for } z = \alpha, \quad \beta \leq r \leq 1; \qquad (6.19d)$$

$$u = v = 0, \quad T = T_x, \quad w = r\Omega_x R_x \qquad \text{for } z = \alpha, \quad 0 \leq r \leq \beta; \qquad (6.19e)$$

where $\alpha = \dfrac{H}{R_c} \quad \beta = \dfrac{R_x}{R_c}$.

In the present study, the aspect ratios are fixed at

$$\alpha = 1, \quad \beta = 0.4 \qquad (6.20)$$

When the boundary conditions for u, v are represented by the relationship between the density distributions, they are more complicated than the first case. There are three different kinds of boundary conditions in this flow: the axisymmetric boundary condition, the wall boundary condition and the free surface condition. For different boundary conditions, the unknown distributions have different relationships with the known distributions. The configuration of particle velocity directions at these boundaries is shown in Figure 6.4.

For $x = 0, \quad 0 \leq y \leq \alpha$, (in our defined coordinate system as shown in Section 6.2.2), this is the axisymmetric boundary condition and the specular reflection boundary condition is used. As shown in Figure 6.4, after the streaming process, the distributions at directions 2, 3, 4, 6, 7 are known which are determined by equation (6.5). The unknown distributions at directions 1, 5, 8 will be determined from the following specular reflection boundary conditions:

$$f_1 = f_3 \quad f_5 = f_6 \quad f_8 = f_7 \qquad (6.21a)$$

For $x = 1, \quad 0 \leq y \leq \alpha$, this is the wall boundary condition and the bounce back rule of the non-equilibrium distribution is used. As shown in Figure 6.4, after the

streaming process, the distributions at directions 1, 2, 4, 5, 8 are known and the unknown distributions at directions 3, 6, 7 can be determined from the following bounce back boundary conditions

$$f_3 = f_3^{eq} + f_1 - f_1^{eq} \quad f_6 = f_6^{eq} + f_8 - f_8^{eq} \quad f_7 = f_7^{eq} + f_5 - f_5^{eq} \tag{6.21b}$$

For $y = 0, \quad 0 \le x \le 1$, this is also the wall boundary and the bounce back rule of the non-equilibrium distribution is used. As shown in Figure 6.4, after the streaming process, the distributions at directions 1, 3, 4, 7, 8 are known and the unknown distributions at directions 2, 5, 6 can be determined from the following bounce back boundary conditions

$$f_2 = f_2^{eq} + f_4 - f_4^{eq} \quad f_5 = f_5^{eq} + f_7 - f_7^{eq} \quad f_6 = f_6^{eq} + f_8 - f_8^{eq} \tag{6.21c}$$

For $y = \alpha, \quad \beta \le x \le 1$, this is the free surface and the specular reflection boundary condition is used. As shown in Figure 6.4, after the streaming process, the distributions at directions 1, 2, 3, 5, 6 are known and the unknown distributions at directions 4, 7, 8 can be determined from the following specular reflection boundary conditions

$$f_4 = f_2 \quad f_7 = f_6 \quad f_8 = f_5 \tag{6.21d}$$

For $y = \alpha, \quad 0 \le x \le \beta$, we consider it as the wall boundary and the bounce back rule of the non-equilibrium distribution is used. As shown in Figure 6.4, after the streaming process, the distributions at directions 1, 2, 3, 5, 6 are known and the unknown distributions at directions 4, 7, 8 can be determined from the following bounce back boundary conditions

$$f_4 = f_4^{eq} + f_2 - f_2^{eq} \quad f_7 = f_7^{eq} + f_5 - f_5^{eq} \quad f_8 = f_8^{eq} + f_6 - f_6^{eq} \tag{6.21e}$$

The macroscopic boundary conditions for w, T are used directly when we solve equations (6.13a) and (6.13b).

6.3.2.3 Results and discussions. In this study, we firstly study how the forced convection and natural convection affect the flow fields differently. So we consider the following three cases $A1$, $B1$ and $C1$, which are defined as

$A1$: $\text{Re}_x = 100.$, $\text{Re}_c = 0.$, $Gr = 0.$

$B1$: $\text{Re}_x = 100.$, $\text{Re}_c = -25.0$, $Gr = 0.$

$C1$: $\text{Re}_x = 0.$, $\text{Re}_c = 0.$, $Gr = 10^5.$

Case $A1$ and $B1$ are forced convection problems caused by different mechanisms. The flow in Case $A1$ is driven by the rotation of the crystal, while the flow in Case $B1$ is generated by the opposite rotations of the crystal and crucible. Case $C1$ is a natural convection problem. The mesh size used for these three cases is 101×101.

Table 6.2 shows the computed minimum and maximum stream functions for these three cases using our new axisymmetric lattice Boltzmann model. The benchmark results using DQ method are also included for comparison. The stream function is computed through

$$\frac{\partial \psi}{\partial x} = -xv, \quad \frac{\partial \psi}{\partial y} = xu \tag{6.22}$$

From Table 6.2, we can see that the maximum absolute value of the stream function for each case agrees very well with that computed by DQ method, and the maximum difference is within 3%. There are some deviations between the computed minimum absolute values of the stream functions and the benchmark results. These deviations can be considered to be negligible since the minimum absolute values are very small.

The streamlines and isotherms for Cases $A1$, $B1$ and $C1$ are shown in Figure 6.5 to Figure 6.7. They have the same trend as those obtained by Shu et al. (1997) using DQ

method. Although the streamlines are quite different for Cases $A1$ and $B1$, the contours of the temperature are very similar. This indicates the similarity of the temperature fields for the forced convection problems. On the contrary, the temperature field for Case $C1$ is quite different from Cases $A1$ and $B1$, and this shows the effect of the buoyancy force on the temperature field.

Since the natural convection has been well studied, while the forced convections are drawn less attention as compared with the natural convection, we put the emphasis on the forced convection in the following study. We studied the influence of the rotations of the crystal and crucible on the forced convection problems. Two more cases which have different rotation velocities are studied. They are defined as

$A2$: $\mathrm{Re}_x = 1000., \mathrm{Re}_c = 0., Gr = 0.$

$B2$: $\mathrm{Re}_x = 1000., \mathrm{Re}_c = -250., Gr = 0.$

The mesh size used for these two cases is 201×201.

Table 6.3 shows the computed minimum and maximum stream functions at different rotations. The benchmark results using Quick scheme (Xu et al., 1997) are also included for validation. From Table 6.3, we can see that the maximum absolute value of the stream function for each case agrees very well with the benchmark result. For Case $A2$, it can be seen from Table 6.3 that the absolute value of the stream function increases with the increase of the rotation velocity, which means that the intensity of the vortex increases. The maximum absolute stream function increases from 0.221 to 5.0575 when the rotation velocity increases from 10^2 to 10^3. The streamlines and temperature contours for Case $A2$ are similar to Case $A1$, which will not be repeated. The only difference for the streamlines is that the center of the vortex induced by the rotation moves towards the sidewall of the

crucible and is deformed increasingly. The highest velocity region moves from the upper left corner to the upper right corner. This shows that with the increase of the rotation velocity, the crystals with better quality can be produced. For Case $B2$, it can be seen from Table 6.3 that the absolute value of the stream function also increases with the increase of the rotation velocities for both the crystal and crucible. The streamlines and temperature contours are also similar to Case $B1$. It can be seen from the streamlines shown in Figure 6.6 that there are two vortices with opposite directions appearing in the upper left corner just under the crystal and the lower right corner. This means that the rotations of both the crystal and crucible cannot produce the crystals with good qualities. With the increase of the rotational speeds for both the crystal and crucible, the upper left vortex will move to the right corner, and the lower vortex will move to the left and dominate the flow field.

6.4 Conclusions

In this chapter, a new axisymmetric lattice Boltzmann model was proposed in order to solve an important kind of quasi- three-dimensional flow problems. Its applications to simulate the flows in the mixed convection in vertical concentric cylindrical annuli and Czochralski crystal growth demonstrated that our new scheme could solve the axisymmetric thermal problems accurately and effectively. The numerical results compared well with the benchmark data. It is worth to mention that our new scheme can solve the axisymmetric thermal flow problems on uniform rectangular two-dimensional grids in the cylindrical coordinate system, avoiding the solution of the real three-dimensional problems on Cartesian coordinate system if the standard LBM is used. So the quasi- three-dimensional property of this kind of flows is kept. In the following chapters,

we will conduct real three-dimensional studies for practical three-dimensional thermal applications.

Table 6.1 Mean Nusselt number on the inner cylinder at various σ with respect to $Re=100$ for the mixed convection in vertical concentric cylindrical annuli

σ	$\overline{Nu}$ (Present)	$\overline{Nu}$ (Ho and Tu)	$\overline{Nu}$ (Ball and Farouk)
0	1.996	2.010	1.991
0.01	1.995	1.997	1.976
0.05	1.906	1.909	1.910

Table 6.2 Comparison of the computed minimum and maximum stream functions with the benchmark results for the Wheeler's benchmark problem

Case	Gr	Re_x	Re_c	ψ_{min} (Present)	ψ_{max} (Present)	ψ_{min} (Shu et al.)	ψ_{max} (Shu et al.)
A1	0.	10^2	0.	-0.221	5.46×10^{-6}	-0.222	5.46×10^{-6}
B1	0.	10^2	-25.	-5.14×10^{-2}	0.114	-6.81×10^{-2}	0.117
C1	10^5	0.	0.	-5.18×10^{-3}	29.884	-7.50×10^{-3}	28.316

Table 6.3 Comparison of the computed minimum and maximum stream functions with the benchmark results for the Wheeler's benchmark problem

Case	Gr	Re_x	Re_c	ψ_{min} (Present)	ψ_{max} (Present)	ψ_{min} (Xu et al.)	ψ_{max} (Xu et al.)
A1	0.	10^2	0.	-0.221	5.46×10^{-6}	-0.217	4.06×10^{-6}
A2	0.	10^3	0.	-5.075	1.06×10^{-4}	-4.994	1.83×10^{-5}
B1	0.	10^2	-25.	-5.14×10^{-2}	0.114	-4.43×10^{-2}	0.117
B2	0.	10^3	-250.	-1.478	1.114	-1.478	1.148
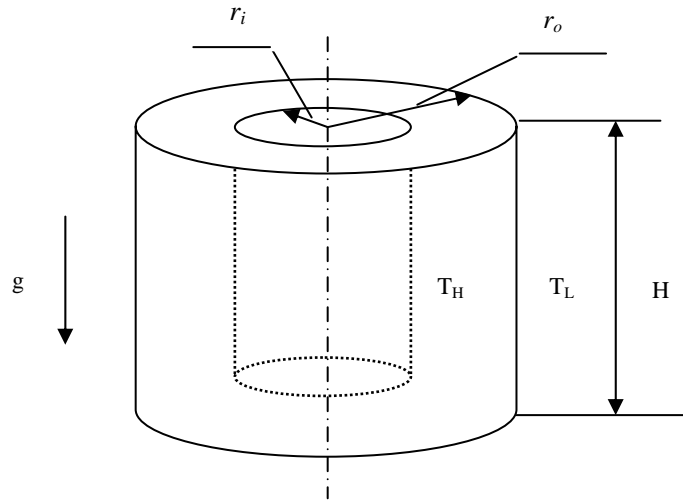
Figure 6.1 Schematic diagram of the physical system for the mixed convection in vertical concentric cylindrical annuli

$\sigma =0$ $\sigma =0.01$
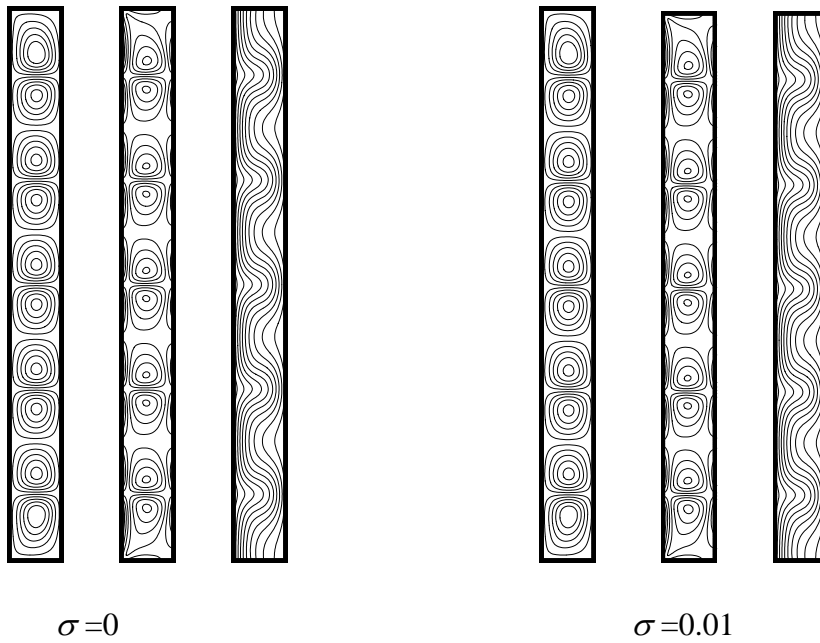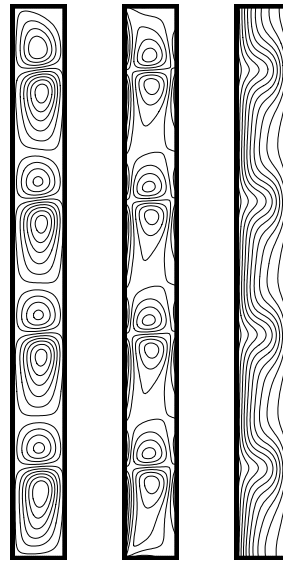
$\sigma = 0.05$

Figure 6.2 Streamlines, vortices and isotherms at various σ with respect to $Re=100$ for the mixed convection in vertical concentric cylindrical annuli
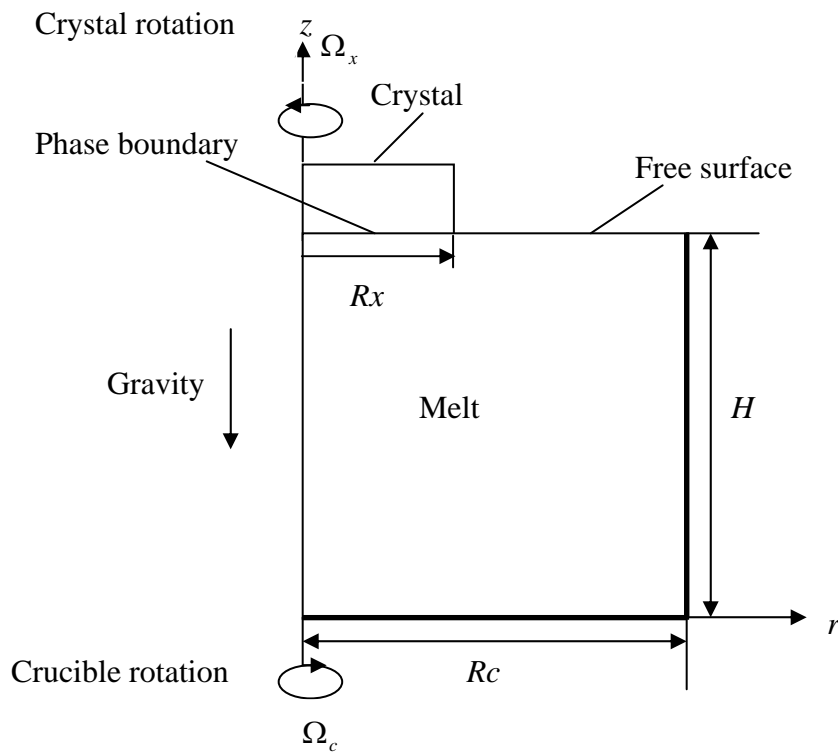
Figure 6.3 Configuration of Wheeler's benchmark problem in Czochralski crystal growth
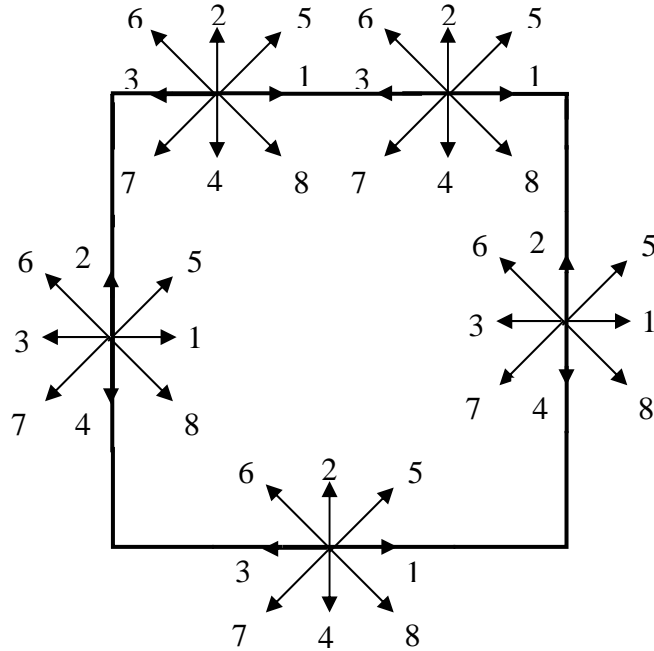
Figure 6.4 Schematic plot of particle velocity directions at boundaries for Wheeler's benchmark problem in Czochralski crystal growth
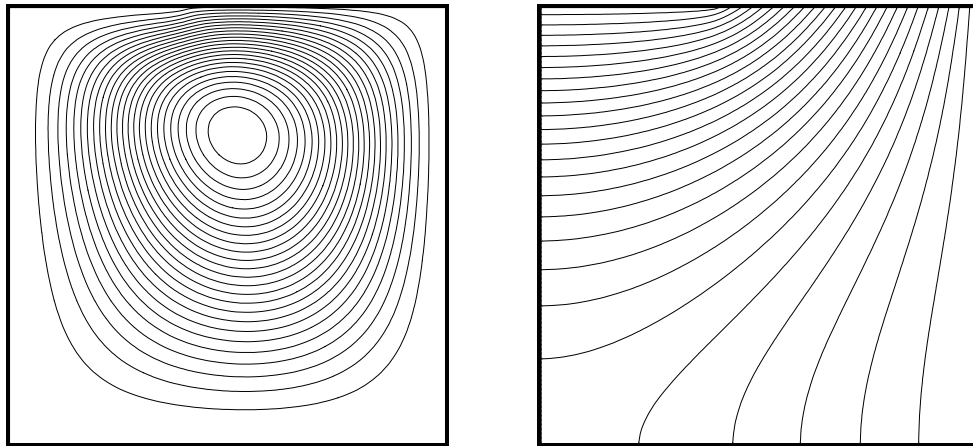
Figure 6.5 Streamlines (left) and temperature contours (right) for the Wheeler's benchmark problem at $\mathrm{Re}_x = 100$
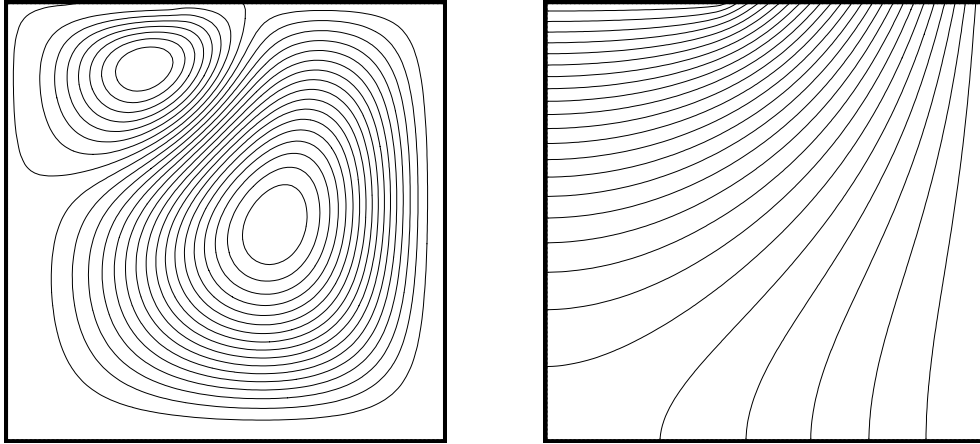
Figure 6.6 Streamlines (left) and temperature contours (right) for the Wheeler's benchmark problem at $\mathrm{Re}_x = 100, \quad \mathrm{Re}_c = -25.0$
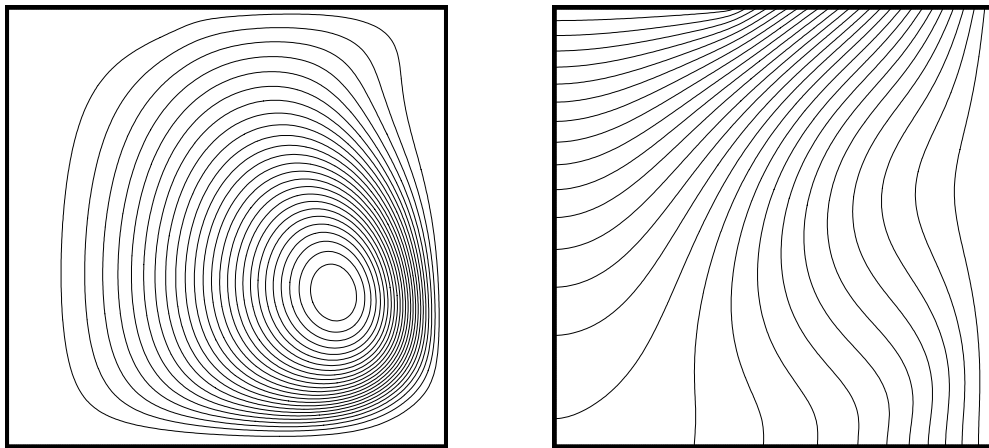
Figure 6.7 Streamlines (left) and temperature contours (right) for the Wheeler's benchmark problem at $Gr = 10^5$

Chapter 7

Simplified thermal LBM for two-dimensional

incompressible thermal flows

7.1 Introduction

Before we develop a new internal energy density distribution function (IEDDF) thermal model for real three-dimensional thermal applications, we re-studied this two-dimensional thermal model. Although the previous work has shown that the IEDDF thermal model is a stable and effective model and has been successfully used to solve some real two-dimensional thermal problems with complex geometries, there still exists some space for improvement for this thermal model when it is used for incompressible flows. On one hand, there is one complicated term which contains the gradient operator in the evolution equation for the internal energy density distribution, so the simplicity property of LBM has been lost. On the other hand, since the viscosity is involved not only in the momentum equation but also in the energy equation, the second-order integration of the governing equations for both the density distribution and internal energy density distribution is needed in order to keep the viscosity consistent in all the governing equations. To avoid the implicitness of such integration, the new variables for the density distribution and internal energy density distribution are introduced. Then the governing equations are transformed to the more complicated form whose variables are the new density distribution and internal energy density distribution. By doing this, another new complication arises. Since the simple bounce-back boundary condition for the non-

Materials in this chapter have been publishes in

Peng, Y., C. Shu and Y. T. Chew. Physical Review E 68, pp. 026701. 2003.

165

equilibrium distribution is the relationship for the old density distributions, such relationship becomes very complicated after changing it to the new formula whose variables are the new density distributions. But we have to do it, since the evolution equations are for the new density distributions. This again leads to another loss of one good feature for LBM that boundary condition can be easily implemented. The detailed explanations on these drawbacks will be shown in the following section.

When it is used for the incompressible thermal flows, the above shortcomings can be overcome by our proposed simplified IEDDF thermal model. This simplified thermal model is based on the assumption that in real incompressible thermal applications, the compression work done by pressure and the viscous heat dissipation can be neglected. Our study (to be shown later) found that the complicated gradient term in the original IEDDF thermal model is mainly used to recover the compression work done by pressure and viscous heat dissipation. So this term is intentionally omitted by us. After this simplification, there is no viscous term in the evolution equation for the internal energy density distribution. The requirement for the viscosity consistency vanishes, so there is no need to do the second-order integration for both governing equations for two density distributions so as to keep the viscosity the same. Besides, there is also no need to introduce the new density distributions. As a result, the above mentioned two shortcomings of the original IEDDF can be overcome.

This simplified IEDDF thermal model is validated by the numerical simulation of the natural convection in a square cavity at a wide range of Rayleigh numbers. Its improvement in the efficiency to obtain the same accurate results is demonstrated by its comparison with the original IEDDF thermal model. Its compressibility is also studied by

its comparison with another new model which uses the incompressible LBGK model proposed by Guo et al. (2000) in this simplified IEDDF thermal model.

This chapter is organized as follows: we will firstly give the detailed explanation on our simplified IEDDF thermal model, in which its accuracy in space has also been studied. Then we will use the benchmark results to validate this new thermal model. In order to study the compressibility property of this thermal model, we will introduce the incompressible isothermal LBGK model proposed by Guo et al. in our simplified IEDDF thermal model. Finally, we will draw some conclusions.

7.2 Simplified IEDDF thermal model

7.2.1 Original IEDDF thermal model

The governing equations for the density distribution and internal energy density distribution in the original IEDDF thermal model are:

$$\partial_t f + (\boldsymbol{e} \cdot \nabla) f = -\frac{f - f^{eq}}{\tau_v} + F \tag{7.1}$$

$$\partial_t g + (\boldsymbol{e} \cdot \nabla) g = -\frac{g - g^{eq}}{\tau_c} - f(\boldsymbol{e} - \boldsymbol{u}) \cdot [\partial_t \boldsymbol{u} + (\boldsymbol{e} \cdot \nabla)\boldsymbol{u}] \tag{7.2}$$

where $F = \dfrac{\boldsymbol{G} \cdot (\boldsymbol{e} - \boldsymbol{u})}{RT} f^{eq}$ and $\boldsymbol{G}$ is the external force acting on the unit mass. It can be seen from equation (7.2) that there exists a complicated gradient term $f(\boldsymbol{e} - \boldsymbol{u}) \cdot [\partial_t \boldsymbol{u} + (\boldsymbol{e} \cdot \nabla)\boldsymbol{u}]$. We have to deal with it properly. So the simplicity property of LBM has partially been lost.

For the isothermal LBM, the evolution equation for the density distribution is the first-order integration of equation (7.1), which is

$$f_\alpha(\boldsymbol{x}+\boldsymbol{e}_\alpha\delta t, t+\delta t)-f_\alpha(\boldsymbol{x},t)=-\frac{1}{\tau_v}\left[f_\alpha(\boldsymbol{x},t)-f_\alpha^{eq}(\boldsymbol{x},t)\right]+\delta t F \tag{7.3}$$

This introduces a second-order truncation error and this truncation error is fortunately nondestructive because it can be totally absorbed into the physical viscous term. The only effect is the change of the viscosity from $\upsilon=\tau_v c_s^2\delta t$ to $\upsilon=(\tau_v-1/2)c_s^2\delta t$. However, for the thermal LBM, the first-order integration of both equations (7.1) and (7.2) will cause some problem, because the density distribution exists in both equations. During the Chapman-Enskog multiscale expansions, the non-equilibrium part of the density distribution, which comes from the first-order Chapman-Enskog approximation and has nothing to do with the second-order Chapman-Enskog approximation, is used by the gradient term in equation (7.2) in order to recover the viscous heat dissipation term in the macroscopic energy equation. This means that the viscosity in the viscous heat dissipation term should be $\upsilon=\tau_v c_s^2\delta t$, which is inconsistent with the viscosity $\upsilon=(\tau_v-0.5)c_s^2\delta t$ if the first-order integration of equation (7.1) is used. To eliminate this inconsistency, the second-order integration for the above two equations (7.1) and (7.2) has to be adopted. At the same time, in order to keep the scheme to be explicit, two new variables $\overline{f}$, $\overline{g}$ for the density distribution and internal energy density distribution are introduced, which have the following relationships with the old variables f, g :

$$\overline{f}_\alpha=f_\alpha+\frac{\delta t}{2\tau_v}\left(f_\alpha-f_\alpha^{eq}\right)-\frac{\delta t}{2}F_\alpha \tag{7.4}$$

$$\overline{g}_\alpha=g_\alpha+\frac{\delta t}{2\tau_c}\left(g_\alpha-g_\alpha^{eq}\right)+\frac{\delta t}{2}f_\alpha q_\alpha \tag{7.5}$$

where $q_\alpha=(\boldsymbol{e}_\alpha-\boldsymbol{u})\cdot\left[\frac{1}{\rho}(-\nabla p+\nabla\cdot\Pi)+(\boldsymbol{e}_\alpha-\boldsymbol{u})\cdot\nabla\boldsymbol{u}\right]$

The integrated equations for the new variables are:

$$\overline{f}_\alpha(x + e_\alpha \delta t, t + \delta t) - \overline{f}_\alpha(x,t) = -\frac{\delta t}{\tau_v + 0.5\delta t}\left[\overline{f}_\alpha(x,t) - f_\alpha^{eq}(x,t)\right] + \frac{\tau_v F_\alpha \delta t}{\tau_v + 0.5\delta t} \qquad (7.6)$$

$$\overline{g}_\alpha(x + e_\alpha \delta t, t + \delta t) - \overline{g}_\alpha(x,t) = -\frac{\delta t}{\tau_c + 0.5\delta t}\left[\overline{g}_\alpha(x,t) - g_\alpha^{eq}(x,t)\right] - \frac{\tau_c f_\alpha(x,t)q_\alpha \delta t}{\tau_c + 0.5\delta t} \qquad (7.7)$$

It is worth to mention that the old density distribution is again used for the expression of

$\overline{g}_\alpha$ and happens in the term $\dfrac{\tau_c f_\alpha(x,t)q_\alpha \delta t}{\tau_c + 0.5\delta t}$ in equation (7.7).

The bounce-back rule of the non-equilibrium distribution proposed by Zou and He (1997) is used for the wall boundary condition. The density distribution at the wall boundary should satisfy the following condition:

$$f_\alpha^{neq} = f_\beta^{neq} \qquad (7.8)$$

where e_α and e_β have the opposite directions. The internal energy density distribution at the wall boundary satisfies:

$$g_\alpha^{neq} - e_\alpha^2 f_\alpha^{neq} = -\left(g_\beta^{neq} - e_\beta^2 f_\beta^{neq}\right) \qquad (7.9)$$

It should be emphasized that the old variables, density distribution f and internal energy density distribution g, are used in the boundary conditions (7.8) and (7.9), while the governing equations (7.6) and (7.7) are for the new variables, $\overline{f}, \overline{g}$. So two sets of the variables are used and transformation between the old and new variables is needed for every time step. As a result, the extra computational effort is introduced.

7.2.2 Simplified IEDDF thermal model

We can see from the above section that the second-order integration and the introduction of the new variables are due to the requirement that the viscosity in two governing equations for the density distribution and internal energy density distribution should be consistent. It is well accepted that for incompressible flows, the viscous heat dissipation term in macroscopic energy equation can be neglected. The omission of the viscous heat dissipation term and compression work term done by pressure in the macroscopic energy equation will be reflected by dropping out the gradient term in the evolution equation for the internal energy density distribution, since such gradient term is mainly used to recover these terms in the macroscopic energy equation through Chapman-Enskog expansion. So based on this, the simplified IEDDF thermal model is proposed.

The governing equations for the density distribution and internal energy density distribution are:

$$f_\alpha(\boldsymbol{x}+\boldsymbol{e}_\alpha\delta t,t+\delta t)-f_\alpha(\boldsymbol{x},t)=-\frac{1}{\tau_v}\Big[f_\alpha(\boldsymbol{x},t)-f_\alpha^{eq}(\boldsymbol{x},t)\Big]+\delta t F \tag{7.10}$$

$$g_\alpha(\boldsymbol{x}+\boldsymbol{e}_\alpha\delta t,t+\delta t)-g_\alpha(\boldsymbol{x},t)=-\frac{1}{\tau_c}\Big[g_\alpha(\boldsymbol{x},t)-g_\alpha^{eq}(\boldsymbol{x},t)\Big] \tag{7.11}$$

D2Q9 lattice model is used here as an example.

Chapman-Enskog expansion for the density distribution can recover the continuity and NS equations. The detailed derivation of this is given by Hou et al. (1995a) and will not be shown here. The viscosity is determined by:

$$\upsilon=\left(\tau_v-\frac{1}{2}\right)c_s^2\delta t \tag{7.12}$$

It can be shown in the following that the macroscopic energy equation for the incompressible flows can be derived from the evolution equation (7.11) for the internal energy density distribution by Chapman-Enskog expansion following the same procedure as Hou et al. (1995a).

Taylor series expansion of equation (7.11) to $O(\delta t^3)$ results in

$$\delta t(\partial_t + \boldsymbol{e}\cdot\nabla)g_\alpha + \frac{\delta t^2}{2}[\partial_t + \boldsymbol{e}\cdot\nabla]^2 g_\alpha + O(\delta t^3) = -\frac{1}{\tau_c}(g_\alpha - g_\alpha^{(0)})$$
(7.13)

where g_α^{eq} is represented as $g_\alpha^{(0)}$.

Expanding g_α about $g_\alpha^{(0)}$, we can get:

$$g_\alpha = g_\alpha^{(0)} + \delta t g_\alpha^{(1)} + \delta t^2 g_\alpha^{(2)} + O(\delta t^3)$$
(7.14)

The first order expansion of equation (7.13) is

$$(\partial_{t0} + \boldsymbol{e}\cdot\nabla)g_\alpha^{(0)} = -\frac{1}{\tau_c}g_\alpha^{(1)}$$
(7.15)

The second order expansion of equation (7.13) is

$$\partial_{t1}g_\alpha^{(0)} + \left(1 - \frac{1}{2\tau_c}\right)(\partial_{t0} + \boldsymbol{e}\cdot\nabla)g_\alpha^{(1)} = -\frac{1}{\tau_c}g_\alpha^{(2)}$$
(7.16)

Taking the summation of equations (7.15) and (7.16), we can get

$$\partial_{t0}(\rho\varepsilon) + \nabla\cdot(\rho\boldsymbol{u}\varepsilon) = 0$$
(7.17)

$$\partial_{t1}(\rho\varepsilon) + \left(1 - \frac{1}{2\tau_c}\right)\Pi^{(1)} = 0$$
(7.18)

where $\Pi^{(1)} = \sum_\alpha (\partial_{t0} + \boldsymbol{e}\cdot\nabla)g_\alpha^{(1)}$ and it is $\Pi^{(1)} = -\tau_c\frac{2}{3}\nabla^2(\rho\varepsilon)$ after neglecting the $O(u^2\delta T)$ terms.

Combining equations (7.17) and (7.18), we can get

$$\partial_t(\rho\varepsilon) + \nabla\cdot(\rho\boldsymbol{u}\varepsilon) = \chi\nabla^2(\rho\varepsilon) \tag{7.19}$$

The thermal diffusivity χ is determined by

$$\chi = \frac{2}{3}\left(\tau_c - \frac{1}{2}\right)c^2\delta t. \tag{7.20}$$

From the above derivations, we can see that the evolution equations (7.10) and (7.11) for the density distribution and internal energy density distribution can recover the macroscopic continuity, momentum equations and energy equation for the incompressible flows through Chapman-Enskog expansion.

When solving the incompressible thermal flows, this simplified IEDDF thermal model has the following good features as compared with the original IEDDF thermal model. Firstly, it does not include any complex gradient term in the evolution equation for the internal energy density distribution and keeps the same simple form as for the isothermal LBM. Secondly, it does not need the second-order integration and the introduction of the new variables. This simplifies the calculation process. Thirdly, although the same bounce-back rule of the non-equilibrium distribution is used for the wall boundary condition for both the simplified IEDDF thermal model and the original IEDDF thermal model, it is easier for the simplified IEDDF thermal model to implement, since for the simplified IEDDF thermal model, the variables for both the evolution equations and the boundary conditions are consistent. It should be pointed out that although this model can be thought of as a passive scalar thermal model, its starting point and derivation procedure are quite different.

7.2.3 Accuracy of the simplified IEDDF thermal model in space

Before we use the benchmark results to validate our simplified IEDDF thermal model, we need to study its accuracy in space. We take the porous plate problem as a test case for this study since it has the analytical solution. This problem has been well studied by Guo et al. in 2002. It is a channel flow where the upper cool plate moves with a constant velocity. A constant normal flow of the same fluid is injected through the bottom warm plate and withdrawn at the same rate from the upper plate. The analytical solution of the velocity distribution along the cross section of the channel in the steady state is given by

$$u = u_0 \left(\frac{e^{(\mathrm{Re}\, y/L)} - 1}{e^{\mathrm{Re}} - 1} \right) \tag{7.21}$$

where u_0 is the velocity of the upper plate; Re is Reynolds number based on the inject velocity v_0 and the channel width L. The temperature profile in the steady state satisfies

$$T = T_0 + \Delta T \left(\frac{e^{(\mathrm{Pr}\cdot\mathrm{Re}\, y/L)} - 1}{e^{\mathrm{Pr}\cdot\mathrm{Re}} - 1} \right) \tag{7.22}$$

where $\Delta T = T_1 - T_0$ is the temperature difference between the hot bottom plate with temperature T_1 and the cool upper wall with temperature T_0. Another two dimensionless parameters are $\mathrm{Pr} = \upsilon/\chi$ and $Ra = \left(g\beta\Delta T L^3 \right)/(\upsilon\chi)$.

Simulations were carried out to evaluate the numerical accuracy of this model in space. In the simulations, Prandtl number is set to be 0.71; Reynolds number is $\mathrm{Re} = 10$ and Rayleigh number is $Ra = 100$. The lattice spacing Δx varies from 1/30 to 1/100. The relative global error for the temperature field is measured, which is defined by

$$E = \frac{\sqrt{\sum_{i,j} \left| T_{i,j} - T_{a\,i,j} \right|^2}}{\sqrt{\sum_{i,j} \left| T_{a\,i,j} \right|^2}} \qquad\qquad (7.23)$$

where the summation is over the entire field and T_a is the analytical solution.

Suppose that the order of the accuracy in space for the model is n. Then we have the following relationship:

$$E = C(\Delta x)^n \qquad\qquad (7.24)$$

where C is a constant. Equation (7.24) can also be written as

$$\log(E) = \log(C) + n\log(\Delta x) \qquad\qquad (7.25)$$

Clearly, $\log(E)$ has a linear relationship with $\log(\Delta x)$. This is confirmed by Figure 7.1, which shows $\log(E)$ versus $\log(\Delta x)$. The fitting curve is a straight line whose slope is n. From Figure 7.1, we obtain $n \approx 2$. This implies that the present model is of second order in space. The velocity and temperature profiles for this case are shown in Figure 7.2. They agree very well with the analytical solutions.

7.3 Results and discussions

In order to validate our simplified IEDDF thermal model, we carried out the computation for a sample problem. The problem considered is a natural convection in a two-dimensional square cavity. It is the same test case that we used to validate the new thermal models that apply FVLBM or TLLBM techniques in the IEDDF thermal model in earlier chapters.

As we know, the dynamical similarity of this problem depends on two dimensionless parameters: Prandtl number Pr and Rayleigh number Ra. The kinetic

viscosity and thermal diffusivity are determined by these two dimensionless numbers. Then by using equations (7.12) and (7.20), the two relaxation times τ_υ and τ_c are determined, respectively.

Nusselt number Nu is one of the most important dimensionless parameters in describing the convective heat transport. Its average in the whole flow domain is used as one of the validation criteria.

7.3.1 Implementation of boundary conditions at four corners

The bounce-back rule of the non-equilibrium distribution is used here. However, for some special particle directions at four corner points, the different treatment has to be used. The schematic plot of particle velocity directions for the nine-speed model at four corner points is shown in Figure 7.3.

Seen from Figure 7.3, at the particle directions 6 and 8 for the left bottom and right upper corner points, the particle directions 5 and 7 for the left upper and right bottom corner points, their values for the density distribution and internal energy density distribution cannot be determined from their evolution equations or the bounce-back boundary conditions. Since these values do not transport any information into the interior points, the equilibrium functions are given for the two density distributions at these special directions.

7.3.2 Validation of the simplified IEDDF thermal model

The uniform grid is used for all the following numerical simulations and the calculations are done on PC PIV-1.6G. The convergence criterion for all the cases is set to

$$\max_{i,j}\left|\sqrt{(u_{i,j}^2+v_{i,j}^2)^{n+1}}-\sqrt{(u_{i,j}^2+v_{i,j}^2)^{n}}\right|\le 10^{-8}, \max_{i,j}\left|T_{i,j}^{n+1}-T_{i,j}^{n}\right|\le 10^{-8} \tag{7.26}$$

where n and $n+1$ represent the old and new time levels, respectively. This convergence criterion is the same as that we used for the calculations of the same sample problem using the original IEDDF thermal model in Chapter 3.

Numerical simulations of this natural convection problem at a wide range of Rayleigh numbers were carried out. Table 7.1 shows the numerical results of the maximum horizontal velocity $u_{\max}$ on the vertical mid-plane of the cavity and its location y, the maximum vertical velocity $v_{\max}$ on the horizontal mid-plane of the cavity and its location x, and the average Nusselt number throughout the cavity $\overline{Nu}$. The numerical results of a NS solver given by Shu and Xue (1998) using DQ method are also included for comparison.

The grid independence property of the original IEDDF thermal model for this natural convection at a wide range of Rayleigh numbers has been examined in Chapter 3. The grid sizes of 101×101 for $Ra=10^3$, 151×151 for $Ra=10^4$, 201×201 for $Ra=10^5$ and 251×251 for $Ra=10^6$ are found to be large enough to obtain the sufficiently accurate results at each Rayleigh number for engineering purpose. So the calculations using our simplified IEDDF thermal model at each Rayleigh number are done on those grids. From Table 7.1, we can see that the numerical results using the simplified IEDDF thermal model generally agree well with the benchmark results of Shu and Xue (1998) at a wide range of Rayleigh numbers. The deviation of the two results at a high Rayleigh number is larger than that at low Rayleigh numbers, but these deviations are quite acceptable. So we can say that the results using the present method are very accurate. This means that the

simplified IEDDF thermal model can be used to solve the incompressible thermal problems accurately and effectively.

From this table, it is also found that Nusselt number obtained using the present method is slightly smaller than that obtained by the NS solver, which agrees well with the phenomenon observed in Chapter 3.

7.3.3 Comparison of the simplified IEDDF thermal model with the original IEDDF thermal model

In order to compare the accuracy and efficiency of the simplified IEDDF thermal model with the original IEDDF thermal model, the numerical simulations at the same Rayleigh number using both the simplified IEDDF thermal model and the original IEDDF thermal model were carried out. Table 7.2 shows these comparisons at Rayleigh numbers of 10^3, 10^4, 10^5 and 10^6.

It can be observed from Table 7.2 that, at the same Rayleigh number and when the same grid size is used, the calculated results using the simplified IEDDF thermal model are almost the same as those using the original IEDDF thermal model. This demonstrates that the compression work done by pressure and the viscous heat dissipation term can be neglected for such an incompressible flow, which leads to the applicability of the omission of the gradient term in the original evolution equation for the internal energy density distribution. So we can say that the simplified IEDDF thermal model can produce the same accurate results as the original IEDDF thermal model.

As far as the computational efficiency is concerned, for the same grid size and Rayleigh number, the calculation time using the simplified IEDDF thermal model is much

less than that using the original IEDDF thermal model. All the calculations are done on Pentium IV-1.6GHz. From Table 7.2, we can see that for $Ra=10^3$, the calculation time using the simplified IEDDF thermal model is 1386.0s, while the original IEDDF thermal model takes 2297.0s to obtain the same converged solution. Similarly, for $Ra=10^4 - 10^6$, only half or even less than half of the calculation time is needed for the simplified IEDDF thermal model to obtain the converged solution as compared with the original IEDDF thermal model at each Rayleigh number using the same grid size. This shows that our simplified IEDDF thermal model is more efficient than the original IEDDF thermal model to get the same accurate results.

7.4 Incompressible isothermal LBGK model and its use in the simplified IEDDF thermal model

In order to study the compressibility property of this new scheme, we introduce an incompressible isothermal LBGK model proposed by Guo et al. (2000) to modify the evolution equation for the density distribution in our simplified IEDDF thermal model.

7.4.1 Incompressible isothermal LBGK model

The common LBGK model cannot recover the incompressible NS equations directly, while the incompressible isothermal LBGK model can exactly recover the incompressible NS equations within the small Mach number limit.

Take the discrete particle velocity model D2Q9 as an example. A new type of the distribution $h_\alpha(x,t)$ is introduced with the equilibrium distribution function $h_\alpha^{eq}(x,t)$ defined by:

$$h_\alpha^{eq} = \begin{cases} -4\sigma p + s_0(\boldsymbol{u}) & \alpha = 0 \\ \lambda p + s_\alpha(\boldsymbol{u}) & \alpha = 1,2,3,4 \\ \gamma p + s_\alpha(\boldsymbol{u}) & \alpha = 5,6,7,8 \end{cases} \qquad (7.27)$$

where $s_\alpha(\boldsymbol{u}) = w_\alpha \left[\dfrac{3\boldsymbol{e}_\alpha \cdot \boldsymbol{u}}{c^2} + \dfrac{9(\boldsymbol{e}_\alpha \cdot \boldsymbol{u})^2}{2c^4} - \dfrac{3\boldsymbol{u}^2}{2c^2} \right]$

The parameters σ, λ, γ should satisfy

$$\lambda + \gamma = \sigma \qquad (7.28)$$

$$\lambda + 2\gamma = \frac{1}{2} \qquad (7.29)$$

The distribution $h_\alpha(x,t)$ satisfies the following conservation laws:

$$\sum_{\alpha=0}^{8} h_\alpha = \sum_{\alpha=0}^{8} h_\alpha^{eq} \qquad (7.30)$$

$$\sum_{\alpha=0}^{8} h_\alpha e_\alpha = \sum_{\alpha=0}^{8} h_\alpha^{eq} e_\alpha \qquad (7.31)$$

The evolution equation for this new distribution is the same as the commonly used LBGK equation:

$$h_\alpha(\boldsymbol{x} + \boldsymbol{e}_\alpha \delta t, t + \delta t) - h_\alpha(\boldsymbol{x},t) = -\frac{1}{\tau_v}\left[h_\alpha(\boldsymbol{x},t) - h_\alpha^{eq}(\boldsymbol{x},t) \right] \qquad (7.32)$$

The macroscopic velocity and pressure for the flows are given by

$$\boldsymbol{u} = \sum_{\alpha=1}^{8} \boldsymbol{e}_\alpha f_\alpha \qquad (7.33)$$

$$p = \frac{1}{4\sigma}\left[\sum_{\alpha=1}^{8} f_\alpha + s_0(\boldsymbol{u}) \right] \qquad (7.34)$$

Through the multiscale expansion, the incompressible NS equations can be derived from this incompressible LBGK model as

$$\nabla \cdot \boldsymbol{u} = 0 \tag{7.35}$$

$$\frac{\partial \boldsymbol{u}}{\partial t} + \nabla \cdot (\boldsymbol{uu}) = -\nabla p + \upsilon \nabla^2 \boldsymbol{u} \tag{7.36}$$

where the kinematic viscosity is determined by

$$\upsilon = \frac{(\tau - 1/2)}{3} c^2 \delta t \tag{7.37}$$

which has the same form as the commonly used LBGK model.

This incompressible LBGK model completely eliminates the compressibility effect that lies in the existing LBGK models and can be used for both steady and unsteady flows. We will use it in our simplified IEDDF thermal model.

7.4.2 Its application in the simplified IEDDF thermal model

When the incompressible isothermal LBGK model is used in the simplified IEDDF thermal model, the two distributions are changed into: the new distribution denoted by h_α and the internal energy density distribution. The new distribution is used to calculate the flow velocity and pressure; the internal energy density distribution is used to calculate the flow temperature. The coupling between these two distributions is established by the Boussinesq approximation. That is adding the following force term

$$F_\alpha = -\frac{1}{2c} (\delta_{\alpha 2} + \delta_{\alpha 4}) \boldsymbol{e}_\alpha \cdot \boldsymbol{g} \beta (T - T_m) \tag{7.38}$$

to the right-hand side of the evolution equation for the new distribution (7.32). Then the governing equations for these two distributions become:

$$h_\alpha (\boldsymbol{x} + \boldsymbol{e}_\alpha \delta t, t + \delta t) - h_\alpha (\boldsymbol{x}, t) = -\frac{1}{\tau_v} [h_\alpha (\boldsymbol{x}, t) - h_\alpha^{eq} (\boldsymbol{x}, t)] + \delta t \, F_\alpha \tag{7.39}$$

$$g_\alpha\left(\boldsymbol{x}+\boldsymbol{e}_\alpha\delta t,t+\delta t\right)-g_\alpha\left(\boldsymbol{x},t\right)=-\frac{1}{\tau_c}\left[g_\alpha\left(\boldsymbol{x},t\right)-g_\alpha^{eq}\left(\boldsymbol{x},t\right)\right] \tag{7.40}$$

In the simulations, the parameters in the incompressible LBGK model are taken as:

$$\sigma=5/12, \quad \lambda=1/3, \quad \gamma=1/12$$

The bounce-back rule of the non-equilibrium distribution cannot be used since the density distribution does not exist any more. So the extrapolation rule for the velocity and temperature boundary conditions proposed by Guo et al. (2002) is used here. It has the second-order accuracy and good numerical stability. The basic idea of the extrapolation method is very similar to the bounce-back rule of the non-equilibrium distribution. It decomposes the distribution h_α and g_α at the boundary node $\boldsymbol{x}_b$ into their equilibrium and non-equilibrium parts:

$$h_\alpha\left(\boldsymbol{x}_b,t\right)=h_\alpha^{eq}\left(\boldsymbol{x}_b,t\right)+h_\alpha^{neq}\left(\boldsymbol{x}_b,t\right) \tag{7.41}$$

$$g_\alpha\left(\boldsymbol{x}_b,t\right)=g_\alpha^{eq}\left(\boldsymbol{x}_b,t\right)+g_\alpha^{neq}\left(\boldsymbol{x}_b,t\right) \tag{7.42}$$

The non-equilibrium parts represent the deviations from the equilibrium distribution functions, which should be much smaller than the equilibrium distribution functions. So it is reasonable to assume that $h_\alpha^{neq}=\delta t\, h_\alpha^{(1)}$ and $g_\alpha^{neq}=\delta t\, g_\alpha^{(1)}$. Thus,

$$h_\alpha^{neq}\left(\boldsymbol{x}_b,t\right)=h_\alpha^{neq}\left(\boldsymbol{x}_f,t\right)+\mathrm{O}\!\left(\delta t^2\right)=h_\alpha\left(\boldsymbol{x}_f,t\right)-h_\alpha^{eq}\left(\boldsymbol{x}_f,t\right)+\mathrm{O}\!\left(\delta t^2\right) \tag{7.43}$$

$$g_\alpha^{neq}\left(\boldsymbol{x}_b,t\right)=g_\alpha^{neq}\left(\boldsymbol{x}_f,t\right)+\mathrm{O}\!\left(\delta t^2\right)=g_\alpha\left(\boldsymbol{x}_f,t\right)-g_\alpha^{eq}\left(\boldsymbol{x}_f,t\right)+\mathrm{O}\!\left(\delta t^2\right) \tag{7.44}$$

where $\boldsymbol{x}_f$ is the nearest neighbor node of $\boldsymbol{x}_b$ in the fluid.

For the velocity boundary condition, the velocity $\boldsymbol{u}\!\left(\boldsymbol{x}_b,t\right)$ is known and pressure $p\!\left(\boldsymbol{x}_b,t\right)$ is unknown, so the equilibrium part $h_\alpha^{eq}\!\left(\boldsymbol{x}_b,t\right)$ is approximated with a modified equilibrium distribution functions defined by

$$\overline{h_{\alpha}^{eq}}(\boldsymbol{x}_b,t) = \begin{cases} -4\sigma\, p(\boldsymbol{x}_f,t) + s_0\big(\boldsymbol{u}(\boldsymbol{x}_b,t)\big) & \alpha = 0 \\ \lambda\, p(\boldsymbol{x}_f,t) + s_{\alpha}\big(\boldsymbol{u}(\boldsymbol{x}_b,t)\big) & \alpha = 1,2,3,4 \\ \gamma\, p(\boldsymbol{x}_f,t) + s_{\alpha}\big(\boldsymbol{u}(x_b,t)\big) & \alpha = 5,6,7,8 \end{cases} \tag{7.45}$$

Note that in the incompressible flows the fluctuation of pressure δp is of the order M^2, so $p(\boldsymbol{x}_b,t) = p(\boldsymbol{x}_f,t) + \mathrm{O}(\delta t\, M^2)$. As a result, the distribution $h_{\alpha}(x_b,t)$ at the boundary node $\boldsymbol{x}_b$ is calculated as

$$h_{\alpha}(\boldsymbol{x}_b,t) = \overline{h_{\alpha}^{eq}}(\boldsymbol{x}_b,t) + h_{\alpha}(\boldsymbol{x}_f,t) - h_{\alpha}^{eq}(\boldsymbol{x}_f,t) \tag{7.46}$$

to the accuracy of $\mathrm{O}(\delta t^2 + \delta t M^2)$.

The thermal boundary condition can be implemented in a similar way. If the temperature at the boundary node $\boldsymbol{x}_b$ is known, the internal energy density distribution is given by

$$g_{\alpha}(\boldsymbol{x}_b,t) = g_{\alpha}^{eq}(\boldsymbol{x}_b,t) + g_{\alpha}(\boldsymbol{x}_f,t) - g_{\alpha}^{eq}(\boldsymbol{x}_f,t) \tag{7.47}$$

If the temperature gradient is known at the boundary node $\boldsymbol{x}_b$, we can use the conventional second-order finite difference to approximate the temperature on the wall from the temperature gradient, and then equation (7.47) can be used.

7.4.3 Compressibility study of the modified simplified IEDDF thermal model

Since we use the incompressible isothermal LBGK in our simplified IEDDF thermal model, Chapman-Enskog expansion of the new evolution equation governing the flow velocity and pressure will recover the incompressible continuity and NS equations exactly. In order to examine the effect of compressibility in our simplified IEDDF thermal

model, we compare the numerical results of the natural convection in a square cavity at a wide range of Rayleigh numbers using the above modified, simplified IEDDF thermal model with those using the simplified IEDDF thermal model without introducing the incompressible LBGK model. Table 7.3 shows the numerical results of the maximum horizontal velocity u_{max} on the vertical mid-plane of the cavity and its location y, the maximum vertical velocity v_{max} on the horizontal mid-plane of the cavity and its location x, and the average Nusselt number throughout the cavity $\overline{Nu}$ using the simplified IEDDF thermal model with and without introducing the incompressible LBGK model. The numerical results of a NS solver given by Shu and Xue (1998) using DQ method are also included as the benchmark data.

From Table 7.3, we can see that the difference between the results with and without incompressible LBGK model in the simplified IEDDF thermal model is very small. The results of the velocities using the incompressible LBGK model agree a little bit better with the benchmark results than those without using the incompressible LBGK model. The higher the Rayleigh number, the better the improvement. For example, for $Ra=10^4$, the result of the maximum horizontal velocity on the vertical mid-plane of the cavity is 16.134 without using the incompressible LBGK model and 16.146 using the incompressible LBGK model, while the benchmark result is 16.190. This shows that there is a little bit improvement for the maximum horizontal velocity on the vertical mid-plane if using the incompressible LBGK model. At high Rayleigh number of 10^6, the maximum horizontal velocity on the vertical mid-plane of the cavity changes from 63.024 without using the incompressible LBGK model to 63.671 using the incompressible LBGK model, while the benchmark result is 64.775. The improvement is more obvious than that at low

Rayleigh number of 10^4. The same trend is observed in the maximum vertical velocity on the horizontal mid-plane of the cavity. There is no much change in the average Nusselt number. This is agreeable with the physical meaning of the incompressible LBGK model. Since the use of the incompressible LBGK model is only for the new evolution equation, which is used to calculate the pressure and velocity, the improvement for the velocities is obvious. However, for the internal energy density distribution, we use the same governing equation. During the implementation, we still need to introduce the assumption that the characteristic velocity $\sqrt{\beta g \Delta T H}$ is within the incompressible limit. So there should be no much difference for the result of Nusselt number using or without using the incompressible LBGK model in the simplified IEDDF thermal model. To sum up, this study shows that compressibility effect of this simplified IEDDF thermal model is very small by itself. Thus the model can be used to solve incompressible thermal flows without introducing any incompressible LBGK model.

7.5 Conclusions

A simplified IEDDF thermal model for the incompressible thermal flows is proposed in this chapter. The simplification for the original IEDDF thermal model is based on the physical background that the compression work done by pressure and the viscous heat dissipation can be ignored for the incompressible flows. This new scheme has the following good features. It does not include any gradient term in the evolution equations and keeps the simplicity of LBM. It is easier to implement as compared with the original IEDDF thermal model. The numerical results of the natural convection in a square cavity at a wide range of Rayleigh numbers show that this simplified IEDDF thermal

model can produce the same accurate results more efficiently as compared with the original IEDDF thermal model. The compressibility effect is also studied in this scheme and the results show that it can be neglected. It is worthwhile to mention that although all the calculations using this simplified IEDDF thermal model are done on the uniform grids, its extension to the arbitrary grids is straightforward by using TLLBM. The use of TLLBM in the thermal model has been thoroughly studied in Chapter 5.

It has to be pointed out that although the starting point and motivation of our new simplified IEDDF thermal model are quite different from the thermal model proposed by Guo (2002), they have some similarity. Our model is one special case within the category of his thermal model.

In the following chapter, the study of real three-dimensional thermal applications using the IEDDF thermal model will be based on this simplified IEDDF thermal model.

Table 7.1 Comparison of the numerical results using the simplified IEDDF thermal model with those using a NS solver for the natural convection in a square cavity

Ra	10^3		10^4		10^5		10^6	
Method	Present	DQ	Present	DQ	Present	DQ	Present	DQ
Grid size	101×101	-	151×151	-	201×201	-	251×251	-
u_{max}	3.644	3.649	16.134	16.190	34.261	34.736	63.024	64.775
y	0.810	0.815	0.820	0.825	0.855	0.855	0.848	0.850
v_{max}	3.691	3.698	19.552	19.638	67.799	68.640	215.26	220.64
x	0.180	0.180	0.120	0.120	0.065	0.065	0.040	0.035
$\overline{Nu}$	1.117	1.118	2.241	2.245	4.511	4.523	8.731	8.762

Table 7.2 Comparison of the numerical results between the simplified and original IEDDF thermal models for the natural convection in a square cavity

Ra		10^3	10^4	10^5	10^6
Grid		101×101	151×151	201×201	251×251
u_{max}	Simplified	3.644	16.134	34.261	63.024
	Original	3.649	16.156	34.245	63.527
y	Simplified	0.810	0.820	0.855	0.848
	Original	0.810	0.820	0.855	0.844
v_{max}	Simplified	3.691	19.552	67.799	215.26
	Original	3.700	19.679	68.276	218.47
x	Simplified	0.180	0.120	0.065	0.040
	Original	0.180	0.120	0.065	0.040
$\overline{Nu}$	Simplified	1.117	2.241	4.511	8.731
	Original	1.117	2.244	4.520	8.781
CPU(s)	Simplified	1386.0	7010.7	35666.0	98617.3
	Original	2297.0	17864.7	96296.6	171659.3

Table 7.3 Comparison of the numerical results using the simplified IEDDF thermal model
with and without introducing the incompressible LBGK model for the natural convection
in a square cavity

Ra		10^3	10^4	10^5	10^6
Grid		101×101	151×151	201×201	251×251
u_{max}	using	3.650	16.146	34.315	63.671
	without	3.644	16.134	34.261	63.024
	DQ	3.649	16.190	34.736	64.775
y	using	0.810	0.820	0.855	0.852
	without	0.810	0.820	0.855	0.848
	DQ	0.815	0.825	0.855	0.850
v_{max}	using	3.704	19.593	68.012	217.57
	without	3.691	19.552	67.799	215.26
	DQ	3.698	19.638	68.640	220.64
x	using	0.180	0.120	0.065	0.040
	without	0.180	0.120	0.065	0.040
	DQ	0.180	0.120	0.065	0.035
$\overline{Nu}$	using	1.117	2.241	4.508	8.737
	without	1.117	2.241	4.511	8.731
	DQ	1.118	2.245	4.523	8.762
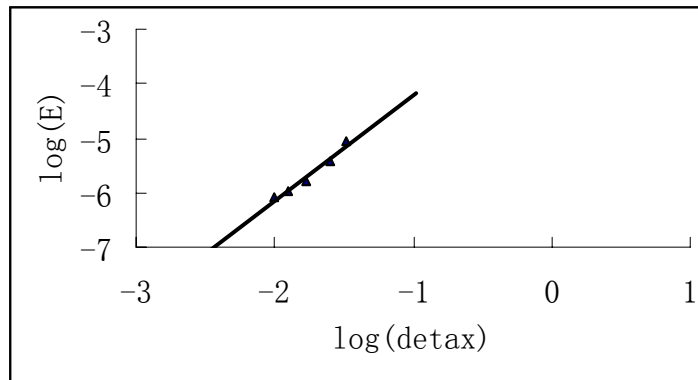
Figure 7.1 Relative global error versus lattice spacing for the porous plate flow
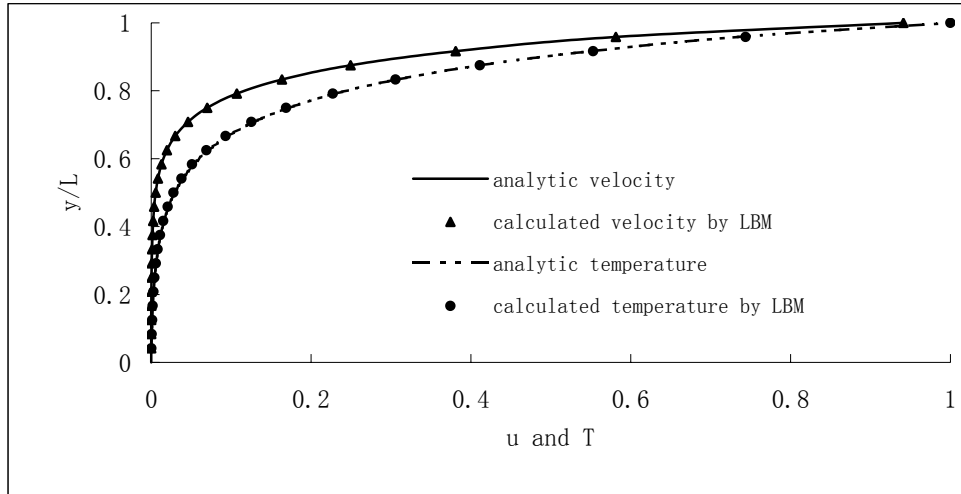
Figure 7.2 Velocity and temperature profiles for the porous plate flow
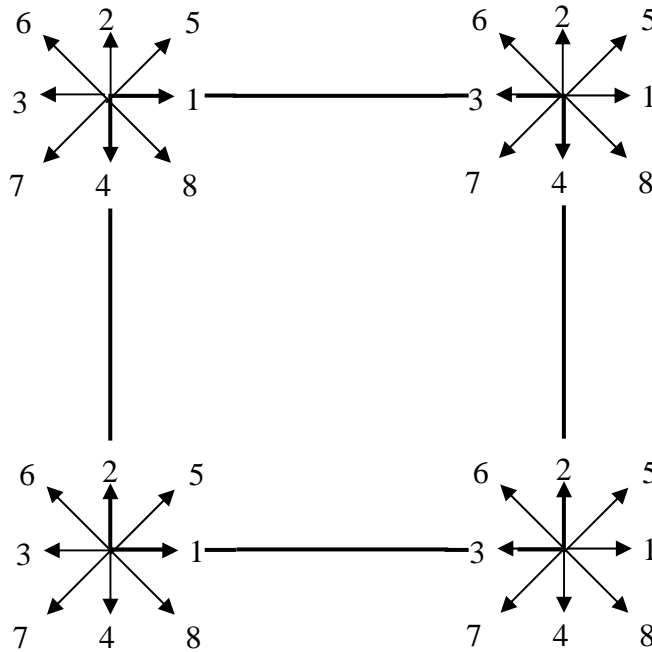
Figure 7.3 Schematic plot of particle velocity directions at four corner points for the natural convection in a square cavity

Chapter 8

A three-dimensional thermal LBM and its applications

8.1 Introduction

In order to develop LBM to become an alternative method to solve fluid dynamics problems and be comparable to the conventional NS solvers, it is necessary to extend its use in three dimensions, especially in three-dimensional thermal applications. From the literature review, we know that there are many thermal models proposed in recent years to solve the thermal flows using LBM. However, most of the applications of these thermal models are limited to two dimensions with some shortcomings that have been addressed in previous chapters. Though Rayleigh-Benard convection in two dimensions and three dimensions has been successfully simulated by Shan (1997) using the passive-scalar method to a certain degree, it may not be a real thermal problem. Because on one hand, only the periodic and Dirichlet boundary conditions are considered; and on the other hand, these applications are limited to using uniform grids. For real engineering thermal applications, they usually contain the solid boundaries and Neumann boundary conditions are often presented in flow configurations. For example, the natural convection flow analysis in the enclosures has many thermal engineering applications, such as cooling of the electronic devices, energy storage systems and compartment fires. In order to solve these real three-dimensional thermal problems for the engineering purpose, a three-dimensional thermal model is proposed in this chapter. It is based on the idea of the two-dimensional simplified IEDDF thermal model presented in the last chapter. It uses two

distributions to model the flow and thermal fields, respectively. The density distribution $f_\alpha(x,t)$ is used to simulate the macroscopic density and velocity fields, and the internal energy density distribution $g_\alpha(x,t)$ is used to simulate the macroscopic temperature field. The derivation procedure will be shown in the following section.

The particle velocity models used in our three dimensional thermal LBM are D3Q15 and D3Q19, which are commonly used for the isothermal flows. Usually we have to use more particle velocities for thermal models when compared with isothermal models. However based on the research work of He et al. (1998b), we know that for the two distribution thermal model, the zeroth- through the second- order moment of the equilibrium internal energy density distribution function involves only the zeroth- through the fifth- order moment as $\int \zeta^m \exp\left(-\zeta^2\right) d\zeta = \sum_\alpha w_\alpha \zeta_\alpha^m$, which has the same requirements as for isothermal models. So the D3Q15 and D3Q19 lattices can still be used here. The detailed explanation for this will be given in the following section. It is worthwhile to mention that there are also some other particle velocity models for other thermal models. For example, Qian (1993) presented D3Q21 and D3Q25 in his new lattice BGK models, in which a proper internal energy is introduced. Chen (1994) proposed D3Q40 for the thermal model using the idea of no nonlinear deviation multi-speed models. Pavlo et al. (1998a) proposed D3Q41 and D3Q53 for the thermal applications using higher order symmetric and no space filling velocity lattice models. Most of these thermal models have not been applied to real thermal applications. Our D3Q15 and D3Q19 models are simpler than these models. There is no additional particle velocity introduced as compared with the isothermal particle velocity models.

In this chapter, firstly, we will introduce our new three-dimensional IEDDF thermal model. Then we will use the numerical simulation of the three-dimensional natural convection in an air-filled cubical enclosure, which is heated differentially at two vertical side walls, to validate this three-dimensional thermal model. Thirdly, we will compare the numerical results using two different particle velocity models, D3Q15 and D3Q19, in order to examine the properties of these two particle velocity models and their effects for the thermal applications. Fourthly, in order to include the effects of the viscous heat dissipation and compression work done by pressure, the extensional form of our three-dimensional thermal LBM will be given. The same case is used to validate this extension. Lastly, we will draw some conclusions.

8.2 New three-dimensional thermal LBM

Since this new model is based on the two-dimensional simplified IEDDF thermal model, it contains two similar density distributions: the density distribution and internal energy density distribution.

8.2.1 Three-dimensional thermal LBM on uniform grids

The governing equations for the two density distributions are:

$$f_\alpha(\boldsymbol{x} + \boldsymbol{e}_\alpha \delta t, t + \delta t) - f_\alpha(\boldsymbol{x}, t) = -\frac{1}{\tau_v}\left[f_\alpha(\boldsymbol{x}, t) - f_\alpha^{eq}(\boldsymbol{x}, t)\right] + \delta t F_\alpha \tag{8.1}$$

$$g_\alpha(\boldsymbol{x} + \boldsymbol{e}_\alpha \delta t, t + \delta t) - g_\alpha(\boldsymbol{x}, t) = -\frac{1}{\tau_c}\left[g_\alpha(\boldsymbol{x}, t) - g_\alpha^{eq}(\boldsymbol{x}, t)\right] \tag{8.2}$$

where F_α is an external force term.

For the density distribution, D3Q15 and D3Q19 are usually used. The configurations for these two particle velocity models and their corresponding equilibrium distribution functions for the density distribution have been shown in Chapter 2. The viscosity in both models is related to the relaxation time through the same equation of $\upsilon = (2\tau_v - 1)/6$.

Similarly, for the internal energy density distribution, the particle velocity space must be discretized appropriately. If we can use the same discrete particle velocities for both density distributions, it will be more computationally efficient. To check whether this is possible, the continuous equilibrium distribution function for the internal energy density distribution is expanded up to $\boldsymbol{u}^2$

$$
\begin{aligned}
g^{eq} = {} & \frac{\rho\varepsilon}{(2\pi RT)^{D/2}} \exp\left(-\frac{\boldsymbol{e}^2}{2RT}\right)\left[\frac{\boldsymbol{e}^2}{DRT} + \left(\frac{\boldsymbol{e}^2}{DRT} - \frac{2}{D}\right)\frac{(\boldsymbol{e}\cdot\boldsymbol{u})}{RT} + \frac{(\boldsymbol{e}\cdot\boldsymbol{u})^2}{2(RT)^2} - \frac{\boldsymbol{u}^2}{2RT}\right] \\
& + \frac{\rho\varepsilon}{(2\pi RT)^{D/2}} \exp\left(-\frac{\boldsymbol{e}^2}{2RT}\right)\left[\left(\frac{\boldsymbol{e}^2}{DRT} - \frac{D+4}{D}\right)\frac{(\boldsymbol{e}\cdot\boldsymbol{u})^2}{2(RT)^2} - \left(\frac{\boldsymbol{e}^2}{DRT} - \frac{D+2}{D}\right)\frac{\boldsymbol{u}^2}{2RT}\right]
\end{aligned}
\tag{8.3}
$$

During the Chapman-Enskog expansion, we have to compute the zeroth- through second-order moment of equation (8.3). It involves zeroth- through sixth- order moment of $\int \zeta^m \exp(-\zeta^2) d\zeta = \sum_{\alpha} w_{\alpha}\zeta_{\alpha}^m$. Therefore, higher-order quadrature is usually necessary for the thermal LBM, which means that more particle velocities are needed. However, based on the discovery that the zeroth- through second- order moment of the second term in equation (8.3) vanishes, this term can be consequently eliminated from equation (8.3) without affecting the recovery of the macroscopic energy equation from the evolution equation of the internal energy density distribution. The zeroth- through second- order moment of the remaining part of the equilibrium internal energy density distribution function involves only zeroth- through fifth- order moment of $\int \zeta^m \exp(-\zeta^2) d\zeta$

$= \sum\limits_{\alpha} w_{\alpha} \zeta_{\alpha}^{m}$. Therefore the third-order Gauss-Hermite quadrature is still valid for this

thermal model as in the isothermal models. So we can choose the same lattice models for

the internal energy density distribution as those used for the isothermal flows, which are

D3Q15 and D3Q19.

After the second term of equation (8.3) is eliminated, the continuous equilibrium

internal energy density distribution function has similar form as the continuous

equilibrium density distribution function:

$$f^{eq} = \frac{\rho}{(2\pi RT)^{D/2}} \exp\left(-\frac{e^2}{2RT}\right)\left[1 + \frac{(e \cdot u)}{3RT} + \frac{(e \cdot u)^2}{(3RT)^2} - \frac{u^2}{3RT}\right] \tag{8.4}$$

except that the coefficient for each term is not the same. So the discrete equilibrium

internal energy density distribution functions can be obtained easily by comparing the

coefficient for each term with the discrete equilibrium density distribution functions. For

the particle velocity model of D3Q15, the equilibrium internal energy density distribution

functions are derived as:

$$g_0^{eq} = -\frac{\rho\varepsilon}{3}\frac{u^2}{c^2} \tag{8.5a}$$

$$g_{1-6}^{eq} = \frac{\rho\varepsilon}{9}\left[1 + \frac{e_{\alpha} \cdot u}{c^2} + \frac{9}{2}\frac{(e_{\alpha} \cdot u)^2}{c^4} - \frac{3}{2}\frac{u^2}{c^2}\right] \tag{8.5b}$$

$$g_{7-14}^{eq} = \frac{\rho\varepsilon}{72}\left[3 + 7\frac{e_{\alpha} \cdot u}{c^2} + \frac{9}{2}\frac{(e_{\alpha} \cdot u)^2}{c^4} - \frac{3}{2}\frac{u^2}{c^2}\right] \tag{8.5c}$$

For the particle velocity model of D3Q19, the equilibrium internal energy density

distribution functions are obtained as:

$$g_0^{eq} = -\frac{\rho\varepsilon}{2}\frac{u^2}{c^2} \tag{8.6a}$$

$$g_{1-6}^{eq} = \frac{\rho\varepsilon}{18}\left[1 + \frac{\boldsymbol{e}_\alpha \cdot \boldsymbol{u}}{c^2} + \frac{9}{2}\frac{(\boldsymbol{e}_\alpha \cdot \boldsymbol{u})^2}{c^4} - \frac{3}{2}\frac{\boldsymbol{u}^2}{c^2}\right] \tag{8.6b}$$

$$g_{7-18}^{eq} = \frac{\rho\varepsilon}{36}\left[2 + 4\frac{\boldsymbol{e}_\alpha \cdot \boldsymbol{u}}{c^2} + \frac{9}{2}\frac{(\boldsymbol{e}_\alpha \cdot \boldsymbol{u})^2}{c^4} - \frac{3}{2}\frac{\boldsymbol{u}^2}{c^2}\right] \tag{8.6c}$$

The internal energy is related to the temperature by $\varepsilon = 3RT/2$, where R is the gas constant.

Then the macroscopic density, velocity and temperature are calculated by

$$\rho = \sum_\alpha f_\alpha \tag{8.7a}$$

$$\rho\boldsymbol{u} = \sum_\alpha \boldsymbol{e}_\alpha f_\alpha \tag{8.7b}$$

$$\rho(3RT/2) = \sum_\alpha g_\alpha \tag{8.7c}$$

The Chapman-Enskog expansion for the density distribution can recover the continuity and NS equations. The detailed derivation of this is given by Hou et al. (1995a) and will not be repeated here. Following the same procedure as Hou et al., it can be seen that the macroscopic energy equation for the incompressible flows can be derived from the evolution equation for the internal energy density distribution by Chapman-Enskog expansion. Taylor series expansion for equation (8.2) to $\mathrm{O}(\delta t^3)$ results in

$$\delta t(\partial_t + \boldsymbol{e} \cdot \nabla)g_\alpha + \frac{\delta t^2}{2}[\partial_t + \boldsymbol{e} \cdot \nabla]^2 g_\alpha + \mathrm{O}(\delta t^3) = -\frac{1}{\tau_c}\left(g_\alpha - g_\alpha^{(0)}\right) \tag{8.8}$$

where g_α^{eq} is represented as $g_\alpha^{(0)}$.

Expanding g_α about $g_\alpha^{(0)}$, we can get:

$$g_\alpha = g_\alpha^{(0)} + \delta t g_\alpha^{(1)} + \delta t^2 g_\alpha^{(2)} + \mathrm{O}(\delta t^3) \tag{8.9}$$

The first order expansion of equation (8.8) is

$$\left(\partial_{t0} + \boldsymbol{e} \cdot \nabla\right)g_{\alpha}^{(0)} = -\frac{1}{\tau_c}g_{\alpha}^{(1)} \tag{8.10}$$

The second order expansion of equation (8.8) is

$$\partial_{t1}g_{\alpha}^{(0)} + \left(1 - \frac{1}{2\tau_c}\right)\left(\partial_{t0} + \boldsymbol{e} \cdot \nabla\right)g_{\alpha}^{(1)} = -\frac{1}{\tau_c}g_{\alpha}^{(2)} \tag{8.11}$$

Taking the summation of equations (8.10) and (8.11), and using the equilibrium internal energy density distribution functions (equation (8.5) for D3Q15 and equation (8.6) for D3Q19), we can get

$$\partial_{t0}(\rho\varepsilon) + \nabla \cdot (\rho\boldsymbol{u}\varepsilon) = 0 \tag{8.12}$$

$$\partial_{t1}(\rho\varepsilon) + \left(1 - \frac{1}{2\tau_c}\right)\Pi^{(1)} = 0 \tag{8.13}$$

where $\Pi^{(1)} = \sum_{\alpha}\left(\partial_{t0} + \boldsymbol{e} \cdot \nabla\right)g_{\alpha}^{(1)}$ and it is $\Pi^{(1)} = -\tau_c\frac{5}{9}\nabla^2(\rho\varepsilon)$ after neglecting the

$O\left(u^2\delta T\right)$ terms.

Combining equations (8.12) and (8.13), we can get

$$\partial_t(\rho\varepsilon) + \nabla \cdot (\rho\boldsymbol{u}\varepsilon) = \chi\nabla^2(\rho\varepsilon) \tag{8.14}$$

The diffusivity χ for both particle velocity models is determined by

$$\chi = \frac{5}{9}\left(\tau_c - \frac{1}{2}\right). \tag{8.15}$$

From the above derivations, we can see that the evolution equations (8.1) and (8.2) can recover the macroscopic incompressible continuity, NS equations and energy equation through Chapman-Enskog expansion.

8.2.2 Its use on the arbitrary grids

The governing equations (8.1) and (8.2) for the three-dimensional thermal applications are derived in the above section and they can be easily used on the uniform grids. When these two equations are used on the arbitrary grids, $(x + e_{\alpha x}\delta t, y + e_{\alpha y}\delta t, z + e_{\alpha z}\delta t)$ is usually not at the grid point $(x + \delta x, y + \delta y, z + \delta z)$. So the TLLBM technique has to be applied to these two equations. Following the same procedure as shown in Chapter 5, the density distribution f and internal energy density distribution g at each grid point are updated by:

$$\overline{f_\alpha}(x_0, y_0, z_0, t + \delta t) = W_1 = \sum_{k=1}^{M_1+1} a_{1,k} \overline{f'_{k-1}} \qquad (8.16a)$$

$$\overline{g_\alpha}(x_0, y_0, z_0, t + \delta t) = W'_1 = \sum_{k=1}^{M_2+1} a'_{1,k} \overline{g'_{k-1}} \qquad (8.16b)$$

where

$$\overline{f'_k} = \left(1 - \frac{1}{\tau_v}\right) f_\alpha(x_k, y_k, z_k, t) + \frac{1}{\tau_v} f_\alpha^{eq}(x_k, y_k, z_k, t) + F_\alpha \delta t \qquad (8.17a)$$

$$\overline{g'_k} = \left(1 - \frac{1}{\tau_c}\right) g_\alpha(x_k, y_k, z_k, t) + \frac{1}{\tau_c} g_\alpha^{eq}(x_k, y_k, z_k, t) \qquad (8.17b)$$

$$\{W\} = \{f_\alpha, \frac{\partial f_\alpha}{\partial x}, \frac{\partial f_\alpha}{\partial y}, \frac{\partial f_\alpha}{\partial z}, \frac{\partial^2 f_\alpha}{\partial x^2}, \frac{\partial^2 f_\alpha}{\partial y^2}, \frac{\partial^2 f_\alpha}{\partial z^2}, \frac{\partial^2 f_\alpha}{\partial x \partial y}, \frac{\partial^2 f_\alpha}{\partial x \partial z}, \frac{\partial^2 f_\alpha}{\partial y \partial z}\}^T \qquad (8.17c)$$

$$\{W'\} = \{g_\alpha, \frac{\partial g_\alpha}{\partial x}, \frac{\partial g_\alpha}{\partial y}, \frac{\partial g_\alpha}{\partial z}, \frac{\partial^2 g_\alpha}{\partial x^2}, \frac{\partial^2 g_\alpha}{\partial y^2}, \frac{\partial^2 g_\alpha}{\partial z^2}, \frac{\partial^2 g_\alpha}{\partial x \partial y}, \frac{\partial^2 g_\alpha}{\partial x \partial z}, \frac{\partial^2 g_\alpha}{\partial y \partial z}\}^T \qquad (8.17d)$$

M_1 and M_2 are the numbers of the selected neighboring points around the calculation point P for the density distribution and internal energy density distribution, respectively.

$a_{1,k}$ and $a'_{1,k}$ are the elements of the first row in the matrix $[A]$ and $[A']$ respectively.

These two matrices are derived in the same way as shown in Chapter 5. In this chapter, we use the same particle velocity model and choose the same fourteen neighboring points around the calculation point P for the density and internal energy density distributions, so M_1 equals M_2 and the geometric matrices A and A' are the same. Figure 8.1 shows the grid point P and its surrounding fourteen points $A, B, C, D, E, F, G, H, I, J, K, L, M, N$ that we choose to form the matrix A (A').

The order of the geometric matrix is $[M+1] \times 6$. For the two-dimensional problems, the Taylor series expansion involves six unknowns, that is, one density distribution at the time level $t + \delta t$, two first order derivatives, and three second-order derivatives. To solve for these unknowns, M should be at least equal to 5. In order to avoid possible ill-conditioning, least squares technique is used and M>5 is needed. For the three-dimensional problems, this expansion involves ten unknowns, that is, one density distribution at the time level $t + \delta t$, three first order derivatives, and six second-order derivatives. So M should be at least equal to 9. M>9 is chosen to avoid possible ill-conditioning using the least squares technique. The value of M does not affect much the accuracy of the numerical results (Ding et al., 2004). For example, the calculations for the natural convection in a cubic cavity at $Ra=10^4$ using $M=14$ and $M=18$ are done. When $M=14$, the maximum horizontal velocity u_{max} on the vertical mid-line in the symmetry plane ($y=0.5$) is 0.206; while the maximum vertical velocity v_{max} on the horizontal mid-line in this plane is 0.221. When $M=18$, the maximum horizontal velocity u_{max} is 0.208 and the maximum vertical velocity v_{max} is 0.222. It can be seen that the change in the

maximum velocities is within 1% when increasing M from 15 to 18. For the following cases in this chapter, M is chosen to be 14 for the convenience, which coincides with the particle model D3Q15.

8.2.3 Wall boundary conditions

The bounce-back rule of the non-equilibrium distribution proposed by Zou and He (1997) is used here for the wall boundary conditions. The outgoing known distributions are determined from the governing equations (8.1) and (8.2) for the uniform mesh or the governing equations (8.16a) and (8.16b) for the arbitrary mesh, and the unknown incoming distributions are determined from the bounce-back rule of the non-equilibrium distribution.

On the boundary, there still exist some special particle directions, at which the particles do not go from the inside flow field to the outside environment or come from the outside environment into the inside flow field. Take D3Q15 as an example. As shown in Figure 8.1, suppose that *HJNL* is the left vertical wall for the flow configuration. At the boundary line *HJ*, the two density distributions at the directions 2, 3, 4, 6, 8 and 12 are determined from the governing equations (Equations (8.1) and (8.2) for the simulations on the uniform grids; equations (8.16a) and (8.16b) for the simulations on the arbitrary mesh). The two density distributions at the directions 1, 5, 7 and 11 can be determined from the boundary conditions, which is the bounce-back rule of the non-equilibrium distribution. The remaining of the directions 9, 10, 13 and 14 are the special directions. At these special particle directions, the values for the density distribution and internal energy density distribution cannot be determined from their evolution equations or the bounce-

back boundary conditions. For the simulations on the uniform grids, since these values do not transport any information into the interior points, the equilibrium distribution functions are given for the two density distributions at these special directions. However, for the simulations on the arbitrary mesh, these values are very important and will affect the values for the interior points at these special directions. So the extrapolation scheme is used for the two density distributions at these special directions as shown in Chapter 5.

For Neumann boundary condition, the temperature on the wall is unknown. In order to use the above-mentioned bounce-back condition, we transfer it to Dirichlet boundary condition by using the conventional second-order finite difference approximation to get the temperature on the boundary wall. Iteration is needed in order to obtain accurate temperature on the wall from the heat flux. The detailed information on this procedure has been given in Chapter 3.

8.3 Numerical simulations

In order to verify whether our three-dimensional thermal LBM can be used to solve the real three-dimensional thermal problems, we carried out the computation for a sample problem. The problem considered is a natural convection in a three-dimensional cubical cavity with two vertical side walls maintained at different temperatures. The temperature difference between walls induces a natural convection. The remaining walls are adiabatic. The definition for this problem and the boundary conditions are displayed in Figure 8.2.

8.3.1 Buoyancy force and the dimensionless parameters

The Boussinesq approximation is applied to the buoyancy force term. The buoyancy force is assumed to depend linearly on the temperature:

$$\rho \boldsymbol{G} = \rho \beta g \left(T - T_m \right) \boldsymbol{k} \tag{8.18}$$

where $T_m = \dfrac{\left(T_H + T_L \right)}{2}$ and $\boldsymbol{k}$ is the vertical direction opposite to that of gravity.

So the external force F_α in equation (8.1) is $F_\alpha = \dfrac{\boldsymbol{G} \cdot \left(\boldsymbol{e} - \boldsymbol{u} \right)}{RT} f_\alpha^{eq}$

The dynamical similarity depends on two dimensionless parameters: Prandtl number Pr and Rayleigh number Ra,

$$\mathrm{Pr} = \upsilon / \chi \quad Ra = \left(\beta g \Delta T L^3 \right) / \left(\upsilon \chi \right) \tag{8.19}$$

where $\Delta T = T_H - T_L$.

To ensure the code working properly in the near incompressible regime, we carefully choose the value of $\beta g \Delta T L$. Once $\beta g \Delta T L$ is determined, the kinematic viscosity and thermal diffusivity are determined from equation (8.19) through the two dimensionless numbers, Pr and Ra. Using the relationship $\upsilon = \left(\tau_\upsilon - \dfrac{1}{2} \right) c_s^2 \delta t$ and

$\chi = \dfrac{5}{3} \left(\tau_c - \dfrac{1}{2} \right) c_s^2 \delta t$, two relaxation times τ_υ and τ_c can be determined from the kinematic viscosity and thermal diffusivity, respectively.

Nusselt number Nu is one of the most important dimensionless parameters in describing the convective heat transport. The Nusselt numbers at the isothermal walls are defined as

$$Nu_{mean}(y) = \int_0^1 \left. \frac{\partial T(y, z)}{\partial x} \right|_{x=0 \, or \, x=1} dz \tag{8.20}$$

$$Nu_{overall} = \int_0^1 Nu_{mean}(y) dy \tag{8.21}$$

8.3.2 Validation of the numerical results and analysis of flow and thermal fields

Numerical simulations of the three-dimensional natural convection in a cubic cavity at Rayleigh numbers of 10^3 to 10^5 were carried out using the particle velocity model of D3Q19. The uniform grid is used for $Ra=10^3$. The non-uniform grids where the grids are stretched towards the walls are used for $Ra=10^4$ and $Ra=10^5$ in order to get the accurate results by using less grid points so as to save the computational time and memory. The convergence criterion for all the cases is set to

$$\max_{i,j,k} \left| \sqrt{(u_{i,j,k}^2 + v_{i,j,k}^2 + w_{i,j,k}^2)^{n+1}} - \sqrt{(u_{i,j,k}^2 + v_{i,j,k}^2 + w_{i,j,k}^2)^n} \right| \leq 10^{-7} \tag{8.22a}$$

$$\max_{i,j,k} \left| T_{i,j,k}^{n+1} - T_{i,j,k}^n \right| \leq 10^{-7} \tag{8.22b}$$

where n and $n+1$ represent the old and new time levels, respectively.

Table 8.1 shows the representative quantities of the flow field and the heat transfer rates in the symmetry plane ($y=0.5$). In this symmetry plane, the representative quantities of the flow field include: the maximum horizontal velocity u_{max} on the vertical mid-line in this plane and its location z, the maximum vertical velocity v_{max} on the horizontal mid-line and its location x. The representative quantities of the heat transfer rates in this symmetry plane contain the following Nusselt numbers defined at the vertical boundary $x=0$. They are the maximum value of the local Nusselt numbers along the z- direction

Nu_{max} and its location z, the minimum value of the local Nusselt numbers Nu_{min} and its location z, and the average Nusselt number Nu_{mean} along this direction. The numerical results of a NS solver by Fusegi et al. (1991) using a high resolution finite difference numerical method are also included for comparison.

From Table 8.1, we can see that our simulation results generally compare well with those from the NS solver. There are some small differences between the results using two different methods. However, these discrepancies are within 3% and acceptable for the engineering applications. For $Ra=10^3$, these discrepancies may be caused by the fact that too few grid points are used by the NS solver, which is only $32\times32\times32$. Our numerical results are grid-independent, which will be shown in the following section. For $Ra=10^4$ and $Ra=10^5$, the reason for these differences may be that the grid sizes of $61\times45\times45$ and $91\times65\times65$ used for $Ra=10^4$ and $Ra=10^5$, respectively, are still not enough, although the non-uniform grid which is stretched towards the walls is used. The numerical simulations of the natural convection in the two-dimensional thermal cavity at $Ra=10^4$ and $Ra=10^5$ using the non-uniform grids were carried out by us in Chapter 5 and the grid sizes of 101×101 and 151×151 were found to be fine enough to obtain accurate results. Based on that study, for the three-dimensional thermal cubic cavity, the same or even larger grid size should be needed for $Ra=10^4$ and $Ra=10^5$. From the current results, we can say that our three-dimensional thermal model has the capability for solving the real three-dimensional thermal problems.

As far as the computation time is concerned, all the calculations for $Ra=10^3$ and $Ra=10^4$ are done on Pentium IV-2.4GHz. The calculation for $Ra=10^5$ is done on the Compaq ES40 workstation. The calculation times (seconds) needed for $Ra=10^3$, $Ra=10^4$,

$Ra=10^5$ are 144437.78, 221268.50 and 433846.54 respectively. The memory needed for the calculation of $Ra=10^5$ is 735MB.

The streamlines and isotherms in the symmetry plane of y=0.5 for $Ra=10^3$ to $Ra=10^5$ are shown in Figure 8.3 and Figure 8.4. The overall flow patterns and isotherms are qualitatively similar to those of the two-dimensional thermal cavity flows. However, the effect of three dimensions is notable and reflected in the overall Nusselt number on the isothermal walls, which is to be described in the following section.

Figure 8.5 and Figure 8.6 show the isovelocity contours. In the u-velocity contours, there are two horizontal eddies, one below the other, for $Ra=10^3$. For higher values of Rayleigh number, these two eddies move closer to the two adiabatic walls. Similarly, two dominant circulations are prominently visible in the vertical isovelocity contours, one on the left and the other on the right zones of the cavity, for $Ra=10^3$. These two eddies subsequently move closer to the hot wall and cold wall, respectively with Rayleigh number increasing. This indded illustrates that the boundary layer gets thinner as a function of the Rayleigh number. These patterns are also similar to those of the two-dimensional thermal cavity flows (Wan et al., 2001).

Figure 8.7 and Figure 8.8 show the isotherms on the middle planes of x=0.5 and z=0.5. They compare well with the results of Sivaloganathan & Karageorghis.

8.3.3 The overall Nusselt number on the isothermal wall

The non-dimensional heat transfer rate on the isothermal walls is a very important parameter in the engineering application. Table 8.2 shows the overall Nusselt number on the isothermal wall of $x=0$ at Rayleigh numbers of 10^3 to 10^5 using D3Q19. The results

of the NS solver are also included for comparison. The agreement of the results using these two different methods is very good.

From Table 8.2, we can see that at $Ra=10^3$, the overall Nusselt number on the isothermal wall for the three-dimensional cubic cavity is 1.076, while for the two-dimensional square cavity, the average Nusselt number on the isothermal wall is 1.117. The three-dimensional result of the overall Nusselt number is smaller than that in two dimensions, which shows the effect of the side walls on the heat transfer. This observation agrees well with the result shown in Figure 8.9. Figure 8.9 represents the profile of the mean Nusselt number along the y-direction on the isothermal wall of $x=0$ for $Ra=10^3$. The mean Nusselt number increases as the symmetry plane is approached, and its peak value occurs at the symmetry plane located at $y=0.5$. This peak value at the symmetry plane is still smaller than the average Nusselt number for the two-dimensional thermal cavity. So the overall Nusselt number for the cubic cavity should be smaller than that for the two-dimensional cavity. The same trend is applied to $Ra=10^4$ and $Ra=10^5$.

8.3.4 Grid-independence study for $Ra=10^3$ using D3Q19

In order to examine the influence of the grid size on the numerical simulation results, the grid-independence study for $Ra=10^3$ using D3Q19 was carried out on three different grid sizes: 71×71×71, 81×81×81 and 91×91×91. Table 8.3 shows the calculated representative quantities of the flow field and the heat transfer rates in the symmetry plane and the overall Nusselt number on the isothermal wall using these different grids.

From Table 8.3, we can see that with the increase of the grid number, the numerical results are improved as compared with those from the NS solver. When the

number of the grid points in each direction is increased from 81 to 91, there is no much improvement on the numerical results. So we can say that the grid size of 81×81×81 is fine enough to obtain the accurate results for this flow at $Ra=10^3$.

8.3.5 Comparison of the results using D3Q15 and D3Q19

In order to examine the influence of the particle velocity models on the numerical simulation results, the calculations for this sample problem were carried out using two different particle velocity models: one is D3Q15 and the other is D3Q19. Table 8.4 shows the comparison of the calculated representative quantities of the flow field and the heat transfer rates in the symmetry plane and the overall Nusselt number on the isothermal wall using two different particle velocity models: D3Q15 and D3Q19.

From Table 8.4, we can see that at $Ra=10^3$, the numerical results are almost the same using D3Q15 and D3Q19. While at $Ra=10^4$, there are some differences in the numerical results. The use of D3Q19 can produce better results than D3Q15 when compared with the NS solver. In addition, during the converging process, small oscillation of solutions occurs for D3Q15, while the computation of D3Q19 model is very stable. This means that although D3Q19 will use more memory than D3Q15 for the same grid number, it is more stable and can produce better results. This is also the reason that the numerical simulation at $Ra=10^5$ is only carried out using D3Q19. This agrees well with the assessment made by Mei et al. (2000). Three three-dimensional lattice models of D3Q15, D3Q19 and D3Q27 have been assessed by Mei et al. in terms of the efficiency, accuracy and robustness for the lid driven cavity flow problem. They found that D3Q19 is the best particle velocity model for the case investigated; D3Q15 exhibits the velocity oscillation

and is prone to the computational instability; the more complicated D3Q27 model does not necessarily give more accurate results than D3Q19 model with the same spatial resolution. So, most of the calculations in this chapter are based on D3Q19 particle velocity model.

8.4 Extension to include the viscous heat dissipation and compression work done by pressure

Compared with the thermal model proposed by Shan (1997) using the passive-scalar method, this new three-dimensional thermal LBM can easily incorporate the effects of viscous heat dissipation and compression work done by pressure. Because for some real three-dimensional thermal applications, these effects cannot be neglected.

8.4.1 Thermal model including the viscous heat dissipation and compression work done by pressure

To include the effects of the viscous heat dissipation and compression work done by pressure, the governing equations for the density and internal energy density distributions are changed from equations (8.1) and (8.2) to:

$$\overline{f}_\alpha\left(\boldsymbol{x}+\boldsymbol{e}_\alpha\delta t,t+\delta t\right)-\overline{f}_\alpha\left(\boldsymbol{x},t\right)=-\frac{\delta t}{\tau_v+0.5\delta t}\left[\overline{f}_\alpha\left(\boldsymbol{x},t\right)-f_\alpha^{eq}\left(\boldsymbol{x},t\right)\right]+\frac{\tau_v F_\alpha \delta t}{\tau_v+0.5\delta t} \qquad (8.23)$$

$$\overline{g}_\alpha\left(\boldsymbol{x}+\boldsymbol{e}_\alpha\delta t,t+\delta t\right)-\overline{g}_\alpha\left(\boldsymbol{x},t\right)=-\frac{\delta t}{\tau_c+0.5\delta t}\left[\overline{g}_\alpha\left(\boldsymbol{x},t\right)-g_\alpha^{eq}\left(\boldsymbol{x},t\right)\right]-\frac{\tau_c f_\alpha\left(\boldsymbol{x},t\right)q_\alpha \delta t}{\tau_c+0.5\delta t} \qquad (8.24)$$

These two equations are the results of the second-order integration of the continuous Boltzmann equations and have the same forms as those for the original two-dimensional IEDDF thermal model shown in Chapter 3. The definitions of the variables $\overline{f}\left(\boldsymbol{x},e,t\right)$,

$\overline{g}(\boldsymbol{x},\boldsymbol{e},t)$ and $q(\boldsymbol{x},\boldsymbol{e},t)$ are the same as those given in Chapter 3. The reason why the second-order integration has to be used and new variables for two density distributions are introduced is given in Chapter 7.

The particle velocity models to be used and their corresponding equilibrium density distribution functions are the same as those given in Section 8.2.1. The Chapman-Enskog expansion of equation (8.23) will recover the continuity and NS equations; while the Chapman-Enskog expansion of equation (8.24) will result in the macroscopic energy equation

$$\partial_t(\rho\varepsilon)+\nabla\cdot(\rho\boldsymbol{u}\varepsilon)=\nabla\cdot(\rho\chi\nabla\varepsilon)+\prod:\nabla\boldsymbol{u}-p\nabla\cdot\boldsymbol{u} \tag{8.25}$$

which contains the viscous heat dissipation and compression work done by pressure. The kinematic viscosity and thermal diffusivity are related to the relaxation times by:

$$\upsilon=\frac{\tau_v}{3}\ ,\ \chi=\frac{5\tau_c}{9} \tag{8.26}$$

8.4.2 Numerical simulations

In order to validate this extensional thermal model, the same sample problem of the natural convection in a cubic cavity was calculated. Only the numerical simulation at Rayleigh number of 10^3 was carried out just to illustrate its applicability. The particle velocity model used is D3Q15. Table 8.5 shows the representative quantities of the flow field and the heat transfer rates in the symmetry plane and the overall Nusselt number on the isothermal wall using this extensional thermal model. The numerical results using the original three-dimensional thermal model proposed in Section 8.2.1 and a NS solver are also included for comparison.

From this table, we can see that the numerical results using the extensional thermal model are almost the same as those using the original three-dimensional thermal model. They all compare very well with the benchmark data of a NS solver. The meanings are in two folds. On one hand, it confirms the validity of this extensional thermal model for real three-dimensional thermal applications; while on the other hand, it shows that the viscous heat dissipation and compression work done by pressure are very small and can be negligible for this test case, which agrees well with the physical background of the incompressible flows.

8.5 Conclusions

A new three-dimensional thermal model for LBM is proposed in this chapter. The numerical simulation results of the three-dimensional steady-state natural convection of air in a cubical enclosure using this new thermal model compare very well with those using a NS solver. This shows that our three-dimensional thermal model has the capability to solve the real three-dimensional thermal problems. Its use on the arbitrary mesh is straight forward by introducing the TLLBM technique, which has also been demonstrated by the numerical results of this sample problem on non-uniform grids at Rayleigh numbers of 10^4 and 10^5. Its extension to include the viscous heat dissipation and compression work done by pressure is very easy. The numerical simulation of the same sample problem at Rayleigh number of 10^3 has validated this extension. The results also confirm that these effects can be negligible for most of the incompressible flows.

For this new three-dimensional thermal LBM, the influences of the grid size used and the particle velocity model chosen on the calculation results have also been studied. In

summary, this new thermal model has the following advantages. It is very simple and easy to implement. No additional particle velocity is used for the particle velocity models as compared with the particle velocity models used by isothermal flows.

Table 8.1 Comparison of the representative field values on the symmetry plane (y=0.5) for the natural convection in a cubic cavity using LBM and a NS solver

Ra	10^3		10^4		10^5	
Method	LBM	NS solver	LBM	NS solver	LBM	NS solver
Grid size	81×81×81	32×32×32	61×45×45	62×62×62	91×65×65	62×62×62
u_{max}	0.132	0.1314	0.206	0.2013	0.149	0.1468
z	0.188	0.2000	0.163	0.1833	0.136	0.1453
v_{max}	0.133	0.1320	0.221	0.2252	0.240	0.2471
x	0.826	0.8333	0.887	0.8833	0.935	0.9353
Nu_{max}	1.432	1.420	3.720	3.652	7.88	7.795
z	0.0625	0.08333	0.1625	0.1623	0.09	0.08256
Nu_{min}	0.729	0.7639	0.595	0.6110	0.750	0.7867
z	1.0	1.0	1.0	1.0	1.0	1.0
Nu_{mean}	1.097	1.105	2.304	2.302	4.658	4.646

Table 8.2 Comparison of the overall Nusselt number at the isothermal wall for the natural convection in a cubic cavity using LBM and a NS solver

Ra	10^3		10^4		10^5	
Method	LBM	NS solver	LBM	NS solver	LBM	NS solver
$Nu_{overall}$	1.076	1.085	2.085	2.100	4.378	4.361

Table 8.3 Comparison of the numerical results for the natural convection in a cubic cavity at $Ra=10^3$ on three different grids

Mesh	71×71×71	81×81×81	91×91×91	NS solver
u_{max}	0.133	0.132	0.132	0.1314
z	0.186	0.188	0.188	0.200
v_{max}	0.133	0.133	0.133	0.1320
x	0.829	0.826	0.833	0.8333
Nu_{max}	1.433	1.432	1.430	1.420
z	0.0571	0.0625	0.0777	0.0833
Nu_{min}	0.727	0.729	0.730	0.7639
z	1.0	1.0	1.0	1.0
Nu_{mean}	1.085	1.097	1.098	1.105
$Nu_{overall}$	1.073	1.075	1.076	1.085

Table 8.4 Comparison of the numerical results for the natural convection in a cubic cavity using D3Q15 and D3Q19

Ra	10^3		10^4	
Particle model	D3Q15	D3Q19	D3Q15	D3Q19
Grid size	81×81×81	81×81×81	61×45×45	61×45×45
u_{max}	0.133	0.132	0.208	0.206
z	0.188	0.188	0.163	0.163
v_{max}	0.133	0.133	0.222	0.221
x	0.826	0.826	0.887	0.887
Nu_{max}	1.440	1.432	3.648	3.720
z	0.0525	0.0625	0.0625	0.1625
Nu_{min}	0.696	0.72	0.490	0.595
z	1.0	1.0	1.0	1.0
Nu_{mean}	1.093	1.097	2.25	2.304
$Nu_{overall}$	1.073	1.075	2.05	2.085

Table 8.5 Comparison of the numerical results for the natural convection in a cubic cavity at $Ra=10^3$ using LBM with different thermal models and a NS solver
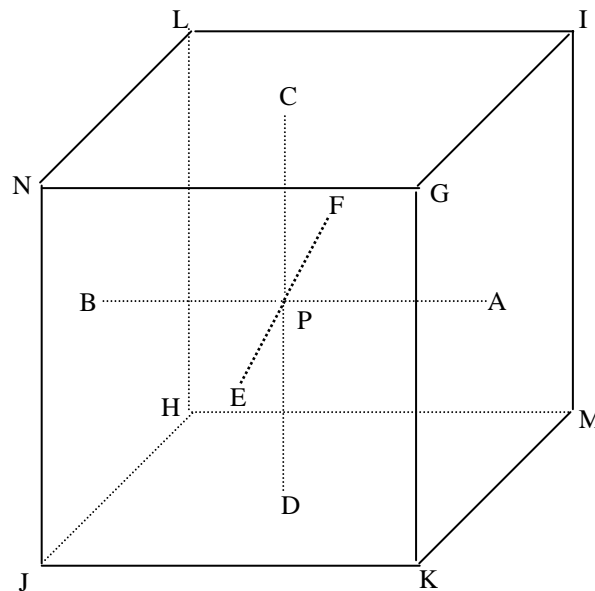
Model	original model	extensional model	NS solver
Mesh	81×81×81	81×81×81	32×32×32
u_{max}	0.132	0.132	0.1314
z	0.188	0.188	0.200
v_{max}	0.133	0.133	0.1320
x	0.826	0.826	0.8333
Nu_{max}	1.432	1.432	1.420
z	0.0625	0.0625	0.0833
Nu_{min}	0.729	0.730	0.7639
z	1.0	1.0	1.0
Nu_{mean}	1.097	1.098	1.105
$Nu_{overall}$	1.075	1.076	1.085

Figure 8.1 Configuration of the calculation point P and selected surrounding fourteen points *ABCDEFGHIJKLMN* in the new three-dimensional thermal LBM
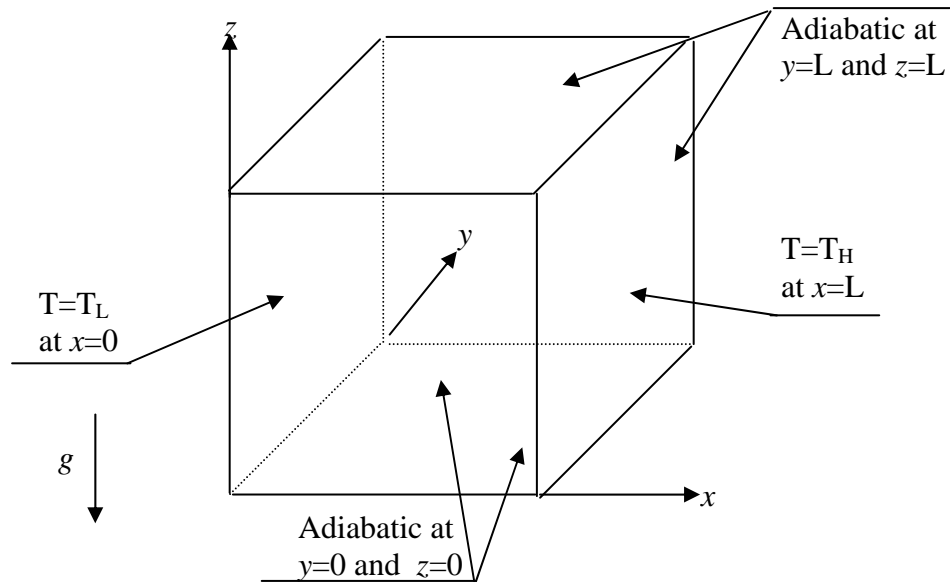
Figure 8.2 Configuration of the natural convection in a cubical cavity

Figure 8.3 Streamlines on the symmetry plane (y=0.5) for the natural convection in a

cubical cavity at Ra=10^3, 10^4,10^5.

Figure 8.4 Isotherms on the symmetry plane (y=0.5) for the natural convection in a cubical

cavity at Ra=10^3,10^4,10^5.

Figure 8.5 Iso-u contours on the symmetry plane (y=0.5) for the natural convection in a

cubical cavity at Ra=10^3,10^4,10^5.

Figure 8.6 Iso-v contours on the symmetry plane (y=0.5) for the natural convection in a

cubical cavity at Ra=10^3,10^4,10^5.

Figure 8.7 Isotherms on the middle plane (x=0.5) for the natural convection in a cubical
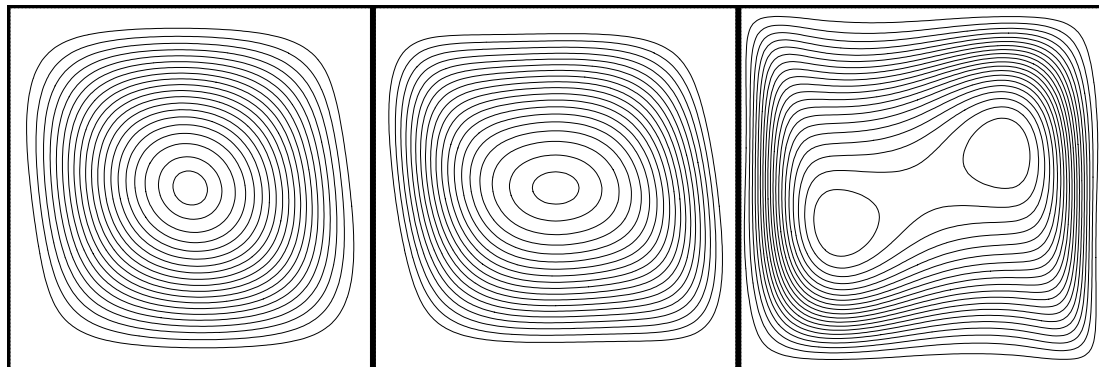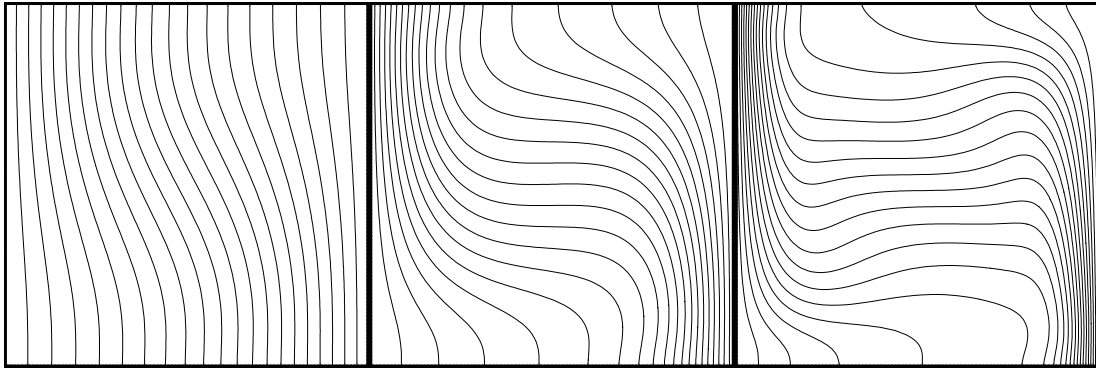
cavity at Ra=10^3,10^4,10^5.
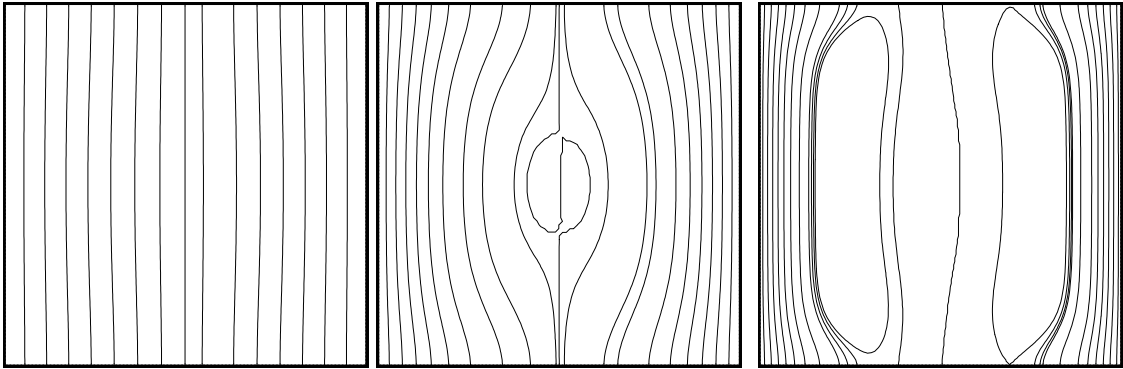
Figure 8.8 Isotherms on the middle plane (z=0.5) for the natural convection in a cubical
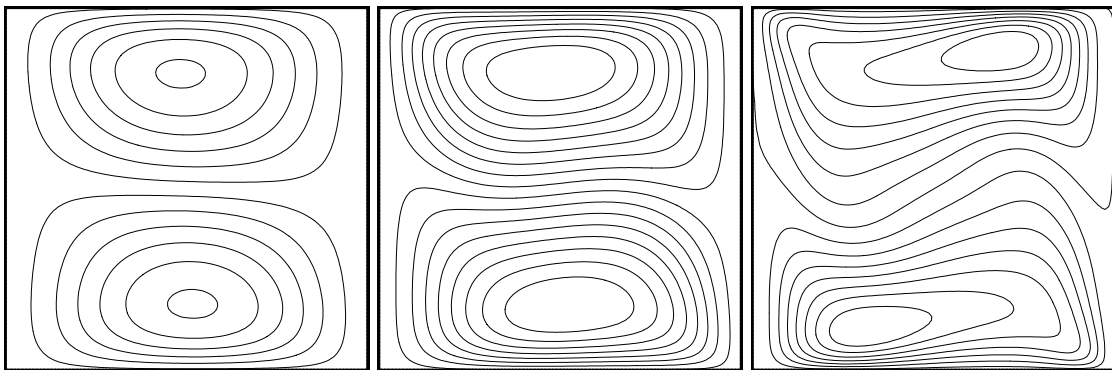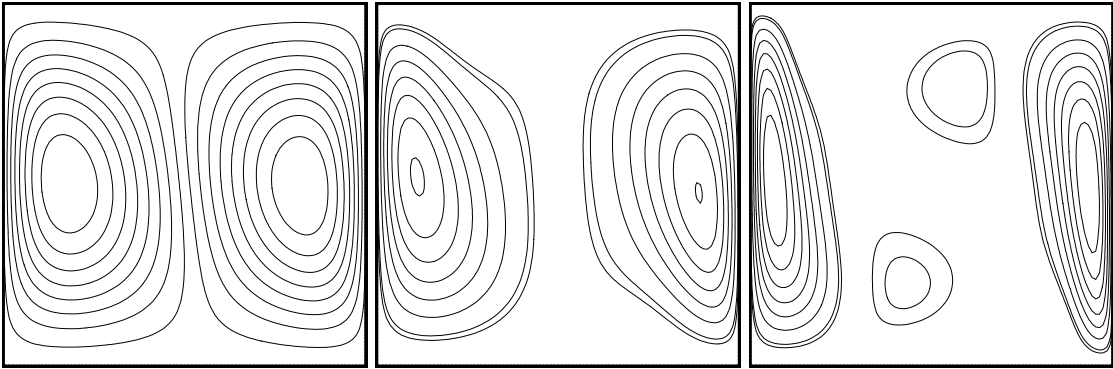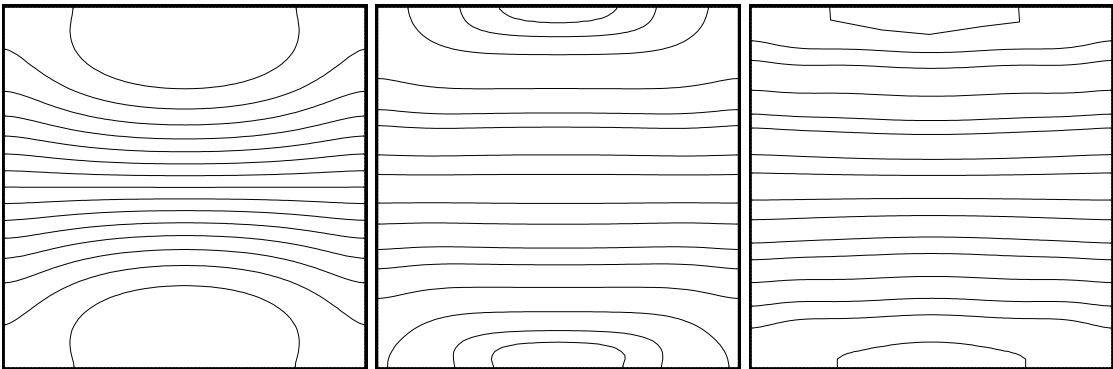
cavity at $Ra=10^3, 10^4, 10^5$.
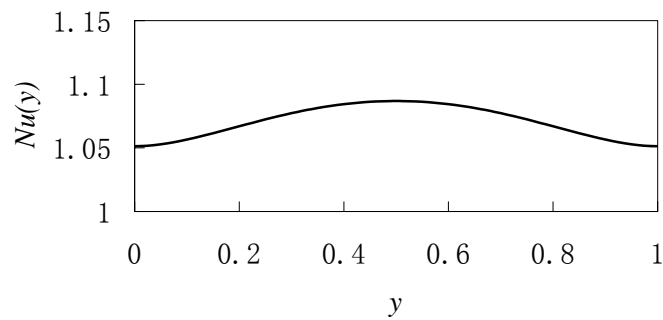
Figure 8.9 Distribution of the mean Nusselt number on the isothermal wall of x=0 along
the y-direction at $Ra=10^3$ for the natural convection in a cubic cavity

Chapter 9

Conclusions and recommendations

9.1 Conclusions

Lattice Boltzmann method has been developed into an alternative method for computational fluid dynamics and it has been widely used in different kinds of fluid flow applications. Currently, the thermo-hydrodynamic LBM is one of the most challenging issues left in the LBM research field. Despite several brilliant attempts, to date, there are still some spaces for improvement. One is to develop good thermal models. The other is the use of the thermal models to solve the practical thermal flows. We have contributed significantly to these two areas in the present project.

9.1.1 Development of the thermal models

There are a lot of thermal models proposed for LBM. Numerical simulations have proven the IEDDF thermal model to be a stable and simple one among these thermal models. So this thermal model is applied in this thesis to study the thermal flows. Since it is a newly developed model, it still needs a lot of improvements.

Firstly, this thermal model was limited to thermal applications with Dirichlet boundary condition. A new implementation of Neumann boundary condition for the IEDDF thermal model was proposed in Chapter 3 in order to solve the practical thermal problems with both Dirichlet and Neumann boundary conditions. The numerical simulation results of the natural convection in a square cavity showed that our new

implementation of boundary condition is valid in solving the thermal problems with Neumann boundary condition.

Secondly, based on the physical background that the compression work done by pressure and the viscous heat dissipation can be ignored for the incompressible flows, a simplified IEDDF thermal model for the incompressible thermal flows was proposed in Chapter 7. This new scheme has the following good features. It does not include any gradient term in the evolution equations and thus keeps the simplicity of LBM. The boundary conditions are easier to be implemented as compared with the original IEDDF thermal model. The numerical results of the natural convection in a square cavity at a wide range of Rayleigh numbers showed that this simplified IEDDF thermal model could obtain the same accurate results more efficiently as compared with the original IEDDF thermal model. The compressibility effect was also studied and the results showed that it could be neglected.

Thirdly, in order to solve an important kind of quasi-three-dimensional flow problems, a new axisymmetric lattice Boltzmann model was proposed in Chapter 6. It was applied to simulate the flows in the mixed convection in the vertical concentric cylindrical annuli and Czochralski crystal growth. The numerical results compared well with the benchmark data and this demonstrated that our new scheme could solve the axisymmetric thermal problems accurately and effectively. It was worthwhile to mention that our new scheme could solve the axisymmetric flow problems on the two-dimensional uniform rectangular grids in the cylindrical coordinate system, avoiding the solution of the real three-dimensional problems in the Cartesian coordinate system if the standard LBM was used. So the quasi-three-dimensional property of this kind of flows is kept.

Lastly, in order to solve the real three-dimensional thermal problems, a new three-dimensional thermal model for LBM was proposed in Chapter 8. The numerical simulation results of the three-dimensional steady-state natural convection of air in a cubical enclosure using this new thermal model compared very well with those from a NS solver. This showed that our three-dimensional thermal model has the capability to solve the real three-dimensional thermal problems. Its extension to include the viscous heat dissipation and compression work done by pressure was straight forward and the corresponding formulae were also given in that chapter. The influences of the grid size used and the particle velocity model chosen on the calculations using this new thermal model have been thoroughly studied. This new three-dimensional thermal model has the following good features. It is very simple and easy to implement. No additional particle velocity is used for the particle velocity model as compared with the isothermal particle velocity models.

9.1.2 Applications of the thermal models

We have used the above-developed thermal models for many practical applications in two and three dimensions. The numerical simulation results are as accurate as those obtained by the conventional NS solvers.

To apply these thermal models to the more complicated and practical thermo-hydrodynamic problems, we extended them to be used on the arbitrary grids. They were realized by using the following two ways. One is the use of the finite volume technique in the thermal models; the other is the use of the TLLBM technique in these thermal models.

During the constructions, the development of their corresponding implementation of boundary conditions was a major challenge.

9.1.2.1 Use of the finite volume technique in the thermal models. Firstly, a new implementation of the wall boundary condition for FVLBM was developed in Chapter 4 in order to make FVLBM be a useful method for practical applications. It was based on the half-covolume technique and the bounce-back rule for the non-equilibrium distribution. Using this new implementation of the wall boundary condition, the flow problems such as the expansion channel flows and driven cavity flows could be correctly solved using FVLBM.

Then this FVLBM scheme was applied in the IEDDF thermal model so as to extend the current thermal model to be used on the arbitrary grids. The numerical simulations of the natural convection in a square cavity at Rayleigh number ranging from 10^3 to 10^5 on the non-uniform grids were carried out. At low Rayleigh numbers, the numerical results compared well with the benchmark data obtained by a NS solver, which showed the validity of using FVLBM technique in the IEDDF thermal model. Compared with the numerical results on uniform grids using the standard LBM, less grid numbers were needed to obtain the same accurate results using the non-uniform grids. However, from the present work, it was found that at high Reynolds numbers or Rayleigh numbers, the numerical diffusion of the FVLBM scheme affected the efficiency, accuracy and convergence of the IEDDF thermal model. So the use of the present FVLBM technique in the IEDDF thermal model was not a perfect way to extend the current thermal models on the arbitrary mesh for practical flow problems when high Reynolds numbers or Rayleigh

numbers were encountered. We need to find another method to solve this problem. This leads to the use of the TLLBM technique in the thermal models.

9.1.2.2 Use of TLLBM technique in the thermal models. The explicit TLLBM was successfully applied to the IEDDF thermal model in Chapter 5 so that it could solve the thermal problems on the arbitrary mesh.

For two dimensions, the numerical simulation of the natural convection in a square cavity at Rayleigh numbers ranging from 10^3 to 10^6 on non-uniform grids was used to validate our new scheme. The numerical results compared very well with the benchmark data obtained by a NS solver. Fewer grid numbers were needed to obtain accurate results using non-uniform grids. Its extension to the applications on the arbitrary mesh for the thermal problems with curved boundaries was straight forward since there was no special requirement on the mesh structure for the TLLBM technique. So this scheme was employed to study the natural convection in a horizontal concentric annulus between a square outer cylinder and a circular inner cylinder, which was a complex thermal flow problem with curved boundaries. Numerical results for Rayleigh numbers ranging from 10^4 to 10^6 and aspect ratios between 1.67 and 5.0 were presented, which agreed well with available data in the literature.

For three dimensions, the numerical simulation of the natural convection in a cubic cavity at high Rayleigh numbers on the non-uniform grids was also done by the introduction of the TLLBM technique in our new three-dimensional thermal model in Chapter 8. The results compared well with the benchmarked data.

From these numerical simulations, we can see that using the TLLBM technique in thermal models is an effective way to extend the current thermal models to be used on the

arbitrary mesh, which is very important for the practical engineering applications. It should be indicated that with the use of TLLBM technique, the thermal models still keep the local feature and no solution of the differential equation is involved. It can be easily applied to solve the thermal problems with any complex geometry.

.

9.2 Recommendations

The future work can be carried out in the following areas.

9.2.1 Development of the thermal models

Currently, most thermal models are suitable for incompressible flows. It is necessary to develop a good thermal model applicable for compressible flows, since the flow will become compressible when Rayleigh number or Grashof number is very high. This is not an easy task. There are some compressible LBM models for the compressible isothermal flows, but there is still no well-accepted model that can solve most compressible isothermal flows successfully, not to mention the compressible thermal flows.

Fluid flows in the microstructures have become an important subject due to many applications of Micro Electro Mechanical Systems (MEMS) in the fields such as instrumentation, microelectronics, microreactors, bioengineering and advance energy systems. The MEMS, such as a micro-motor, micro-resonator, micro-beam and micro-channel, usually involves gas or liquid flows in a device of which the characteristic dimension is in the order of one micron, which is only about 10 times of the mean free path of the gas molecules under normal conditions. For the gas flows in this size, the

usually applied continuum approximation for fluids is no longer valid. LBM can cover a wide range from the continuum limit to the free molecule flow limit, so it is an ideal method to solve the micro flow problems. A satisfactory LBM thermal model for the micro flow needs to be developed. Since the flow in the microstructure is usually compressible, so the thermal model should also be able to consider the compressibility property.

9.2.2 Applications of the thermal models

Since we have developed some good thermal models in two dimensions and three dimensions, and the use of TLLBM technique in these thermal models is found to be able to solve the thermal problems with any complex geometry, these schemes can be used to solve more complex thermal flows with practical engineering applications in the future. They can also be used to conduct in depth study of thermal flow problems in order to understand the physics of such complicated flows better.

References

1. Abe, T. Note: Derivation of the Lattice Boltzmann method by means of the discrete ordinate method for the Boltzmann equation, J. Comp. Phys., 131, pp.241-246. 1997.

2. Aharonov, E. and D. H. Rothman. Non-Newtonian flow (through porous media): a lattice Boltzmann method, Geophys. Res. Lett., 20, pp.679-682. 1993.

3. Aidum, C. K. and Y.N. Lu. Lattice Boltzmann simulation of solid particles suspended in fluid, J. Stat. Phys., 81, pp.49-61. 1995.

4. Alexanders, F., S. Chen and J. Sterling. Lattice Boltzmann thermo-hydrodynamics, Phys. Rev. E, 47, pp.R2249-2252. 1993.

5. Ball, K. S. and B. Farouk. On the development of Taylor vortices in a vertical annulus with a heated rotating inner cylinder, Int. J. Numer. Meth. Fluids, 7, pp.857-867. 1987

6. Bartoloni, A., C. Battista, S. Cabasino, P. S. Paolucci and J. Pech. LBE simulations of Rayleigh-Bernard convection on the APE100 parallel processor, Int. J. Mod. Phys. C, 4, pp.993-1006. 1993.

7. Behrend, O. Solid-fluid boundaries in particle suspension simulations via the lattice Boltzmann method, Phys. Rev. E., 52, pp.1164-1175. 1995.

8. Benzi, R., M. V. Struglia and R. Tripiccione. Extended self-similarity in numerical simulations of three-dimensional anisotropic turbulence, Phys. Rev. E, 53, pp.R5565-5568. 1996.

9. Bhatnagar, P., E. P. Gross and M. K. Krook. A model for collision processes in gases, I. Small amplitude processes in charged and neutral one-component systems, Phys. Rev., 94 (3), pp.511-525. 1954.

10. Boghosian, B. M., P. V. Coveney and A. N. Emerton. A lattice-gas model for microemulsions, Proc. Roy. Soc. London. Ser. A, 452, pp.1221-1250. 1996.

11. Bouzidi, M., M. Firdaouss and P. Lallemand. Momentum transfer of a Boltzmann-lattice fluid with boundaries, Phys. Fluid, 13(11), pp. 3452-3459. 2001.

12. Buckles, J., R. Hazlett, S. Chen, K. G. Eggert, D. W. Grunau and W. E. Soll. Flow through porous media using lattice Boltzmann method, Los Alamos Sci., 22, pp.112-121. 1994.

13. Cancelliere, A., C. Chang, E. Foti, D. H. Rothman and S. Succi. The permeability of a random medium: comparison of simulation with theory, Phys. Fluids A, 2, pp.2085-2088. 1990.

14. Cao, N., S. Chen, S. Jin and D. Martinez. Physical symmetry and lattice symmetry in lattice Boltzmann method, Phys. Rev. E., 55, pp.R21-R24. 1997.

15. Chen, H. Volumetric formulation of the lattice Boltzmann method for fluid dynamics: Basic concept, Phys. Rev. E, 58, pp.3955-3963. 1998.

16. Chen, H. and C. Teixeira. H-theorem and origins of instability in thermal lattice Boltzmann models, Comp. Phys. Comm., 129, pp.21-31. 2000.

17. Chen, H., S. Kandasamy, S. Orszag, R. Shock, S. Succi and V. Yakhot. Extended Boltzmann kinetic equation for turbulent flows, Science, 301, pp.633-636. 2003.

18. Chen, S., Z. Wang, X. W. Shan and G. D. Doolen. Lattice Boltzmann computational fluid dynamics in three dimensions, J. Stat. Phys., 68, pp.374-400. 1992.

19. Chen, S., S. P. Dawson, G. D. Doolen, D. R. Janecky and A. Lawniczak. Lattice methods and their applications to reacting systems, Comp. Chem. Eng., 19, pp.617-646. 1995.

20. Chen, S., D. Martinez, R. Mei. On boundary conditions in lattice Boltzmann methods, Phys. Fluids, 8, pp.2527-2536. 1996.

21. Chen, S. and G. D. Doolen. Lattice Boltzmann method for fluid flows, Annu. Rev. Fluid Mech., 30, pp.329-364. 1998.

22. Chen, Y. Thermal lattice Bhatnagar-Gross-Krook model without nonlinear deviations in macrodynamic equations, Phys. Rev. E, 50, pp.2776-2783. 1994a.

23. Chen, Y. Lattice Bhatnagar-Gross-Krook method for fluid dynamics: compressible, thermal and multiphase models. Ph.D. Thesis, Dept. of Quantum Engineering and System Science, University of Tokyo. 1994b.

24. Chen, Y., H. Ohashi and M. Akiyama. Two-parameter thermal lattice BGK model with a controllable Prandtl number, J. Sci. Comp, 12(2), pp. 169-185. 1997.

25. Chew, Y. T., C. Shu, X. D. Niu, Simulation of unsteady incompressible flows by using Taylor series expansion- and least square- based lattice Boltzmann method, Int. J. Mod. Phys. C, 13, pp. 719-738. 2002.

26. David,G. D. V. Natural convection of air in a square cavity: a benchmark numerical solution, Int. J. Numer. Meth. Fluids, 3, pp.249-264. 1983.

27. Dawson, S. P., S. Chen and G. D. Doolen. Lattice Boltzmann computations for reaction-diffusion equations, J. Chem. Phys., 98, pp.1514-1523. 1993.

28. Ding, H., C. Shu, K. S. Yeo and D. Xu. Development of least-square-based two-dimensional finite-difference schemes and their application to simulate natural convection in a cavity, Computer & Fluids, 33 (1), pp.137-154. 2004.

29. Dufty, J. W. and M. H. Ernst. Lattice Boltzmann Langevin equation, Fields Inst. Comm., 6, pp.99-107. 1996.

30. Eggels, J. G. M. Direct and large-eddy simulation of turbulent fluid flow using the lattice Boltzmann scheme, Int. J. Heat Fluid Flow, 17, pp.307-323. 1996.

31. Feiz, H., J. H. Soo and S. Menon. LES of turbulent jets using the lattice Boltzmann approach, AIAA Paper 2003-0780. 2003a.

32. Feiz, H. and S. Menon. LES of multiple jets in crossflow using a coupled lattice Boltzmann-finite volume solver, AIAA Paper 2003-5206. 2003b.

33. Ferreol, B. and D. H. Rothman. Lattice Boltzmann simulations of flow through Fontainebleau sandstone, Transp. Por. Med., 20, pp.3-20. 1995.

34. Filippova, O. and D. Hanel. Grid refinement for Lattice-BGK models, J. Comp. Phys., 147, pp.219-228. 1998.

35. Filippova, O. and D. Hanel. A novel lattice BGK approach for low Mach number combustion, J. Comp. Phys., 158, pp.139-160. 2000a.

36. Filippova, O. and D. Hanel. Acceleration of Lattice-BGK schemes with grid refinement, J. Comp. Phys., 165, pp.407-427. 2000b.

37. Flekkøy, E. G., T. Rage, U. Oxaal and J. Feder. Hydrodynamic irreversibility in creeping flow, Phys. Rev. Lett., 77, pp.4170-4173. 1996.

38. Frisch, U., B. Hasslacher and Y. Pomeau. Lattice-gas automata for the Navier-Stokes equation, Phys. Rev. Lett., 56 (14), pp.1505-1508. 1986.

39. Fusegi, T., J. M. Hyun, K. Kuwahara and B. Farouk. A numerical study of three-dimensional natural convection in a differentially heated cubical enclosure, Int. J. Heat Mass Transfer, 34 (6), pp.1543-1557. 1991.

40. Ghia, U., K. N. Ghia and C. T. Shin. High-Re solutions for incompressible flow using the Navier-Stokes equations and a multigrid method, J. Comp. Phys., 48, pp.387-411. 1982.

41. Ginzburg, I. and D. d'Humieres. Multireflection boundary conditions for lattice Boltzmann models, Phys. Rev. E, 68, pp.066614. 2003.

42. Giraud, L., D. d'Humières and P. Lallemand. A lattice Boltzmann model for viscoelasticity, Int. J. Mod. Phys. C., 8(4), pp. 806-816. 1997.

43. Giraud, L., D. d'Humières and P. Lallemand. A lattice Boltzmann model for Jeffreys viscoelastic fluid, Europhys. Lett., 42(6), pp. 625-630. 1998.

44. Grad, H. On the kinetic theory of rarefied gases, Comm. Pure App. Math., 2, pp.331-407. 1949.

45. Gunstensen, A. K., D. H. Rothman, S. Zaleski and G. Zanetti. Lattice Boltzmann model of immiscible fluids, Phys. Rev. A, 43, pp.4320-4327. 1991.

46. Guo, Z., B. Shi and N. Wang. Lattice BGK model for incompressible Navier-Stokes equation, J. Comp. Phys., 165, pp.288-306. 2000.

47. Guo, Z., B. Shi and C. Zheng. A coupled lattice BGK model for the Boussinesq equations, Int. J. Numer. Meth. Fluids, 39, pp.325-342. 2002.

48. Halliday, I., L. A. Hammond, C. M. Care, K. Good and A. Stevens. Lattice Boltzmann equation hydrodynamics, Phys. Rev. E, 64, pp.011208. 2001.

49. He, X., L. S. Luo and M. Dembo. Some progress in lattice Boltzmann method, Part I. Non-uniform mesh grids, J. Comp. Phys., 129, pp.357-363. 1996.

50. He, X. and G. D. Doolen. Lattice Boltzmann method on curvilinear coordinates system: vortex shedding behind a circular cylinder, Phys. Rev. E., 56, pp.434-440. 1997.

51.   He, X. and L. S. Luo. A priori derivation of the lattice Boltzmann equation, Phy. Rev. E, 55, pp.R6333-6336. 1997.

52.   He, X., X. Shan and G. Doolen. Discrete Boltzmann equation model for nonideal gases, Phys. Rev. Lett., 57, pp.R13-R16. 1998a.

53.   He, X., S. Chen and G. D. Doolen. A novel thermal model for the lattice Boltzmann method in incompressible limit, J. Comp. Phys., 146, pp.282-300. 1998b.

54.   He, X., S. Chen and R. Zhang. A lattice Boltzmann scheme for incompressible multiphase flow and its application in simulation of Rayleigh-Taylor instability, J. Comp. Phys., 152, pp.642-663. 1999.

55.   Heijs, A. W. J. and C. P. Lowe. Numerical evaluation of the permeability and the Kozeny constant for two types of porous media, Phys. Rev. E, 51, pp.4346-4352. 1995.

56.   Henkes, R. A. W. M., A. M. Y. Lankhost and C. J. Hoogendoom. Structure of laminar natural convection flow in a square cavity heated from the side for infinitely large Rayleigh number, In Natural Convection in Enclosures, ASME, HTD, 99. 1988.

57.   Higuera, F. and J. Jimenez. Boltzmann approach to lattice gas simulations, Europhys. Lett., 9 (7), pp.663-668. 1989.

58.   Higuera, F. J. and S. Succi. Simulating the flow around a circular cylinder with a lattice Boltzmann equation, Europhys. Lett., 8, pp.517-521. 1989.

59.   Hinton, F. L., M. N. Rosenbluth, S. K. Wong, Y. R. Lin-Liu and R. L. Miller. Modified lattice Boltzmann method for compressible fluid simulations, Phys. Rev. E, 63, pp.061212. 2001.

60.   Hirsch, C., Numerical computation of internal and external flows, Vol. I: fundamentals of numerical discretization, Wiley, Chichester, 1988.

61.   Ho, C. J. and F. J. Tu. An investigation of transient mixed convection of cold water in a tall vertical annulus with a heated rotating inner cylinder, Int. J. Heat & Mass Transfer, 36(11), pp.2847-2859. 1993.

62.   Hou, S., Q. Zou, S. Chen, G. Doolen and A. C. Cogley. Simulation of cavity flow by the lattice Boltzmann method, J. Comp. Phys., 118, pp.329-347. 1995a.

63.   Hou, S. Lattice Boltzmann method for incompressible viscous flow. Ph. D. thesis, Kansas State Univ., Manhattan, Kansas. 1995b.

64.   Hou, S., J. Sterling, S. Chen and G. D. Goolen. A lattice Botlzmann subgrid model for high Reynolds number flows, Fields Inst. Comm., 6, pp.151-166. 1996.

65.   Huang, J. Thermal lattice BGK models for fluid dynamics. Ph. D. thesis, Drexel Univ. 1998.

66.   Inamuro, T., M. Yoshino and F. Ogino. A nonslip boundary condition for lattice Boltzmann simulations, Phys. Fluids, 7, pp.2928-2930. 1995.

67.   Jeffreys, H. and B. S. Jeffreys. Methods of Mathematical Physics. 3rd Edition. Cambridge: Cambridge University Press. 1956.

68.   Koelman, J. M. V. A. A simplified lattice Boltzmann scheme for Navier-Stokes fluid flow, Europhys. Lett., 15 (6), pp.603-607. 1991.

69.   Koschmieder, E. L. Benard cells and Taylor vortices. Cambridge, England: Cambridge university press. 1993.

70.   Kuksenok, O., J. M. Yeomans and A. C. Balazs, Creating localized mixing stations within micro fluidic channels, Langmuir, 17(23), pp.7186-7190. 2001.

71.   Kuksenok, O., J. M. Yeomans and A. C. Balazs. Using patterned substrates to promote mixing in microchannels, Phys. Rev. E, 65(3), pp.031502. 2002.

72.   Ladd, A. J. C. Short-time motion of colloidal particles: numerical simulation via a fluctuating lattice-Boltzmann equation, Phys. Rev. Lett., 70, pp.1339-1342. 1993.

73.   Ladd, A. J. C. Numerical simulations of particulate suspensions via a discretized Boltzmann equation, Part I: Theoretical foundation, J. Fluid Mech., 271, pp.285-309. 1994a.

74.   Ladd, A. J. C. Numerical simulations of particulate suspensions via a discretized Boltzmann equation, Part II: Numerical results, J. Fluid Mech., 271, pp.285-309. 1994b.

75.   Ladd, A. J. C. Sedimentation of homogeneous suspensions of non-Brownian spheres, Phys. Fluids, 9, pp.491-499. 1997.

76.   Ladd, A. J. C. Effects of container walls on the velocity fluctuations of sedimenting spheres, Phys. Rev. Lett., 88, pp.048301. 2002.

77.   Lallemand, P., D. d'Humières, L. S. Luo and R. Rubinstein. Theory of the lattice Boltzmann method: Three-dimensional model for linear viscoelastic fluids, Phys. Rev. E, 67, pp. 021203. 2003.

78.   Lallemand, P. and L. S. Luo. Theory of the lattice Boltzmann method: Dispersion, dissipation, isotropy, Galilean invariance and stability, Phys. Rev. E, 61, pp. 6546-6562. 2000

79.   Lallemand, P. and L. S. Luo. Theory of the lattice Boltzmann method: Acoustic and thermal properties in two and three dimensions, Phys. Rev. E, 68, pp. 036706. 2003a.

80.   Lallemand, P. and L. S. Luo. Hybrid finite-difference thermal lattice Boltzmann equation, Int. J. Mod. Phys. B, 17(1/2), pp.41-47. 2003b.

81.   Liboff, R. L. Kinetic theory. Prentice Hall, Englewood Cliffs, NJ. 1990.

82.   Lim, C. Y., C. Shu, X. D. Niu and Y. T. Chew. Application of lattice Boltzmann method to simulate microchannel flows, Phys. Fluids, 14(7), pp.2299-2308. 2002.

83.   Lor, W. B. and H. S. Chu. Forced and mixed convection in finite vertical concentric cylindrical annuli. In AIAA/ASME joint thermophysics and heat transfer conference, 2, ASME. 1998.

84.   Lu, Z. Y., Y. Liao, D. Y. Qian, J. B. McLaughlin, J. J. Derksen and K. Kontomaris. Large eddy simulations of a stirred tank using the lattice Boltzmann method on a nonuniform grid, J. Comp. Phys., 181, pp.675-704. 2002.

85.   Luo, L. Symmetry breaking of flow in 2-D symmetric channels: simulations by lattice Boltzmann method, Int. J. Mod. Phys. C, 8(4), pp.859-868. 1997.

86.   Luo, L. S., Unified theory of the lattice Boltzmann models for nonideal gases, *Phys. Rev. Lett.* 81(8): 1618-1621, 1998.

87.   Luo, L. S. and S. S. Girimaji. Lattice Boltzmann model for binary mixtures, Phys. Rev. E, 66, pp.035301. 2002.

88.   Luo, L. S. and S. S. Girimaji. Theory of the lattice Boltzmann method: two-fluid model for binary mixtures, Phys. Rev. E, 67, pp.036302. 2003.

89.   Maier, R. S., R. S. Bernard and D. W. Grunau. Boundary conditions for the lattice Boltzmann method, Phys. Fluids, 8, pp.1788-1801. 1996.

90.   Martinez, D., W. H. Matthaeus, S. Chen and D. C. Montgomery. Comparison of spectral method and lattice Boltzmann simulations of two-dimensional hydrodynamics, Phys. Fluids, 6, pp.1285-1298. 1994a.

91.   Martinez, D., S. Chen and W. H. Matthaeus. Lattice Boltzmann magneto-hydro-dynamics, Phys. Plasmas, 1, pp.1850-1867. 1994b.

92.   Mason, R. J. A multi-speed compressible lattice Boltzmann model, J. Stat. Phys., 107(1/2), pp.385-400. 2002.

93.   Massaioli, F., R. Benzi and S. Succi. Exponent tails in two-dimensional Rayleigh-Benard convection, Europhy. Lett., 21(3), pp.305-310. 1993.

94.   McNamara, G. and G. Zanetti. Use of the Boltzmann equation to simulate lattice-gas automata, Phys. Rev. Lett., 61, pp.2332-2335. 1988.

95.   Mei, R., L. S. Luo and W. Shyy. An accurate curved boundary treatment in the lattice Boltzmann method, J. Comp. Phys., 155, pp.307-330. 1999.

96.   Mei, R., W. Shyy, D. Yu and L. Luo. Lattice Boltzmann method for 3-D flows with curved boundary, J. Comp. Phys., 161, pp.680-699. 2000.

97.   Mlaouah, H., T. Tsuji and Nagano Y. A study of non-Boussinesq on transition of thermally induced flows in a square cavity, Int. J. Heat & Fluid Flow, 18(2), pp.100-106. 1997.

98.   Moukalled F. and S. Acharya. Natural convection in the annulus between concentric horizontal circular and square cylinders, AIAA J. Thermophysics & Heat Transfer, 10(3), pp.524-531. 1996.

99.   Napolitano, M. and P. Orlandi. Laminar flow in a complex geometry: a comparison, Int. J. Numer. Methods Fluids, 5, pp. 667-683. 1985.

100.   Niu, X. D., Y. T. Chew and C. Shu, Simulation of flows around an impulsively started circular, J. Comp. Phys., 188, pp. 176-193. 2003.

101. Niu, X. D., C. Shu, Y. T. Chew and T. G. Wang. Investigation of stability and hydrodynamics of different lattice Boltzmann models, J. Stat. Phys., 117(3-4), pp. 665-680. 2004.

102. Noble, D. R., S. Chen, J. G. Georgiadis and R. O. Buckius. A consistent hydro-dynamic boundary condition for the lattice Boltzmann method, Phys. Fluids, 7, pp.203-209. 1995.

103. Noble, D. R., J. G. Georgiadis and R. O. Buckius. Comparison of accuracy and performance for lattice Boltzmann and finite differences simulations of steady viscous flow, Int. J. Numer. Mech. Fluids, 23, pp.1-18. 1996.

104. Onishi, J., Y. Chen and H. Ohashi. Lattice Boltzmann simulation of natural convection in a square cavity, JSME Int. J. B, 44 (1), pp.53-62. 2001.

105. Paspo, I., J. Ouazzani and R. Peyret. A special multidomain technique for the computation of the Czochralski melt configuration, Int. J. Numer. Methods Heat Fluid Flow, 6, pp. 31-58.1996.

106. Pavlo, P., G. Vahala and L. Vahala. Higher-order isotropic velocity grids in lattice methods, Phys. Rev. Lett., 80 (18), pp.3960-3963, 1998a.

107. Pavlo, P., G. Vahala, L. Vahala and M. Soe. Linear stability analysis of thermo-lattice Boltzmann models, J. Comp. Phys., 139, pp79-91, 1998b.

108. Pavlo, P., G. Vahala and L. Vahala. Preliminary results in the use of energy-dependent octagonal lattices thermal lattice Boltzmann simulations, J. Stat. Phys., 107, pp.499-519, 2002.

109. Peng, G., H. Xi and C. Duncan. Lattice Boltzmann method on irregular meshes, Phys. Rev. E, 58, pp.4124-4127. 1998.

110. Peng, G., H. Xi and S. Chou. On boundary conditions in the finite volume lattice Boltzmann method on unstructured meshes, Int. J. Mod. Phys. C, 10 (6), pp.1003-1016. 1999a.

111. Peng, G., H. Xi and C. Duncan. Finite volume scheme for the lattice Boltzmann method on unstructured meshes, Phys. Rev. E, 59, pp.4675-4682. 1999b.

112. Prasad, A. K. and J. R. Koseff. Reynolds-number and end-wall effects on a lid-driven cavity flow, Phys. Fluids A, 1, pp.208-218. 1989.

113. Qi, D. Lattice-Boltzmann simulation of particles in non-zero-Reynolds-number flows, J. Fluid. Mech., 385, pp.41-62. 1999.

114. Qi, D. and L. S. Luo. Transitions in rotations of a non-spherical particle in a three-dimensional moderate Reynolds number Couette flow, Phys. Fluids, 12, pp.4440-4443. 2002a.

115. Qi, D., L. S. Luo, R. Aravamuthan and W. Strieder. Lateral migration and orientation of elliptical particles in Poiseuille flows, J. Stat. Phys., 107, pp.101-120. 2002b.

116. Qi, D. and L. S. Luo. Rotational and orientational behaviour of a three-dimensional spheroidal particle in Couette flow, J. Fluid. Mech., 447, pp.201-203. 2003.

117. Qian, Y. H., D. d' Humieres and P. Lallemand. Lattice BGK models for Navier-Stokes equation, Europhys. Lett., 17 (6), pp.479-484. 1992.

118. Qian, Y. H. Simulating thermo-hydrodynamics with lattice BGK models, J. Sci. Comp., 8 (3), pp.231-241. 1993.

119. Qian, Y. H., S. Succi and S. A. Orszag. Recent advances in lattice Boltzmann computing, Annu. Rev. Comp. Phys., 3, pp.195-242. 1995.

120.   Segre, P. N., O. P. Behrend and P. N. Pusey. Short-time Brownian motion in colloidal suspensions: experiment and simulation, Phys. Rev. E, 52, pp.5070-5083. 1995.

121.   Shan, X. and H. Chen. Lattice Boltzmann model for simulating flows with multiple phases and components, Phys. Rev. E, 47, pp.1815-1819. 1993.

122.   Shan, X. and G. D. Doolen. Multicomponent lattice-Boltzmann model with interparticle interaction, J. Stat. Phys., 81, pp.379-393. 1995.

123.   Shan, X. Solution of Rayleigh-Benard convection using a lattice Boltzmann method, Phy. Rev. E, 55, pp.2780-2788. 1997.

124.   Shi, W., W. Shyy and R. Mei. Finite-difference-based lattice Boltzmann method for inviscid compressible flows, Numer. Heat Transfer B, 40, pp.1-21. 2001.

125.   Shu, C, Y. T. Chew and Y. Liu. An efficient approach for numerical simulation of flows in Czochralski crystal growth, J. Crystal Growth, 181, pp.427-436. 1997.

126.   Shu, C. and H. Xue. Comparison of two approaches for implementing stream function boundary condition in DQ simulation of natural convection in a square cavity, Int. J. Heat & Fluid Flow, 19, pp.59-68. 1998.

127.   Shu, C., Y. T. Chew and X. D. Niu. Least square-based LBM: a meshless approach for simulation of flows with complex geometry, Phy. Rev. E., 64, pp.045701. 2001.

128.   Shu, C. and Y. Zhu. Efficient computation of natural convection in a concentric annulus between an outer square cylinder and an inner circular cylinder, Int. J. Numer. Meth. Fluids, 38, pp.429-445. 2002.

129. Shu, C., X. D. Niu and Y. T. Chew, Taylor-series expansion and least squares-based lattice Boltzmann method: two-dimensional formulation and its applications, Physical Review E, 65, pp. 036708. 2002.

130. Shu, C., X. D. Niu and Y. T. Chew, Taylor series expansion and least squares-based lattice Boltzmann method: three-dimensional formulation and its applications, Int. J. Mod. Phys. C, 14, pp. 925-944. 2003.

131. Sivaloganathan S. and A. Karageorghis. Numerical solution of the 3-D Buoyancy driven cavity problem by a pseudospectral method. Appl. Math. Comp., 75, pp.43-58. 1996.

132. Skordos, P. A. Initial and boundary conditions for the lattice Boltzmann method, Phys. Rev. E, 48, pp.4823-4842. 1993.

133. Soll, W., S. Chen, K. Eggert, D. Grunau and D. Janecky. Application of the lattice Boltzmann/ lattice gas techniques to multifluid flow in porous media. In Computational Methods. in Water Resources X, ed by A. Peters, pp.991-999. Dordrecht: Academic. 1994.

134. Spaid, M. A. A. and F. R. Jr. Phelan. Lattice Boltzmann methods for modeling microscale flow in fibrous porous media, Phys. Fluids., 9, pp.2468-2474. 1997.

135. Sterling, J. and S. Chen. Stability analysis of lattice Boltzmann methods, J. Comp. Phys., 123, pp.196-206. 1996.

136. Succi, S., E. Foti and F. Higuera. Three dimensional flows in complex geometries with the lattice Boltzmann method, Europhys. Lett., 10, pp.433-438. 1989.

137. Succi, S., G. Amati and R. Benzi. Challenges in lattice Boltzmann computing, J. Stat. Phys., 81, pp.5-16. 1995.

138.   Succi, S. The lattice Boltzmann equation for fluid dynamics and beyond. Oxford: Clarendon Press. 2001

139.   Sun, C. Simulations of compressible flows with strong shocks by an adaptive lattice Boltzmann model, J. Comp. Phys., 161, pp.70-84. 2000.

140.   Swift, M. R., W. R. Osborn and J. M. Yeomans. Lattice Boltzmann simulation of non-ideal fluids, Phys. Rev. Lett., 75, pp.830-833. 1995.

141.   Swift, M. R., S. E. Orlandini, W. R. Osborn and J. M. Yeomans. Lattice Boltzmann simulations of liquid-gas and binary-fluid systems, Phys. Rev. E, 54, pp.5041-5052. 1996.

142.   Teixeira, C., H. Chen and D. Freed. Multi-speed thermal lattice Boltzmann method stabilization via equilibrium under-relaxation, Comp. Phys. Comm, 129, pp.207-226. 2000.

143.   Thamida, S. K. and H. C. Chang. Nonlinear electrokinetic ejection and entrainment due to polarization at nearly insulated wedges, Phys. Fluids, 14(12), pp.4315-4328. 2002.

144.   Tölke, J. M. Krafczyk, M. Schulz and E. Rank. Lattice Boltzmann simulations of binary fluid through porous media, Phil. Trans. R. Soc. Lond. A, 360, pp.535-545. 2002.

145.   Trevino, C. and F. Higuera. Lattice Boltzmann and spectral simulation of non-linear stability of Kolmogorov flows, Rev. Mex. Fis., 40, pp.878-890. 1994.

146.   Vahala, G., P. Pavlo, L. Vahala and H. Chen. Effect of velocity shear on a strong temperature gradient- a lattice Boltzmann approach, Phys. Lett. A, 202, pp.376-382. 1995.

147.   Vahala, G., P. Pavlo, L. Vahala and N. S. Martys. Thermal lattice-Boltzmann models (TLBM) for compressible flows, Int. J. Mod. Phys. C 9 (8), pp.1247-1261. 1998.

148.   Wang, D. C., B. S. V. Patnaik and G. W. Wei. A new benchmark quality solution for the buoyancy-driven cavity by discrete singular convolution, Numer. Heat Trans. B, 40, pp. 199-228. 2001.

149.   Wagner, L. Pressure in lattice Boltzmann simulations of flow around a cylinder, Phys. Fluids, 6, pp.3516-3518. 1994.

150.   Wheeler A. A. Four test problems for the numerical simulation of flow in Czochralski crystal growth, J. Crystal Growth, 102, pp.691-695. 1990.

151.   Wolfram, S. Cellular automaton fluids. 1: Basic theory, J. Stat. Phys., 45, pp.471-526. 1986.

152.   Xi, H., G. Peng and S. Chou. Finite-volume lattice Boltzmann method, Phys. Rev. E, 59, pp.6202-6205. 1999a.

153.   Xi, H., G. Peng and S. Chou. Finite-volume lattice Boltzmann schemes in two and three dimensions, Phys. Rev. E, 60, pp.3380-3388. 1999b.

154.   Xu, D., C. Shu and B. C. Khoo. Numerical simulation of flows in Czochralski crystal growth by second-order upwind QUICK scheme, J. Crystal Growth, 173, pp.123-131. 1997.

155.   Yoshino, M. and T. Inamuro. Lattice Boltzmann simulations for flow and heat/mass transfer problems in a three-dimensional porous structure, Int. J. Numer. Meth. Fluids, 43, pp.183-198. 2003.

156.   Zeiser, T., M. Steven, H. Freund, P. Lammers, G. Brenner, F. Durst and J. Bernsdorf. Analysis of the flow field and pressure drop in fixed-bed reactors with

the help of lattice Boltzmann simulations, Philo. Trans. Royal Soci. London A, 360, pp.507-520. 2002.

157.   Ziegler, D. P. Boundary conditions for lattice Boltzmann simulation, J. Stat. Phys., 71, pp.1171-1177. 1993.

158.   Zou, Q. and X. He. On pressure and velocity boundary conditions for the lattice Boltzmann BGK model, Phys. Fluids., 9, pp.1591-1598. 1997.

Vita

NAME: Peng Yan
DATA OF BIRTH: Sep. 1973
PLACE OF BIRTH: HUNAN, CHINA

I was born in HUNAN province, China in 1973. I obtained my *B. Eng* degree (1996) and *M. Eng* degree (1999) from Nanjing University of Aeronautics and Astronautics (NUAA) of China. In the end of 1999, I came to Singapore and studied as a *Ph. D.* candidate in Department of Mechanical Engineering at the National University of Singapore till the end of 2002. The following are the publications related to my *Ph. D.* work:

1. Shu, C., Y. Peng and Y. T. Chew. Simulation of natural convection in a square cavity by Taylor series expansion- and least squares- based lattice Boltzmann method, International Journal of Modern Physics C, 13(10), pp. 1399-1414. 2002.

2. Chew, Y. T., C. Shu and Y. Peng. On implementation of boundary conditions in the application of finite volume lattice Boltzmann method, Journal of Statistical Physics, 107 (1/2), pp. 539-556. 2002.

3. Peng Y., C. Shu and Y. T. Chew. Simulation of natural convection by Taylor series expansion- and least square- based LBM, International Journal of Modern Physics B, 17 (1/2), pp. 165-168. 2003.

4. <u>Peng Y.</u>, Y. T. Chew and C. Shu. Numerical simulation of natural convection in a concentric annulus between a square outer cylinder and a circular inner cylinder using the Taylor-series-expansion and least-squares-based lattice Boltzmann method, Physical Review E 67, pp. 026701. 2003.

5. <u>Peng Y.</u>, C. Shu and Y. T. Chew. Simplified thermal lattice Boltzmann model for incompressible thermal flows, Physical Review E 68, pp. 026701. 2003.

6. <u>Peng Y.</u>, C. Shu, Y. T. Chew and J.Qiu. Numerical investigation of flows in Czochralski crystal growth by an axisymmetric lattice Boltzmann method, Journal of Computational Physics, 186, pp. 295-307. 2003.

7. <u>Peng Y.</u>, C. Shu and Y. T. Chew. Simulation of Czochralski crystal growth by using lattice Boltzmann method, Materials Science Forum, 437-438, pp. 355-358. 2003

8. <u>Peng Y.</u>, C. Shu and Y. T. Chew. A 3D incompressible thermal lattice Boltzmann model and its application to simulate natural convection in a cubic cavity, Journal of Computational Physics, 193, pp. 260-274. 2003.